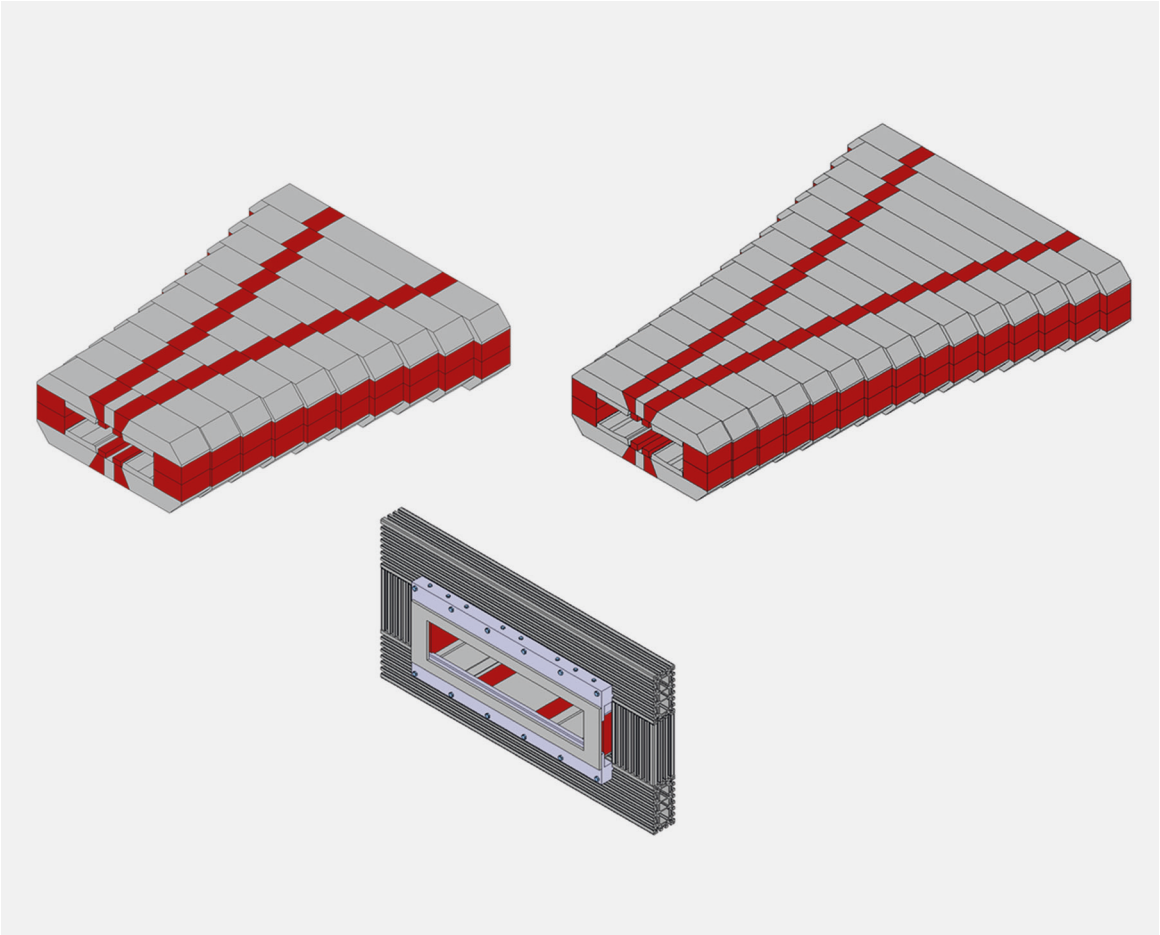

Development of a Multiplexer System and Measurement of the Neutron Yield for a Low-Energy Accelerator-Driven Neutron Source

Marius Rimmler

Schlüsseltechnologien / Key Technologies
Band / Volume 250
ISBN 978-3-95806-600-7

Mitglied der Helmholtz-Gemeinschaft

JÜLICH
Forschungszentrum

Schriften des Forschungszentrums Jülich
Reihe Schlüsseltechnologien / Key Technologies Band / Volume 250

Forschungszentrum Jülich GmbH
Institut für Kernphysik
Kernphysikalische Großgeräte (IKP-4)

Development of a Multiplexer System and Measurement of the Neutron Yield for a Low-Energy Accelerator-Driven Neutron Source

Marius Rimmler

Schriften des Forschungszentrums Jülich
Reihe Schlüsseltechnologien / Key Technologies Band / Volume 250

ISSN 1866-1807 ISBN 978-3-95806-600-7

Bibliografische Information der Deutschen Nationalbibliothek.
Die Deutsche Nationalbibliothek verzeichnet diese Publikation in der
Deutschen Nationalbibliografie; detaillierte Bibliografische Daten
sind im Internet über http://dnb.d-nb.de abrufbar.

Herausgeber und Vertrieb:	Forschungszentrum Jülich GmbH Zentralbibliothek, Verlag 52425 Jülich Tel.: +49 2461 61-5368 Fax: +49 2461 61-6103 zb-publikation@fz-juelich.de www.fz-juelich.de/zb
Umschlaggestaltung:	Grafische Medien, Forschungszentrum Jülich GmbH
Druck:	Grafische Medien, Forschungszentrum Jülich GmbH
Copyright:	Forschungszentrum Jülich 2021

Schriften des Forschungszentrums Jülich
Reihe Schlüsseltechnologien / Key Technologies, Band / Volume 250

D 82 (Diss. RWTH Aachen University, 2021)

ISSN 1866-1807
ISBN 978-3-95806-600-7

Vollständig frei verfügbar über das Publikationsportal des Forschungszentrums Jülich (JuSER)
unter www.fz-juelich.de/zb/openaccess.

Abstract

The High-Brilliance neutron Source (HBS) project aims at developing a low-energy accelerator-driven neutron source facility providing neutron beam brilliances at the corresponding instruments, which are very competitive to medium-flux fission-based research reactors. To obtain a large beam brilliance at HBS, the full-fledged facility simultaneously operates different neutron instruments, which subdivide into three target stations, each efficiently operated to supply different neutron pulse structures. This will be realized by generating an interlaced proton pulse structure containing three different proton beam timing schemes, which are then distributed to the individual target stations. The distribution of the different proton pulse sequences to the target stations is performed by a proton beam multiplexer system which is developed in the frame of this thesis.

A test setup of this multiplexer system, which primarily consists of a kicker and a septum magnet, is developed at the 45 MeV proton accelerator facility JULIC of Forschungszentrum Jülich GmbH. Here, the main focus is on the development of a new type of permanent-magnet-based septum magnet featuring three different magnetic dipole field regions in close proximity. The design process of such a septum magnet is presented in detail together with the analysis of a prototype based on the corresponding magnet technology. Furthermore, proton pulse distribution is demonstrated with the operation of the kicker magnet of the multiplexer test setup being synchronized to the proton beam chopper of JULIC. The integration of the multiplexer system at HBS is described thoroughly including the design of a septum magnet based on the developments at JULIC and scaled to serve the larger proton beam energy of 70 MeV. In the context of the HBS multiplexer system, the HBS High-Energy Beam Transport (HEBT) beamline is designed and associated beam-dynamics calculations are carried out. The effect of the field quality of the HBS septum magnet on the transmission through the HEBT is investigated by particle tracking studies.

In addition, another contribution to the maximization of the neutron beam brilliance at HBS is made by measurements of the neutron yield for different target materials applicable at low-energy accelerator-driven neutron sources in the proton energy range of 22 MeV to 42 MeV. The measurement technique is based on the analysis of the 2.2 MeV prompt gamma line induced by thermal neutron capture in the hydrogen nuclei of a polyethylene moderator. The experimental results are used to benchmark the results obtained from numerical simulations and extrapolated to 70 MeV, which helps selecting the appropriate target material at HBS providing the largest proton-energy-dependent neutron yield and thus neutron beam brilliance.

Contents

Danksagung

1. Introduction: Optimizing low-energy accelerator-driven neutron sources

The potential of neutrons as probe for complex phenomena in soft and hard matter science manifests in several of its elementary properties and interactions [1]. With neutrons being subject to the strong nuclear force, they are scattered from the atomic nucleus which makes them very sensitive to light atoms and thus superior to x-rays when it comes to the localization of hydrogen atoms. Since neutrons are neutral particles, they penetrate deeply through matter without energy loss from ionization making them advantageous for non-destructive investigations. Due to their nuclear spin, neutrons possess a magnetic moment, which makes them suitable for studies of microscopic magnetic structures. Consequently, neutrons are a very promising candidate for scattering experiments by nature. However, the generation of free neutrons is challenging. The most common processes for the production of free neutrons are nuclear fission, spallation or nuclear reactions, with the first two processes being employed routinely at medium to high-flux neutron sources. While various nuclear fission research reactors in Europe are currently shut off as they reach the end of their political and technical lifetime, new spallation sources such as ESS emerge [2, 3]. Nonetheless, the continuously high request for neutron experiments exceeds the capacity available, especially since the construction and operation of spallation neutron sources is very challenging and cost-intensive. Low-energy accelerator-driven neutron sources represent a promising new type of neutron source generating neutrons through nuclear reactions with sub-100 MeV proton or deuteron accelerators. The emerging field of high current particle accelerators allows the realization of medium-flux low-energy accelerator-driven neutron sources compatible with research reactors and complementary applicable with high-flux spallation sources leading to a future healthy neutron eco-system.

Such a high-power low-energy accelerator-driven neutron source is currently planned at the Forschungszentrum Jülich GmbH in the frame of the High-Brilliance neutron Source (HBS) project [4, 5, 6]. The HBS project aims at developing a neutron source based on nuclear reactions driven by a pulsed 70 MeV, 100 mA proton accelerator. As the efficiency of nuclear reactions in terms of the neutron yield, i.e. around 0.1 neutrons per proton at HBS, is much lower than for fission, i.e. one usable neutron per fission event [7, p. 50], or spallation sources, i.e. 20 - 30 neutrons per proton

[7, p. 52], the HBS facility needs to be optimized throughout all subsystems ranging from the ion source via the target-moderator-reflector unit to the individual instruments. The figure of merit at HBS will be the neutron beam brilliance being defined as neutrons per source area, wavelength band, time interval and solid angle. In order to account for the repetitiveness of the pulsed proton beam, the brilliance is further normalized to the number of primary protons yielding the dimension of the source brilliance at HBS [5]

$$[B] = \frac{1}{\mathrm{s\,cm^2\,sr\,(1\%\Delta\lambda/\lambda)\,(mA\,s)}}. \tag{1.1}$$

The HBS concept thus does not aim to provide the highest source strength, i.e. the neutron flux, but intends to optimize the beam brilliance to source strength ratio, which is particularly beneficial for the investigation of small samples.

In this thesis, the focus is on the optimization of two different parameters directly affecting the source brilliance at HBS. One is the relative wavelength uncertainty $\Delta\lambda/\lambda$, the other being the neutron yield (neutrons per mAs). To maximize the source brilliance, one aims for a minimum relative wavelength uncertainty $\Delta\lambda/\lambda$ and a maximum neutron yield.

Optimization of the relative wavelength uncertainty $\Delta\lambda/\lambda$

In order to obtain a minimum $\Delta\lambda/\lambda$ of the neutron beam at HBS, the corresponding proton beam pulsing needs to be adjusted. The interplay between the proton beam pulse length and $\Delta\lambda/\lambda$ of the neutrons at the instrument is presented in figure 1.1.

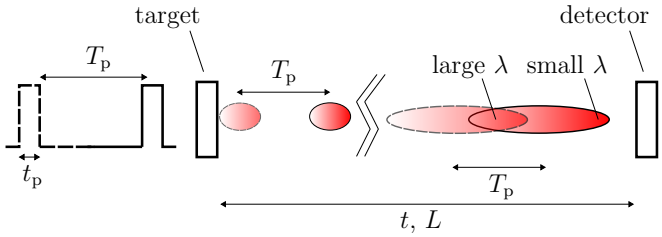

Figure 1.1.: Schematic drawing of interplay between proton pulsing and neutron time structure. The neutron pulses disperse whilst propagating to the detector due their continuous energy spectrum. t_p: proton pulse length, T_p: proton pulse period length, t: neutron time-of-flight, L: distance target-detector, λ: neutron wavelength.

Neutrons generated at the target propagate to the detector at the instrument with their wavelength-dependent velocity $v = h/(m\lambda)$ (h: Planck's constant, m: neutron mass). The velocity is related to the distance from target to detector L, i.e. the instrument length, and the time-of-flight t via $v = L/t$ such that the relative wavelength

uncertainty can be expressed as $\Delta\lambda/\lambda = \sqrt{(\Delta t/t)^2 + (\Delta L/L)^2}$. For a given instrument length L and its uncertainty ΔL, $\Delta\lambda/\lambda$ scales with the relative time-of-flight uncertainty of a neutron at the detector $\Delta t/t$. With Δt depending on the proton beam pulse width t_p as any proton in the proton pulse could have contributed to the generation of a neutron, as well as on the moderation time t_m and the absorption or die-away time t_d in the moderator, one gets $\Delta t \propto \sqrt{t_\mathrm{p}^2 + t_\mathrm{m}^2 + t_\mathrm{d}^2}$ from a convolution. Thus, t_p should be adjusted depending on t_m and t_d, in order to minimize $\Delta\lambda/\lambda$. On the other hand, the proton pulse period length T_p should be chosen such that for experiments with large wavelength neutrons an overlap with small wavelength neutrons of a subsequent neutron pulse, i.e. the so-called frame overlap as shown in figure 1.1, is avoided. Generally requesting a fixed proton beam duty cyle $t_\mathrm{p}/T_\mathrm{p}$ = const., a small relative wavelength uncertainty $\Delta\lambda/\lambda$ and a reduced frame overlap therefore require different configurations of t_p and T_p when considering experiments with different neutron wavelengths λ. For small λ (high energy neutrons), t_p and T_p should be small and large for large λ (low energy neutrons), respectively. At HBS, the proton beam pulsing should be adapted equally well for all instruments operating at different neutron energies. This is realized by the simultaneous operation of different target stations with individual proton beam pulsing. Such operation is maintained by a multiplexer system which is developed in the frame of this thesis.

Optimization of the neutron yield

The second objective of this thesis is to establish a measurement technique for the characterization of different potential target materials for low-energy accelerator-driven neutrons sources in terms of their neutron yield. The target material should be chosen such that it provides the highest neutron yield at the corresponding ion energy, good mechanical stability and radiation hardness. Calculations based on the TALYS nuclear code suggest that the proton induced neutron yield from light (low Z) materials, e.g. beryllium, is optimal below 20 MeV, while at proton energies above 20 MeV, i.e. at HBS, heavy target materials (high Z) such as tantalum appear to be beneficial [8]. However, various experiments on the determination of the neutron yield of beryllium [9] as well as tantalum [10] irradiated by protons show differing results when compared with analytical calculations as well as with numerical simulations using MCNP [11]. Thus, in order to benchmark MCNP as well as analytical calculations from Zakalek et al. [8], a novel method for the determination of the neutron yield is introduced and corresponding measurements are evaluated within this thesis (following [12]).

The outline of this thesis is:

Chapter 1: An introduction to low-energy accelerator-driven neutron sources and HBS is given. The motivation for this work being the maximization of the neutron beam brilliance at HBS is presented.

Chapter 2: The theoretical concepts of charged particle beams in an electromagnetic field with focus on bending magnets is presented. The mechanism of the neutron production in low-energy accelerator-driven neutron sources based on nuclear reactions is explained.

Chapter 3: The layout and a technical overview of the HBS facility and the corresponding test facility at the JULIC accelerator are given.

Chapter 4: A detailed description of the multiplexer system and the corresponding subsystems developed at JULIC for HBS is given.

Chapter 5: The integration of the multiplexer system into the framework of the HBS facility in terms of proton beam transport and radiation hardness is described.

Chapter 6: A neutron yield measurement technique via gamma-ray spectrometry is described. The corresponding results of such experiment at JULIC are presented.

Chapter 7: The outcome of this thesis is summarized and evaluated in terms of a conclusion. An outlook regarding the continuation and future improvements of the work presented in this thesis is given.

2. Theory: Ion beam dynamics and neutron production

This chapter covers the theoretical foundations of charged particle beams, the manipulation of charged particle beams as well as fundamentals of the neutron production at low-energy accelerator-driven neutron sources.

2.1. Beam physics

A particle moving on a curved trajectory is characterized in a curvilinear coordinate system (x, y, s) with s being the distance traveled by the so-called *reference particle*, i.e. at $(x, y) = (0, 0)$, from an arbitrary but fixed start point. Moreover, a co-moving right-handed cartesian coordinate system (x, y, z) starting with z being tangential to the path of the reference particle is introduced. Both representations are displayed in figure 2.1. An ensemble of charged particles traveling with momentum $\boldsymbol{p} = (p_x, p_y, p_z)$

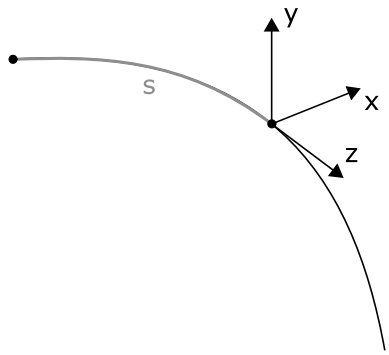

Figure 2.1.: Curvilinear coordinate system (x, y, s) and co-moving cartesian coordinate system (x, y, z) for the characterization of charged particles on curved trajectories.

for which $p_x, p_y \ll p_z$ holds is called *beam*. Generally an ensemble of N point-like particles can be described by a point in $6N$-dimensional phase space [13, p. 114]. For convenience, the $6N$-dimensional phase space can be factorized into N points in 6-dimensional phase space assuming that interactions between the particles can be described by a a smooth continuous field that acts externally on the particles [14, p.

21]. Furthermore, the influence of purely conservative forces is considered such that the particle density in phase space stays constant according to LIOUVILLE'S theorem [15, p. 215]. This allows to conveniently determine the particle beam's phase space distribution at any point along s in figure 2.1 by knowing the occupied area in phase space of the particles in the beginning, which will be described in the following two sections.

2.1.1. Phase space and beam emittance

A single particle of a beam is fully described by the six component vector

$$\boldsymbol{x}(s) = \begin{pmatrix} x \\ x' \\ y \\ y' \\ l \\ \delta \end{pmatrix}. \tag{2.1}$$

Here, x and y represent the transversal coordinates according to figure 2.1 whereas x' and y' denote the directional deviation with respect to the reference particle with

$$x' = \frac{\mathrm{d}x}{\mathrm{d}s} \overset{1}{=} \frac{\mathrm{d}x}{\mathrm{d}z} = \frac{p_x}{p_z} = \tan\Theta_x. \tag{2.2}$$

For $p_z \gg p_x$, as for a beam, the divergence angle Θ_x is small, such that $\tan\Theta_x \approx \Theta_x$. Hence, $x' \approx \Theta_x$ is typically given as divergence angle with respect to the reference particle. The same holds for y'. In equation 2.1, l and δ represent the longitudinal coordinates of the particle with l being the longitudinal spatial displacement along s and

$$\delta = \frac{p - p_0}{p_0} = \frac{\Delta p}{p_0} = \frac{\gamma}{\gamma + 1}\frac{\Delta T}{T_0} \tag{2.3}$$

being the relative momentum deviation of a particle with momentum p with respect to the reference particle with momentum p_0. Here, ΔT and T_0 denote the kinetic energy deviation and kinetic energy of the reference particle, respectively, and $\gamma = 1/\sqrt{1-\beta^2}$ is the LORENTZ factor with $\beta = v/c$. Here, v is the velocity of the reference particle and c is the speed of light. Equation 2.1 represents the particle's phase space coordinates as it represents the particle as a point in 6-dimensional phase space.

A particle beam is described by a statistical set of points in phase space, which can be monitored transversally by a projection onto the subspaces (x, x') and (y, y'). In the following, only the (x, x')-subspace is considered, as the formalism is identical for (y, y') and as both subspaces are fully decoupled in linear approximation in the presence of beam manipulations with mid-plane symmetry. In (x, x')-subspace, particles are centered around their arithmetic mean

[1] This holds in linear approximation.

$$\begin{aligned} \bar{x} &= \frac{1}{N}\sum_i^N x_i \\ \bar{x'} &= \frac{1}{N}\sum_i^N x'_i. \end{aligned} \tag{2.4}$$

The variances are given by

$$\begin{aligned} \sigma_x &= \sqrt{\frac{1}{N}\sum_i^N \left(x_i - \bar{x}\right)^2} \\ \sigma_{x'} &= \sqrt{\frac{1}{N}\sum_i^N \left(x'_i - \bar{x'}\right)^2} \\ \sigma^2_{xx'} &= \frac{1}{N}\sum_i^N \left(x_i - \bar{x}\right)\left(x'_i - \bar{x'}\right) \end{aligned} \tag{2.5}$$

and are referred to as the spatial and angular root mean square (rms) envelopes of the beam (enclosing 68.27 % of the particles in the x-projection as well as in the x'-projection of a 2-dimensional GAUSSIAN distribution), as well as the covariance between x and x', respectively. A GAUSSIAN distribution is generally a good approximation for charged particle beams with 6 rms beam envelopes, i.e. $6\sigma_x$ and 99.73 % of all particles, representing the diameter of the beam [16, p. 155 f.].

In the presence of linear forces only, it can be shown that all particle trajectories in (x, x')-subspace lie on ellipses [15, p. 227]. It is thus convenient to introduce a so-called *phase space ellipse* that is represented by its 2-dimensional ellipse matrix

$$\Sigma_x = \begin{pmatrix} \sigma_{11} & \sigma_{12} \\ \sigma_{12} & \sigma_{22} \end{pmatrix}. \tag{2.6}$$

Note that a symmetric matrix with $\sigma_{21} = \sigma_{12}$ is considered. An ellipse in (x, x')-subspace has to fulfill the general equation of a 2-dimensional ellipse, which can be written as

$$(x, x') \cdot \Sigma_x^{-1} \cdot \begin{pmatrix} x \\ x' \end{pmatrix} = 1. \tag{2.7}$$

The inverse matrix of Σ_x in equation 2.6 is

$$\Sigma_x^{-1} = \frac{1}{\det \Sigma_x} \begin{pmatrix} \sigma_{22} & -\sigma_{12} \\ -\sigma_{12} & \sigma_{11} \end{pmatrix} \tag{2.8}$$

and thus equation 2.7 gives

$$\sigma_{22}x^2 - 2\sigma_{12}xx' + \sigma_{11}x'^2 = \det \Sigma_x. \tag{2.9}$$

The volume of an n-dimensional ellipse with ellipse matrix Σ can be written as

$$V_n = \frac{\pi^{n/2}}{\Gamma(1+n/2)}\sqrt{\det \Sigma} \tag{2.10}$$

where $\Gamma(n) = (n-1)!$ (with $n \in \mathbb{N}$) is the Gamma function. Thus the area of a 2-dimensional ellipse can be written as $A = V_2 = \pi\sqrt{\det \Sigma}$.

The transversal equation of motion for x (identical for y)

$$x'' + k(z)x = 0 \tag{2.11}$$

of a particle flying through an arbitrary beam transport system with a function $k(z)$ representing the manipulation of the particle in phase space along z can be solved with the ansatz

$$x(z) = \sqrt{\epsilon}\sqrt{\beta(z)}\cos\left[\psi(z) - \psi_0\right]. \tag{2.12}$$

Here, ϵ and ψ_0 are integration constants and $\beta(z)$ represents the amplitude and $\psi(z)$ the phase function along z, respectively. Equation 2.11 is called Hill's differential equation. Inserting equation 2.12 into equation 2.11 and following [15, p. 227], one gets

$$\gamma x^2 + 2\alpha x x' + \beta x'^2 = \epsilon \tag{2.13}$$

by defining $\alpha = -\beta'/2$ and $\gamma = (1+\alpha^2)/\beta$. Equation 2.13 is called Courant-Snyder invariant [17].

Comparing equation 2.13, multiplied by ϵ, and equation 2.9, one can deduce a physical interpretation of the Courant-Snyder invariant. It shows that a particle always moves on an ellipse in phase space whilst traveling along s in real space. While the shape of this ellipse changes along z or s with $\beta(s)$, $\alpha(s)$ and $\gamma(s)$, its area $A = \pi\sqrt{\det \Sigma} = \pi\epsilon$ stays constant. Referring to Liouville's theorem [15, p. 215], every particle that starts on an ellipse in phase space stays on an ellipse with constant ϵ. Furthermore, all the particles of a beam that travel on smaller ellipses in phase space than that of a specified particle will stay on these smaller ellipses. Thus, it is sufficient to use one sufficiently large ellipse to describe the beam in its 2-dimensional phase space. This ellipse is characterized by the so-called *beam matrix*

$$\Sigma_x = \begin{pmatrix} \sigma_{11} & \sigma_{12} \\ \sigma_{12} & \sigma_{22} \end{pmatrix} = \epsilon \begin{pmatrix} \beta_x & -\alpha_x \\ -\alpha_x & \gamma_x \end{pmatrix}. \tag{2.14}$$

The parameters $\beta(s)$, $\alpha(s)$ and $\gamma(s)$ are called betatron functions, lattice functions or Twiss parameters. The parameter ϵ is called emittance of the beam. With equation 2.12, it can be shown [15, p. 223] that together with equation 2.14, one gets

$$\begin{aligned} \sigma_{11} &= \epsilon_x \beta_x = \sigma_x^2 \\ \sigma_{22} &= \epsilon_x \gamma_x = \sigma_{x'}^2 \\ \sigma_{12} &= -\epsilon_x \alpha_x = \sigma_{xx'}^2 \end{aligned} \tag{2.15}$$

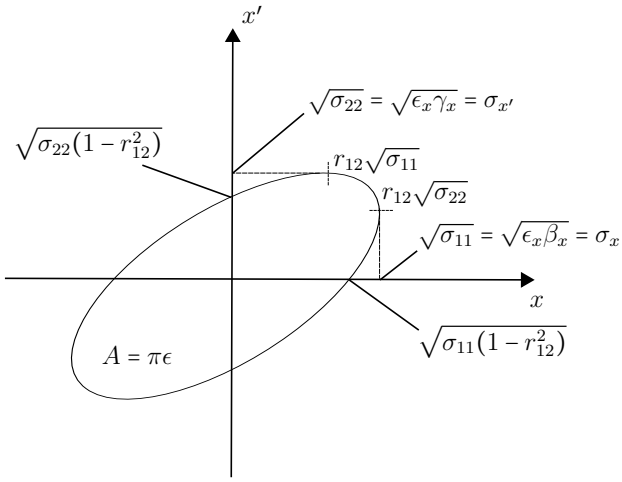

Figure 2.2.: Phase space ellipse in (x, x')-subspace. The size and the shape of the ellipse is defined by the beam matrix elements σ_{11}, σ_{12} and σ_{22}, with $r_{12} = \sigma_{12}/\sqrt{\sigma_{11}\sigma_{22}}$ being a dimensionless correlation parameter. Note that the maximal extent of the ellipse in x and x' is given by the rms variances of the particles σ_x and $\sigma_{x'}$, respectively. The occupied area in phase space $A = \pi\epsilon$ is defined by the emittance ϵ.

when assuming a GAUSSIAN particle distribution. With equation 2.15 the phase space ellipse in (x, x')-subspace, represented by figure 2.2, surrounds all the particles in phase space deviating by the rms variances (equation 2.5) from the reference particle at most. In this scenario, the emittance ϵ of the beam is referred to as rms-emittance, a measure for the occupied area in phase space and the beam quality. In order to compare the beam quality of different accelerators at different energies, it is convenient to use the so-called normalized emittance

$$\epsilon_n = \beta\gamma\epsilon \tag{2.16}$$

in order to account for adiabatic damping, i.e. emittance decrease, at higher energies [15, p. 345].

Having set up the formalism for particles in horizontal (x, x') (and analogous vertical (y, y')) phase space, a full representation of the particle beam can be given by extending to a phase space ellipsoid depicted by the 5-dimensional symmetric beam matrix

$$\Sigma = \begin{pmatrix} \sigma_{11} & \sigma_{12} & \sigma_{13} & \sigma_{14} & \sigma_{16} \\ \sigma_{12} & \sigma_{22} & \sigma_{23} & \sigma_{24} & \sigma_{26} \\ \sigma_{13} & \sigma_{23} & \sigma_{33} & \sigma_{34} & \sigma_{36} \\ \sigma_{14} & \sigma_{24} & \sigma_{34} & \sigma_{44} & \sigma_{46} \\ \sigma_{16} & \sigma_{26} & \sigma_{36} & \sigma_{46} & \sigma_{66} \end{pmatrix} = \begin{pmatrix} \multicolumn{2}{c}{\multirow{2}{*}{$\boldsymbol{\Sigma_x}$}} & 0 & 0 & \sigma_{16} \\ & & 0 & 0 & \sigma_{26} \\ 0 & 0 & \multicolumn{2}{c}{\multirow{2}{*}{$\boldsymbol{\Sigma_y}$}} & 0 \\ 0 & 0 & & & 0 \\ \sigma_{16} & \sigma_{26} & 0 & 0 & \sigma_{66} \end{pmatrix}, \tag{2.17}$$

where the horizontal and vertical subspaces are assumed to be decoupled and the dispersion, i.e. the energy-dependent evolution of the beam envelope, is solely introduced in the horizontal plane. The consideration of a 5-dimensional subspace is valid, when a beam without longitudinal structure[2] is considered, such that $x_5 = l$ is dropped in equation 2.1. In equation 2.17, Σ_x and Σ_y represent the transversal beam matrices as described in equation 2.14 and σ_{16}, σ_{26} and σ_{66} represent the spatial dispersion, angular dispersion and momentum uncertainty, with $\sigma_{66} = \delta^2$ from equation 2.3, respectively. The matrix element σ_{16}, depicting the spatial dispersion, correlates x and δ, while the matrix element σ_{26}, depicting the angular dispersion, correlates x' and δ. It is sometimes convenient to introduce the so-called dispersion function η as well as the derivative of the dispersion function $\eta' = \mathrm{d}\eta/\mathrm{d}s$ given by

$$\eta = \frac{\sigma_{16}}{\sigma_{66}} \tag{2.18}$$

$$\eta' = \frac{\sigma_{26}}{\sigma_{66}}. \tag{2.19}$$

Dispersion primarily arises in the horizontal plane from the deflection by dipole magnets. Here, a finite momentum uncertainty δ allows certain particles to travel on different trajectories compared to the reference particle as shown in figure 2.3. This is due to the energy-dependent Lorentz force (equation 2.21).

Once a beam obtains finite dispersion, i.e. σ_{16} or σ_{26} non-zero, it is altered by any further beam manipulation and drift. Considering the effect of dispersion on the transversal (primarily horizontal) beam envelope in more detail, one observes a dispersive broadening of the horizontal phase space ellipse shown in figure 2.4 [16, p. 168]. In this Figure, it can be seen that $(\sigma_{16}, \sigma_{26}) \neq (0, 0)$ alters the size and shape of the actual horizontal phase ellipse, such that the rms beam size and divergence of a dispersive beam is described by

$$\begin{aligned} \sigma_x &= \sqrt{\sigma_{11}^{(0)} + \frac{\sigma_{16}^2}{\sigma_{66}}} \\ \sigma_{x'} &= \sqrt{\sigma_{22}^{(0)} + \frac{\sigma_{26}^2}{\sigma_{66}}} \end{aligned} \tag{2.20}$$

[2] In this work, the focus is on above-µs time structures of the particle beam, such that the bunched time structure of the beam in the sub-100 ns range from acceleration is not considered. Thus, a longitudinally continuous beam is assumed.

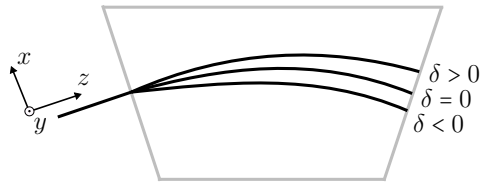

Figure 2.3.: Dispersion, i.e. energy-dependent evolution of the beam envelope, induced in a dipole magnet deflecting horizontally. Particles with higher energy than the reference particle, $\delta > 0$, experience weaker deflection, while particles with lower energy than the reference particle, $\delta < 0$, experience stronger deflection than the reference particle. This results in a horizontal beam envelope at the end of the dipole magnet which depends on δ.

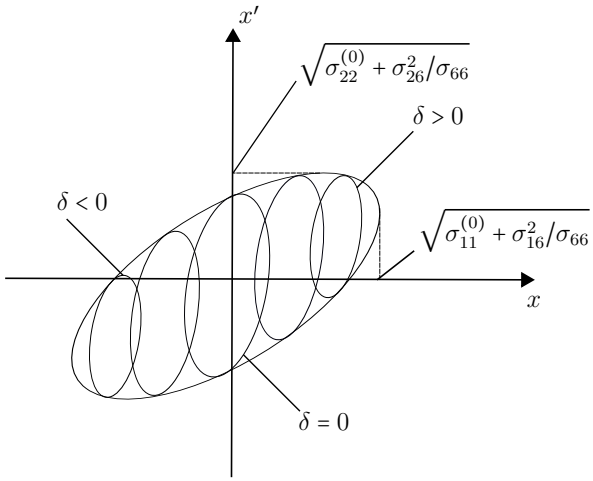

Figure 2.4.: Dispersive broadening of the phase space ellipse in (x, x') phase space. The figure shows phase space ellipses at $\delta = 0$, i.e. the actual phase space ellipse in the absence of dispersion, and additional phase space ellipses with $\delta \neq 0$ and $\sigma_{16}, \sigma_{26} > 0$. These additional phase space ellipses represent cross-sections of the 3-dimensional phase space ellipsoid (x, x', δ), resembling the shape of the dispersion-free phase space ellipse and scaled according to the decreasing number of particles in this energy interval.

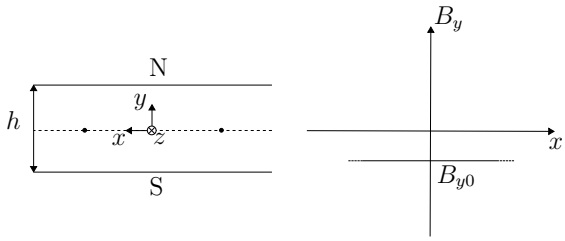

Figure 2.5.: Dipole geometry (left) and constant magnetic flux density B_{y0} versus horizontal position x. Here, $B_x = 0$, i.e. a horizontal bending magnet. h is the pole gap height.

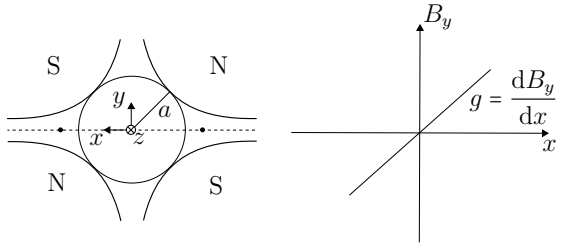

Figure 2.6.: Quadrupole geometry (left) and linear magnetic flux density $B_y = gx$ versus horizontal position x. Here, $B_x = gy$ and $g > 0$, i.e. a focusing quadrupole in x and defocusing in y. a is the aperture radius.

with $\sigma_{11}^{(0)}$ and $\sigma_{22}^{(0)}$ being the beam matrix elements without dispersion. Note that the emittance is typically specified without dispersive broadening. When $(\sigma_{36}, \sigma_{46}) \neq (0, 0)$ in equation 2.17, the same formalism applies for the vertical phase ellipse.

2.1.2. Transverse linear beam dynamics

Equation 2.11 gives the transverse equation of motion in the approximation of linear beam dynamics. This means non-linear contributions are either neglected or treated separately as perturbations. Manipulation of charged particle beams is performed via the LORENTZ force

$$\vec{F}_L = q\left(\vec{E} + \vec{v} \times \vec{B}\right). \tag{2.21}$$

In this work, the focus is on magnetic elements for beam manipulation and thus, in linear approximation, consider the linear magnetic fields for dipole (bending) and quadrupole magnets

$$\begin{aligned} B_x &= B_{x0} + gy \\ B_y &= B_{y0} + gx, \end{aligned} \tag{2.22}$$

where B_{x0}, B_{y0} are the dipole field in x and y, respectively, and g is the gradient of the quadrupole as shown in figure 2.5 and figure 2.6. The constant dipole field is employed in order to bend the trajectory of the beam either horizontally or vertically.

The linear quadrupole field acts as focusing device in x for $g > 0$, deflecting all particles with x being different from the reference particle towards the reference particle. At the same time, all particles with y being different from the reference particle are deflected away from the reference particle in y. Here, the deflection scales with the offset of the individual particles from the reference particle. In summary, a quadrupole with $g > 0$ is called focusing quadrupole, i.e. focusing in x and defocusing in y, and a quadrupole with $g < 0$ is called defocusing quadrupole, i.e. defocusing in x and focusing in y. Both dipole and quadrupole field contributions in equation 2.22 contribute via equation 2.21 to the magnet strength parameter $k(z)$ in the equation of motion (see HILL'S differential equation in equation 2.11) yielding

$$x'' + \left(k_0(z) + \kappa_0^2(z)\right) x = 0 \tag{2.23}$$

where $k_0(z)$ and $\kappa_0(z)$ take into account the focusing power from quadrupole and bending magnets along z, respectively[3].

In a beam transport line, one typically obtains a sequence of different magnets and drift spaces, i.e. regions without any magnetic field, resulting in an arbitrary distribution of the magnet strength parameter $k(z)$. This makes it impossible to formulate a general solution of equation 2.23. A tool to analytically calculate the trajectory of particles based on its equation of motion is the matrix formalism [17]. It uses the fact that the solution of any second-order differential equation (as equation 2.23) is uniquely determined by its initial values x_0' and x_0, which can be expressed in matrix notation as

$$\begin{pmatrix} x(z) \\ x'(z) \end{pmatrix} = \begin{pmatrix} M_{11} & M_{12} \\ M_{21} & M_{22} \end{pmatrix} \begin{pmatrix} x_0 \\ x_0' \end{pmatrix}, \tag{2.24}$$

with the 2×2 matrix M being the so-called *transport matrix*. Equation 2.24 holds under the assumption that during propagation from 0 to z, the magnet strength parameter $k(z)$ undergoes a step-like evolution, such that small pieces Δz where $k(z \to z + \Delta z) = \text{const.}$ can be obtained. In this scenario, M is composed of an array of matrices, each matrix characterizing the trajectory of a particle through a drift, bending or quadrupole element with different strength subsequently attached onto each other by regular matrix multiplication as $M = M_i M_{i-1} .. M_1 M_0$ with M_0 being the transport matrix of the first element traversed by the beam.

The transport matrix can be extended to a more general formulation when taking into account both transversal dimensions (x, x') and (y, y') as well as the dispersion originating from the relative momentum uncertainty δ (see equation 2.3). The latter leads to an inhomogeneous differential equation

$$x'' + \left(k_0(z) + \kappa_0^2(z)\right) x = \kappa_0 \delta. \tag{2.25}$$

[3]The structure of the equation of motion for y is the same.

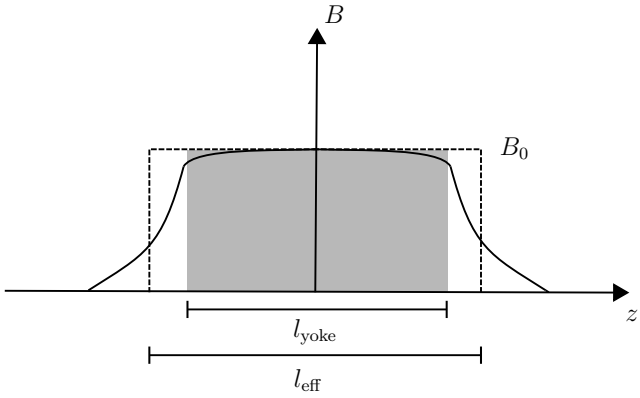

Figure 2.7.: Hard-edge model of a dipole magnet. The actual magnetic flux density $B(z)$ at fixed horizontal coordinates x and y is indicated by the solid line. B changes with z depending on the geometry of the magnet which is indicated by the gray shaded area marking the yoke of the magnet with length l_{yoke}. The dashed line represents a constant substitute of the actual field with B_0 and length l_{eff} where $B(z = 0) = B_0$.

With this the transport matrix is represented by a 5-dimensional matrix

$$M = \begin{pmatrix} (x|x) & (x|x') & 0 & 0 & (x|\delta) \\ (x'|x) & (x'|x') & 0 & 0 & (x'|\delta) \\ 0 & 0 & (y|y) & (y|y') & 0 \\ 0 & 0 & (y'|y) & (y'|y') & 0 \\ 0 & 0 & 0 & 0 & (\delta|\delta) \end{pmatrix}, \tag{2.26}$$

with $(.|.)$ indicating the connection between initial and final value. As in the previous section, a longitunally continuous beam is considered and thus the longitudinal spatial coordinate l in equation 2.1 is neglected.

With the 5-dimensional transport matrix in equation 2.26, the beam matrix in equation 2.17 can be propagated as [18, p. 153]

$$\Sigma = M\Sigma_0 M^T. \tag{2.27}$$

Note that the transport matrix formalism works under the assumption that the magnetic strength parameter $k(z)$ evolves as step-like function. However, real magnets do not feature sudden changes of the magnetic flux density. Therefore, the so-called *hard-edge model* is employed to approximate smooth transitions of the magnetic flux density by a step function as shown in figure 2.7. With this, $B(z)$ is replaced by a box-shaped field distribution along z with B_0 and length

$$l_{\text{eff}} = \frac{\int_{-\infty}^{\infty} B(z)\mathrm{d}z}{B_0}. \tag{2.28}$$

A similar approximation is employed for quadrupole magnets with

$$l_{\text{eff}} = \frac{\int_{-\infty}^{\infty} g(z)\mathrm{d}z}{g_0} \tag{2.29}$$

taking into account the z-dependent evolution of the quadrupole gradient $g(z)$ and $g(z=0) = g_0$. The length l_{eff} is called effective length. In general the effective length can be approximated to be

$$\begin{aligned} l_{\text{eff}} &= l_{\text{yoke}} + 1.3\,g, \\ l_{\text{eff}} &= l_{\text{yoke}} + a \end{aligned} \tag{2.30}$$

for a dipole and for a quadrupole magnet with g being the dipole gap height and a being the quadrupole aperture radius as indicated in figure 2.5 and figure 2.6, respectively.

The fundamental elements of transverse linear beam dynamics, i.e. drift, dipole (bending) and quadrupole elements are represented by the following 5-dimensional transport matrices [16, p. 135 ff.]. The drift transport matrix can be written as

$$M_{\text{drift}} = \begin{pmatrix} 1 & L & 0 & 0 & 0 \\ 0 & 1 & 0 & 0 & 0 \\ 0 & 0 & 1 & L & 0 \\ 0 & 0 & 0 & 1 & 0 \\ 0 & 0 & 0 & 0 & 1 \end{pmatrix}, \tag{2.31}$$

with L being the drift length. A (horizontally) focusing quadrupole (QF) is represented by

$$M_{\text{QF}} = \begin{pmatrix} \cos(\sqrt{k}L) & \sin(\sqrt{k}L)/\sqrt{k} & 0 & 0 & 0 \\ -\sqrt{k}\sin(\sqrt{k}L) & \cos(\sqrt{k}L) & 0 & 0 & 0 \\ 0 & 0 & \cosh(\sqrt{k}L) & \sinh(\sqrt{k}L)/\sqrt{k} & 0 \\ 0 & 0 & \sqrt{k}\sinh(\sqrt{k}L) & \cosh(\sqrt{k}L) & 0 \\ 0 & 0 & 0 & 0 & 1 \end{pmatrix} \tag{2.32}$$

and a (horizontally) defocusing quadrupole (QD), i.e. vertically focusing, by

$$M_{\text{QD}} = \begin{pmatrix} \cosh(\sqrt{k}L) & \sinh(\sqrt{k}L)/\sqrt{k} & 0 & 0 & 0 \\ \sqrt{k}\sinh(\sqrt{k}L) & \cosh(\sqrt{k}L) & 0 & 0 & 0 \\ 0 & 0 & \cos(\sqrt{k}L) & \sin(\sqrt{k}L)/\sqrt{k} & 0 \\ 0 & 0 & -\sqrt{k}\sin(\sqrt{k}L) & \cos(\sqrt{k}L) & 0 \\ 0 & 0 & 0 & 0 & 1 \end{pmatrix}, \tag{2.33}$$

with L being the effective length of the quadrupole magnet and k being the quadrupole strength $k = g/(B\rho)$. Here, $(B\rho)$ is a parameter that quantifies the magnetic rigidity of the beam. The larger the rigidity of the beam, the stronger the magnets required

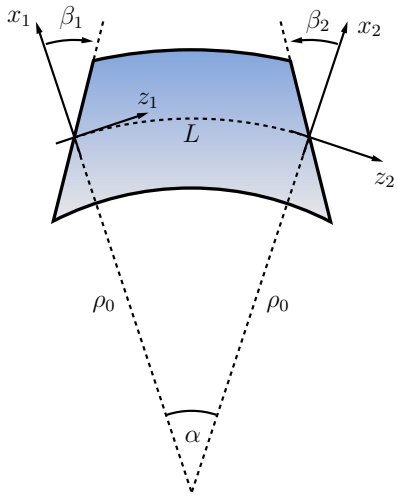

Figure 2.8.: Sector bending magnet with length L, bend angle α and bend radius ρ_0. β_1 and β_2 are called edge angles. Taken and adapted from [19].

to focus or bend the beam. The transport matrix of a (sector) bending magnet or dipole magnet is

$$M_{\text{sbend}} = \begin{pmatrix} \cos\alpha & \rho_0 \sin\alpha & 0 & 0 & \rho_0(1-\cos\alpha) \\ -\sin\alpha/\rho_0 & \cos\alpha & 0 & 0 & \sin\alpha \\ 0 & 0 & 1 & \rho_0\alpha & 0 \\ 0 & 0 & 0 & 1 & 0 \\ 0 & 0 & 0 & 0 & 1 \end{pmatrix}, \tag{2.34}$$

with the bend angle α and the bend radius ρ_0 as displayed in figure 2.8. Bending magnets are represented by two different types. The sector bending magnet is constructed such that the edges are orthogonal to the trajectory of incoming and outgoing beam as shown in figure 2.8 for $\beta_1 = \beta_2 = 0$. The rectangular bending magnet yields an angle of $\alpha/2$ with the trajectory of the beam as shown in figure 2.9 for $\beta_1 = \beta_2 = 0$. The design of a rectangular bending magnet can be deduced from the sector bending magnet by setting $\beta_1 = \beta_2 = \alpha/2$ in figure 2.8.

Apart from bending the particle beam trajectory, dipole magnets have focusing properties. Particles with a horizontal offset $x > 0$ with respect to the reference particle travel on a larger path in the dipole magnet and thus experience a larger deflection than the reference particle. Vice versa for $x < 0$ and thus particles with $x \neq 0$ obtain horizontal focusing in a dipole field, i.e. so-called *dipole focusing* being described by equation 2.34. Furthermore, particles, which enter a bending magnet on a path that is not orthogonal to the edge of the magnet yoke obtain so-called *edge focusing*. This effect occurs in any bending magnet that is different from the design

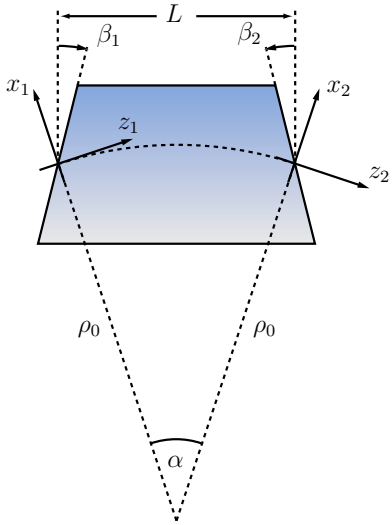

Figure 2.9.: Rectangular bending magnet with length L, bend angle α and bend radius ρ_0. β_1 and β_2 are called edge angles. The rectangular bend magnet can be constructed from the sector bending magnet with $\beta_1 = \beta_2 = \alpha/2$ in figure 2.8. Taken and adapted from [19].

in figure 2.8 when $\beta_1 = \beta_2 \neq 0$. In such bending magnets, the incoming and outgoing beam sees a field gradient which is vertically focusing and horizontally defocusing for $\beta_{1,2} > 0$, and vice versa for $\beta_{1,2} < 0$. The transport matrix for edge focusing can be expressed as

$$M_{\text{edge}} = \begin{pmatrix} 1 & 0 & 0 & 0 & 0 \\ \tan\beta/\rho_0 & 1 & 0 & 0 & 0 \\ 0 & 0 & 1 & 0 & 0 \\ 0 & 0 & -\tan\beta/\rho_0 & 1 & 0 \\ 0 & 0 & 0 & 0 & 1 \end{pmatrix}, \tag{2.35}$$

with $\beta_1 = \beta_2 = \beta$ [16, p. 139 ff.]. With this, a rectangular bending magnet can be described as

$$M_{\text{rbend}} = M_{\text{edge}}(\beta = \alpha/2) M_{\text{sbend}} M_{\text{edge}}(\beta = \alpha/2). \tag{2.36}$$

More details on the design of magnets for beam deflection are presented in the following section.

2.2. Magnets for beam deflection

For the deflection of charged particles in the MeV energy range, dipole magnets are the tool of choice. This section treats the basics of the deflection of charged particles in dipole magnets followed by the presentation of different concepts of generating magnetic fields in dipole magnets. Then, a measure for the quality of accelerator magnets in terms of the so-called *harmonic content* is introduced. Finally, special dipole magnets as investigated in this thesis, i.e. *kicker* and *septum* magnets, are presented.

2.2.1. Magnetic beam deflection

Charged particles in a magnetic field experience a deflection which is characterized by the LORENTZ force (equation 2.21). Consequently, particles with mass m and charge q traveling with velocity v orthogonal to a static homogeneous magnetic field B follow a circular orbit with radius ρ with

$$\frac{mv^2}{\rho} = qvB. \tag{2.37}$$

With this,

$$(B\rho) = \frac{p}{q} \tag{2.38}$$

gives the momentum and charge specific quantity $(B\rho)$ relating the magnetic field B and the bending radius ρ. $(B\rho)$ is referred to as so-called *magnetic rigidity* or *beam rigidity* (or $(B\rho)$-*value*). The larger $(B\rho)$, the larger the required magnetic field at constant bending radius. For singly charged ions ($q = \mathrm{e}$), $(B\rho)$ can be expressed as

$$(B\rho)[\mathrm{T\,m}] \overset{4}{=} \frac{p[\mathrm{GeV/c}]}{0.3} \tag{2.39}$$

or with natural units, i.e. $\mathrm{c} = 1$, and $p = \sqrt{T^2 + 2Tm}$,

$$(B\rho)[\mathrm{T\,m}] = \frac{\sqrt{T^2[\mathrm{MeV}^2] + 2T[\mathrm{MeV}]m[\mathrm{MeV}]} \cdot 1 \times 10^{-3}}{0.3} \tag{2.40}$$

with T being the ion kinetic energy and m being the ion mass. For protons, $m \approx 938\,\mathrm{MeV}$.

Similar to magnetic deflection, electric fields can be employed to deflect charged particles. In order to obtain a circular orbit, the electric field E has to act in the plane of the orbit. Furthermore, it needs to act always orthogonal to the particles' velocity v and thus the electrodes generating the electric field E resemble the shape of the particles' circular trajectory. Analogous to the magnetic rigidity (equation 2.38), an *electric rigidity* $(E\rho)[\mathrm{V}] = (B\rho[\mathrm{T\,m}]) \cdot v$ can be defined. As the electric rigidity scales

[4] with $1\,\mathrm{e\,T\,m} = 1\,\mathrm{eV/(m/s)} = 3 \times 10^8\,\mathrm{eV}/(3 \times 10^8\,\mathrm{m/s}) \approx 0.3\,\mathrm{GeV/c}$.

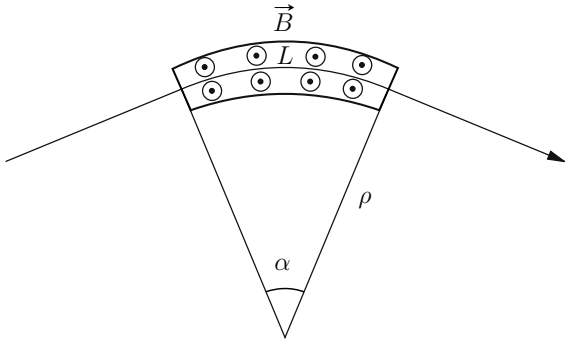

Figure 2.10.: Magnetic deflection of a dipole magnet with length L and magnetic field B. The charged particle beam follows a circular orbit in the magnet with bending radius ρ. The deflection angle is $\alpha = L/\rho$.

with the square of the particle velocity v and the magnetic rigidity scales linearly with v, electric deflection of particles with larger kinetic energy becomes increasingly inefficient. A rule of thumb states that magnetic deflection shall primarily be employed above an electric rigidity of 1 MV, i.e. a kinetic energy of the protons of 500 keV [16, p. 27]. Since the developments in this thesis focus on proton beams with energies of 45 MeV and 70 MeV, magnetic deflection is considered exclusively in the following.

With $(B\rho)$ fixed, the bending radius ρ in a homogeneous magnetic field B is $\rho = (B\rho)/B$. Thus according to the geometry presented in figure 2.10 the deflection angle α of a beam after passing a dipole magnet with magnetic field B and length L is $\alpha = BL/(B\rho)$ or more generally

$$\alpha = \frac{\int B\mathrm{d}l}{(B\rho)} = \frac{B_{\max} l_{\mathrm{eff}}}{(B\rho)}, \tag{2.41}$$

with $\int B\mathrm{d}l$ being the integrated magnetic field along the trajectory of the reference particle in the magnet. Here, $B_{\max}$ being the maximum field and l_{eff} being the effective length of the dipole. Note that figure 2.10 shows a sector bending magnet design as presented in figure 2.8 where the length of the magnet corresponds to the length of the beam trajectory in the magnet. Considering a rectangular bending magnet as in figure 2.9, where magnet and trajectory length differ, equation 2.41 holds for small deflection angles, where $\alpha \approx \sin\alpha$.

The horizontal offset Δx of a beam in the laboratory frame after passing a rectangular straight dipole magnet as shown in figure 2.11 can be derived geometrically as

$$\Delta x = \rho - \sqrt{\rho^2 - L^2}. \tag{2.42}$$

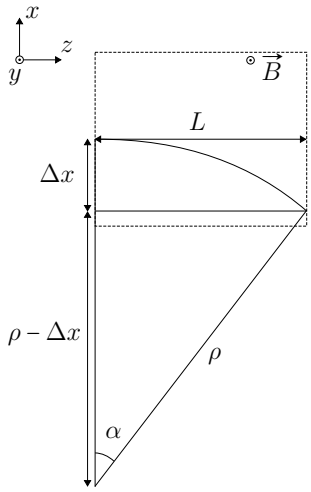

Figure 2.11.: Horizontal offset Δx of positive particles passing with velocity $\vec{v} = (0, 0, v_z)$ through a rectangular (straight) dipole magnet with magnetic field $\vec{B} = (0, B_y, 0)$, bending radius ρ, deflection angle α and length L.

With $\alpha \approx \tan\alpha = L/\rho$ and $\sqrt{1-\alpha^2} \approx 1 - \alpha^2/2 + \mathcal{O}(\alpha^3)$ for small α, one obtains in second-order approximation

$$\Delta x \approx L\frac{\alpha}{2}. \tag{2.43}$$

Thus, the horizontal offset of a beam in the laboratory frame after passing a straight dipole magnet with deflection angle α is given by

$$\Delta x(l) = \Delta x_{\text{out}}(l) + \Delta x_{\text{in}} = l\alpha + l_{\text{eff}}\frac{\alpha}{2} \tag{2.44}$$

where $\Delta x_{\text{out}}(l)$ and Δx_{in} account for the horizontal offset accumulated after and inside the magnet, respectively. l is the downstream distance to the magnet and l_{eff} is the effective length of the magnet.

2.2.2. Excitation of dipole magnets

In this thesis, the focus is on *iron-dominated magnets*, i.e. magnets which use magnetic steel yokes in order to efficiently generate magnetic fields in the area of the charged particle beam. Here, one distinguishes between iron-dominated magnets from coil excitation (so-called *normal-conducting magnets*) and iron-dominated magnets based on permanent magnet excitation. This section primarily follows the explanations given in [20, p. 270 ff.] and [20, p. 282 ff.].

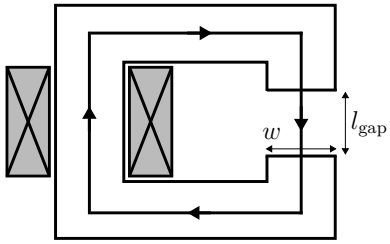

Figure 2.12.: C-shaped dipole magnet driven by a coil. The air gap has a gap height of l_{gap} and width w. The integration path for the left hand side of equation 2.46 is indicated by arrows.

Iron-dominated magnets based on coil excitation

Applying the Stokes theorem to Ampère's law

$$\nabla \times \frac{\vec{B}}{\mu} = \vec{j} \tag{2.45}$$

one gets

$$\frac{1}{\mu} \oint \vec{B} \mathrm{d}\, \vec{l} = \int_S \vec{j}\, \mathrm{d}\vec{S} = I_{\mathrm{total}}. \tag{2.46}$$

Here, I_{total} represents the current going through the cross-section of the conductor drawn in figure 2.12. For simplicity, the geometry of a so-called *C-shape* dipole magnet is considered. With equation 2.46 and the integration path drawn in the dipole magnet in figure 2.12 one gets

$$Bl_{\mathrm{gap}} + \frac{1}{\mu_{\mathrm{r}}} \int_{\mathrm{iron}} \vec{B} \mathrm{d}\, \vec{l} = \mu_0 I_{\mathrm{total}}. \tag{2.47}$$

Here the contribution which accounts for the integration path through the yoke can be neglected due to the very large relative permeability μ_{r}, and thus

$$NI = \frac{B}{\mu_0} l_{\mathrm{gap}} \tag{2.48}$$

can be obtained, with NI being the Ampère turns of the magnet, i.e. the number of turns N times the current through a single conductor I, and equivalent to the total current I_{total}.

Exciting a dipole magnet similar to the one in figure 2.12 with finite extent into the drawing plane generates a total magnetic energy in the gap of the magnet E, which is given by

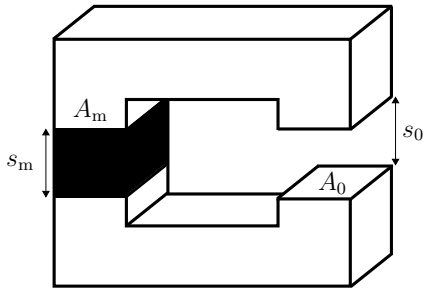

Figure 2.13.: C-shaped dipole magnet driven by a permanent magnet with height s_m and cross section A_m. The air gap has a height of s_0 with cross section A_0.

$$E = \frac{1}{2} L I^2, \tag{2.49}$$

with L being the inductance of the magnet. The magnetic energy in equation 2.49 can be deduced from the energy density in the magnetic field ρ_m by integration via

$$E = \int_V \rho_m \mathrm{d}V \tag{2.50}$$

Thus, the insertion of the magnetic energy density

$$\rho_m = \frac{1}{2} \vec{B} \vec{H} = \frac{B^2}{2\mu_0} \tag{2.51}$$

into equation 2.50 allows to deduce L via equation 2.49 and equation 2.48 to be

$$L = \mu_0 N^2 l_\mathrm{eff} \frac{w}{l_\mathrm{gap}}, \tag{2.52}$$

where $\int_V \mathrm{dV} = w \cdot l_\mathrm{gap} \cdot l_\mathrm{eff}$. With equation 2.52, an expression for the inductance of a dipole magnet as drawn in figure 2.12, taking into account a longitudinal extent of the magnetic field over an effective length l_eff, can be obtained, which is entirely determined by its geometric parameters.

Iron-dominated magnets based on permanent magnet excitation

As for the coil excitation in the previous paragraph, it is referred to Ampère's law in equation 2.45 and equation 2.46 in order to investigate the effect of permanent magnet excitation in an iron yoke on the magnetic flux density in the air gap. For this, the geometry shown in figure 2.13 with a C-shaped dipole magnet similar to the one in figure 2.12 is considered. In the absence of currents ($I_\mathrm{total} = 0$), one obtains

$$\oint \vec{H} \mathrm{d}\vec{l} = H_0 s_0 + H_\mathrm{m} s_\mathrm{m} = 0, \tag{2.53}$$

when neglecting the contribution of H from the iron yoke due to the large permeability (large μ_r, as when going from equation 2.47 to equation 2.48). In the geometry of figure 2.13, the magnetic flux $\Phi = BA$ on the magnet surface and on the pole surface equal, such that

$$B_\mathrm{m} A_\mathrm{m} = B_0 A_0 = \mu_0 H_0 A_0. \tag{2.54}$$

Inserting H_0 from equation 2.54 into equation 2.53 allows to relate the magnetic flux density B_m in the permanent magnet to the field H_m according to

$$B_\mathrm{m} = -\mu_0 \frac{s_\mathrm{m}}{s_0} \frac{A_0}{A_\mathrm{m}} H_\mathrm{m}. \tag{2.55}$$

Here, a so-called *permeance coefficient*

$$P := \frac{s_\mathrm{m}}{s_0} \frac{A_0}{A_\mathrm{m}} \tag{2.56}$$

can be defined, which relates the magnetic field H_m to the magnetic flux density B_m in the permanent magnet depending on the geometry of the setup. With equation 2.55, representing a straight line, called *load line*, with slope P in the $B(H)$ diagram of the permanent magnet, a working point of the permanent magnet, i.e. a set of $(B_\mathrm{m}, H_\mathrm{m})$-coordinates obtained from the underlying geometry of the setup, can be derived from the intersection of equation 2.55 with the material-specific $B(H)$-curve.

A typical $B(H)$-curve of a rare-earth permanent magnet[5] is schematically shown in figure 2.14. In figure 2.14, with $\mu_\mathrm{r} = 1$, the $B(H)$-curve is deduced from the $J(H)$-curve via

$$B(H) = \mu_0 H + J(H) \tag{2.57}$$

and referred to as *normal curve* representing the flux density produced by the permanent magnet. The $J(H)$-curve is called *intrinsic curve* representing the response of the magnet to an external field. Since the focus is on the magnetic flux provision of the permanent magnet to a magnetic system considering external magnetizing and demagnetizing influences, the normal curve is primarily considered in the following. Application of an external magnet field H in figure 2.14 magnetizes the material following the initial curve (dashed line) until the *saturation polarization* J_s is reached at H_s, i.e. when B scales linear with H. During subsequent decrease of the external field H, the magnetic flux density B follows the hysteresis loop and remains at the *remanent field* B_r at $H = 0$ with $J(0) = B_\mathrm{r}$. When the external field is then reversed, B decreases linearly until the net magnetic flux density of the magnet material is zero at $H_{\mathrm{c},B}$, i.e. the *normal coercivity*. The magnetic polarization vanishes at the *intrinsic coercivity* $H_{\mathrm{c},J}$. Further decrease of H reverses the polarity of the magnet. From equation 2.57, it follows that $H_{\mathrm{c},B} < H_{\mathrm{c},J}$. For rare-earth permanent magnets, $B_\mathrm{r} \approx J_\mathrm{s}$, i.e.

[5] In this thesis, Sm_2Co_{17} as rare-earth magnet material is used.

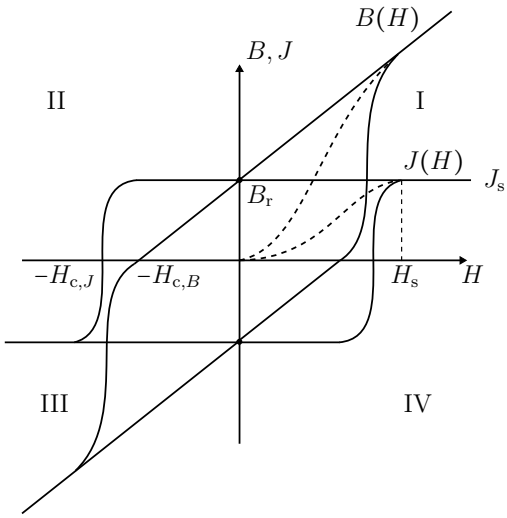

Figure 2.14.: Schematic drawing of the $B(H)$, $J(H)$-curve of a rare-earth permanent magnet.

$J(H)$ is almost constant when decreasing H. For these so-called *hard magnetic materials*, $J(H)$ follows approximately a rectangular hysteresis loop. Therefore, $B(H)$ is typically linear in the second quadrant of figure 2.14. The transition region from a linear to a non-linear $B(H)$ dependency is referred to as *knee* and is positioned in the third quadrant in figure 2.14. In a permanent-magnet-based system, there is usually no external driving field $H > 0$ but an inevitable demagnetization, i.e. $H \leq 0$, since all flux lines which are not guided back end-to-end into the permanent magnet, as it would be attained when the yoke in figure 2.13 is closed, point in opposite direction of the flux lines in the magnet. Therefore, one typically concentrates on the second quadrant of figure 2.14, i.e. the *demagnetization curve*, when studying the working point of permanent magnets integrated in a magnetic system. Figure 2.15 shows the demagnetization curve of a permanent-magnet-based system including load lines with different slope P (according to equation 2.56) and thus working points of different yoke geometries. A short circuit geometry is obtained when $s_\mathrm{m} >> s_0$ in equation 2.56 and thus $P \to -\infty$. Here, almost all flux lines originating from the permanent magnet are guided back into the magnet with only small leakage due to the finite reluctance of the yoke. In an open circuit, i.e. $s_0 >> s_\mathrm{m}$, the leakage and thus demagnetizing field is maximum. Depending on s_m, A_m, s_0 and A_0 the working point moves along the demagnetization curve. With a linear demagnetization curve, there is typically no flux loss associated with magnetizing the permanent magnet as a bare magnet and subsequent handling of the magnet, i.e. bringing it into the circuit. It should be noted that the demagnetization curve is temperature-dependent and thus the knee of $B(H)$ in figure 2.14 can be shifted from the third into the second quadrant as shown

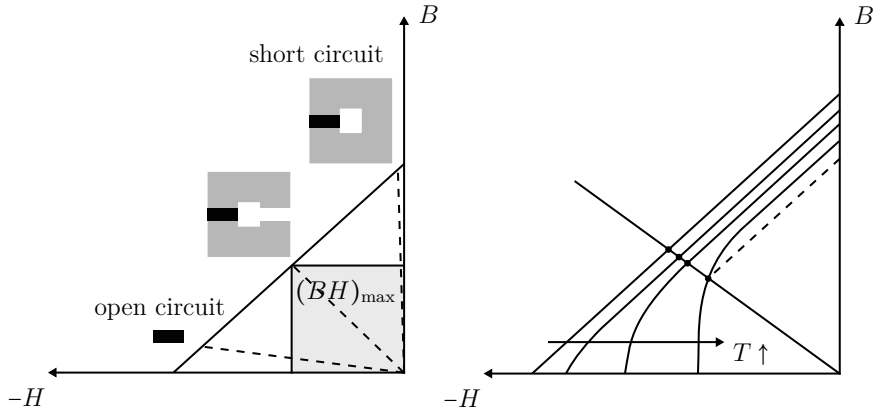

Figure 2.15.: Left: Demagnetization curve (second quadrant of figure 2.14) with load lines and thus working points (B, H) for different geometries of a permanent-magnet-based system as shown by the schematic drawings (referring to a geometry similar to figure 2.13). The gray area shows the maximum energy product $(BH)_{\mathrm{max}}$. Each working point is associated with a corresponding energy density product BH. Right: Demagnetization curve for different temperatures T of the permanent magnet. B_{r} and $H_{\mathrm{c},J}$ decrease with larger temperature. Thus the knee of $B(H)$ moves into the second quadrant and the working point changes.

on the right side of figure 2.15. For a fixed geometry of a permanent-magnet-based system, the working point thus changes with temperature. If the working point is shifted such that it is positioned below the knee of the $B(H)$-curve, the magnetic flux density returns to a smaller remanent field at $H = 0$ shown by the dashed line on the right side of figure 2.15, i.e. the magnetic flux loss is irreversible. For a permanent-magnet-based system, the working point should always be above the knee within the expected temperature fluctuations.

Multiplying equation 2.54 by s_{m} and replacing s_{m} on the right hand side of the equation by the expression obtained from equation 2.53 for s_{m} yields

$$B_{\mathrm{m}} A_{\mathrm{m}} s_{\mathrm{m}} = -\mu_0 H_0 A_0 \frac{H_0 s_0}{H_{\mathrm{m}}} \tag{2.58}$$

and thus

$$H_0 = \sqrt{\frac{-B_{\mathrm{m}} H_{\mathrm{m}} V_{\mathrm{m}}}{\mu_0 V_0}}, \tag{2.59}$$

with $V_{\mathrm{m(0)}} = A_{\mathrm{m(0)}} \cdot s_{\mathrm{m(0)}}$ being the volume of the permanent magnet or air gap, respectively. Thus, for a given air gap volume V_0 and a required field H_0 or flux

density $B_0 = \mu_0 H_0$ in the air gap, the required volume of the permanent magnet can be minimized by adjusting the geometry of the setup, i.e. the permeance coefficient (equation 2.56), such that a working point of the permanent magnet is obtained where $B_\mathrm{m} \cdot H_\mathrm{m}$ is maximum. Therefore $(BH)_\mathrm{max}$, i.e. the so-called *energy product* is a measure for the quality of the permanent-magnet material. For Sm_2Co_{17}, which is used during this thesis, the energy product $(BH)_\mathrm{max}$ ranges between $159\,\mathrm{kJm^{-3}}$ to $264\,\mathrm{kJm^{-3}}$ which is the second largest energy product obtainable from rare-earth permanent magnets with NdFeB ranging between $199\,\mathrm{kJm^{-3}}$ to $444\,\mathrm{kJm^{-3}}$ [21].

In order to characterize a system based on rare-earth permanent magnets with a linear demagnetization curve as shown in figure 2.15 and $\mu_\mathrm{r} \approx 1$, it is typically sufficient to consider the material specific remanent field or flux density B_r. The flux density B_m of the permanent magnet follows according to equation 2.57

$$B_\mathrm{m} = \mu_0 H_\mathrm{m} + B_\mathrm{r} \tag{2.60}$$

with $J \approx \text{const.} = B_\mathrm{r}$. The intersection of equation 2.60 with the load line in equation 2.55 defines the working point and yields the demagnetization field

$$H_\mathrm{m} = -\frac{B_\mathrm{r}}{\mu_0 \left(1 + s_\mathrm{m}/s_0 \cdot A_0/A_\mathrm{m}\right)} \tag{2.61}$$

and thus the corresponding B_m via equation 2.60. Hence, given the geometry of the magnet system, the flux density in the air gap B_0 can obtained purely from the remanent flux density B_r using equation 2.59 to be

$$B_0 = \frac{B_\mathrm{r}}{s_0/s_\mathrm{m} + A_0/A_\mathrm{m}}. \tag{2.62}$$

For example a geometry with $s_0 = s_\mathrm{m}$ and $A_0 = A_\mathrm{m}$ gives a magnetic flux density in the air gap of $B_0 = B_\mathrm{r}/2$.

Equation 2.62 holds for a C-Shaped geometry as presented in figure 2.13 and approximates the flux density in systems with slightly different geometry (e.g. shims). For more complex permanent-magnet-based systems, numerical simulations have to be performed yielding the working point and thus the flux density in the air gap by specifying the remanent flux density and the relative permeability.

2.2.3. Magnetic field characterization

For accelerator magnets and the effect of these magnets onto the traversing charged particle beam, the magnetic flux density $\vec{B} = \mu\vec{H}$ plays the central role. Here, μ and $\vec{H}$ are referred to as permeability and magnetic field, respectively. In accelerator physics, the term magnetic field is used as synonym for the magnetic flux density [15]. To judge the quality of the magnetic field in an accelerator magnet, it is essential to obtain a description of the magnetic field in the geometry of the magnets. This can

be done by introducing the so-called *multipole coefficients* of a magnet.

In order to obtain an expression for the multipole coefficients in a magnet, a general expression of the magnetic field in the aperture of the magnet has to be derived from the MAXWELL formulas by solving the magnetostatic boundary value problem in the magnet aperture. The magnet aperture is free of currents, such that AMPÈRE'S law (equation 2.45) simplifies to

$$\nabla \times \vec{B} = 0. \tag{2.63}$$

GAUSS'S law of magnetism states

$$\nabla \cdot \vec{B} = 0. \tag{2.64}$$

Equation 2.63 and equation 2.64 can be used to formulate the boundary value problem either in terms of a scalar potential Φ_m with $\vec{B} = -\nabla\Phi_m$ or in terms of a vector potential $\vec{A}$ with $\vec{B} = \nabla \times \vec{A}$. Both formulations yield identical results in terms of the multipole coefficients. Following the formulation with a magnetic vector potential $\vec{A}$, one inserts $\vec{B} = \nabla \times \vec{A}$ into equation 2.63 to obtain

$$\nabla \times (\nabla \times \vec{A}) = \nabla(\nabla \cdot \vec{A}) - \Delta\vec{A} = 0 \tag{2.65}$$

with the vector identity. With the COULOMB gauge, i.e. $\nabla \cdot \vec{A} = 0$, the LAPLACE equation

$$\Delta\vec{A} = \Delta A_z = 0 \tag{2.66}$$

can be obtained if a purely transversal magnetic field with $\vec{B} = (B_x, B_y, 0)$ and the corresponding vector potential $\vec{A} = (0, 0, A_z)$ is considered, which holds inside accelerator magnets with much larger extent in z than in the transversal plane. Solving equation 2.66 in the aperture of the magnet gives a general expression of the magnetic field therein. For the geometry of accelerator magnets, equation 2.66 can be solved by introducing polar coordinates (r, ϕ). With the separation of variables method with $A_z(r, \phi) = \rho(r)\Phi(\phi)$, equation 2.66 yields two ordinary differential equations. Solving these while taking into account the boundary condition in the magnet aperture, i.e. finite field in the centre of the magnet at $r = 0$, one obtains the general expression of the magnetic vector potential in the magnet aperture following [20, p.238 f.]

$$A_z(r, \phi) = \sum_{n=1}^{\infty} r^n (C_n \sin n\phi - D_n \cos n\phi). \tag{2.67}$$

Thus, the magnetic field components in polar coordinates are

$$B_r(r, \phi) = \frac{1}{r}\frac{\partial A_z}{\partial \phi} = \sum_{n=1}^{\infty} n r^{n-1} (C_n \cos n\phi + D_n \sin n\phi), \tag{2.68}$$

$$B_\phi(r, \phi) = -\frac{\partial A_z}{\partial r} = -\sum_{n=1}^{\infty} n r^{n-1} (C_n \sin n\phi - D_n \cos n\phi). \tag{2.69}$$

The physical interpretation of the n-th contribution (mathematically originating from a separation constant n^2 in the separation of variables technique [20, p.238]) in equation 2.68 and equation 2.69 is that of a $2n$-pole magnetic flux density distribution, i.e. $n = 1, 2, ..$ representing a dipole, quadrupole and higher-order multipole magnetic flux density distribution. Thus, the magnetic field is represented by a linear combination of different $2n$-pole magnetic flux density distributions with C_n and D_n being the multipole coefficients.

The multipole coefficients can be obtained from a FOURIER series of the radial field B_r. Since the radial field is single-valued, it is periodic with ϕ, such that at a fixed radius $r = r_0$, i.e. called *reference radius*, B_r can be written as

$$B_r(r_0, \phi) = \sum_{n=1}^{\infty} (B_n(r_0) \sin n\phi + A_n(r_0) \cos n\phi) \tag{2.70}$$

with the FOURIER coefficients

$$A_n(r_0) = \frac{1}{\pi} \int_0^{2\pi} B_r(r_0, \phi) \cos n\phi \, \mathrm{d}\phi \tag{2.71}$$

$$B_n(r_0) = \frac{1}{\pi} \int_0^{2\pi} B_r(r_0, \phi) \sin n\phi \, \mathrm{d}\phi. \tag{2.72}$$

The FOURIER coefficient $A_0 = 1/\pi \int_0^{2\pi} B_r(r_0, \phi) \mathrm{d}\phi$ drops since GAUSS'S law states $\nabla \cdot \vec{B} = \oiint \vec{B} \mathrm{d}\vec{A} = r_0^2 \int_0^{2\pi} B_r(r_0, \phi) \mathrm{d}\phi = 0$ for $r_0 \neq 0$. With equation 2.70, the azimuthal field component can be derived from equation 2.68 and equation 2.69 to be

$$B_\phi(r_0, \phi) = \sum_{n=1}^{\infty} (B_n(r_0) \cos n\phi - A_n(r_0) \sin n\phi), \tag{2.73}$$

with $A_n(r_0) = n r_0^{n-1} C_n$ and $B_n(r_0) = n r_0^{n-1} D_n$. With this, $A_n(r_0)$ and $B_n(r_0)$ represent the multipole coefficients at the reference radius r_0.

Computation and measurement of the FOURIER coefficients in equation 2.71 and equation 2.72 can be performed by determining the radial field components B_r at N discrete points equally distributed on a circle with reference radius r_0. In this case, the FOURIER coefficients in equation 2.71 and equation 2.72 can be obtained from the discrete FOURIER transform [20, p. 333 f.]:

$$A_n(r_0) \approx \frac{2}{N} \sum_{k=0}^{N-1} B_r(r_0, \phi_k) \cos n\phi_k, \tag{2.74}$$

$$B_n(r_0) \approx \frac{2}{N} \sum_{k=0}^{N-1} B_r(r_0, \phi_k) \sin n\phi_k \tag{2.75}$$

with $\phi_k = 2\pi k/N$ $(k = 0, 1, 2, ..., N-1)$ being the angular coordinate of the N observations of B_r.

The horizontal and vertical magnetic field components B_x and B_y in cartesian coordinates can be derived from equation 2.70 and equation 2.73 according to

$$B_x(r_0, \phi) = B_r(r_0, \phi)\cos\phi - B_\phi \sin\phi \tag{2.76}$$
$$B_y(r_0, \phi) = B_r(r_0, \phi)\sin\phi + B_\phi \cos\phi. \tag{2.77}$$

For convenience, one typically introduces the *complex magnetic field*

$$\boldsymbol{B(z)} = B_y + iB_x = \sum_{n=1}^{\infty}(B_n + iA_n)\left(\frac{x+iy}{r_0}\right)^{n-1}. \tag{2.78}$$

Here, the multipole coefficient B_n represents the upright (vertical) contributions and is called *normal multipole coefficient*, whereas A_n represents the horizontal contributions and is named *skew multipole coefficient*. The set of all B_n and A_n is called *harmonic content*.

2.2.4. Kicker and Septum magnets

Particle accelerators generally cover a certain range in terms of kinetic energy of the particles, i.e. the difference between the lowest energy, so-called *injection energy*, and the final energy. In synchrotrons for example both the frequency of the RF system and the synchronized current of the dipole magnets are ramped during acceleration [16, p. 61 ff.]. Here, both systems are limited to some dynamic range, and thus it is required to use a chain of accelerators with different RF systems and main dipole magnets, which are connected by transfer lines in order to reach a large final energy of the particles. For example, a chain of five accelerators is used at CERN in order to provide TeV-protons from LHC [22]. The consequential demand to transfer particles between different accelerators as well as other requirements like periodic refilling of accelerators with particles and access to ionized particles from accelerators at external experiments led to the development of so-called *kicker magnets* and *septum magnets*[6]. The combination of these two special dipole magnets allows fast injection and extraction of particles from accelerators. Both are employed for different injection techniques [23].

In figure 2.16, the single-turn injection and single-turn extraction process with combinations of kicker and septum magnet are shown. The septum magnet features two different and closely arranged magnetic field regions, i.e. a homogeneous field region and a field-free region, with the field-free region typically covering the circulating beam. In single-turn injection (figure 2.16a), the injected beam passes through

[6] septum: latin for *something that encloses*.

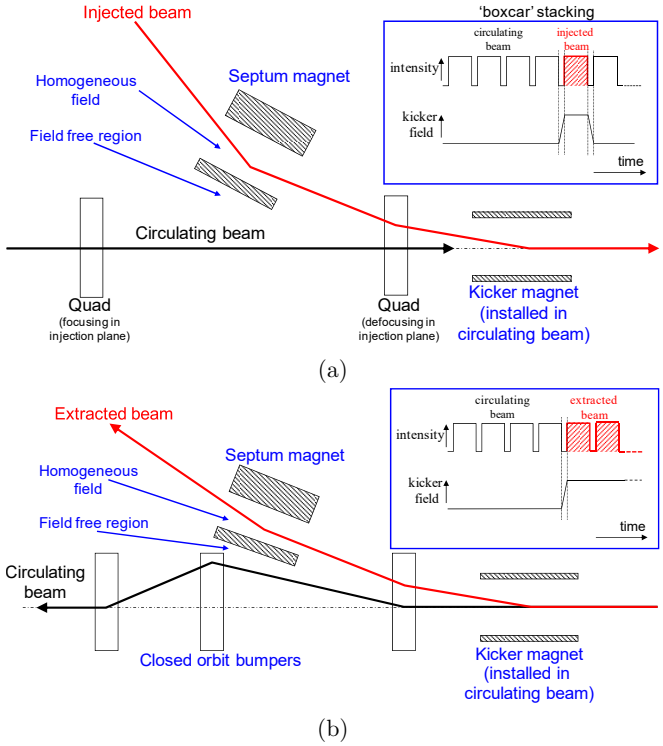

Figure 2.16.: Fast single-turn injection (a) and extraction (b) of the beam into and from a machine with circulating beam, respectively, using a combination of kicker and septum magnet. The insets show the temporal evolution of the magnetic field in the kicker magnet with respect to the beam intensity. The drawing shows the horizontal plane, i.e. the xz-plane in figure 2.1. Taken from [23].

the homogeneous field region of a pulsed or DC septum magnet, which deflects the injected beam onto the position of the circulating beam at the centre of the kicker magnet. The kicker magnet then compensates the remaining angle. Typically, a horizontally defocusing quadrupole of the accelerator is used in order to support the kicker magnet by deflecting the off-center injected beam. The kicker magnet is installed within the aperture of the circulating beam. Therefore, fast rise and fall times of the kicker magnet's magnetic field are required in order not to affect the circulating beam but only the injected beam. Single-turn extraction (figure 2.16b) works very similar but with reversed order of kicker and septum magnets. Fast ramping of the kicker magnet in a time interval without beam allows to direct the beam towards the homogeneous field region of the septum magnet. With this, the extracted beam is separated from the circulating beam, which passes the field free region of the septum

magnet. The fall time of the kicker magnet during extraction is normally less critical since typically the whole beam is extracted. Sometimes a closed orbit bump of the circulating beam, which is generated with minimum of three pulsed dipole magnets, is generated in order to move the beam closer to the homogeneous field region of the septum magnet. In the following, design characteristics of kicker as well as septum magnets are presented.

Kicker magnets

Kicker magnets are dipole magnets, which are designed to provide very short rise and fall times of the respective magnetic field. The conceptual design of kicker magnets is generally based on a C-core yoke similar to figure 2.12 [23]. In order to obtain a small inductance, the number of turns is as small as possible, i.e. mostly $N = 1$ (for kicker magnets with rise and fall times less than a few hundreds of ns [24]), and the horizontal aperture is minimized (equation 2.52). The horizontal aperture can be smallest when the kicker magnet is integrated with the vacuum system such that no beam tube is required. However, if the kicker magnet is positioned external to the vacuum system, e.g. due to outgassing of some material in the kicker magnet, beam tubes with low electrical conductivity are used to minimize eddy current losses, e.g. ceramic beam tubes [25]. For the minimization of eddy current losses, the yoke of kicker magnets is mostly based on ferrites, which feature a very low electrical conductivity and thus a large bandwidth. Regardless of the yoke material, the yoke is usually laminated, i.e. made from thin layers, which are glued together providing an intermediate insulating layer thus additionally reducing eddy current losses. Typical sheet thicknesses of the magnetic steel of the yoke are between 0.3 mm and 1.5 mm [26]. Since the inductance depends also on the length of the magnet (equation 2.52), arrangements of many but short kicker magnets can be used. Despite small inductances in kicker magnets, the fast rise and fall times in combination with only few turns per coil, which require larger currents to generate the magnetic field, demand large voltages for the operation of kicker magnets according to $U = -L \cdot \mathrm{d}I/\mathrm{d}t$. The large current and voltage pulses are generated by discharging a capacitor over a high voltage thyratron switch, which can hold-off up to 80 kV providing 6 kA within 30 ns rise time [23]. In order to provide fast rise times below 100 ns, modern kicker magnets are usually segmented into cells, which consist of ferrite C-cores sandwiched between HV capacitance plates with intermediate grounded plates such that the magnet resembles a broadband coaxial cable and the overall inductance is distributed over all such cells [27]. These kicker magnets are then called *transmission line kicker magnets*, whereas the bulk ferrite kicker magnets (similar to figure 2.12) are called *lumped-inductance kicker magnets*.

Septum magnets

The umbrella term septum applies to electrostatic deflectors as well as to magnets featuring an electric field or magnetic dipole field region, respectively, and a field-free region in close proximity. Electric field septa are mostly operated DC, whereas mag-

netic septa are usually pulsed or DC. Both concepts are presented in figure 2.17. While the electrostatic septum benefits from a much thinner septum thickness (< 100 µm), the electrostatic deflection is much weaker. With a maximum electric field of electrostatic septa of 10 MV/m and the maximum flux density of septum magnets being 1 T [16, p. 331], the required length of electrostatic septa for e.g. 70 MeV protons in order to provide the same deflection angle is one order of magnitude larger than for septum magnets (equation 2.41 for magnetic deflection and $\alpha = El/(B\rho)/v$ [16, p. 331] for electrostatic deflection). For this reason, the focus is on septum magnets in the following paragraph.

The driving current required for DC electromagnetic septum magnets can reach up to 4 kA leading to large current densities in the thin septum conductor (figure 2.17b) as high as 85 $\mathrm{A\,mm^{-2}}$ [28]. This causes a power consumption of up to 100 kW due to ohmic heat losses and thus water cooling with large flow rates of up to 60 $\mathrm{l\,min^{-1}}$ is required which results in excessive pumping and erosion of the conductors. Due to the large current densities in the septum the operating point of electromagnetic septum magnets is generally close to the damage threshold which demands a proper machine protection system. Further issues in most septum magnets are the strong radiation exposure of the septum, which is irradiated by the beam or beam halo leading to material degradation of the conductors and complicating maintenance as well as the mechanical stability of the thin septum bearing the electromagnetic forces. An overview of different types of electromagnetic septum magnets is given in [29]. One type of septum magnet, in which some of the above problems, i.e. radiation exposure and mechanical stability, can be reduced is the so-called *massless septum* [30] which provides a dipole and a zero field region without a physical septum to separate the two field regions. The conceptual design of an electromagnetic massless septum is presented in figure 2.18. Here, the leakage field from the dipole field region is canceled by the addition of a third conductor such that a slow transition between the dipole field and the zero field region is obtained, i.e. an effective septum. According to [30] a septum magnet with a dipole field of 0.8 T and an effective septum thickness of 40 mm can be obtained. The septum thickness can be further reduced by approximately 10 mm when using permanent magnets to support I_2 in figure 2.18.

For the design of septum magnets, a less stringent consideration of the beam size is applied in this thesis when compared to standard accelerator magnets such as dipole and quadrupole magnets. With the septum magnets being special magnets which follow a more challenging design process, a beam diameter of 4 rms beam widths (rather than 6 rms beam widths), i.e. 4σ and 95.45 % of the beam intensity, is considered, which facilitates the design. This has only minor influences on the beam quality throughout a beamline containing septum magnets as they are employed less frequent, i.e. typically once, when compared to dipole or quadrupole magnets.

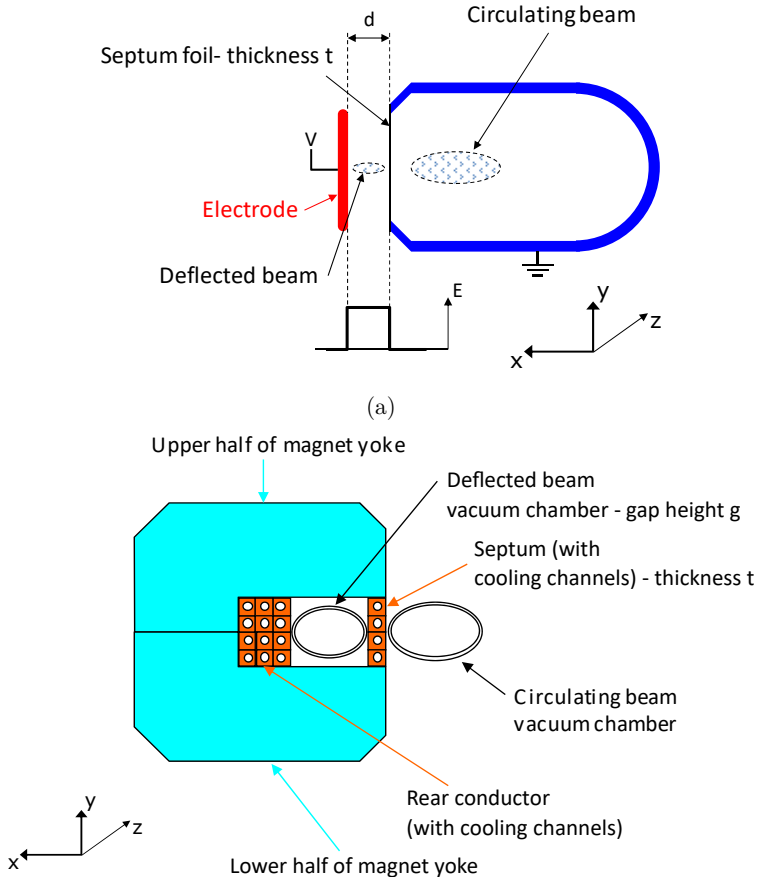

Figure 2.17.: Conceptual design of an electrostatic septum with foil septum (a) and a DC septum magnet (b). The gap width d of the electrostatic septum magnet generally varies between 10 mm and 35 mm with the septum foil thickness t being less than 100 µm. For the magnetic septum, a gap height g of 25 mm to 60 mm can be obtained with a septum thickness (septum conductor) t of 6 mm to 20 mm. All data and graphics taken and adapted from [28].

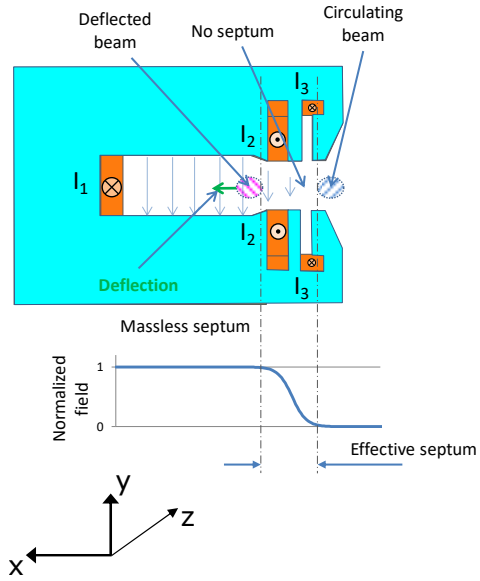

Figure 2.18.: Conceptual design of a massless septum [30] with three different conductors I_1, I_2, I_3 to cancel the leakage field of the dipole field region without physical septum. Taken and adapted from [29].

2.3. Neutron production in low-energy accelerator-driven neutron sources

The neutron production in low-energy accelerator-driven neutrons sources is based on the interactions of light ions, e.g. protons for HBS, in the energy range below 100 MeV with the nuclei of a metal target. Depending on the energy of the primary particle, i.e. the projectile, and the target material, different nuclear reactions contribute with their individual energy-dependent cross sections to the generation of neutrons. While the projectiles propagate through the target, they loose energy and thus the cross section of the contributing nuclear reactions changes with the penetration depth of the projectiles. This has to be taken into account when classifying the efficiency of different target materials in terms of their neutron generation per primary ion, i.e. the neutron yield, as explained in the following. The energy-dependent neutron yield is an important parameter for the target material selection at low-energy accelerator-driven neutron sources and investigated experimentally in chapter 6 of this thesis.

2.3.1. Nuclear reactions

Nuclear reactions can be considered as reactions between two or more nuclei or between nuclei and other fundamental particles, e.g. electrons or photons. In the follow-

ing, the focus is on nuclear reactions involving two nuclei as this is the main reaction driving the generation of neutrons in low-energy accelerator-driven neutron sources. When two nuclei collide, many different final products with different quantum states can be created. A reaction branch with well defined initial and final participants as well as their associated quantum states is referred to as *reaction channel*. The probability for a nuclear reaction to follow a particular reaction channel is determined by the cross section σ of that channel. Nuclear reactions proceed through different mechanisms. For nuclear reactions involving light mass projectiles in the MeV energy range impinging on a target nuclei, one can concentrate on three distinct mechanisms, which are briefly introduced in the following (following the explanations in [31]).

At low projectile energies, the projectile particle can be captured by the target nucleus forming a highly excited *compound nucleus*. The excitation energy of the compound nucleus can be transferred to all of its nucleons and if the energy is concentrated in one or more nucleons, the excited nucleus decays with the emission of these nucleons (typically neutrons). With a time scale of $\tau \gg 1\times10^{-22}\,\mathrm{s}$, the compound nucleus reaction is a slow process since the distribution of the projectile energy in the target nucleus requires some periods of the orbiting nucleons, i.e. $\approx 1\times10^{-22}\,\mathrm{s}$. Due to this large time scale, the information about the formation of the compound nucleus is lost and therefore the decay products of the reaction are independent of the initial participants. The final products only depend on the energy, angular momentum and parity of the quantum state of the compound nucleus. The particle emission is almost isotropic with some minor dependence on the direction of the projectile nucleus. A compound nucleus reaction contributing to the generation of neutrons with protons impinging on a beryllium target is for example

$$\mathrm{p} + {}^{9}_{4}\mathrm{Be} \rightarrow {}^{10}_{5}\mathrm{Be}^{*} \rightarrow {}^{9}_{5}\mathrm{B} + \mathrm{n} \tag{2.79}$$

or denoted as $^{9}\mathrm{Be}(\mathrm{p},\mathrm{n})^{9}\mathrm{B}$ with ${}^{10}_{5}\mathrm{Be}^{*}$ representing a beryllium nucleus in an excited state.

At higher projectile energies, the wavelength associated to the projectile particle decreases such that localized areas at the surface of the target nuclei can be probed and thus only a few nucleons of the target participate. The projectile can hereby transfer energy or transfer one or more nucleons to the target. This type of reaction is called *direct reaction*. The corresponding time scale is $< 1\times10^{-22}\,\mathrm{s}$. Typical direct reactions are *elastic scattering* where no energy is transferred between the nuclei but the propagation of the projectile may change and *inelastic scattering* where the projectile can excite the target nucleus by transferring energy. Direct reactions, where a nucleon is transferred from the projectile to the target and vice versa, are called *stripping reactions* and *pick-up reactions*, respectively. The differential cross section $\mathrm{d}\sigma/\mathrm{d}\Omega$ of direct reactions is strongly forward peaked as the projectile continues to move along its initial direction.

It is possible that the interaction of the projectile and the target neither processes through a direct reaction nor by the formation of a compound nucleus. If the projectile energy is transferred only to a part of the target nucleus, no statistical equilibrium, as in the case of a compound nucleus, occurs. Instead, the projectile nucleons initiate a cascade of interactions in the target nucleus eventually leading to the emission of nucleons. Since the emission of particles from the target nucleus occurs before the formation of a compound nucleus such reaction is called *pre-equilibrium reaction*. The corresponding time scale is 1×10^{-18} s.

For processes involving two initial nuclei with an electrical charge of identical polarity, nuclear reactions are only feasible if the interacting nuclei have sufficient energy to overcome the COULOMB barrier. Therefore, for protons impinging on metal targets a particle accelerator is required to open the reaction channels required for neutron generation. The heavier the target material (higher atomic number Z), the higher the charge of the target nucleus and thus the larger the repulsive effect from the COULOMB potential of the target nucleus. Thus a larger projectile energy is required for heavy target materials, e.g. tantalum with respect to beryllium, when operating a low-energy accelerator-driven neutron source. However, heavy target materials allow to open reaction channels which contribute with more neutrons per primary ion, e.g. (p,5n) and (p,7n+α) for protons on tantalum [32].

In low-energy accelerator-driven neutron sources with a specific target material and projectile ion, the neutron generation generally involves a multitude of nuclear reactions. Some secondary nuclear reactions can be triggered by the products of previous nuclear reactions while the probability of the individual reactions depends on the energy of the nuclei which in turn is influenced by the environment of the target, i.e. moderator and reflector material as well as the corresponding geometry. Thus, in order to evaluate the efficiency of a low-energy accelerator-driven neutron source numerically in terms of its neutron yield, i.e. neutrons per primary ion, Monte-Carlo simulations have to be performed with for example MCNP [11] using the cross sections of the nuclear reactions from databases, e.g. ENDF [33].

For HBS, analytical calculations of the neutron yield can be performed when considering only primary proton-induced nuclear reactions that contribute to the generation of neutrons, i.e. (p,n) reactions. Here, the energy-dependent probability of all occurring (p,n) reactions is summed up yielding a proton-induced neutron yield [8]. As the protons propagate through the target material, they loose energy and thus the cross section for the neutron generation changes. This has to be taken into account for the calculation of the proton-induced neutron yield by considering the energy-dependent penetration depth of the protons in the target as well as the energy loss along their path which is described in the following.

2.3.2. Stopping power

When ions travel through matter, they loose energy through collisions with electrons and nuclei. The total energy loss in the material per unit path length is given by [34]

$$-\frac{\mathrm{d}E}{\mathrm{d}x} = -\left.\frac{\mathrm{d}E}{\mathrm{d}x}\right|_{\mathrm{e}} - \left.\frac{\mathrm{d}E}{\mathrm{d}x}\right|_{\mathrm{n}} \tag{2.80}$$

with $S(E) = -\mathrm{d}E/\mathrm{d}x$ being defined as *stopping power*. The larger the stopping power, the higher the energy loss per unit path length of a projectile in a target. In equation 2.80, the contribution from radiative energy loss through the emission of photons, i.e. *bremsstrahlung*, is not considered as this is negligibly small for ions penetrating with a kinetic energy which is below their rest mass (< 938 MeV for protons) [35]. The subscript e in equation 2.80 denotes the *electronic stopping power* which is due to interactions of the projectile ion with atomic electrons in the target causing ionization or excitation of the target atoms. The subscript n marks the *nuclear stopping power* which accounts for elastic Coulomb interactions between the projectile and target nuclei. Here, recoil energy is transferred from the projectile to the target. The nuclear stopping power scales with the mass of the projectile and increases with lower projectile energy, e.g. from 0.2 % to 15 % with respect to the electronic stopping power for 100 keV to 1 keV protons on Be [36]. For protons impinging on potential target materials for low-energy accelerator-driven neutron sources, the nuclear stopping power is orders of magnitude below the electronic stopping power [8]. Thus, the focus is on the electronic stopping power which can be characterized by the *Bethe relativistic formula* [36, p. 39]

$$\left.\frac{\mathrm{d}E}{\mathrm{d}x}\right|_{\mathrm{e}} = \frac{4\pi n z^2 e^4}{m_e v^2}\left\{\ln\left[\frac{2m_e v^2}{I(1-\beta^2)}\right] - \beta^2\right\} \tag{2.81}$$

for a projectile with velocity v, $\beta = v/c$ with c being the speed of light and charge number z. In equation 2.81, m_e is the electron mass, n is the electron density of the target material and I is the mean excitation energy of the atoms of the target material. The mean excitation energy I describes how easily a target atom can absorb kinetic energy from the projectile. It can be approximated with $I \approx 11.5 \cdot Z \cdot 1 \times 10^{-6}\,\mathrm{MeV}$ [37] with Z being the charge number of the target material. For protons in the MeV energy range impinging on metal targets, equation 2.81 is well applicable to determine the stopping power in the target [36, p. 47].

As the projectile looses energy whilst traveling through the target material via equation 2.81, it slows down. With this, the energy loss per unit path length further increases yielding a maximum energy loss just before all particles are stopped in the target. This maximum energy loss at end of the track of the projectiles in the target is called *Bragg peak*. The total path length of the projectiles in the target is given by the *stopping range* [37]

$$R = \int_0^E \frac{1}{S(E)}\mathrm{d}E = \int_0^E \frac{1}{-\mathrm{d}E/\mathrm{d}x}\mathrm{d}E \tag{2.82}$$

with E being the initial kinetic energy of the projectile and $S(E)$ being the stopping power. With equation 2.82 and equation 2.81, it is for example evident that protons have a larger stopping range than deuterons at identical initial kinetic energy and target material as the mass of the deuteron is larger which leads to a smaller velocity and thus a larger energy loss per unit path length.

The stopping range and the energy loss along the track through the target material of the projectiles has to be considered when calculating the neutron yield at low-energy accelerator-driven neutron sources as described in the following paragraph.

2.3.3. Neutron Yield

At low-energy accelerator-driven neutron sources, the neutron yield, i.e. the neutrons generated per primary ion (e.g. proton at HBS), is an important parameter when considering the efficiency of such sources. The neutron yield directly influences the brilliance of neutron beams obtained from low-energy accelerator-driven neutron sources (equation 1.1) which is the figure of merit at HBS. Hence, analytical calculations, numerical simulations as well as measurements of the neutron yield for different target materials irradiated with protons are inevitable during the design process of HBS. Numerical simulations and measurements of the neutron yield are performed in chapter 6 of this thesis. Analytical calculations of the neutron yield from a specific target material considering only primary nuclear reactions, e.g. proton-induced neutron generation for HBS, allow to compare the efficiency of different target materials. Considering all proton-induced nuclear reactions that generate neutrons with their individual energy-dependent cross sections $\sigma_{i,(\mathrm{p,n})}(E)$, the proton-induced neutron yield $\mathrm{Y}_{(\mathrm{p,n})}$ can be calculated according to

$$Y_{(\mathrm{p,n})} = \sum_i \int_0^R \frac{N_\mathrm{A}}{M} \rho \sigma_{i,(\mathrm{p,n})}(E) \mathrm{d}x \tag{2.83}$$

with N_A being the Avogardo constant, ρ being the mass density and M being the molar mass of the target material. Here, R is the stopping range according to equation 2.82. Such calculations have been performed for various target materials in [8]. The results are presented in figure 2.19. It can be seen that for protons at 70 MeV as employed at HBS, high neutron yields in the order of 9 to $10 \times 10^{14}\,\mathrm{s^{-1}\,mA^{-1}}$ can be obtained when selecting the appropriate target material. At HBS tantalum ($Y_{(\mathrm{p,n})} = 9 \times 10^{14}\,\mathrm{s^{-1}\,mA^{-1}}$) will be used due to its beneficial material properties, such as a large blistering threshold and corrosion resistance [5].

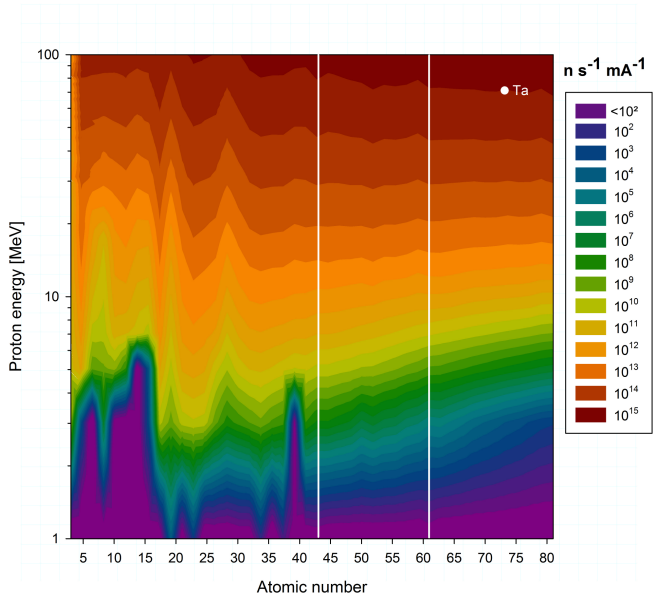

Figure 2.19.: Proton-induced neutron yield calculated according to equation 2.83 with cross sections from the TALYS nuclear code [38] and stopping range calculated with SRIM [39]. The white lines mark Tc and Pm which have no stable isotopes. The white dot marks Ta at 70 MeV proton energy. Taken from [5].

3. Low-energy accelerator-driven neutron sources

In low-energy accelerator-driven neutron sources, an ion beam with a kinetic energy below 100 MeV impinges on a metal target generating neutrons via nuclear reactions. Depending on the target material and ion species, typically protons or deuterons, a different variety of potential reactions contribute to the neutron generation. With the neutron yield from nuclear reactions ranging between 1×10^{-3} and some 1×10^{-1} neutrons per primary particle, the yield is orders of magnitude smaller than for fission or spallation reactions. However, the low ion energy, especially when compared to spallation sources with typically $E_{\mathrm{kin}} \approx 1\,\mathrm{GeV}$, allows compact assemblies of target and moderator such that a larger fraction of neutrons can be made useful for the instruments. With this, low-energy accelerator-driven neutron sources being highly competitive to medium-flux fission-based research reactors can be developed.

In the following, the High-Brilliance neutron Source (HBS) facility is presented. The HBS is a pulsed medium-flux, high brilliance accelerator-driven neutron source facility based on a high current linear proton accelerator, scalable up to 70 MeV proton energy, and optimized to deliver high brilliance neutron beams to a large variety of neutron instruments [4]. At Forschungszentrum Jülich GmbH, a test facility for HBS is being set up at the JUelich Light Ion Cyclotron (JULIC) accelerator which is presented thereafter.

3.1. HBS facility

A floor plan of the High-Brilliance neutron Source (HBS) facility is shown in figure 3.1. The HBS facility is driven by a high-power linear accelerator (linac) providing 70 MeV protons with high intensity of up to 100 mA peak current. The linac is supplied by an Electron Cyclotron Resonance (ECR) source which is connected to a Radio Frequency Quadrupole (RFQ) accelerator via a Low Energy Beam Transport (LEBT) line. Inside the LEBT, a chopper system is installed to provide different proton pulsing schemes. The chopper system generates an interlaced proton pulse structure comprising three different periodical pulse sequences in terms of pulse and period length. After the linac, the protons are transported by the High-Energy Beam Transport (HEBT) to the target stations. This is done by transferring the protons to a top floor where the multiplexer system is installed in order to unravel the interlaced proton pulse structure and to send the individual pulse sequences separately to the three different

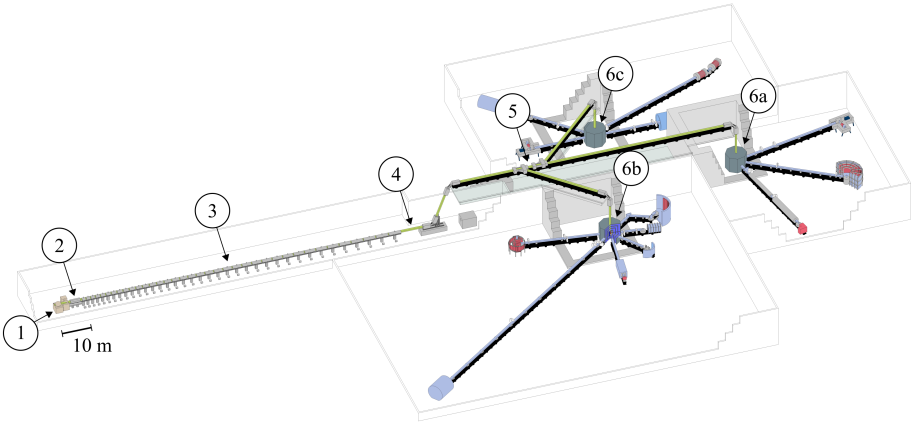

Figure 3.1.: Floor plan of the HBS facility. 1: Electron Cyclotron Resonance (ECR) proton source and Low Energy Beam Transport (LEBT) including an E×B-chopper system, 2: Radio Frequency Quadrupoles (RFQ) for acceleration of protons to 2.5 MeV with subsequent Medium Energy Beam Transport (MEBT), 3: Drift Tube Linac (DTL) for acceleration of protons to 70 MeV, 4: High-Energy Beam Transport (HEBT) from DTL to the individual target stations, 5: Proton beam multiplexer system for the distribution of different proton pulse schemes to different target stations, 6a: 384 Hz target station, 6b: 96 Hz target station, 6c: 24 Hz target station. Taken and adapted from [5].

target stations. A detailed explanation of the multiplexer system for HBS as well as the layout of the HEBT can be found in chapter 5 of this thesis. The different target stations are then operated at different proton pulse frequency with the corresponding proton pulse length being coupled via a fixed duty cycle. At HBS, a 384 Hz target station is foreseen at the centered position downstream the multiplexer system. A 24 Hz and a 96 Hz target station will be installed on the left and right side, respectively. A detailed overview of the HBS facility including the subsystems, which are described in the following, is given in [5].

3.1.1. Proton accelerator

As shown in figure 3.2, the HBS facility uses a Crossbar-H mode Drift Tube Linac (CH-DTL) consisting of 35 cavities to provide 70 MeV protons. Between the cavities magnetic quadrupole doublets are used for focusing of the beam which allows a highly modular structure. The DTL is designed to be operated with beam currents from a few mA to 100 mA. The DTL operates at a maximum RF power duty factor of 20 %.

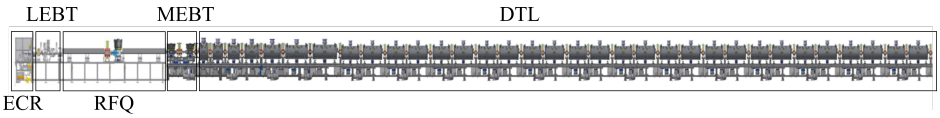

Figure 3.2.: Layout of the HBS proton accelerator with about 90 m length. The accelerator system is based on a DTL. The front-end of the accelerator consists of an ECR-source, LEBT, RFQ and MEBT. Taken and adapted from [5].

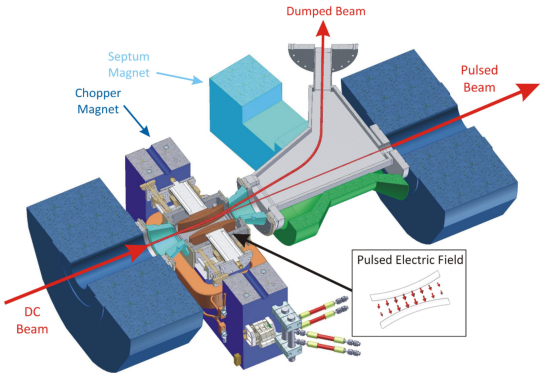

Figure 3.3.: Chopper system for proton pulse generation in the LEBT at HBS with E×B-chopper consisting of a chopper magnet together with a deflector electrode and a septum magnet to transport the beam into a beam dump. Proton pulses are generated when the pulsed electric field is switched on. Taken from [40].

Prior to the DTL, the proton beam is extracted from an Electron Cyclotron Resonance (ECR) source. Driving the plasma generation in the ECR source by RF waves which meet the ECR condition allows to generate high plasma densities and thus high beam intensities. The ECR source delivers a 110 mA proton beam with an energy of 100 keV in DC mode operation. After the ECR source, the proton beam is transported by the Low Energy Beam Transport (LEBT) to the first acceleration stage, i.e. the Radio Frequency Quadrupoles (RFQ). In the LEBT, the beam is caught from the extraction system of the ECR source and matched to fit the acceptance of the RFQ. Furthermore, the LEBT contains a chopper which allows to generate a time structure of the beam.

The E×B-chopper (figure 3.3) consists of a static dipole magnet and a deflector electrode which is controlled by a high-voltage switch [40]. The beam pulsing is controlled via the deflector electrode. When no high voltage is applied, the beam is permanently deflected by the static magnetic field of the E×B-chopper and the subsequent septum magnet and transported to a beam dump. Proton pulses can be generated by ramp-

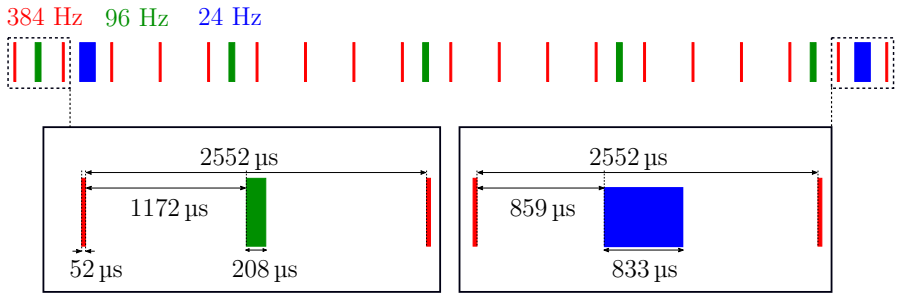

Figure 3.4.: Interlaced HBS proton pulse structure as generated by the E×B-chopper in figure 3.3 when operating with a duty cycle of 2 % per pulse sequence (6 % in total).

ing up the electric field in the E×B-chopper such that the Wien condition is met, i.e. the magnetic field is compensated by the electric field, such that the protons go straight through the chopper. The proton pulses can be generated with a maximum repetition rate of 250 kHz. The rise and fall time of the electric field are in the order of tens of ns. The E×B-chopper system has the advantage that the duty cycle of the electrostatic deflector is decreased compared to a conventional electrostatic chopper.

In order to supply the different target stations of HBS in figure 3.1 with the proton pulse frequencies of 384 Hz, 96 Hz and 24 Hz, an interlaced proton pulse structure as shown in figure 3.4 is generated by the E×B-chopper. The corresponding pulse lengths are correlated by the duty cycle. The duty cycle is chosen such that 100 kW average beam power is deposited on each target. For operation at maximum intensity of 100 mA at 70 MeV, a duty cycle of 1.4 % per target station should be chosen to stay within the thermo-mechanical limitations of the target. However, by reducing the proton beam current to 70 mA, the duty cycle can be ramped up to 2 %. This is chosen to be the upper limit of the duty cycle per target station and the performance limit of the multiplexer as it defines the smallest time gap between two different proton pulse sequences. Figure 3.4 shows the interlaced proton pulse structure at HBS with a duty cycle of 2 %.

Having passed the LEBT, the beam is guided into the RFQ representing the first acceleration stage. The RFQ focuses, bunches and accelerates the proton beam. The input energy of the RFQ is 100 kV while the final energy amounts for 2.5 MeV. Inside the RFQ, a time-dependent electric quadrupole field is generated acting as strong focusing device in the transversal plane while together with the mechanical modulation of the electrodes of the RFQ the particles are accelerated simultaneously [41]. With this, the RFQ helps to reduce the defocusing effect of space-charge forces which is especially large at very low energies as in the LEBT. Furthermore, the acceleration through the RFQ helps to operate the subsequent DTL with reasonable cavity length

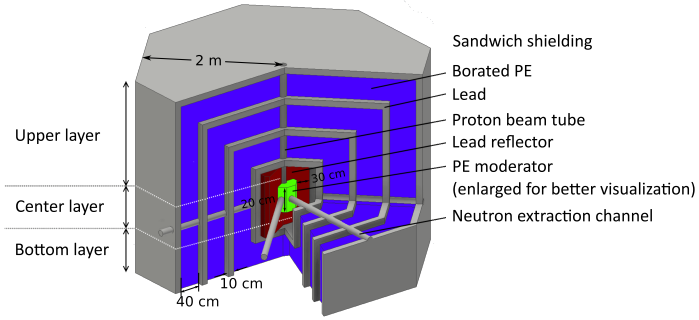

Figure 3.5.: HBS target station design. The HBS target stations are arranged according to figure 3.1. The tantalum target is irradiated from the top and incorporated in the thermal polyethylene (PE) moderator. A lead reflector surrounds the PE moderator building a Target-Moderator-Reflector assembly (TMR). Outside of the TMR an alternating shielding structure made of borated PE and lead is used to absorb neutrons and gammas emerging from the TMR. Taken and adapted from [5].

since the cavity length l_c scales directly with the relativistic $\beta = v/c$ of the particles, i.e. $l_c = \beta\lambda/2$ with λ being the RF wavelength. The RFQ is a 4-rod RFQ and will be fed by an RF frequency of 176.1 MHz [42].

Before injection into the final accelerating structure, i.e the DTL, providing the 70 MeV proton beam, a short Medium Energy Beam Transport (MEBT) section is used to match the beam transversally and longitudinally into the DTL. The DTL uses 35 CH cavities, which are arranged in a quasi-periodic lattice. Up to an energy of 20 MeV, a periodic arrangement of cavities and quadrupole doublets is used. At higher energies, where space-charge induced defocusing effects are less severe, two identical cavities are combined to form a cavity doublet without intermediate quadrupole magnets. Both the DTL and the RFQ are driven by 37 solid state RF amplifiers with up to 500 kW RF power operating at 176.1 MHz.

3.1.2. Target station

The HBS target station represents a key component of the facility producing neutrons and supplying them to the neutron guides for the different instruments after moderation to the required neutron energies. In addition the target station provides shielding which allows to keep the dose rates outside the target station as low as possible. The layout of the target station is presented in figure 3.5.

In the centre of the target station an internally-cooled tantalum target is installed which is designed to be irradiated with 100 kW beam power. Tantalum is the material

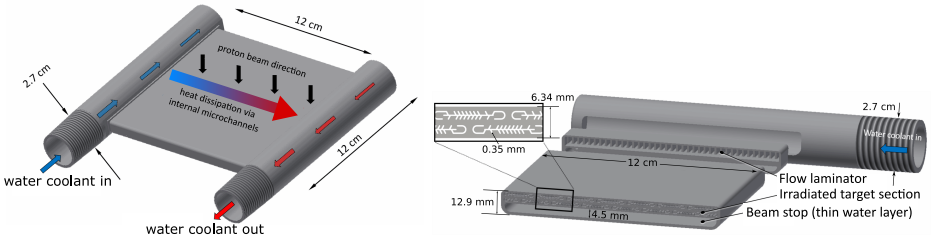

(a) (b)

Figure 3.6.: (a): Internally-cooled tantalum target employed at HBS with proton beam from the top. The target area is 12 cm x 12 cm. (b): Cross-section of the HBS target with microchannel structure and proton beam dump. Taken and adapted from [5].

of choice as it offers a large neutron yield for operation with 70 MeV protons, i.e. $9 \times 10^{14}\,\mathrm{s^{-1}\,mA^{-1}}$ according to [5], as well as good workability and a large blistering threshold. In order to reduce the thermal and mechanical stress induced by heating of the target during irradiation, a cooling concept based on microchannels for internal cooling is proposed for the HBS target as shown in figure 3.6. Here, heat dissipation is obtained via water flow with $8\,\mathrm{m\,s^{-1}}$ through 0.35 mm thick microchannels which penetrate the target. After propagating through the 6.34 mm thick target layer, the protons are stopped in a dedicated beam stop layer, which is made of water. The design of the microchannels is adjusted such that the proton beam penetration depth is similar for protons impinging and propagating at different positions of the target. This yields a fishbone-type structure with inclined microchannels. The cooling capacity of the target allows operation with a power density of $1\,\mathrm{kW\,cm^{-2}}$.

3.2. Test facility at JULIC

Parallel to its purpose of supplying protons and deuterons to the COoler SYnchrotron (COSY) at the nuclear physics institute (IKP) of Forschungszentrum Jülich GmbH, the JUelich Light Ion Cyclotron (JULIC) accelerator operates different experimental areas. This allows to build a test facility of a low-energy accelerator-driven neutron sources on site enabling various experiments for the development of HBS components. In this context, various experiments have been performed such as neutron yield measurements to evaluate the choice of target material at HBS (described in detail in chapter 6) [12], the efficiency of a cold moderator with mesitylene [43] as well as with mixtures of liquid ortho- and para-hydrogen. Further progress towards HBS at JULIC is made with the setup of a multiplexer system (described in detail in chapter 4) and the installation of a prototype of the HBS target station.

In the following, the layout of the cyclotron accelerator JULIC as well as an overview

of a low-energy accelerator-driven neutron source test facility at JULIC is presented.

3.2.1. JULIC

The cyclotron JULIC is in use since the end of the 1960s. For operation with COSY in the early 1990s, most systems of the cyclotron were refurbished enabling operation with unpolarized and polarized H^- and D^- at 45 MeV and 76 MeV, respectively. An overview of the JULIC facility with associated experimental areas is given in figure 3.7.

Two independent ion sources are used to supply JULIC with unpolarized H^- and D^-. Both are multicusp filament volume sources from the commercial manufacturers AEA and IBA. For the generation of polarized H^- and D^-, a colliding beam source (CBS) is used [44]. The proton and deuteron beams are extracted at 4.5 keV and 7.6 keV, respectively, and transported to the cyclotron through a source beamline. In the source beamline, a chopper electrode is installed enabling the generation of a micropulse time structure of the beam. The micropulsing superimposes the macropulse which gates the beam. The beam is injected from below into the centre of the cyclotron after passing a double gap buncher system which helps to match the beam to the acceptance of the cyclotron. The cyclotron JULIC is of azimuthally varying field (AVF) type with the magnet poles providing three hills and three valleys. Three double gap RF cavities for acceleration are installed in the magnet valleys. For extraction of the beam from the cyclotron, an electrostatic septum is used to guide the beam on the outer turn in the cyclotron to the subsequent beamline.

The proton or deuteron beam which is provided by JULIC is directed by dipole and quadrupole magnets to the synchrotron COSY or to different experimental areas and irradiation sites. At IBP[1], irradiations can be performed. For further experiments with larger spatial requirements, the beam can be guided through the NESP[2] beamline into the *Big Karl* experimental area. Here, a low-energy accelerator-driven neutron source test facility will be installed which is presented in the following section.

3.2.2. JULIC Neutron Platform

The JULIC Neutron Platform represents a low-energy accelerator-driven neutron source supplied by a pulsed 45 MeV proton beam with 10 µA maximum beam current obtained from the cyclotron JULIC. The facility will be installed in the Big Karl experimental area shown in figure 3.7 and will be operated with protons from the JULIC accelerator provided through the NESP beamline. The JULIC Neutron Platform project aims to provide an experimental test stand for the development of components for the future HBS facility in terms of targetry, neutron provision, moderator development, optimization of the TMR unit and proton beam multiplexing.

[1] Industriebestrahlungsplatz, engl.: industry irradiation site.
[2] Niederenergiebestrahlungsplatz, engl.: low energy irradiation site.

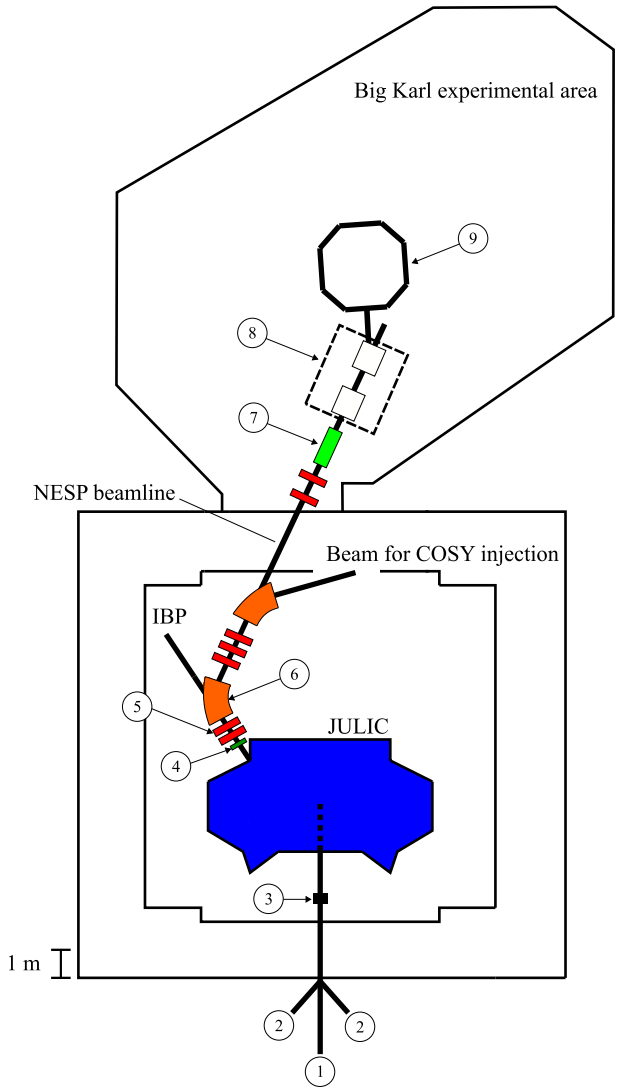

Figure 3.7.: Layout of the JUelich Light Ion Cyclotron (JULIC) accelerator facility with associated experimental areas in building 07.2 of Forschungszentrum Jülich GmbH. 1: Colliding beam source for polarized H^- and D^--beams, 2: Multi cusp filament volume sources supplying unpolarized H^- and D^--beams, 3: Electrostatic chopper, 4: Moveable graphite degrader, 5: Quadrupole magnets (all in red), 6: 38.25° dipole magnets (all in orange), 7: Non-destructive diagnostics, i.e. beam position monitor (BPM) and fast current transformer (FCT), 8: Multiplexer system, 9: HBS prototype target station.

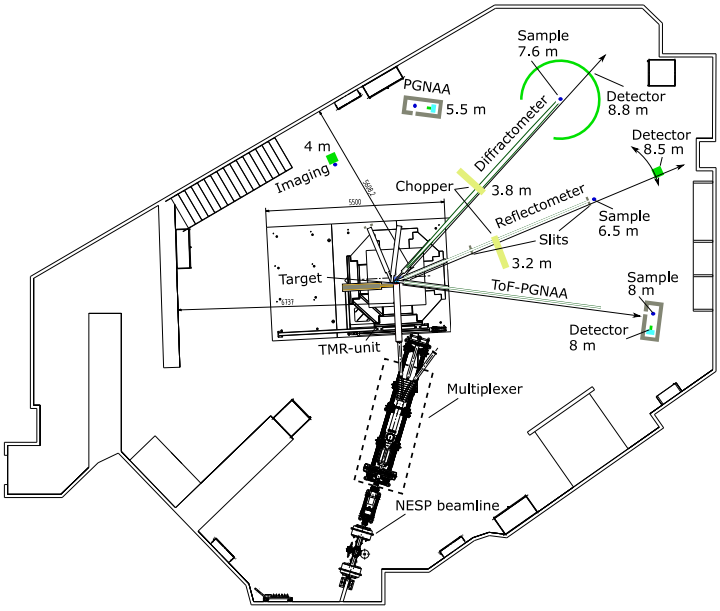

Figure 3.8.: Floor plan of the planned JULIC Neutron Platform in the Big Karl experimental area. The facility is based on a test setup of a HBS type target station, which is irradiated with protons from the NESP beamline in the horizontal plane. Five extraction channels are planned with three subsequent neutron beamlines offering a time-of-flight (ToF) option for a reflectometer, ToF-PGNAA (prompt gamma neutron activation analysis) and a diffractometer. Two other beamlines offer a future use for imaging and PGNAA.

Furthermore, it allows to set up and operate neutron scattering and neutron analytics instruments for the development, training and research together with university groups and industry. An overview of the JULIC Neutron Platform is given in figure 3.8.

For neutron generation at the JULIC Neutron Platform a tantalum target with microchannel cooling structure as shown in figure 3.6 is employed which is framed by a Target-Moderator-Reflector assembly (TMR) and subsequent shielding as shown in figure 3.5. This represents a test setup of the HBS target station with the exception that the target is irradiated from the side rather than from the top as shown in figure 3.1. The HBS prototype target station at JULIC will allow testing of neutron extraction as well as target cooling and handling. The target station is installed after

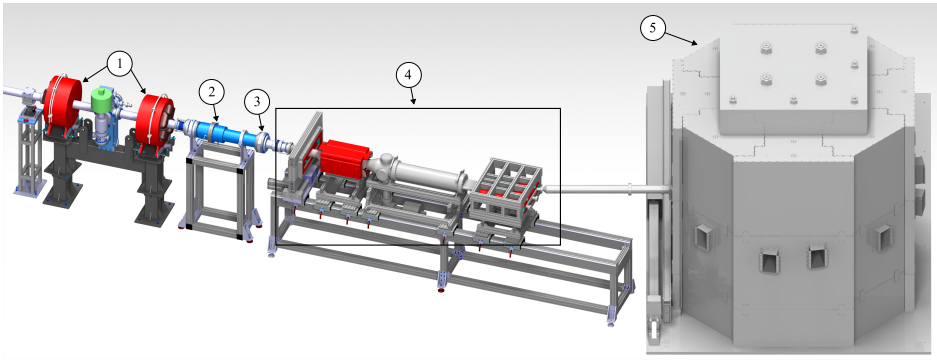

Figure 3.9.: Layout of the JULIC Neutron Platform. 1: Quadrupole doublet, 2: Beam position monitor (BPM), 3: Fast current transformer (FCT), 4: Multiplexer system test setup (discussed in detail in chapter 4), 5: HBS prototype target station. The facility is supplied with 45 MeV H^- stripped to protons shortly behind the FCT before the multiplexer system. The drawing does not show the neutron guides and instruments which will be installed according to figure 3.8.

the multiplexer test setup. It uses the left beamline of multiplexer system which is tilted by 17° with respect to the NESP beamline from JULIC. This provides a larger area on the right side of the target station to arrange different instruments using the time-of-flight option. Here, a reflectometer, a TOF-PGNAA and a diffractometer are planned with instrument lengths ranging between 8 m and 10 m. Behind the target station, a neutron imaging beamline and a PGNAA setup are foreseen. The target station will be operated with 4 % duty cycle which provides an average beam power on the target of 18 W. This is comparable with respect to existing compact accelerator-driven neutron sources as for example at RANS [45] operating at 7 W average power.

A technical drawing of the JULIC Neutron Platform without neutron guides and instruments is shown in figure 3.9. Three beamlines emerge from the multiplexer test setup with the left beamline being connected to the target station. The two other beam ports can be accessed independently with limited space available due to the large extent of the target station. However, small experiments such as e.g. neutron yield measurements (as described in chapter 6) can be connected to the right beam port. The straight beamline coming from the multiplexer test setup is used for diagnostics of the proton beam and performance tests of the multiplexer system. Operating all three beam ports of the multiplexer in parallel limits the outer beamlines to 2 % duty cycle with the centered beamline being supplied with 4 % duty cycle. Independent operation of the three beamlines can be performed without limitations in the duty cycle which is explained in the following chapter covering the detailed design of the multiplexer test setup at JULIC.

4. Development of a multiplexer system for HBS at JULIC

As mentioned in the previous chapter, the realization of a multiplexer system for use and proof of feasibility is realized in the experimental area Big Karl at the NESP beamline from the injector JULIC of the COSY facility. The individual components of such a multiplexer system are developed on the one hand to fit the beam parameters and to meet the spatial constraints at JULIC, but also to be scalable to the requirements of the HBS facility.

As presented in chapter 1, the efficient operation of a variety of different instruments at low-energy accelerator-driven neutron sources requires the operation of multiple targets stations with different proton pulsing schemes simultaneously. At HBS, three different proton pulsing schemes are multiplexed, i.e. interlaced, with a chopper system as shown in figure 3.4. Further downstream, the multiplexer system is employed to separate the two lower proton pulse frequency components from the highest frequency component and to send them to the dedicated target stations as shown in figure 3.1 requiring synchronization of the multiplexer system to the chopper system. At JULIC, the same concept is implemented. Here, the chopper system consists of an electrostatic deflector positioned in the source beamline of JULIC as shown in figure 3.7. The conceptual layout of the multiplexer system is identical for both JULIC and HBS and shown in figure 4.1.

The conceptual setup of the multiplexer system in figure 4.1 is based on the combination of a kicker and a septum magnet as established technology for the selected deflection of short pulses in charged-particle pulse sequences as presented in section 2.2.4. In order to account for the separation of three different interlaced proton pulse sequences a bipolar kicker magnet and a septum magnet with three different field regions are implemented. The three field regions in the septum magnet are arranged such that the left outer field region deflects positive particles further to the left and vice versa for the right outer field region. The centered region represents a zero field region (field-free region). The kicker magnet directs the two lower frequency components towards the outer field regions of the septum magnet while the higher frequency component passes the system without perturbation. In this manner, a spatial separation of the three pulse sequences is obtained. The angular separation of the emerging beamlines is dominated by the 17° deflection of the septum magnet and the 45° sector bending magnet, which amounts to 62°. The setup can be operated simultaneously with eight quadrupole magnets such that the arcs of the multiplexer

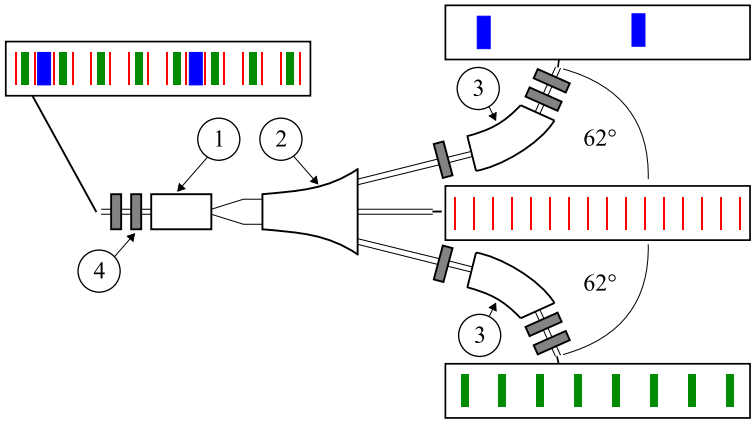

Figure 4.1.: Conceptual layout of the multiplexer system as realized at HBS and partly at JULIC. 1: Bipolar kicker magnet, 2: Septum magnet with three different field regions, 3: 45° sector bending magnet, 4: Quadrupole magnet (all in gray). The higher frequency proton pulse components are indicated in red while the lower frequency proton pulse components are indicated in green and blue. After the multiplexer system, the multiplexed pulse structure is unraveled into three beamlines inclined by 62°. Note that the multiplexer setup at JULIC does not include sector bending magnets (3) and quadrupole magnets (4) due to spatial limitations and limited availability of resources.

system yield an achromat, i.e. dispersion-free optics ($\sigma_{16} = \sigma_{26} = 0$ in equation 2.20 behind the multiplexer system[1]), which will be presented in detail in the following chapter.

The design goals for the multiplexer system at JULIC and at HBS differ slightly as listed in table 4.1. For the development of the multiplexer system at JULIC, which is described in the following, one generally targets a system operated at lower proton energy. Furthermore, this system is less elaborated since the first stage of realization demands less stringent timing parameters in terms of 30 Hz and 0.2 Hz for the proton pulse sequences sent straight and into the arcs, respectively. Also, no achromatic optics are envisaged due to the restricted spatial requirements.

In the following[2], the realization of a multiplexer system at JULIC, following the

[1] This holds only for $\sigma_{16} = \sigma_{26} = 0$ prior to the multiplexer system

[2] Parts of this chapter have been published [46]. The contributions of the authors are given in the following (according to `https://www.elsevier.com/authors/policies-and-guidelines/credit-author-statement`): **Marius Rimmler:** Writing - original draft, Conceptualization, Investigation. **Olaf Felden:** Supervision. **Ulrich Rücker:** Supervision. **Helmut Soltner:**

Table 4.1.: Summary of the design parameters for the multiplexer system at JULIC and at HBS. $(B\rho)$ is the beam rigidity. $f_{\text{straight(deflected)}}$ is the frequency of the pulse sequence, which is sent straight or which is deflected, respectively. $\text{dc}_{\text{straight(deflected)}}$ is the corresponding duty cycle. $\text{dc}_{\text{deflected}}$ applies to both left and right deflected pulse sequences. For JULIC, the respective $f_{\text{straight(deflected)}}$ and $\text{dc}_{\text{deflected}}$ in parentheses gives the design values for a first experimental proof of principle with relaxed performance.

	JULIC	HBS
Particle	Proton	Proton
Beam energy	45 MeV	70 MeV
$(B\rho)$	0.98 T m	1.23 T m
Beam current	10 µA	100 mA
$f_{\text{straight}}, f_{\text{deflected}}$	400(30) Hz,100(0.2) Hz	400 Hz,100 Hz
$\text{dc}_{\text{straight}}$, $\text{dc}_{\text{deflected}}$	4 %,2 %(1 ‰)	2 %
Total length	5 m	10 m
Beam optics	-	Achromat

concept displayed in figure 4.1 and fulfilling the design goals in table 4.1, is described. First, the technical layout with its three major components is presented. Then, developments in terms of calculations of beam dynamics including measurements of the Twiss parameters and the design of the main components of the multiplexer system are shown. Finally, first results obtained during operation of the dynamic kicker part of the setup are shown.

4.1. Layout

Figure 4.2 shows the technical layout of the multiplexer system as realized at JULIC. The position inside the experimental area is indicated in figure 3.9. The multiplexed proton beam is obtained from the COSY injector cyclotron JULIC from the left. The multiplexer system is based on three components. The dynamic component is realized by an air-cooled kicker electromagnet with length l = 520 mm (effective length l_{eff} = 610 mm) and a gap height of 180 mm. The kicker magnet is capable of generating a beam deflection angle of more than 40 mrad. The gap height of the kicker magnet is reduced by 68 mm (to 112 mm) for the more performant operation with $f_{\text{deflected}} \leq 50$ Hz, which is described in more detail in section 4.3.2. The kicker magnet is positioned at 1500 mm distance to a newly developed permanent magnet based septum magnet with three field regions which will be referred to as Three-Field Septum Magnet (TFSM) in the following. At the front side of the TFSM, two

Conceptualization. **Paul Zakalek:** Supervision, **Ralf Gebel:** Funding acquisition. **Thomas Gutberlet:** Project administration. **Thomas Brückel:** Project administration.

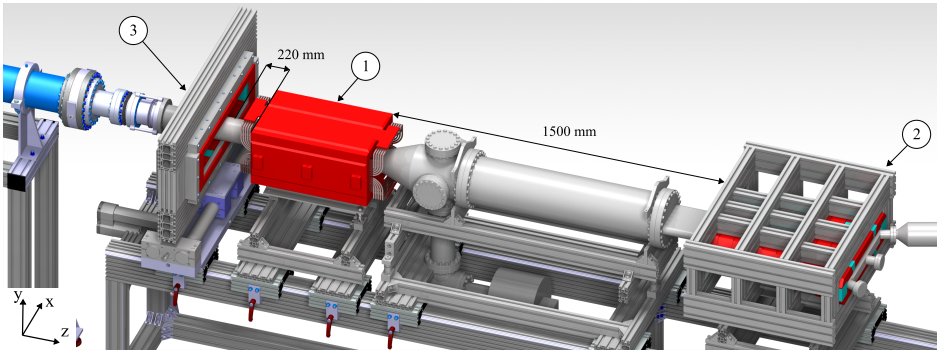

Figure 4.2.: Technical layout of multiplexer system as realized at JULIC. The position inside the experimental area is shown in figure 3.9. The three main components of the multiplexer system are labeled. 1: Kicker magnet, 2: Three-Field Septum Magnet (TFSM), 3: Three-Field Magnet (TFM). The labeling order is according to the description in this chapter. The important dimensions, i.e. distance from kicker magnet to the TFSM and distance from the TFM to the kicker magnet, are indicated. Note that the vacuum aperture is enlarged from 100 mm to 200 mm inner diameter just behind the kicker magnet in order to accommodate the different beam trajectories originating from the deflection by the kicker magnet or the TFM. At the end of the TFSM, three different beam ports can be accessed.

outer dipole field regions of different polarity and a field-free central region are each separated by 62 mm, which is well reachable with a deflection angle of 35 mrad from the kicker magnet. The TFSM is designed for a length of l = 650 mm (l_{eff} = 700 mm) with a gap height l_{gap} = 43 mm generating a deflection angle of 265 mrad. Thus, the total deflection angle at the the end of the multiplexer setup amounts to 35 mrad + 265 mrad = 300 mrad. Inside the septum magnet, a vacuum chamber featuring a broad horizontal acceptance at the front side and three beamline ports at the rear side is installed. Just in front of the kicker magnet, a magnet featuring a similar field distribution as the TFSM representing a prototype of the concept with length l = 140 mm (l_{eff} = 240 mm) and gap height l_{gap} = 110 mm is installed. This so-called Three-Field Magnet (TFM) generates a deflection angle of 27 mrad of the proton beam. It is installed on a horizontally movable support, which allows to perform permanent deflection into either one of the outer field regions of the TFSM depending on the position. This single target operation mode enables us to irradiate the outer target stations without being limited to the performance of the kicker magnet such that the according proton pulse time sequence is either completely controlled by the chopper of the cyclotron or set to continuous wave (CW). An overview of the different operation modes with either usage of the kicker or the TFM is presented in figure 4.3.

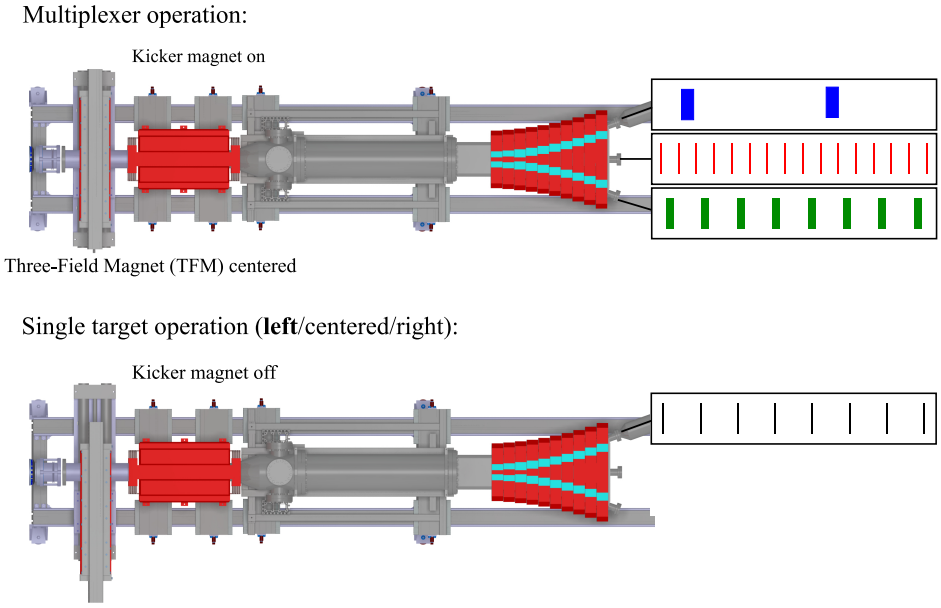

Figure 4.3.: Different operation modes of the multiplexer system at JULIC. The figure shows a top view of figure 4.2. If parallel operation of all three beam ports after the septum magnet is required, the kicker magnet is used to operate the multiplexer system such that the interlaced proton pulse structure is unraveled. In this case, the TFM is centered and the proton beam passes through the zero field region of the TFM. If a single target station is to be operated with an arbitrary pulsing scheme or in CW-operation, the kicker magnet is off. The TFM is moved depending on the operating target station, e.g. moving the TFM to the right introduces a dipole field to the beam which deflects the beam towards the left beam port after the septum magnet as shown.

A detailed report on the developments of the three main components of the multiplexer system and on the beam dynamics within this setup is presented in the following sections.

4.2. Beam dynamics

As mentioned in section 4.1, the multiplexer system is installed at the Big Karl experimental area at JULIC shown in figure 3.9. This area is supplied with 45 MeV protons

from the JULIC cyclotron, which is presented in detail in section 3.2. The corresponding beamline (NESP beamline) connecting the Big Karl area, and thus the multiplexer system, and the cyclotron JULIC is the main subject of investigation in terms of beam dynamics for our setup. As shown in figure 3.7, a total of seven quadrupole magnets and one dipole magnet dominate the beam dynamics in this beamline. In order to properly iterate to an optimal setting of these magnets, it is important to know the initial conditions of the beam prior to this beamline. Therefore, the beam is characterized completely by measurements of the beam matrix using only one quadrupole in the beamline. For this, the so-called quad scan method [15, p. 224 ff.] is employed to obtain the 2-dimensional beam matrix (equation 2.14) for both horizontal and vertical planes, i.e. the 4-dimensional beam matrix. Furthermore, a method solving a set of six non-linear coupled equations with the NEWTON-RAPHSON method [47] is used in order to extract the full 5-dimensional beam matrix (equation 2.17). The results are then propagated back to the beginning of the NESP beamline and employed for beam transport simulations, which take into account all quadrupole magnets in the beamline.

4.2.1. Beam characterization

The measurements of the beam matrix are carried out with the second quadrupole after the cyclotron JULIC in figure 3.7 labeled as QI12 together with a beam monitor in the IBP-beamline. All other quadrupole magnets are shut off for the measurements. The measurement setup uses a Multi-Wire Proportional Chamber (MWPC) as beam monitor and is shown in figure 4.4 together with an overview of ion-optical elements in the NESP beamline.

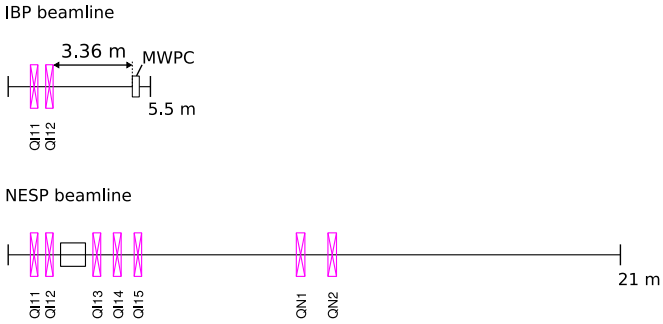

Figure 4.4.: Lattice layout of the IBP beamline and the NESP beamline from figure 3.7 for the beam characterization and beam dynamics calculations. The IBP beamline layout (top) shows the geometry for the measurements of the beam matrix elements with the MWPC being positioned 3.36 m downstream of QI12. A detailed list of the elements in the beamlines is given in appendix B.

For the beam characterization, the quadrupole QI12 is used to vary the beam size at the MWPC in order to extract the beam matrix at the beginning of the quadrupole. The beam transport from the beginning of QI12 to the MWPC is described by the beam transport matrix

$$M = M_{\text{drift}} \cdot M_{\text{QF(D)}}, \tag{4.1}$$

with M_{drift} being the drift transport matrix from equation 2.31 and $M_{\text{QF(D)}}$ being the quadrupole transport matrix from equation 2.32 or equation 2.33 depending on the polarity of the quadrupole magnet. With M in equation 4.1, the beam matrix Σ_0 prior to the quadrupole transforms to the beam matrix at the MWPC Σ_{MWPC} according to equation 2.27. In the so-called thin lens approximation of quadrupole magnets, i.e. the quadrupole strength k and length L are small such that the first-order TAYLOR-approximation of $\sin\sqrt{k}L \approx \sqrt{k}L$ and $\cos\sqrt{k}L \approx 1$ is a good approximation, the (1,1)-element of the beam matrix at the MWPC $\sigma_{\text{MWPC},11}$ and thus the horizontal rms beam size squared at the MWPC[3], i.e. $\sigma_x^2 = \sigma_{\text{MWPC},11}$ (according to equation 2.15), can be a deduced to be

$$\begin{aligned}\sigma_x^2 =& k^2 d^2 L^2 \sigma_{0,11} - 2kdL(d\sigma_{0,12} + \sigma_{0,11}) + d^2\sigma_{0,22} \\ &+ 2d\sigma_{0,12} + \sigma_{0,11} + \frac{(d\sigma_{0,26} + \sigma_{0,16}(1 - dkL))^2}{\sigma_{0,66}}\end{aligned} \tag{4.2}$$

and analogous for the vertical rms beam size[4]. Here, d represents the distance from the quadrupole to the MWPC ($d = 3.36\,\text{m}$ in figure 4.4) and $\sigma_{0,ij}$ is the (i,j)-element of the beam matrix in front of quadrupole QI12. In the following, the formalism for the calculation of the beam matrix elements $\sigma_{0,ij}$ with focus on the horizontal dimension will be examined. However the formalism is identical for the vertical dimension.

In the quad scan method, the dispersive elements of the beam matrix are neglected, i.e. $\sigma_{0,16} = \sigma_{0,26} = \sigma_{0,36} = \sigma_{0,46} = 0$, such that the last term in equation 4.2 cancels. With this, varying k and recording the respective σ_x^2 allows to calculate $\sigma_{0,11}$, $\sigma_{0,12}$ and $\sigma_{0,22}$ by fitting the parabolic model

$$\sigma_x(k) = Ak^2 + Bk + C \tag{4.3}$$

to the data. From the parameters of the fit and equation 4.2, one gets

$$\sigma_{0,11} = \frac{A}{d^2L^2} \tag{4.4}$$

$$\sigma_{0,12} = \frac{B + 2dL\sigma_{0,11}}{-2d^2L} \tag{4.5}$$

[3] In the following, the subscript MWPC is dropped for the rms beam size squared.

[4] For σ_y^2, replace $\sigma_{0,11}$, $\sigma_{0,12}$, $\sigma_{0,22}$, $\sigma_{0,16}$ and $\sigma_{0,26}$ with $\sigma_{0,33}$, $\sigma_{0,34}$, $\sigma_{0,44}$, $\sigma_{0,36}$ and $\sigma_{0,46}$ on the right hand side of equation 4.2, respectively.

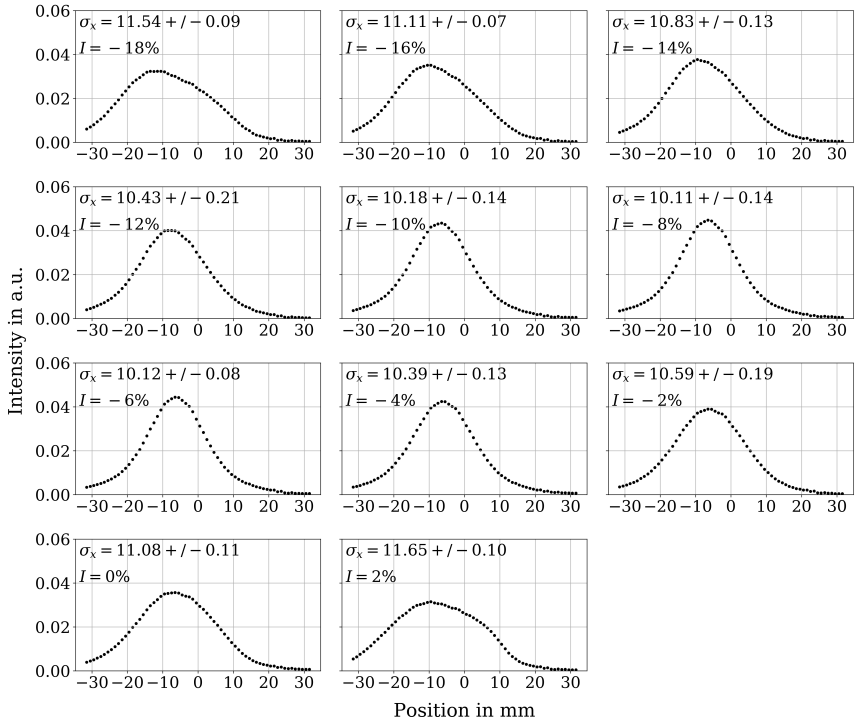

Figure 4.5.: Normalized horizontal beam profile as recorded on the MWPC for different quadrupole currents of QI12 in percent of the maximum current $I_{\max} = 80\,\mathrm{A}$. For each setting, the corresponding horizontal rms beam size σ_x is calculated (given in mm). The beam waist is obtained at $I = -8\,\%$.

$$\sigma_{0,22} = \frac{C - \sigma_{0,11} - 2d\sigma_{0,12}}{d^2}, \tag{4.6}$$

such that the 2-dimensional beam matrix Σ_x is fully characterized.

In figure 4.5 and figure 4.6, the horizontal and vertical beam profiles as recorded on the MWPC for different settings of the quadrupole magnet QI12 are shown. The beam profiles are averaged over five consecutive measurements at a constant setting of the quadrupole. The graphs show a scan of the quadrupole current over the beam waist. The quadrupole setting is given in percent of the maximum current such that it transforms to a quadrupole strength with

$$k\left[\mathrm{m}^{-2}\right] = \frac{g_{\max}}{(B\rho)} I\,[\%] = \frac{B_{\mathrm{tip}}}{a\,(B\rho)} I\,[\%], \tag{4.7}$$

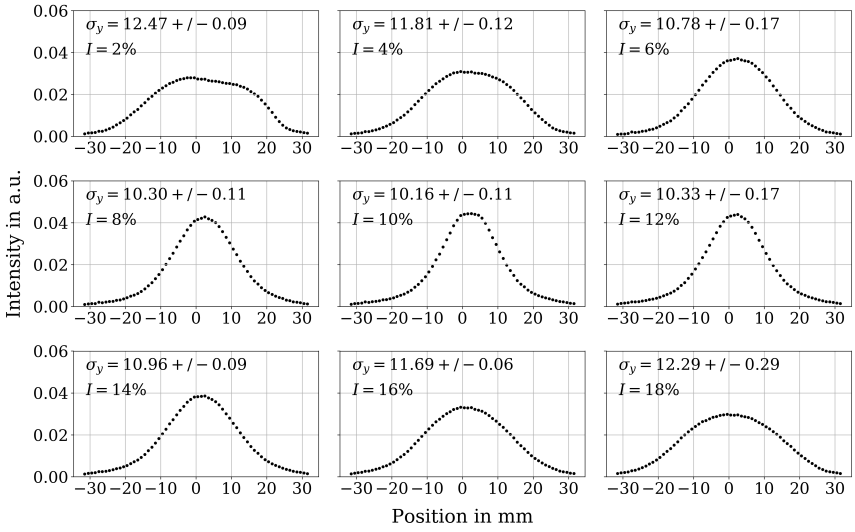

Figure 4.6.: Normalized vertical beam profile as recorded on the MWPC for different quadrupole currents of QI12 in percent of the maximum current $I_{\max}$ = 80 A. For each setting, the corresponding vertical rms beam size σ_y is calculated (given in mm). The beam waist is obtained at $I = 10\,\%$.

with $g_{\max} = B_{\text{tip}}/a$ being the maximum gradient of the quadrupole magnet. B_{tip} is the pole-tip field, i.e. the maximum magnetic flux density on the outermost position of the quadrupole which is described by the aperture radius a. For QI12, $B_{\text{tip}} = 0.52\,\text{T}$ and $a = 36\,\text{mm}$. Note that equation 4.7 holds for positively charged particles such that $I\,[\%] > 0$ results in $k\,[\text{m}^{-2}] > 0$, i.e. a horizontally focusing quadrupole. Furthermore, the formalism in equation 4.2 is derived for positive particles. Since H^- is used throughout the beamline where the measurements are conducted, equation 4.7 has to be multiplied with -1 to apply the formalism correctly to negative particles. With this and the results presented in figure 4.5 and figure 4.6, one obtains figure 4.7, which shows the rms beam size squared versus the quadrupole strength.

In figure 4.7, a fit curve according to the model in equation 4.3 is shown, which allows to calculate the horizontal and vertical beam matrix (following equations 4.4 to 4.6). The results in terms of emittance ϵ and Twiss parameters β, α, γ in front of QI12 calculated according to

$$\epsilon_{0,x} = \sqrt{\sigma_{0,11}\sigma_{0,22} - \sigma_{0,12}^2} \tag{4.8}$$

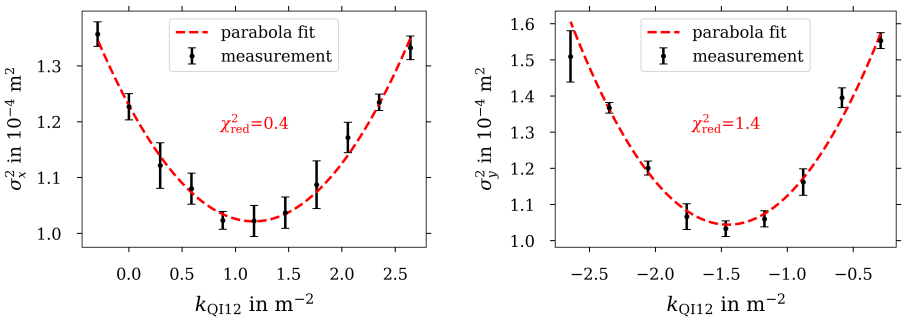

Figure 4.7.: Horizontal (left) and vertical (right) rms beam size squared σ_x^2 and σ_y^2 versus quadrupole strength of quadrupole QI12, k_{QI12}, with data taken from measurements (shown in black) in figure 4.5 and figure 4.6, respectively. The red curve shows a parabola fit according to equation 4.3 to the data. The corresponding reduced chi-square χ^2_{red} are displayed.

$$\beta_{0,x} = \frac{\sigma_{0,11}}{\epsilon_{0,x}} \tag{4.9}$$

$$\alpha_{0,x} = -\frac{\sigma_{0,12}}{\epsilon_{0,x}} \tag{4.10}$$

$$\gamma_{0,x} = \frac{\sigma_{0,22}}{\epsilon_{0,x}} \tag{4.11}$$

(and analogous for y) are presented in table 4.2.

The quad scan method neglects the dispersion prior to the quadrupole by setting $\sigma_{0,16} = \sigma_{0,26} = \sigma_{0,36} = \sigma_{0,46} = 0$. However, the beam extracted from the cyclotron naturally has a finite dispersion due to the deflection of the beam during acceleration. Thus, the results presented in table 4.2 represent the area and shape of a dispersively broadened ellipse in 2-dimensional phase space as shown in figure 2.4 due to the finite momentum uncertainty of the beam, i.e. $\delta_0 = \sqrt{\sigma_{0,66}} \neq 0$.

In order to access the dispersion-free emittance with $\delta = 0$ in figure 2.4 and therefore all elements of the 5-dimensional beam matrix in equation 2.17, one needs to consider equation 4.2 completely, i.e. including the last term, together with the measurements in figure 4.5 and figure 4.6. Equation 4.2 contains six beam matrix elements to be calculated. Thus, solving six non-linear coupled equations by setting six different values for the quadrupole strength $k_{QI12,i}$ and by measuring six different values for the rms beam size squared $\sigma^2_{x(y),i}$, with the subscript i representing the number of the measurement, for both x and y gives us the 5-dimensional beam matrix. This set of non-linear equations is solved numerically using the Newton-Raphson method [48]. With $\sigma^2_{x,i}$ for $i = 2,3,4,5,6,7$ and $\sigma^2_{y,i}$ for $i = 3,4,5,6,7,8$ in figure 4.7 when

Table 4.2.: Summary of the results from the quad scan method with quadrupole QI12. The results characterize the beam at the beginning of the quadrupole QI12. Note that the quad scan method does not consider dispersion of the beam, which, however, is finite at JULIC. Thus the corresponding emittances $\epsilon_{0,x(y)}$ describe a dispersively-broadened ellipse as introduced in figure 2.4.

	Quad scan
$\epsilon_{0,x}$/mm mrad	10.1(3)
$\beta_{0,x}$/m	1.09(5)
$\alpha_{0,x}$	-0.11(3)
$\gamma_{0,x}$/m^{-1}	0.93(2)
$\epsilon_{0,y}$/mm mrad	17(2)
$\beta_{0,y}$/m	1.8(1)
$\alpha_{0,y}$	1.43(6)
$\gamma_{0,y}$/m^{-1}	1.71(4)

counting from left to right, the beam parameters in table 4.3 can be obtained.

With the beam properties at the beginning of QI12 from table 4.3, the beam is completely characterized. Here ϵ_0, β_0, α_0 and γ_0 represent emittance and TWISS parameters of the phase ellipse with $\delta = 0$ in figure 2.4. The parameters $\delta_0 = \sqrt{\sigma_{0,66}}$, $\eta_0 = \sigma_{0,16}/\sigma_{0,66}$ and $\eta_0' = \mathrm{d}\eta_0/\mathrm{d}s = \sigma_{0,26}/\sigma_{0,66}$ describe the momentum uncertainty, dispersion function and derivative of the dispersion function, respectively. $\epsilon_{0,\mathrm{disp.}}$ is the emittance of the dispersively broadened phase ellipse according to

$$\epsilon_{0,\mathrm{disp.},x} = \sqrt{\left(\sigma_{0,11}^{(0)} + \frac{\sigma_{0,16}^2}{\sigma_{0,66}}\right)\left(\sigma_{0,22}^{(0)} + \frac{\sigma_{0,26}^2}{\sigma_{0,66}}\right) - \left(\sigma_{0,12}^{(0)} + \frac{\sigma_{0,16}\sigma_{0,26}}{\sigma_{0,66}}\right)^2} \tag{4.12}$$

and analogous for y. The results of $\epsilon_{0,\mathrm{disp.}}$ in table 4.3 agree with the results of ϵ_0 in table 4.2 proving that both methods are consistent. Furthermore, the results in table 4.3 seem plausible as there is good agreement of the independently calculated momentum uncertainties δ_0. The propagation of the beam described by the results in table 4.3 from QI12 to the MWPC with the different quadrupole settings gives figure 4.8.

Both the quad scan method and the application of the NEWTON-RAPHSON method yield compatible results for the 4-dimensional and 5-dimensional beam matrix at the beginning of quadrupole QI12 which can be associated with the beam profile measurements in figure 4.5 and figure 4.6. One can see from figure 4.8 that the measured vertical rms beam size deviates slightly from the calculations with the NEWTON-RAPHSON method when considering small quadrupole strengths. Here, the parabola fit obtained from the quad scan method in figure 4.7 appears to be more consistent

Table 4.3.: Summary of the results obtained from a set of six non-linear coupled equations following equation 4.2 via the Newton-Raphson method. The results characterize the beam at the beginning of the quadrupole QI12.

	Newton-Raphson method
$\epsilon_{0,x}$/mm mrad	9.70
$\beta_{0,x}$/m	1.14
$\alpha_{0,x}$	-0.06
$\gamma_{0,x}$/m^{-1}	0.88
δ_0	1.84×10^{-3}
$\eta_{0,x}$/m	0.41
$\eta'_{0,x}$	0.43
$\epsilon_{0,\mathrm{disp.},x}$/mm mrad	10.20
$\epsilon_{0,y}$/mm mrad	10.80
$\beta_{0,y}$/m	1.95
$\alpha_{0,y}$	1.15
$\gamma_{0,y}$/m^{-1}	1.20
δ_0	1.84×10^{-3}
$\eta_{0,y}$/m	1.37
$\eta'_{0,y}$	-2.00
$\epsilon_{0,\mathrm{disp.},y}$/mm mrad	15.90

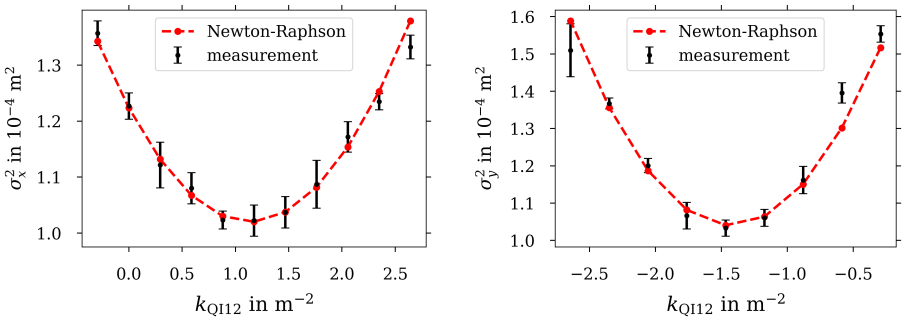

Figure 4.8.: Horizontal (left) and vertical (right) rms beam size squared σ_x^2 and σ_y^2 versus quadrupole strength of quadrupole QI12, k_{QI12}, with data taken from measurements (shown in black) in figure 4.5 and figure 4.6, respectively. The red curve shows the beam size obtained from the propagation of the results in table 4.3 from QI12 to the MWPC with equation 4.2 for the different quadrupole strengths.

with the data. However, with the quad scan method one can only access the dispersively broadened phase ellipse and there is no information on the position of the particles in phase space depending on their momentum uncertainty (figure 2.4). For simulation of the beam transport through a beamline containing dipole magnets, it is required to know the initial beam parameters completely in terms of dispersion and momentum uncertainty. Therefore, the following beam transport simulation is based on the parameters in table 4.3.

4.2.2. Beam transport

The beam transport simulations are carried out with the *Bmad* library [49]. Here, the focus is on the simulation of the longitudinal evolution of the rms beam size $\sigma(s)$ given by

$$\sigma(s) = \sqrt{\epsilon\beta(s) + (\eta(s)\delta)^2}, \tag{4.13}$$

with the rms emittance ϵ, the betatron function $\beta(s)$ (equation 2.15), the dispersion function $\eta(s)$ (equation 2.19) and the momentum uncertainty δ. In the *Bmad* code, the kinetic energy uncertainty $\Delta T/T_0$ is considered which is deduced from the momentum uncertainty $\delta = \Delta p/p_0$ via

$$\frac{\Delta T}{T_0} = \frac{\gamma + 1}{\gamma}\delta, \tag{4.14}$$

with γ being the LORENTZ factor (see equation A.2). For 45 MeV protons, i.e. $\gamma = 1.048$, and thus with the results from table 4.3, i.e. $\delta = 1.84 \times 10^{-3}$, one gets $\Delta T/T_0 = 3.8 \times 10^{-3}$.

The beam propagation in the NESP beamline shown in figure 3.7 is investigated. This beamline contains seven quadrupole magnets for beam focusing and one dipole magnet. The beginning of the NESP beamline is defined to be 0.86 m in front of quadrupole QI11. The starting parameters of the beam for the beam transport simulation are derived from table 4.3. In order to define these parameters at the beginning of the NESP beamline, the results obtained at QI12 need to be propagated upstream by a distance of $s = -1.46$ m. The TWISS parameters and dispersion function transform via the transport matrix M according to

$$\begin{pmatrix}\beta(s)\\ \alpha(s)\\ \gamma(s)\end{pmatrix} = \begin{pmatrix} M_{11}^2 & -2M_{11}M_{12} & M_{12}^2 \\ -M_{11}M_{21} & M_{11}M_{22} + M_{12}M_{21} & -M_{12}M_{22} \\ M_{21}^2 & -2M_{21}M_{22} & M_{22}^2 \end{pmatrix} \begin{pmatrix}\beta(0)\\ \alpha(0)\\ \gamma(0)\end{pmatrix} \tag{4.15}$$

and

$$\begin{pmatrix}\eta(s)\\ \eta'(s)\\ 1\end{pmatrix} = \begin{pmatrix} M_{11} & M_{12} & M_{16} \\ M_{21} & M_{22} & M_{26} \\ 0 & 0 & 1 \end{pmatrix} \begin{pmatrix}\eta(0)\\ \eta'(0)\\ 1\end{pmatrix} \tag{4.16}$$

Table 4.4.: Twiss parameters and dispersion function at the beginning of the NESP beamline as calculated from table 4.3 when going to $s = -1.46\,\mathrm{m}$ in front of QI12. Emittances and momentum spread are constant during propagation.

	Beginning of NESP beamline
$\beta_{0,x}/\mathrm{m}$	2.84
$\alpha_{0,x}$	1.22
$\gamma_{0,x}/\mathrm{m}^{-1}$	0.88
$\eta_{0,x}/\mathrm{m}$	-0.22
$\eta'_{0,x}$	0.43
$\beta_{0,y}/\mathrm{m}$	7.87
$\alpha_{0,y}$	2.90
$\gamma_{0,y}/\mathrm{m}^{-1}$	1.20
$\eta_{0,y}/\mathrm{m}$	4.29
$\eta'_{0,y}$	-2.00

following the references [16, p. 262] and [16, p. 266], respectively. With this, the inverse of the matrices can be built to propagate the parameters to the beginning of the NESP beamline, which results in table 4.4.

Table 4.5.: Quadrupole strengths corresponding to the beam transport simulation in figure 4.9.

Quadrupole	k/m^{-2}
QI11	0.24
QI12	1.05
QI13	-2.74
QI14	4.65
QI15	-2.74
QN1	1.84
QN2	-1.78

With the starting parameters of the beam given in table 4.4 and table 4.3, the rms beam size throughout the NESP beamline can be calculated. By iteratively adjusting the quadrupole strength of the seven quadrupoles in the beamline and by taking into account the corresponding aperture diameter, one attains more than 90 % transmission when going from the beginning of the NESP beamline to the end, i.e. the position of the target in the TMR-unit as displayed in figure 3.9. The longitudinal evolution of the transversal rms beam envelope is presented in figure 4.9. The corresponding quadrupole strengths are given in table 4.5.

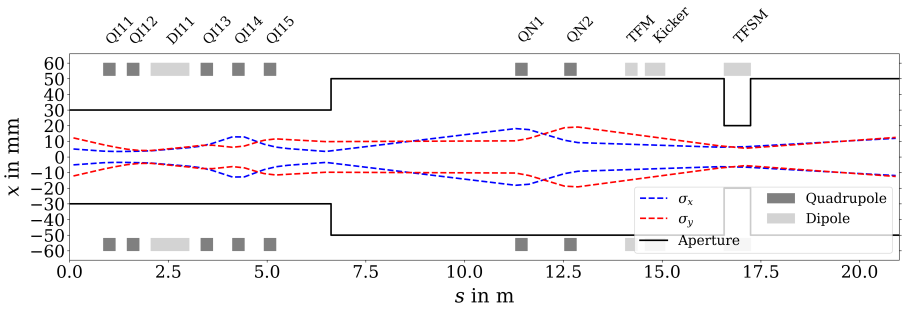

Figure 4.9.: Simulated longitudinal evolution of the transversal rms beam envelopes σ_x and σ_y in the NESP beamline. In addition, the size of the aperture and the position of the main magnets, i.e. quadrupoles and dipoles, as well as of the magnets of the multiplexer setup are presented. The element positions are listed in appendix B. The simulated transmission is around 90 %.

The result in figure 4.9 is important for the design of the three main components of the multiplexer system in terms of gap height of the magnets (figure 4.2). It is especially important for the TFSM, which is introduced in section 4.4, to obtain an aperture in the order of 40 mm without significant beam loss. Note that the beam transport simulation is based on a beam characterization. However, the beam parameters may vary slightly for different beamtimes since beam injection into the cyclotron, acceleration and extraction are not completely reproducible. Thus, the beam characterization and beam transport simulation presented only give a proof of principle, i.e. that it is generally possible to obtain similar beam sizes as presented in figure 4.9. During the commissioning of the beamline the transmission needs to be optimized iteratively by tuning the quadrupoles and monitoring the beam current and beam profile at different positions throughout the beamline.

4.3. Kicker magnet

The kicker magnet, which is used in the multiplexer system, is taken from unused existing stock of the synchrotron COSY. There, it has been employed as a bumper magnet together with two other identical magnets in order to perform stripping injection of the H^- (and D^-) ions into COSY [50]. This magnet has been replaced in COSY by a similar but shorter magnet due to spatial constraints. The kicker magnet is shown in figure 4.10. Its position within the multiplexer system is indicated in figure 4.2. The parameters of the magnet are summarized in table 4.6.

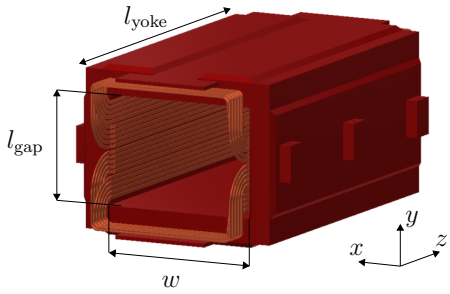

Figure 4.10.: Kicker magnet used in the multiplexer system. Its position in the setup is indicated in figure 4.2. Length l_{yoke}, gap height l_{gap} and aperture width w are specified in table 4.6. The origin of the coordinate system is set to be in the center of the magnet.

Table 4.6.: Specifications of the kicker magnet shown in 4.10.

Name	Symbol	Value
Length	$l_{\text{yoke}}/\text{mm}$	520
Gap height	l_{gap}/mm	180
Aperture width	w/mm	250
Effective length	l_{eff}/mm	610
Turns	N	$2 \cdot 10$
Conductor area	A/mm^2	$8.6 \cdot 4$
Inductance	$L/\mu\text{H}$	393
Resistance	$R/\text{m}\Omega$	24
Design field	B/mT	35
Design current	I/A	250
Design voltage	U/V	150
Design slope	$\dot{B}/(\text{T}\,\text{s}^{-1})$	35

Table 4.7.: Specifications of the kicker magnet power supply. Bipolar operation is realized by contactors at the output of the power supply. This limits the switching time to tens of ms and the maximum number of switch cycles to less than 1×10^5.

Name	Symbol	Value
Current	I/A	0.1-250
Voltage	U/V	0-150
Polarity		Bipolar
Rise time	t_r/ms	1-10
Flat top time	t_ft/ms	15-50
Fall time	t_f/ms	10-50
Repetition rate	f/Hz	<0.25

For the current supply to the kicker magnet, a dedicated and available spare power supply is used. The specifications of the power supply are given in table 4.7. The timing parameters, i.e. rise, flat top and fall time as well as repetition rate, are optimized for the injection process at COSY. Therefore, an asymmetric trapezoidal current-time diagram is obtained. In the power supply, a capacitor bank with 90 mF is charged by an external DC power supply with 4 A, 200 V. When triggered, the capacitor bank is discharged through an array of transistors into the magnet to generate the desired current pulse. The repetition rate is primarily limited by the thermal load in the transistors of the power supply as well as by the current of the charging DC power supply I_DC. With $\mathrm{d}U/\mathrm{d}t = I_\mathrm{DC}/C$ and thus $150\,\mathrm{V}/T = 4\,\mathrm{A}/90\,\mathrm{mF}$, a period length of $T = 4\,\mathrm{s}$ is obtained, i.e. $f = 0.25\,\mathrm{Hz}$, when charging the 90 mF capacitor bank in the power supply to its maximum operating voltage $U = 150\,\mathrm{V}$.

As indicated in figure 4.2, the kicker magnet is positioned such that it is 1500 mm (kicker yoke end to septum yoke front) upstream with respect to the TFSM. With the effective length $l_\mathrm{eff} = 610\,\mathrm{mm}$ and yoke length $l_\mathrm{yoke} = 520\,\mathrm{mm}$ in table 4.6, the distance from the end of the kicker magnet, in terms of its magnetic field in the hard-edge model, to the beginning of the septum magnet reduces to $l = 1500\,\mathrm{mm} - (610\,\mathrm{mm} - 520\,\mathrm{mm})/2 = 1455\,\mathrm{mm}$. The TFSM is designed such that three different field regions with a centered zero field region and two field regions of opposite polarity on the left and right side are obtained with a separation of $\Delta x = 62\,\mathrm{mm}$ each. Thus, the deflection angle Θ, which has to be provided by the kicker magnet can be derived via equation 2.44 to be

$$\Theta = \frac{\Delta x}{l + l_\mathrm{eff}/2} = \frac{62\,\mathrm{mm}}{1455\,\mathrm{mm} + 610\,\mathrm{mm}/2} = 35.2\,\mathrm{mrad}. \tag{4.17}$$

According to equation 2.41, the field maximum required by the kicker magnet, taking into account $(B\rho) = 0.98\,\mathrm{T\,m}$ for 45 MeV protons, amounts to $B = 57\,\mathrm{mT}$, which is

well above the design field given in table 4.6.

In the following, several upgrades of the kicker magnet, which are carried out in order to obtain a stronger magnet field and thus fulfilling the geometrical constraints given by the multiplexer system, are discussed. For this, a second identical power supply, which is connected in parallel, is used. Furthermore, a modification of the yoke of the magnet is performed, which allows to reduce the gap height and thus the current density at constant magnetic field. This allows to increase the operation frequency of the kicker magnet to $\approx 50\,\mathrm{Hz}$. Finally, the concept of an all-new development of a power supply is presented, which performs at a higher repetition rate in order to meet the requirements of operation up to a frequency of 100 Hz for the deflected pulse sequences as issued in table 4.1. To exploit the full potential of such a power supply for future multiplexer operation, a new kicker magnet of identical design but with water-cooled coils will have to be procured.

4.3.1. Parallel connection of power supplies

In order to generate at least 57 mT in the kicker magnet, a current of $I = 409\,\mathrm{A}$ is required according to equation 2.48 with the parameters given in table 4.6. Therefore a second identical and available power supply is employed and connected in parallel, thus generating a total of $I = 500\,\mathrm{A}$ at maximum. A direct parallel connection of the two power supplies results in an oscillation from the controls of the power supplies causing a power supply failure. Thus, an inductance of 330 µH needs to be connected in series with each power supply before performing the parallel connection in order to decouple the controls of the two power supplies. The schematic circuit diagram is shown in figure 4.11. Here, the power supplies are synchronized by a shared trigger line such that both power supplies discharge simultaneously into the magnet. With

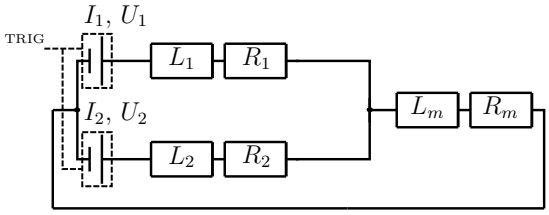

Figure 4.11.: Schematic circuit of parallel connection of two power supplies ($I_1 = I_2 = 250\,\mathrm{A}$, $U_1 = U_2 = 150\,\mathrm{V}$ from table 4.7) in order to supply up to 500 A to the kicker magnet. The inductances $L_1 = L_2 = 330\,\mu\mathrm{H}$ decouple the controls of the power supplies ($R_1 = R_2 = 20\,\mathrm{m\Omega}$). $L_m = 393\,\mu\mathrm{H}$ and $R_m = 24\,\mathrm{m\Omega}$ are inductance and DC resistance of the kicker magnet. The dotted line indicates the control trigger line to the power supplies.

this scheme, 500 A can be supplied to the magnet. The operation of the kicker magnet

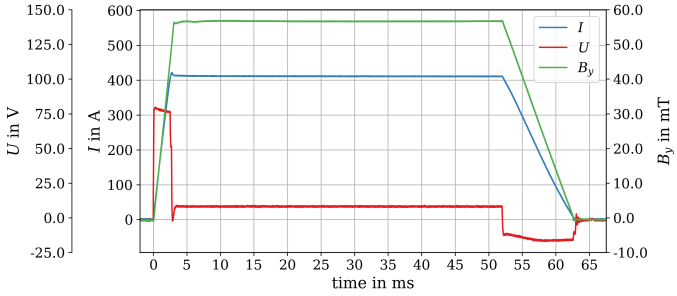

Figure 4.12.: Current, voltage and magnetic field diagram for operation of the kicker magnet with 409 A. The rise, flat top and fall time is set to 3 ms, 49 ms and 11 ms, respectively. The voltage of the power supply is set to 80 V maximum.

with 409 A is displayed in figure 4.12 in terms of a current, voltage and magnetic field diagram showing the generation of 57 mT measured in the center of the kicker magnet.

The additional inductances in figure 4.11 and the larger current supplied to the magnet result in an increase of the rise time of the current and thus the magnetic field. Thus, setting the current rise time at the power supply to the minimum of 1 ms (see table 4.7) results in a larger actual rise time of the magnetic field. Figure 4.13 shows measurements of the rise time of the magnetic field in the center of the magnet, i.e. the time it takes from the beginning of the ramping of the magnetic field to the maximum field, with a 10 kHz HALL probe for different power supply configurations with the kicker magnet.

In figure 4.13, one can see that the parallel operation of a second power supply according to figure 4.11 results in an increase of the magnetic field rise time by 1.37 ms compared to the conventional powering of the magnet. This can be explained by the relation $U = -L \cdot \mathrm{d}I/\mathrm{d}t$. With this, a larger inductance L and a twice as large current difference ΔI at constant voltage U of the power supply as given from the parallel connection of two power supplies results in an at least twice as large time difference Δt when compared to conventional wiring of the magnet. In addition to the configuration with two power supplies, the magnetic field rise time for a configuration with one power supply and an inductance of 330 µH in series is investigated. This is done in order to simulate the increase of the inductance in the magnet that would be caused by potential lowering of the magnet gap height as explained in detail in the following section. Decreasing the gap height by 50 % doubles the magnetic field in the magnet at constant current (see equation 2.48). In addition, the inductance doubles at constant horizontal aperture according to equation 2.52. However, when considering an inset in the magnet which, in addition to decreasing the gap height

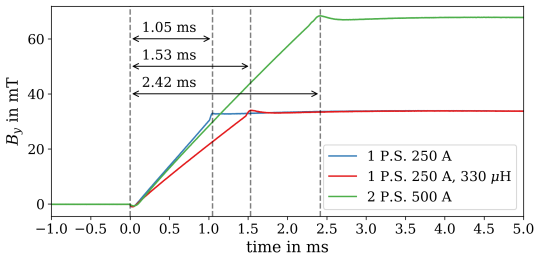

Figure 4.13.: Measurement of the magnetic field rise time, i.e. from the start of the field ramp to the maximum, of different power supply combinations connected to the kicker magnet. The blue line shows the conventional connection of one power supply. The red line shows the same connection with an additional inductance of 330 µH in series while the green line shows the connection of two power supplies according to figure 4.11. All individual power supplies are powered with 250 A and 150 V. The current rise time of the power supplies is set to 1 ms.

by 50 %, decreases the horizontal aperture, one gets a system with one power supply that generates a field comparable to the situation with two power supplies but with competitive magnetic field rise time. In figure 4.13, such a system is investigated by simulating an inset with 50 % gap reduction (current remains at 250 A compared to the two power supply configuration) and 16 % horizontal aperture reduction by a parallel connection of additional 330 µH (84 % of the kicker magnet inductance being 393 µH - table 4.6). Here, an increase of the magnetic field rise time by 0.48 ms is observed when compared to the conventional powering of the magnet, which is a smaller increase of the magnetic field rise time when compared to the two power supply option. This and a lower thermal load in the magnet coils due to a smaller current make the method of gap reduction superior to the wiring with two power supplies. Therefore, an inset for gap reduction was designed and employed for long-term use of the kicker magnet.

4.3.2. Gap reduction

In the previous section, it was concluded that a larger magnetic field in the kicker magnet can either be provided by parallel connection of two power supplies thus increasing the current in the magnet coils, or by reduction of the gap height l_{gap}, i.e. according to equation 2.48 a larger field generated at constant current. The first option has the advantage that no technical modification of the kicker magnet is required and it is instantly operational. Therefore, this option is established first. The second option is not only advantageous in terms of timing, i.e. rise and fall time, as discussed in the previous section, but also when considering the thermal load due to the current inside the kicker magnet coils during operation.

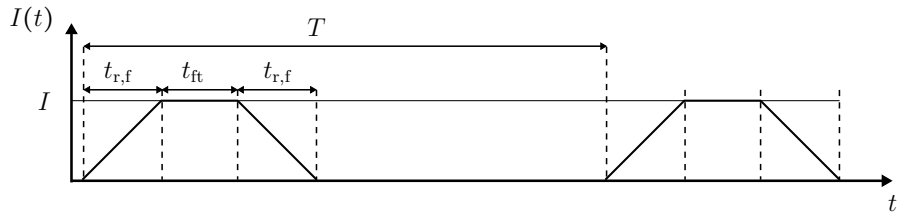

Figure 4.14.: Symmetric, trapezoidal current pulse sequence with rise and fall time $t_{\mathrm{r,f}}$, flat top time t_{ft}, maximum current I and period length T.

The kicker magnet is operated in a pulsed mode such that the effective current

$$I_{\mathrm{eff}} = \sqrt{\frac{1}{T}\int_0^T I^2(t)\,\mathrm{d}t} \tag{4.18}$$

needs to be considered to get the DC equivalent with T being the period length and $I(t)$ being the time-dependent current pulse sequence. Assuming a symmetric, trapezoidal current pulse sequence with rise and fall time $t_{\mathrm{r,f}}$, flat top time t_{ft} and maximum current I as drawn in figure 4.14, I_{eff} can be calculated to be

$$I_{\mathrm{eff,trap.}} = I\sqrt{\frac{1}{T}\left[\frac{2}{3}t_{\mathrm{r,f}} + t_{\mathrm{ft}}\right]}. \tag{4.19}$$

Here, the first term accounts for the slopes of the current pulse while the second term accounts for the flat top. The term t_{ft}/T is defined as flat top duty cycle of the current pulse sequence, which determines directly the maximum duty cycle of the deflected beam of the kicker and thus multiplexer.

For air-cooled electromagnets, i.e the kicker magnet in figure 4.10, where the coils are cooled solely by convection, the maximum current density j in the coils is $1\,\mathrm{A/mm^2}$ for DC operation ($10\,\mathrm{A/mm^2}$ for water-cooled coils) [26, p. 92], such that

$$j = \frac{I_{\mathrm{eff}}}{A_{\mathrm{cond}}} < 1\,\mathrm{A/mm^2}. \tag{4.20}$$

Here, A_{cond} is the conductor cross section area. Thus, the current density j limits the flat top duty cycle of the current pulse sequence in the kicker magnet and therefore the duty cycle of the beam, which is deflected by the multiplexer system. With equation 4.20 and equation 4.19, a limitation of the flat top duty cycle of the current pulse sequence can be derived being

$$\frac{t_{\mathrm{ft}}}{T} < \left(1\,\mathrm{A/mm^2}\cdot\frac{A_{\mathrm{cond}}}{I}\right)^2 - \frac{2}{3}\frac{t_{\mathrm{r,f}}}{T} \tag{4.21}$$

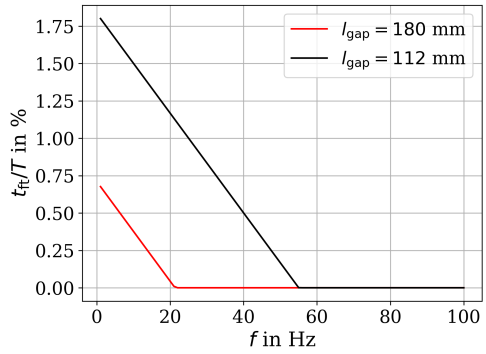

Figure 4.15.: Maximum current pulse sequence duty cycle t_{ft}/T versus current pulse frequency of the kicker magnet in figure 4.10 at 57 mT. Reducing the gap height l_{gap} by an inset from 180 mm to 112 mm increases t_{ft}/T and the maximum operation frequency.

and with equation 2.48 one gets

$$\frac{t_{\mathrm{ft}}}{T} < \left(1\,\mathrm{A/mm^2} \cdot \frac{\mu_0 A_{\mathrm{cond}} N}{B l_{\mathrm{gap}}}\right)^2 - \frac{2}{3}\frac{t_{\mathrm{r,f}}}{T}. \tag{4.22}$$

Thus, the current pulse duty cycle t_{ft}/T scales with the inverse of the gap height l_{gap} squared at constant T. In the setup shown in figure 4.2, a beam tube with 100 mm inner diameter throughout the aperture of the kicker magnet is employed in order to accommodate the beam trajectories emerging from the TFM, which is positioned in front of the kicker magnet. With typically 2 mm wall thickness, one needs to consider an outer diameter of the beam tube of 104 mm. Additional free space for adjusting the beam tube limits the minimum gap height of the kicker magnet to 112 mm. From table 4.6, one gets the kicker magnet conductor cross section being $A_{\mathrm{cond}} = 34.4\,\mathrm{mm^2}$. Considering the nominal field in the kicker magnet of $B = 57\,\mathrm{mT}$ (given by the geometrical constraints as derived in equation 4.17), $N = 20$ turns for the kicker magnet, and a minimum rise and fall time $t_{\mathrm{r,f}}$ of 0.5 ms, which is envisaged for the performant kicker magnet power supply as presented in the next section, one can derive the frequency-dependent maximum current pulse duty cycle as presented in figure 4.15. It can be seen that the maximum operation frequency and the maximum current pulse duty cycle increase by a factor of $(180\,\mathrm{mm}/112\,\mathrm{mm})^2 \approx 2.6$ when decreasing the gap height from 180 mm to 112 mm.

Thus, with the addition of two insets with a height of 34 mm each to the kicker magnet, the gap height is reduced to $l_{\mathrm{gap}} = 112\,\mathrm{mm}$ defining the upper threshold for the duty cycle that can technically be operated. In figure 4.16, the kicker magnet with two insets with 34 mm height which are mounted to the yoke is shown. Each

inset consists of 520 iron sheets with 1 mm thickness and an insulating adhesive layer in order to minimize eddy current effects during the ramping of the magnetic field. The contour of these insets is optimized by shims of 6 mm height on the outer edges to improve the field homogeneity in the field region of the beam.

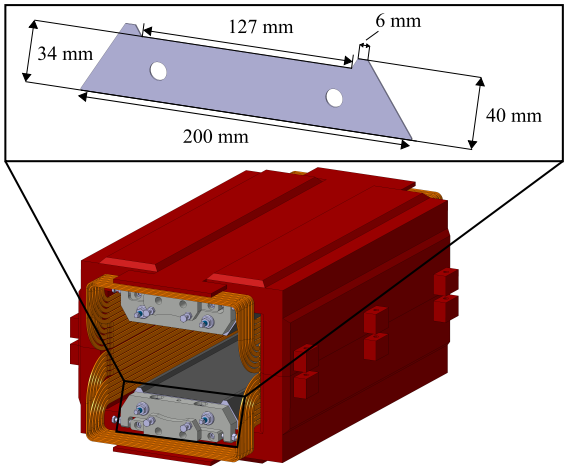

Figure 4.16.: Kicker magnet from figure 4.10 with two insets of 34 mm height mounted on the original pole areas, which reduce the gap height to l_{gap} = 112 mm. The insets consist of 520 x 1 mm thick iron sheets with 6 mm shims on the outer edges. The sheets feature holes in order to stack the sheets onto two tubes for mechanical stability and precise positioning. The inner area of the poles is 127 mm wide.

The design of the insets, i.e. the iron sheets, is optimized with a FEM simulation[5] of the cross section of the magnet. Figure 4.17 shows the magnetic flux density distribution in the magnet yoke with insets as well as the field lines in the gap. Here, no saturation in the insets is present. On the right side of the figure, the horizontal dependence of the vertical magnetic field is shown for different scenarios. One can see that a vertical magnetic field of 57 mT, which is required to obtain the correct deflection angle of 35.2 mrad (equation 4.17), can be easily obtained with the insets and a reduced current of 253 A. The current scales with the gap height according to equation 2.48. The kicker magnet without insets requires 409 A to generate 57 mT at 180 mm gap height. Thus $112/180 \cdot 409\,\text{A} = 253\,\text{A}$ should be required for 57 mT at 112 mm gap height. Due to the trapezoidal design of the insets, the magnetic field at 253 A is in fact larger than 57 mT. Correspondingly, the kicker magnet with insets driven with 250 A, i.e. one power supply, provides 56.6 mT, which causes a

[5]The FEM simulations throughout this thesis are carried out with *COMSOL Multiphysics v. 5.6* [51].

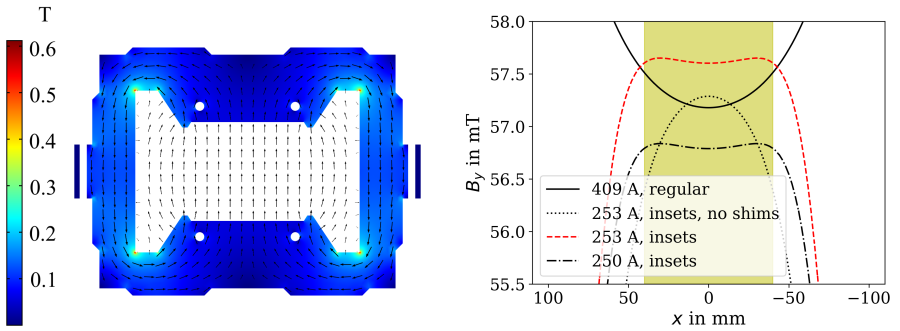

(a) (b)

Figure 4.17.: FEM simulation of the cross section of the kicker magnet with insets as shown in figure 4.16. (a): Magnetic flux density distribution in the yoke in units of T as well as the field lines. (b): Vertical magnetic flux density B_y versus horizontal coordinate x at $y = 0$ in the kicker magnet according to the coordinate system in figure 4.10 with and without insets and for different currents (The nominal scenario with insets is indicated as red line). The yellow area marks the expected position of the beam. Note that the plot's x-axis is inverted such that the beam propagation is into the image plane. This representation is kept for similar plots in the following.

horizontal offset of the beam at front face of the septum magnet of 0.5 mm to the nominal position. This is acceptable for operation of the multiplexer and therefore operation with one power supply is feasible. The effect of the shims of the insets on the field quality is well visible by the plateau in figure 4.17b. In order to quantify the field quality one can calculate the field homogeneity according to

$$\max\left(\left|\frac{\Delta B}{B_0}\right|\right) = \max\left(\left|\frac{B_y(x,0) - B_y(0,0)}{B_y(0,0)}\right|\right) \tag{4.23}$$

for $-40\,\text{mm} < x < 40\,\text{mm}$, which is the expected extent of the beam ($B_y(x,y)$ is the vertical magnetic flux density at x, y and $z = 0$). Furthermore, the inductance of the different configurations presented in figure 4.17b is calculated from the total magnetic energy stored in the gap, which is extracted from the FEM simulation. From equation 2.49 and equation 2.50, the inductance is calculated with

$$L = \frac{2\int_V \rho_m \mathrm{d}V}{I^2} = \frac{2l_{\text{eff}}\int_A \rho_m \mathrm{d}A}{I^2}, \tag{4.24}$$

with $\int_A \rho_m \mathrm{d}A$ being the magnetic energy per unit length in the gap. The results in terms of field homogeneity and inductance are summarized in table 4.8. Here, it can be seen that the addition of insets to the kicker magnet significantly improves the field

Table 4.8.: Summary of FEM simulation results from figure 4.17.

Geometry	I/A	$\max(\lvert\Delta B/B_0\rvert)/10^{-3}$	$\int_A \rho_m \mathrm{d}A/(\mathrm{J\,m^{-1}})$	L/µH
Regular	409	6.5	40.3	294
Insets, no shims	253	17.7	31.2	595
Insets	253	0.9	33.5	639
Insets	250	0.9	32.5	634

homogeneity. However, as expected from equation 2.52, the inductance increases with the insets. At constant voltage, the gap reduction by addition of two insets increases the minimum current rise time by 35 % considering $U = -L \cdot \mathrm{d}I/\mathrm{d}t$ and a factor 2.2 larger inductance at a factor 0.62 smaller current for the kicker magnet with insets. Nonetheless, the above 150 % increase in maximum current pulse duty cycle and operation frequency (see figure 4.15) in combination with the 35 % increase of the current rise time justifies the addition of the insets.

Measurements of the vertical magnetic flux density of the kicker magnet with insets are shown in figure 4.18. The measurements are carried out at 6 A such that DC operation of the magnet can be performed within the thermal limitations of the air-cooled copper coils which facilitates the recording of a field map in the kicker magnet. The results can then be scaled linearly (according to equation 2.48) to the nominal current of 253 A which is required according to figure 4.17 to obtain at least 57 mT. The results agree well with the simulations. The measured integrated magnetic field amounts to 35.2 mT m such that 35.2 mrad (equation 4.17) kicker magnet deflection angle are well reachable according to figure 2.10 (with $(B\rho) = 0.98\,\mathrm{T\,m}$).

In order to study the temporal behavior of the modified kicker magnet with insets, a measurement of the transfer function has been performed. For this, the magnet is driven by a sinusoidal current waveform. The magnetic field, which is generated by the kicker magnet is monitored with a measurement coil which is placed in the center of the magnet. From the voltage signal induced in the measurement coil, one deduces the effective measured magnetic field B_{meas}. The effective expected magnetic field is calculated from the effective current $\hat{I}$ with equation 2.48 yielding $B_{\mathrm{exp}} = \mu_0 N \hat{I} l_{\mathrm{gap}}$ with $N = 20$ being the number of turns and $l_{\mathrm{gap}} = 112\,\mathrm{mm}$ being the gap height of the kicker magnet. The ratio $B_{\mathrm{meas}}/B_{\mathrm{exp}}$ is recorded for frequencies of the input current in the range of 1 Hz to 100 kHz yielding the transfer function of the magnet, which is shown in figure 4.19. In the low frequency range (below 100 Hz), the measurement shows a high-pass behavior. This comes from the measurement setup acting as a voltage transformer. In [52, p. 242 ff.], it is shown that the transfer function of voltage transformers with high load resistance (input resistance of voltage measurement of measurement coil is 10 MΩ) can be described by a RL high-pass filter with lower cut-off frequency of $f_{lc} = R/(2\pi k^2 L)$. Here, R and L are the primary coil resistance

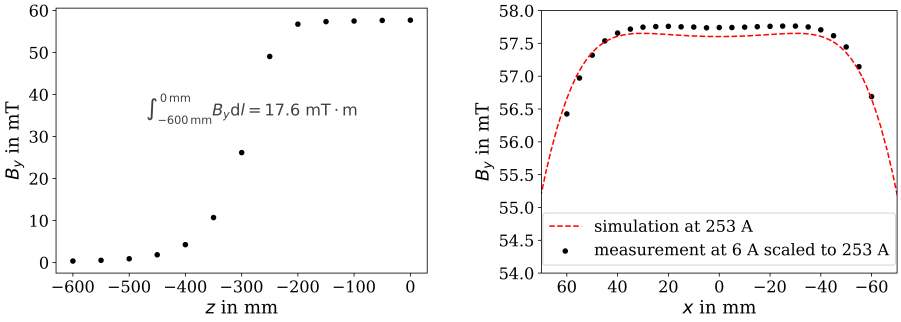

(a) (b)

Figure 4.18.: (a): Measured vertical magnetic flux density B_y from $z = -600\,\mathrm{mm}$ to $z = 0\,\mathrm{mm}$ at $x = y = 0\,\mathrm{mm}$. The measurement is carried out at 6 A magnet current and scaled to 253 A. The integrated magnetic field of the kicker magnet can be calculated to be $\int_{-600\,\mathrm{mm}}^{600\,\mathrm{mm}} B_y \mathrm{d}l = 2\int_{-600\,\mathrm{mm}}^{0\,\mathrm{mm}} B_y \mathrm{d}l = 35.2\,\mathrm{mT\,m}$. Here, the integration is along the z-axis. (b): Measured and simulated B_y versus horizontal coordinate x at $y = z = 0\,\mathrm{mm}$ in the kicker magnet with insets. The measurement is carried out at 6 A magnet current and scaled to 253 A while the simulation is carried out at 253 A. The coordinate system which is used is shown in figure 4.10 with the origin in the center of the magnet.

and inductance, respectively, whereas k is the coupling coefficient of the transformer ($k \leq 1$). In our setup, R and L correspond to the kicker magnet. Measurements with an LCR meter yield $R = 178\,\mathrm{m\Omega}$ and $L = 619\,\mu\mathrm{H}$ (complying within $\approx 3\,\%$ with the simulated inductance in table 4.8). The coupling coefficient k can be obtained from a linear fit of the RL high-pass transfer function to the data in figure 4.19 giving $k = 0.88$ and thus a lower cut-off frequency of $f_{lc} = 60\,\mathrm{Hz}$. The transfer function $B_{\mathrm{meas}}/B_{\mathrm{exp}}$ in figure 4.19 shows a plateau above 100 Hz and a slight decrease above 10 kHz. At 100 kHz the transfer function seems to rise again which can be explained by the stray capacitance and inductance of the magnet coils forming a resonant LC circuit and thus counteracting the decay of the transfer function from eddy current and hysteresis losses. From figure 4.19, one can deduce that the upper cut-off frequency f_{uc} of the system is above 100 kHz, which is the maximum setting of the employed signal generator. Thus, the corresponding time constant of the system is $\tau < 1/(2\pi f_{uc}) < 1.6\,\mu\mathrm{s}$. The minimum rise time of magnetic field of the kicker magnet can be approximated by $t_{\mathrm{r,min}} \approx 5\tau$ (1 % - 99 % of the magnetic field), which gives $t_{\mathrm{r,min}} \approx 8\,\mu\mathrm{s}$. This is far below the envisaged magnetic field rise times for the multiplexer operation as presented in the next section.

To exploit the maximum current pulse duty cycle of 1.8 % of the kicker magnet with

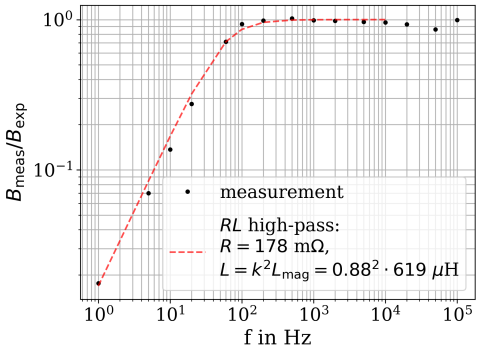

Figure 4.19.: Transfer function of the kicker magnet with insets as shown in figure 4.16. The magnetic field is generated with a sinusoidal current waveform with effective current $\hat{I}$. The expected magnetic field B_{exp} is calculated from the effective current via equation 2.48 (N = 20, l_{gap} = 112 mm). The magnetic field is measured with an air coil in the magnet yielding B_{meas}. The setup works as RL high-pass filter with the kicker magnet resistance (including cables) R = 178 mΩ and inductance L_{mag} = 619 µH. The coupling coefficient of the transformer k = 0.88 is obtained from a linear fit.

insets (figure 4.15), the engineering of a more performant power supply is required. Such a power supply will also feature smaller flat top and rise and fall times than the power supplies in table 4.7. The concept of this power supply is discussed in the following.

4.3.3. Performant power supply concept

The power supply is designed in order to meet the requirements summarized for the JULIC multiplexer system in table 4.1. With this, the maximum current duty cycle of 1.8 % for the kicker magnet with insets as well as the maximum operation frequency of 56 Hz in figure 4.15 are well reachable. In the future, the full potential of the power supply can be exploited together with a kicker magnet which is specifically designed for higher thermal load, i.e. a kicker magnet with water-cooled coils. This kind of magnet can be of identical geometry as the kicker magnet with insets in figure 4.16. According to equation 4.22 with a current density of 10 A/mm² for water-cooled coils [26], a 2 % current duty cycle at 2 × 100 Hz can easily be maintained with such a kicker magnet. The design goals of the performant kicker magnet power supply are summarized in table 4.9. An exemplary current pulse sequence as it would be supplied by the performant power supply to the kicker magnet and a corresponding proton pulse sequence are shown in figure 4.20. The concept of the performant power supply is

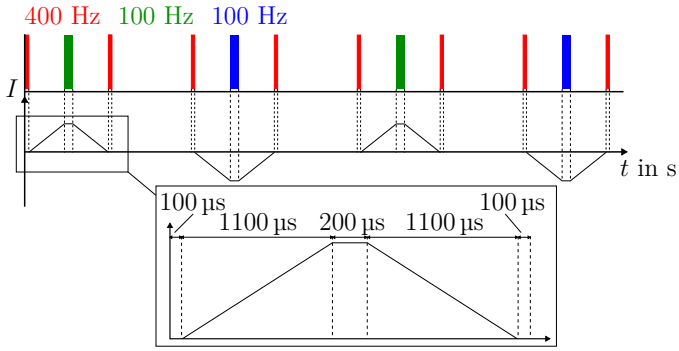

Figure 4.20.: Exemplary proton pulse sequence (top) and associated current pulse sequence (bottom) as supplied by the performant kicker magnet power supply. The proton pulse sequence shows a 400 Hz pulse component with 4 % duty cycle being sent straight through the multiplexer. The 100 Hz proton pulse components with 2 % duty cycle are deflected to the left and right. The inset shows the detailed timing of the current pulse sequence.

Table 4.9.: Design goals of performant kicker magnet power supply. Note that the polarity of two subsequent current pulses should be invertible in between these two pulses.

Name	Symbol	Value
Current	I/A	0.1-300
Voltage	U/V	0-300
Polarity		Bipolar (inter-pulse)
Rise time	t_r/ms	0.5-10
Flat top time	t_ft/ms	0.1-10
Fall time	t_f/ms	0.5-10
Repetition rate	f/Hz	2×(1 – 100)
Duty cycle	t_ft/T	2×2 %
Load inductance	L/µH	1000
Load DC resistance	R/mΩ	200

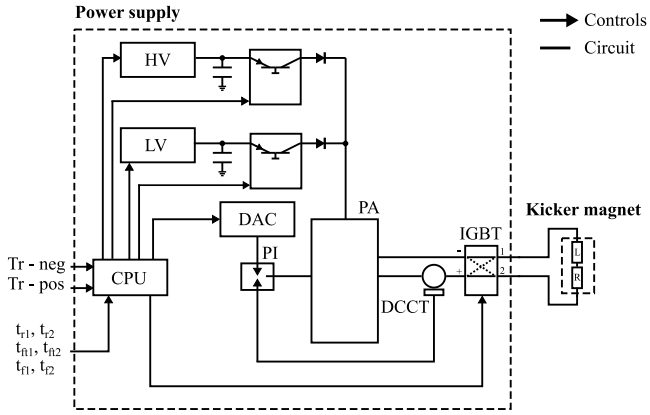

Figure 4.21.: Concept of the performant power supply connected to the kicker magnet.

presented in figure 4.21. The power supply is mainly based on a powerful power amplifier (PA) with a series of transistor boards to amplify the input signal of the current pulse sequence. Two different capacitor banks are discharged via the output stage being charged with high (HV) or low (LV) voltage for operation during the ramping of the current or during the flat top, respectively. The current pulse sequence of the PA is controlled by a PI controller, which receives feedback through a DC current transformer (DCCT) at the output of the PA and receives the reference signal from a DAC. The DAC specifies the current pulse sequence, which is given by the CPU and programmed there. In this manner, specifying the current pulse sequence (rise time, flat top and fall time), the CPU drives the DAC and at the same time gives information to a switch (insulated-gate bipolar transistor - IGBT) that decides the output polarity of the power supply's current pulse sequence. Before the power supply is operated, information about the current pulse sequence of the positive current output signal and the negative current output signal is stored in the CPU. Both pulse shapes are then independently retrieved via separate trigger inputs.

The design goals in terms of timing as presented in table 4.9 define the combinations of proton pulse sequences that can be operated with the kicker magnet power supply and thus multiplexer. The time interval between two subsequent straight pulses with period length T and duty cycle $\mathrm{dc}_{\mathrm{straight}}$ amounts to $T - \mathrm{dc}_{\mathrm{straight}}T$. With this, the maximum flat top time $t_{\mathrm{ft,max}}$ of the power supply and thus maximum proton pulse length depends on the rise and fall time of the power supply $t_{\mathrm{r,f}}$ according to

$$t_{\mathrm{ft,max}} = T - \mathrm{dc}_{\mathrm{straight}}T - 2t_{\mathrm{r,f}}. \tag{4.25}$$

If the duty cycle of the deflected proton pulse component $\mathrm{dc}_{\mathrm{deflected}}$ is fixed, the minimum possible frequency of the deflected pulse component scales with

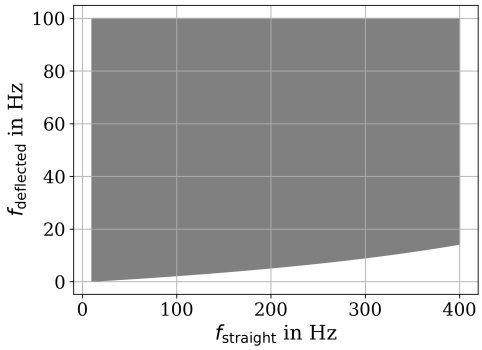

Figure 4.22.: Possible combinations of frequencies for the straight pulse components and the deflected pulse components with $\mathrm{dc}_{\text{straight}} = 4\,\%$ and $\mathrm{dc}_{\text{deflected}} = 2\,\%$ realizable with the performant kicker magnet power supply with a minimum rise and fall time $t_{\text{r,f}}$ of 0.5 ms (table 4.9). f_{straight} needs to be an integer multiple of $f_{\text{deflected}}$.

$$f_{\text{deflected,min}} = \mathrm{dc}_{\text{deflected}} / t_{\text{ft,max}}. \tag{4.26}$$

Figure 4.22 shows the possible combinations of frequencies for the straight pulse components and the deflected pulse components with $\mathrm{dc}_{\text{straight}} = 4\,\%$ and $\mathrm{dc}_{\text{deflected}} = 2\,\%$ following equation 4.25 and equation 4.26. One can see that for higher frequencies of the straight pulse components, the lower limit of deflected frequencies increases slightly due to the decreasing period length of the straight pulse components and the large flat top times of the deflected pulse components with low frequency at fixed duty cycle.

4.4. Three-Field Septum Magnet (TFSM)

The Three-Field Septum Magnet (TFSM) as positioned in figure 4.2 marks the centerpiece of the multiplexer system. It serves the purpose to further deflect the beam after having passed the kicker magnet in order to introduce three separated beamlines within a compact overall design. For this purpose, it provides three different horizontally arranged field regions with outer dipole field regions of opposite polarity and a central zero field region. The septum magnet is based on permanent magnets. This technology is employed due to the typically fixed beam parameters of the test facility at JULIC (and at HBS) as stated in table 4.1 and at low-energy accelerator-driven neutron sources in general. Here, particle species, beam energy and thus ($B\rho$) are fixed and therefore static permanent-magnet-based elements for permanent beam deflection are more economic than dynamic electromagnets as no power supply or as-

sociated water cooling is required. Furthermore, using permanent magnet technology in a septum magnet allows to work without return conductor such that a massless septum without physical separation of the different field regions can be obtained more easily compared to an electromagnetic massless septum with complex conductor design as presented in figure 2.18. In this section, the concept of the TFSM is discussed first. Then, the technical layout and associated optimizations are explained yielding the required particle trajectories taking into account the beam size given in figure 4.9. In addition, the field quality of the septum magnet is studied in terms of its harmonic content.

4.4.1. Concept

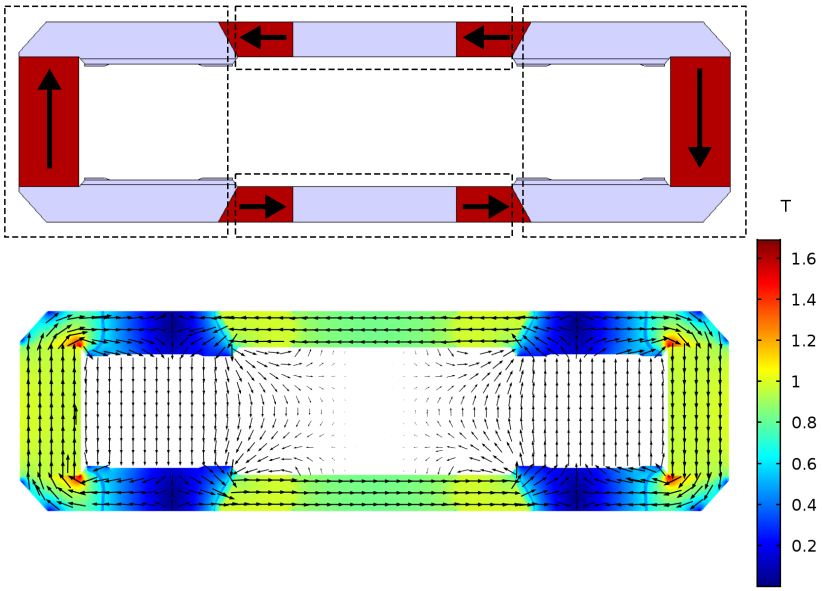

Figure 4.23.: Top: Conceptual design of the TFSM based on SmCo permanent magnets (red) with anisotropic unidirectional magnetization indicated by arrows and a remanent flux density $B_\mathrm{r} = 1.1\,\mathrm{T}$. The gray area marks the yoke material, i.e. carbon steel, guiding the field lines. Bottom: Corresponding FEM simulation indicating the three different magnetic field regions. The color scale shows the absolute value of the magnetic flux density $B = \left|\vec{B}\right|$ in the structural material. The arrows show the direction of the magnetic flux density. The size of the arrows scales logarithmically in the range of $B > B_\mathrm{max} \cdot 1 \times 10^{-3}$, i.e. $B > 1.69 \times 10^{-3}\,\mathrm{T}$.

The concept of the TFSM is shown in figure 4.23. The septum magnet is based on

an arrangement of vertically and horizontally magnetized SmCo permanent magnets with a remanent flux density of 1.1 T together with a carbon steel yoke to guide the magnetic field lines. The setup has a 2-fold rotational or point symmetry with respect to the center. The FEM simulation results in figure 4.23 show that the setup generates three distinct field regions. A field region with the magnetic flux density pointing downwards on the left side and upwards on the right side as well a field region with vanishing magnetic flux density in the center of the setup. Thus, a proton beam traversing the left field region of the magnet experiences a deflection to the left side. A proton beam traversing the right field region is deflected to the right side. In the center, the proton beam passes without disturbance. The three different field regions in the setup can be envisaged by the combination of two opposing C-shaped dipole magnet geometries (similar to figure 2.13) together with two connecting arrangements consisting of two horizontally magnetized permanent magnets (HPM) and one centered iron brick each. The breaking down of the overall geometry in these subsystems is indicated in the top of figure 4.23 by the dashed boxes. The HPMs allow to drag the magnetic field lines into the intermediate iron bricks which can be seen from the FEM simulation results in figure 4.23 focusing on the top left HPM. The bottom left HPM on the other hand pushes the magnetic field lines into the air gap opposing the direction of the fringe field from the left dipole field region of the septum magnet. Together, both HPM weaken the stray field of the left dipole field region. The same applies to the right side of the septum magnet. With this, a broad zero field region in the center can be obtained in combination with the two outer dipole field regions.

4.4.2. Layout

The dimensions of the septum magnet have a large impact on the overall geometry of the multiplexer system. With the distance between the septum magnet and the kicker magnet being fixed in figure 4.2 due to spatial constraints from the experimental area, it is important to horizontally arrange the three different field regions in the septum as closely as possible next to each other. This helps to reduce the magnetic field that has to be generated by the kicker magnet, which facilitates the fast ramping of the magnet. On the other hand, the horizontal separation of the three different field regions should be large enough in order to provide a reasonable field quality, i.e. the subsequent beam optical elements should be able to transport the beam reliably to the target. Furthermore, the vertical separation of the poles in the dipole field regions of the septum magnet should be wide enough in order to accommodate the beam without absorption but not too large as the magnetic flux density scales inversely with the gap height (see equation 2.62). Taking into account all these considerations and a beam size of less than 40 mm (i.e. four times[6] the rms beam envelope taken from figure 4.9 at the position of the septum magnet), the front

[6] As explained in section 2.2.4 of this thesis, 4 rms beam widths, i.e. 4σ and thus 95.45 % of the beam intensity, are considered as beam size in the septum magnets for construction.

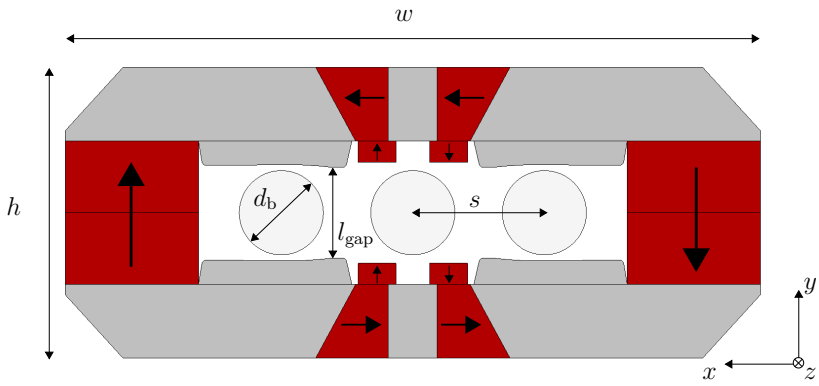

Figure 4.24.: Technical layout of the septum magnet front face based on the concept in figure 4.23. The width of the front face is w = 330 mm and the height h amounts to 138 mm. The gap height l_{gap} = 43 mm allows to accommodate a beam diameter d_b of 40 mm. The septum front face is designed to obtain a separation of the beam spots of s = 62 mm. The red parts indicate SmCo magnets with B_r = 1.1 T, the gray parts show the magnet yoke. The magnetization of the permanent magnets is indicated with arrows.

face of the septum magnet was designed.

The design is based on the concept in figure 4.23. Note, however, that four additional vertically magnetized permanent magnets, in the following called compensator magnets, are added to the central field region. These are arranged such that the magnetic flux density gradient, between the left and right dipole field regions is reduced. This is required for the septum front face design, since the separation of the different beam spots is smallest at this position and otherwise a plateau of the magnetic flux density in the center can not be obtained. As explained in section 4.1, the septum magnet is required to generate a deflection angle of the outer beam trajectories with respect to the centered unperturbed trajectory of 265 mrad within 650 mm length of the magnet (yoke dimensions). Thus, with $(B\rho)$ = 0.98 T m from table 4.1 and equation 2.41, an integrated field of 260 mT m has to be provided by the outer dipole field regions of the septum magnet. This consideration has been taking into account for the layout presented in figure 4.24. The design is iterated such that an elongation of the layout in figure 4.24 along z to a length of 650 mm, i.e. forming a 3-dimensional monolithic magnet, yields an integrated vertical magnetic field of 261 mT m in the middle of the outer field regions, i.e. at x = ±62 mm as presented in figure 4.25. Figure 4.25b presents the integrated vertical magnetic flux density vs x. Here, one observes a step-like vertical magnetic flux density distribution featuring two outer opposite field regions covering 4 rms beam widths with a field homogeneity of 1.3 %

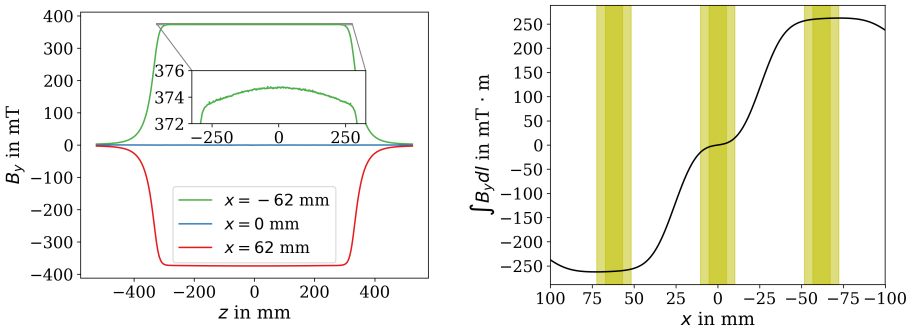

(a) (b)

Figure 4.25.: (a): Vertical magnetic flux density B_y versus z of the septum magnet front face in figure 4.24 extended in z to 650 mm length (monolith). B_y is shown for different horizontal coordinates x representing the beam centers as positioned in figure 4.24 at $y = 0$. The inset shows B_y at $x = -62$ mm inside the magnet. The origin of the coordinate system is the geometric center of the magnet. (b): Corresponding integrated vertical magnetic flux density $\int_{-525\,\mathrm{mm}}^{525\,\mathrm{mm}} B_y \mathrm{d}l$ versus horizontal coordinate x at $y = 0$. The integration is along the z-axis. The yellow shaded area marks the beam position (4 rms beam widths: light shaded area, 2 rms beam widths: dark shaded area). The effective length of the magnet is calculated to be $l_{\mathrm{eff}} = 697$ mm.

(at $y = 0$) according to

$$\max\left(\left|\frac{\int B_y(\pm 62\,\mathrm{mm} - 2\sigma_x \leq x \leq \pm 62\,\mathrm{mm} + 2\sigma_x, 0)\mathrm{d}l - \int B_y(\pm 62\,\mathrm{mm}, 0)\mathrm{d}l}{\int B_y(\pm 62\,\mathrm{mm}, 0)\mathrm{d}l}\right|\right). \quad (4.27)$$

Note that the centered plateau zero field region does not extend to the full beam size but covers 4 rms beam widths with a maximum deviation of the integrated field of 14 mT m from the centered zero crossing. However, this can be accepted when adapting the layout of the septum magnet to the beam trajectories resulting from the dipole field in the outer field regions. With this, the horizontal aperture of the magnet and thus the centered zero field region successively increases with z, as described in the following.

The outer dipole field regions of the septum magnet generate a deflection angle of 265 mrad throughout the effective length of the magnet $l_{\mathrm{eff}} = 697$ mm. Here, the beam follows a circular trajectory inside the magnet and therefore accumulates a horizontal offset while traversing the magnet similar to figure 2.11. This has to be taken into account by broadening the horizontal aperture of the magnet with respect to its length. As shown in figure 4.26, the beam in the outer field regions of the

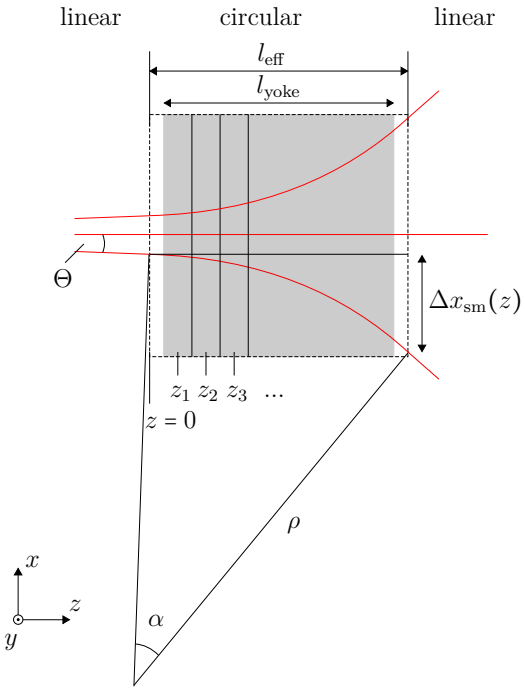

Figure 4.26.: Beam trajectories (red) inside the septum magnet. The gray shaded area marks the septum yoke and the dashed rectangle marks the extent of the magnetic field of the septum magnet in terms of its effective length l_{eff}. The trajectory is linear in front of the septum magnet. The beam sent to the center of the septum magnet follows a straight trajectory. The beam sent to the outer field regions of the septum magnet obtains a horizontal deflection from the kicker magnet Θ. Inside the septum magnet's magnetic field, i.e. within its effective length l_{eff}, the beam in the outer field regions follows a circular orbit with a bending radius ρ generating a deflection angle α. Behind the septum magnet, the beam travels on a linear trajectory with deflection angle $\Theta + \alpha$. While traversing the septum magnet, the beam accumulates a horizontal offset $\Delta x_{\text{sm}}(z)$ (equation 4.28) described by a circular orbit, which is tilted by Θ. Dividing the septum magnet into different layers with each i-th layer being adapted to the additional horizontal extent $\Delta x_{\text{sm}}(z_i)$ at the center of the layer z_i allows to accommodate the beam.

septum magnet crosses three different regimes. First and prior to the magnetic field of the septum magnet, the beam follows a linear trajectory inclined with respect to the z-axis by the deflection angle Θ of the kicker magnet. Inside the septum magnet, the beam follows a circular path similar to figure 2.11 with an inclination of the circular segment of Θ. Behind the septum magnet, the beam follows a linear trajectory with an inclination with respect to the z-axis which is the sum of the kicker magnet deflection angle Θ and the septum deflection angle α. For the adjustment of the septum aperture to the beam trajectories, one has to consider the horizontal offset $\Delta x_{\mathrm{sm}}(z)$ accumulating with the beginning of the hard-edge magnetic field region (figure 2.7) of the septum magnet. Here, one sets $z = 0$ for the following considerations. With $\Delta x_{\mathrm{sm}}(z)$ following a tilted circular segment, one obtains

$$\Delta x_{\mathrm{sm}}(z) = \Delta x(\rho, z + \rho \sin\Theta) - \Delta x(\rho, \rho \sin\Theta) \tag{4.28}$$

with ρ being the bending radius from the septum magnet and Θ being the kicker magnet deflection angle. Here, $\Delta x(\rho, L)$ represents the horizontal offset from a circular segment without tilt from equation 2.42. In order to successively broaden the aperture of the septum magnet, the magnet is divided along the z-axis into ten layers of equal length. The number of layers is a compromise between technical practicability and magnetic field strength. The fewer the number of layers, the easier is the manufacturing of the magnet since the number of individual components is reduced. However, if only a few layers are employed, each layer has to cover a larger horizontal aperture and the magnetic field reduces due to a larger required pole area according to equation 2.62. Considering the pole area of the individual layers to be fixed according to the design in figure 4.24, a total of ten layers has been chosen for the septum magnet. Dividing the septum magnet with a length of $l_{\mathrm{yoke}} = 650\,\mathrm{mm}$ into ten layers of each $l_{\mathrm{layer}} = 65\,\mathrm{mm}$ length, one can calculate the broadening of each layer from equation 4.28. The results are summarized in table 4.10. Note that the septum magnet front face in figure 4.24 is designed for a beam spot separation of 62 mm requiring a kicker magnet deflection angle of approximately 35 mrad according to equation 4.17. However, these considerations did not consider the extending magnetic field of the septum magnet with an effective length $l_{\mathrm{eff}} = 697\,\mathrm{mm}$ with respect to the yoke dimensions, i.e. $l_{\mathrm{yoke}} = 650\,\mathrm{mm}$. Nevertheless, the outward shift of the beam on a trajectory as in figure 4.26 (lower trajectory) $\Delta x_{\mathrm{sm}}((l_{\mathrm{eff}} - l_{\mathrm{yoke}})/2) = x_{\mathrm{sm}}(23.5\,\mathrm{mm}) = 0.9\,\mathrm{mm}$ (equation 4.28 with $\rho = 2.63\,\mathrm{m}$ and $\Theta = 35\,\mathrm{mrad}$) at the front face of the septum magnet, i.e the beginning of the magnet yoke, is comparable to the shift obtained from the pure kicker magnet deflection, i.e. a linear trajectory, which is $23.5\,\mathrm{mm} \cdot \sin(35\,\mathrm{mrad}) = 0.8\,\mathrm{mm}$. Therefore the beam spot separation at the front face of the septum magnet of 62 mm as shown in figure 4.24 is still valid. The broadening of the layers is taken into account by adjusting the intermediate iron parts in figure 4.24, which are connecting the four horizontally magnetized permanent magnets. The width of these iron parts as shown in figure 4.24 is $d = 23.3\,\mathrm{mm}$. By stacking ten layers with individual widths of the intermediate iron parts as listed in table 4.10, one gets the final design of the septum magnet as shown

Table 4.10.: Horizontal broadening of septum magnet layers. $\Delta x_{\mathrm{sm}}(z_i)$ is the horizontal offset at the center of the i–th layer z_i from equation 4.28 with the bending radius being approximated with $\rho = l_{\mathrm{eff}}/\alpha = 2.63\,\mathrm{m}$ and the kicker magnet deflection angle $\Theta = 35\,\mathrm{mrad}$. Here, z starts at the front side of the hard-edge magnetic field region as shown in figure 4.26 and thus $z_1 = (l_{\mathrm{eff}} - l_{\mathrm{yoke}})/2 + l_{\mathrm{layer}}/2$ with $l_{\mathrm{eff}} = 697\,\mathrm{mm}$, $l_{\mathrm{yoke}} = 650\,\mathrm{mm}$ and $l_{\mathrm{layer}} = 65\,\mathrm{mm}$. Considering the first layer to remain unchanged as presented in figure 4.24, $\Delta w_i = 2(\Delta x_{\mathrm{sm}}(z_i) - \Delta x_{\mathrm{sm}}(z_1))$ shows the additional horizontal extent per layer. $d_i = d_1 + \Delta w_i$ is the width of the intermediate iron parts in figure 4.24 for each layer.

i	z_i/mm	$\Delta x_{\mathrm{sm}}(z_i)$/mm	Δw_i/mm	d_i/mm
1	56	2.56	0.00	23.2
2	121	7.03	8.95	32.1
3	186	13.13	21.14	44.3
4	251	20.86	36.59	59.8
5	316	30.23	55.35	78.6
6	381	41.28	77.44	100.6
7	446	54.01	102.91	126.1
8	511	68.46	131.80	155.0
9	576	84.65	184.17	187.4
10	641	102.61	200.10	223.3

in figure 4.27.

Each layer of the final design of the septum magnet features a step-like vertical magnetic flux density distribution B_y with respect to x. The strength of the outer dipole field regions of the septum magnet is almost constant in each layer since only the centered iron parts with high magnetic conductivity are adapted. The horizontal separation of the outer dipole field regions and the horizontal extent of the centered zero field plateau region increases with z as shown in figure 4.28. Note that the four small vertically magnetized permanent magnets which are used in figure 4.24 to shape the central zero field region are employed only in the first six layers of figure 4.27. For the other layers, the horizontal distance between the outer field regions is large enough to provide a plateau region covering the beam without these compensator magnets. The position of the compensator magnets is iterated in each layer ($i = 1-6$) to maximize the extent of the plateau region. The integrated magnetic field of the final setup in figure 4.27 can be obtained for the outer field regions by following the beam trajectories. The integration path then resembles the top and bottom beam trajectories in figure 4.26. The outer and centered integration paths adapted to the geometry of the septum magnet are shown in figure 4.29a presenting a top view of the final setup in figure 4.27. The different integration paths coincide with the beginning

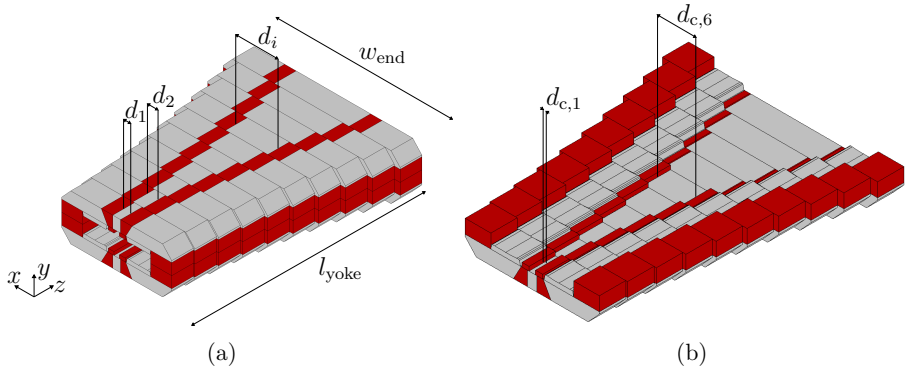

Figure 4.27.: (a): Final design of the TFSM. The basic design is taken from figure 4.24, extended in z to $l_{\mathrm{yoke}} = 650\,\mathrm{mm}$ and segmented into ten layers with the intermediate iron parts' thicknesses d_i adjusted to accommodate the beam trajectories according to table 4.10. The maximum width of the magnet is $w_{\mathrm{end}} = 530\,\mathrm{mm}$. (b): Lower half of the TFSM. The small vertically magnetized compensator magnets surrounding the centered zero field region in figure 4.24 are employed in the first six layers of the setup. The horizontal position of the compensator magnets is optimized within each layer to obtain a minimum deviation of the integrated field in the zero field region. The horizontal separations of these magnets are $d_{\mathrm{c},1-6} = 16\,\mathrm{mm}, 29\,\mathrm{mm}, 43\,\mathrm{mm}, 59\,\mathrm{mm}, 78\,\mathrm{mm}, 99\,\mathrm{mm}$. The origin of the coordinate system is positioned in the center of the magnet.

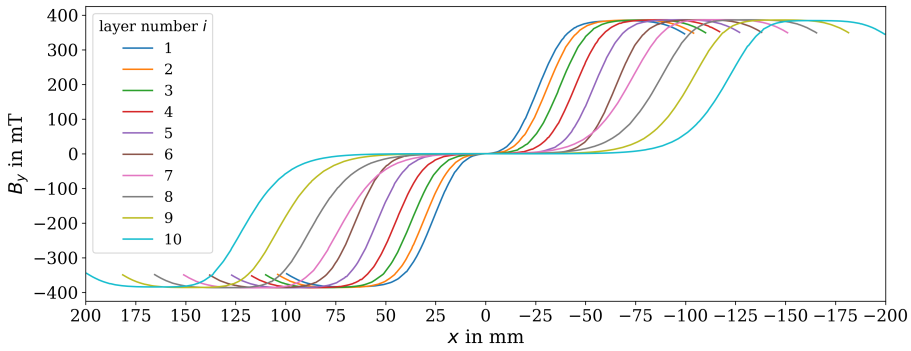

Figure 4.28.: Vertical magnetic flux density B_y versus x at $y = 0$ in the center of each of the ten layers in figure 4.27.

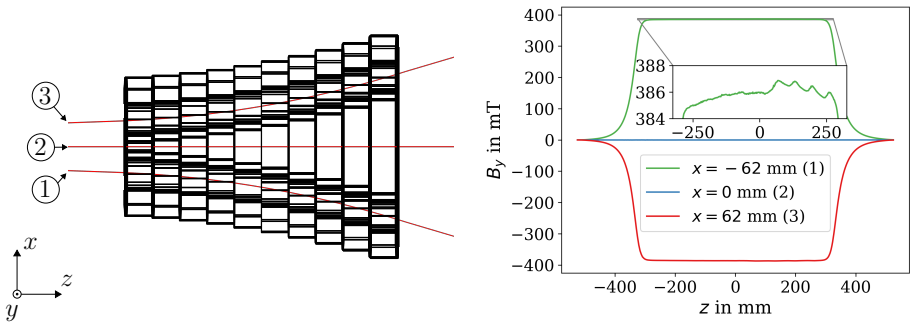

(a) (b)

Figure 4.29.: (a): Integration paths for the calculation of the integrated magnetic field of the septum magnet (figure 4.27). The integration paths follow the beam trajectories calculated similar to figure 4.26 with three different regimes at $y = 0$. The parameters are the same as used in table 4.10. 1: Right integration path intersecting with the beginning of the magnet yoke at $x = -62\,\mathrm{mm}$ 2: Centered integration path intersecting at $x = 0\,\mathrm{mm}$, 3: Left integration path intersecting at $x = 62\,\mathrm{mm}$. (b): Vertical magnetic field B_y versus z following the different integration paths in (a). The effective length for the outer field regions can be derived to be $l_{\mathrm{eff}} = 709\,\mathrm{mm}$. The integrated magnetic field at 1 and 3 is $\int_{z=-525\,\mathrm{mm}}^{z=525\,\mathrm{mm}} B_y \mathrm{d}l(z) = \pm 274\,\mathrm{mT\,m}$, respectively. The inset shows B_y at $x = -62\,\mathrm{mm}$ inside the magnet. The origin of the coordinate system is the center of the magnet.

of the septum magnet yoke at different horizontal coordinates $x = -62, 0, 62$ mm. The integrated magnetic field of the outer field regions, i.e. at $x = \pm 62\,\mathrm{mm}$ amounts to $\mp 274\,\mathrm{mT\,m}$.

The increase of about 5 % of the integrated magnetic field in the outer field regions with respect to the setup without broadened layered structure as presented in figure 4.25b (274 mT m with respect to 261 mT m) can be attributed to three effects induced by the broadening of the magnet. One effect is the longer integration path in the outer field regions of figure 4.29a compared to the straight integration paths employed in figure 4.25. The integration path increases by 2 %, which applies almost directly to the integrated field. Another contributing effect is caused by the limited number of layers, i.e. ten layers in figure 4.27, which are used to adapt the septum aperture to the beam trajectories. As shown in the inset of figure 4.29, the vertical magnetic field B_y increases slightly and fluctuates when approaching the rear part of the septum magnet (layer number $i \geq 6$). This is due to the horizontal sizes of the layers that are increasingly different with larger z as listed in table 4.10. Since the individual layers feature an adapted pole shimming (figure 4.24), which partly

compensates the decreasing magnetic field when going from the outer field regions to the centered region, the magnetic field within one layer is influenced by the shim of a subsequent layer. This influence scales with z as with increasing difference of horizontal aperture of the layers the shims of a subsequent layer protrude further into the center of a current layer. The effect can be compensated when increasing the number of layers with z and thus decreasing the difference of horizontal aperture between the layers. However, this heavily increases the amount of necessary individual parts to build the septum magnet. The effect of neighbouring protruding pole shims can be quantified when assuming a symmetric longitudinal evolution of B_y inside the magnet in figure 4.29. By mirroring B_y for $z < 0$ at $z = 0$ to $z > 0$, the difference in the integrated magnetic field caused by neighbouring shims can be calculated to be $\approx 0.2\,\mathrm{mT\,m}$ which is negligible for the setup of the septum magnet. A more dominant effect from the broadening of the septum magnet causing an increase in integrated magnetic field between figure 4.29 and figure 4.25 is the larger difference between the different field regions with increasing layer number as shown in figure 4.28. For the layers with larger horizontal aperture, the influence between different field regions is smaller. Thus, the magnetic field in the outer field regions is less attenuated by the centered zero field region and therefore larger. This can be studied systematically by evaluating the integrated magnetic field of different setups, each representing one single layer of the septum magnet (figure 4.27) extended along the z-axis to 650 mm length. This allows to compare the horizontal aperture-dependent gain of the magnetic field in the outer field regions with respect to the setup without broadened layered structure (figure 4.25b).

Figure 4.30 shows the integrated magnetic field in the outer field regions of a setup similar to figure 4.24 for different horizontal apertures, i.e. different thicknesses of intermediate iron parts d_i (table 4.10), each extended in z by 650 mm. For interpolation of the data points a logarithmic model is used resulting in a horizontal aperture-dependent, i.e. d_i-dependent, gain of the integrated magnetic field in the outer field regions of

$$\begin{aligned} G_{B_y,\mathrm{int.}}(d_i) &= \frac{(\int B_y \mathrm{d}l)(d_i)}{(\int B_y \mathrm{d}l)(d_1)} \\ &= \frac{2.7 \ln\left((d_i - 20.8\,\mathrm{mm})/\mathrm{mm}\right)\mathrm{mT\,m} + 258.6\,\mathrm{mT\,m}}{261.3\,\mathrm{mT\,m}}. \end{aligned} \tag{4.29}$$

Note that in figure 4.30 the integration paths are adjusted according to d_i. With the d_i-dependent gain in equation 4.29, one can calculate the overall gain from the broadening of the TFSM in figure 4.27 with respect to the initial structure (figure 4.25b) via $1/10 \sum_{i=1}^{10} G_{B_y,\mathrm{int.}}(d_i)$ with all d_i taken from table 4.10, which yields 3 %. Thus, the larger differences of the different field regions in the layers with larger horizontal aperture in figure 4.27 primarily cause the stronger integrated magnetic field.

The gain from broadening of the septum magnet can in principle be considered in the initial design of figure 4.24 to meet the required 260 mT m precisely. However, the

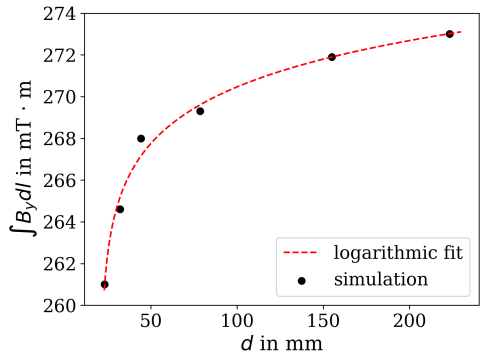

Figure 4.30.: Integrated vertical magnetic field in the outer field regions $\int B_y \mathrm{d}l$ of setups similar to figure 4.24 but with different width d of the intermediate iron parts which connect the horizontally magnetized permanent magnets. Each setup is extended longitudinally, in z, by 650 mm. $\int B_y \mathrm{d}l$ is calculated for d_i with $i = 1, 2, 3, 5, 8, 10$ from table 4.10. The integration is along the z-axis for $y = 0$, $x_1 = -62\,\mathrm{mm}$ and $x_i = -62\,\mathrm{mm} - d_i/2$ (if $i > 1$). For interpolation of the results, a logarithmic model is applied yielding the formulation in equation 4.29.

design process of the septum magnet at JULIC advanced faster than the findings in figure 4.30. For the setup of the multiplexer at JULIC, the increase of the integrated magnetic field of 5 % which results in a smaller bending radius of 2.5 m rather than 2.63 m for the outer field regions thus needs to be considered. This gives a maximal horizontal offset of the beam with respect to the nominal trajectory shown in figure 4.29a of less than 4 mm, which is acceptable for the setup at JULIC according to the particle tracking simulations in figure 4.35. A modified design strategy to consider the horizontal aperture-dependent gain of the integrated magnetic field ab initio can be developed from the findings from the JULIC TFSM. For this, the layered structure with the corresponding intermediate iron pieces with varying thickness should be designed from the beginning based on the desired bending radius and kicker and septum magnet deflection angles. Then, the design of the layers is adjusted to yield the required integrated magnetic field in the outer field regions while keeping the intermediate iron pieces' thickness constant. This strategy is employed for the HBS septum magnet which is presented in figure 5.2.

The horizontal distribution of the integrated magnetic field of the septum magnet can be evaluated separately for the three different field regions by introducing the three different cut planes in the central ($y = 0$) xz-plane of figure 4.27 which are shown in figure 4.31a. The cut planes in the outer field regions follow the integration paths in figure 4.29a. This yields the results in figures 4.31b to 4.31d. The field

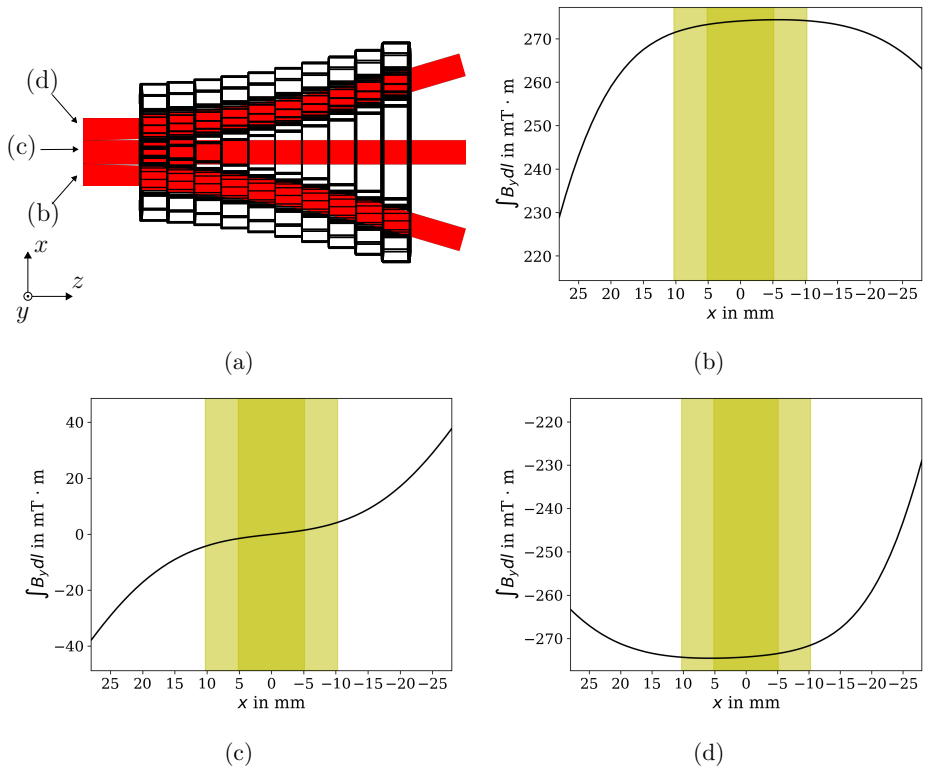

Figure 4.31.: (a): Integration planes (xz-planes at $y = 0$) for the calculation of the horizontal distribution of the integrated magnetic field of the septum magnet in figure 4.27. The integration planes follow the integration paths in figure 4.29a with identical integration limits, i.e. from −525 mm to 525 mm. (b)-(d): Integrated vertical magnetic field $\int B_y \mathrm{d}l$ versus x as indicated in (a). In each integration plane a horizontally centered co-moving cartesian coordinate system is used. The extent of the proton beam is indicated by the yellow shaded area (dark yellow: 2 rms beam widths, light yellow: 4 rms beam widths).

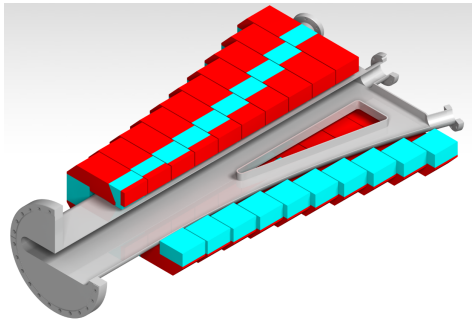

Figure 4.32.: Sketch of the septum magnet in figure 4.27 with a custom made vacuum chamber inserted. The wall thickness of the vacuum chamber is 1 mm resulting in an effective gap height of 41 mm (43 mm in figure 4.24). The vacuum chamber features additional supporting structures in the rear part of the septum magnet when the beam spot separation is larger. The large flange at the front is welded on after the chamber has been inserted into the fully assembled magnet.

homogeneity (similar to equation 4.27) of the outer field regions according to

$$\max\left(\left|\frac{\int B_y(\pm\Delta x(z) - 2\sigma_x \leq x \leq \pm\Delta x(z) + 2\sigma_x, 0)\mathrm{d}l - \int B_y(\pm\Delta x(z), 0)\mathrm{d}l}{\int B_y(\pm\Delta x(z), 0)\mathrm{d}l}\right|\right), \quad (4.30)$$

with $\Delta x(z) = \Delta x_{\mathrm{sm}}(z) + 62\,\mathrm{mm}$ being the z-dependent beam centroid position in the outer integration planes (equation 4.28), is 1 % within 4 rms beam widths. The maximum deviation in integrated magnetic field in the centered field region from zero results in 4 mT m.

For operation of the septum magnet, a custom made vacuum chamber is inserted into the magnet as shown in figure 4.32. The wall thickness amounts to 1 mm reducing the effective gap height in figure 4.24 to 41 mm, which is still in accordance with the beam size calculated in figure 4.9.

4.4.3. Harmonic content

In order to evaluate the magnetic field quality in the dipole field regions and to quantify the fringe field in the zero field region of the septum magnet, a decomposition of the magnetic field into the harmonic content, or multipole coefficients which is used as synonym in the following, is performed following the explanations in section 2.2.3.

The multipole coefficients can be calculated according to equation 2.74 and equation 2.75. For this, the radial magnetic field $B_{\mathrm{r}}(r_0, \Phi_k)$ is extracted from a circle with radius $r_0 = 13\,\mathrm{mm}$ representing 2/3 of the expected beam radius, i.e. 20 mm.

The circle is extended to a tube following the different integration paths as shown in figure 4.29a for all field regions of the septum magnet. The radial field $B_\mathrm{r}(r_0 = 13\,\mathrm{mm}, \Phi_k)$ is then calculated for $\Phi_k = 0...2\pi$ with $\Delta\Phi = 2\pi/360$ from the horizontal and vertical magnetic field components on the reference radius $r_0 = 13\,\mathrm{mm}$ via:

$$B_r(\Phi_k) = B_x(\Phi_k)\cos(\Phi_k) + B_y(\Phi_k)\sin(\Phi_k). \tag{4.31}$$

The multipole coefficients can be averaged throughout the respective integration paths by using the hard-edge approximation of the radial magnetic field following

$$B_{r,\mathrm{h.e.}}(\Phi_k) = \frac{\int_{-525\,\mathrm{mm}}^{525\,\mathrm{mm}} B_r(\Phi_k)\mathrm{d}l}{l_\mathrm{eff}} \tag{4.32}$$

with l_eff being the effective length of the magnet, i.e. 697 mm for the zero field region and 709 mm for the outer field regions. With equation 4.32 inserted in equation 2.74 and equation 2.75, one can deduce the multipole coefficients in hard-edge approximation for the different integration paths in figure 4.29a. For the outer dipole field regions of the septum magnet, the B_1 component, i.e. dipole component, is expected to be by far the strongest component. For this reason, the multipole coefficients for the hard-edge approximation in the dipole field regions are normalized according to

$$a_n = \frac{A_n}{B_1} \cdot 1 \times 10^4, \quad b_n = \frac{B_n}{B_1} \cdot 1 \times 10^4. \tag{4.33}$$

For the centered and right integration path in figure 4.29a, the harmonic content in the hard-edge approximation is presented in figure 4.33. Note that, the left field region can obtained from the right field region of the septum magnet by point reflection. Their harmonic content is therefore almost identical with the exception that odd multipole coefficients, i.e. $B_1, B_3, ...$, change their sign. Thus, it is sufficient to consider the right dipole field region to characterize the septum magnet. For the centered field region in figure 4.33a, there is a dominant quadrupole and octupole component with $-4.2\,\mathrm{mT}$ and $-4.6\,\mathrm{mT}$, respectively. For the right field region in figure 4.33b, quadrupole, sextupole, octupole and decapole components are observed with -72, -58, -22 and -32 units, respectively. According to equation 4.33, one unit of the normalized multipole components represents a fraction of 1×10^{-4} with respect to the main dipole component.

In order to localize the emergence of the individual multipole components throughout the magnet, figure 4.34 shows the longitudinal evolution of the normal components B_n for the centered and the right field region. The skew components A_n can be neglected as shown in figure 4.33. Here, B_r is calculated according to equation 4.31 every 1 mm following the integration paths in figure 4.29a. The normal components B_n are then calculated according to equation 2.75. For the centered field region, the first three layers of the septum magnet in figure 4.27 appear to be the main contributors to the quadrupole and octupole component with the quadrupole component

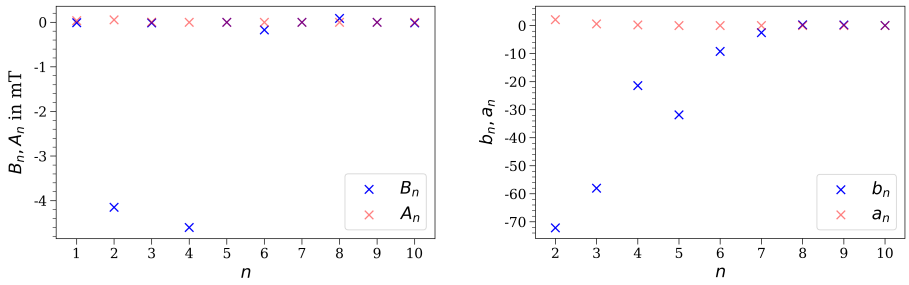

(a) (b)

Figure 4.33.: (a): Harmonic content of zero field region of septum, i.e. at $x = 0$ (path (2) in figure 4.29a). (b): Harmonic content of the right dipole field region of the septum magnet, i.e. the right integration path (1) in figure 4.29a. Here, the multipole coefficients are normalized to the main dipole component B_1 and multiplied by 1×10^4 according to equation 4.33. Both (a) and (b) are evaluated on a reference radius $r_0 = 13\,\text{mm}$ in the hard-edge approximation.

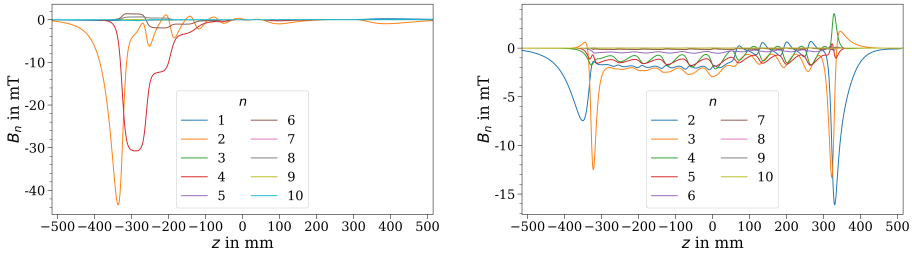

(a) (b)

Figure 4.34.: Normal components B_n of harmonic content versus z following the integration paths from figure 4.29a for the centered (a) and the right field region (b). The skew components A_n are not shown as they are neglectable as shown by the hard-edge approximation in figure 4.33. For the right field region, B_1 is not shown as this is the dominant main component.

decreasing with the beginning of the magnet and the octupole component decreasing gradually throughout the first three layers. Thus, the small separation between the different dipole field regions in the beginning of the septum magnet seems to be the largest influence on the emergence of unwanted multipole components. For the right dipole field region, higher-order multipole components, i.e. $n > 2$, occur predominantly in the beginning and the end of the septum magnet. Here, especially the quadrupole and sextupole components experience a peak right in front of and behind the magnet yoke. Moreover, the average contribution of $n > 2$ multipole components seems to be larger in the first six layers of the septum magnet which can probably be attributed to the presence of the small compensator magnets, shown in figure 4.24, therein. The periodic changes of higher-order multipole components in figure 4.34 for the centered and right field region occur with the layer thickness.

4.4.4. Particle tracking

The interaction of the septum magnet with the particle beam is studied directly via particle tracking within the three different field regions. This allows to study the trajectories of the particles in the different field regions with the integrated magnetic field in figure 4.31. Thus, the effect of the 5 % increase of the integrated magnetic field in the outer field regions presented in figure 4.29 with respect to figure 4.25a is investigated. Furthermore, the beam quality in terms of the dispersive emittance (see equation 4.12) after the septum magnet can be examined and related to the harmonic content, which is presented in the previous section. The particle tracking is carried out with an FEM simulation comprising 2.5×10^4 particles per beam [51].

The initial parameters of the particle beam are taken from figure 4.9. In order to take into account the fringe field extending the magnet yoke on both sides completely (figure 4.29), the longitudinal starting position of the beam for the tracking studies is chosen to be 150 mm in front of the septum magnet. Here, the beam transport calculations yield the beam parameters summarized in table 4.11. These parameters are implemented for the particle beam before arriving at the septum magnet together with different horizontal coordinates and initial deflection angles depending on the different field regions that the beam is supposed to pass. For the outer field regions, where the beams are expected to intersect with the beginning of the septum magnet yoke at $x = \pm 62\,\text{mm}$ as shown in figure 4.29a, the associated horizontal beam positions are $x = \pm 62\,\text{mm} \mp 35\,\text{mrad} \cdot 150\,\text{mm}$ in order to account for the linear trajectory with a kicker magnet deflection angle of 35 mrad. Taking into account the kicker magnet deflection angle, the outer beams are inclined accordingly. The dispersion in table 4.11 is considered by introducing several phase space ellipses coupled to different kinetic energies and displaced in the (x, x') and (y, y') subspace similar to figure 2.4. The number of particles of each of this ellipses is weighted by the kinetic energy distribution with δ in table 4.11. The results obtained from particle tracking are presented in figure 4.35.

Table 4.11.: Beam parameters at $z = -150\,\text{mm}$ in front of the septum magnet as used for the particle tracking studies. Taken from the calculations presented in figure 4.9 and table 4.3.

$\epsilon_x/\text{mm mrad}$	9.7
β_x/m	2.1
α_x	-0.2
η_x/m	-1.3
η'_x	0.1
$\epsilon_{\text{disp.},x}/\text{mm mrad}$	10.2
$\epsilon_y/\text{mm mrad}$	10.8
β_y/m	4.0
α_y	2.2
η_y/m	-1.2
η'_y	0.0
$\epsilon_{\text{disp.},y}/\text{mm mrad}$	15.9
δ	1.84×10^{-3}

For all beam trajectories shown in figure 4.35a, the transmission is almost 100 %. A cross-section of the particle beam is shown in figure 4.35b at $z = -145\,\text{mm}$ in front of the septum magnet and at $z = 145\,\text{mm}$ after the septum magnet. Figure 4.35 shows that the beam in the outer field regions follows the aperture of the magnet and thus, despite the larger integrated magnetic field, the beam is well accommodated by the magnet. However, a slight horizontal broadening of the beam in all three field regions is visible. In the outer field regions, this can be attributed to the degrading dipole field at the outer face of the beam as shown in figure 4.31b and figure 4.31d. In the central region, the beam is defocused horizontally due to the increasing field at larger x in figure 4.31c.

A more detailed analysis of the beam quality after the septum magnet is obtained when considering the phase space distribution of the beam. Figure 4.36 shows the horizontal and vertical phase space of the left beam, i.e. $x > 0$, and the centered beam in figure 4.35a. Here, the initial phase space distribution, which is deduced from table 4.11 is compared to the phase space distribution obtained 145 mm after the septum magnet. The right beam has a similar behavior as the left beam and is therefore not shown. The results from the phase space distributions in terms of emittances, spatial and angular rms envelopes (according to equation 2.5 and equation 4.8) are summarized in table 4.12. In addition, the average divergence $\bar{x'}$ is shown, which represents the deflection angle for the outer beam trajectories after the septum magnet. Here, $\bar{x'}$ amounts to approximately $\pm 318\,\text{mrad}$ for the left and right trajectory, respectively. Taking into account the integrated field of $274\,\text{mT m}$ in the outer field regions from

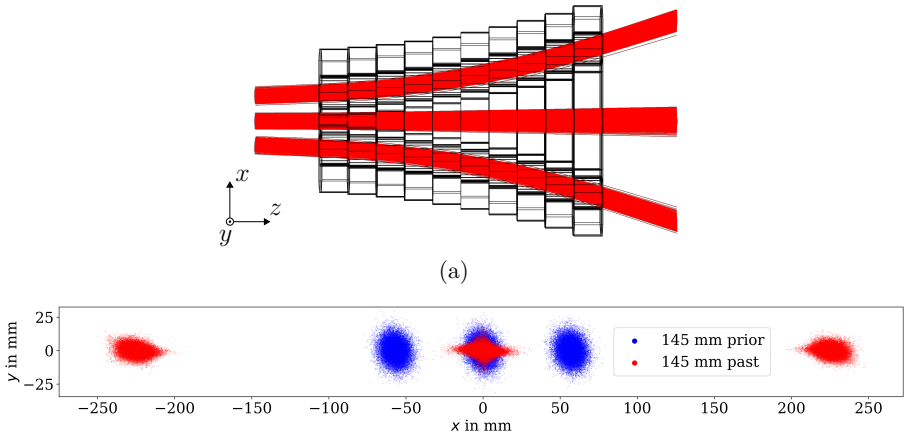

Figure 4.35.: (a): Particle tracking of 45 MeV protons through the septum magnet for different settings of the kicker magnet with each setting serving a different field region of the septum magnet. The simulated transmission through all three field regions is above 99.998 % (b): Cross-section of the beam 145 mm in front of and behind the septum magnet. The initial beam parameters for all three beam trajectories are taken from table 4.11.

figure 4.29, one gets[7] $\alpha = \arcsin(274\,\mathrm{mT\,m}/0.98\,\mathrm{T\,m}) = 283\,\mathrm{mrad}$ deflection from the septum magnet and, including the 35 mrad kicker magnet deflection angle, 318 mrad in total which is in agreement with the results from table 4.12. The results in table 4.12 show an increase of the horizontal emittance up to 20 % as well as up to 13 % growth of the vertical emittance, which is due to the higher-order multipole components shown in figure 4.33. Multipole coefficients with $n > 2$ introduce non-linear forces on the particle beam such that the phase space area, i.e. emittance, changes inside the septum magnet [16, p. 343]. The emittance growth primarily occurs for the centered particle beam with its zero field plateau region being smaller than the beam itself within the first few layers of the septum magnet (shown in figure 4.28). The presence of non-linear forces from higher-order multipole components is also apparent in figure 4.36 (Center) which shows non-elliptical phase space distributions after the septum magnet such that the Courant-Snyder invariant (equation 2.13) is violated.

[7]Note that for initial design studies of the septum magnet, equation 2.41, i.e. small-angle approximation, is used, which underestimates the deflection angle slightly thus being a conservative assumption.

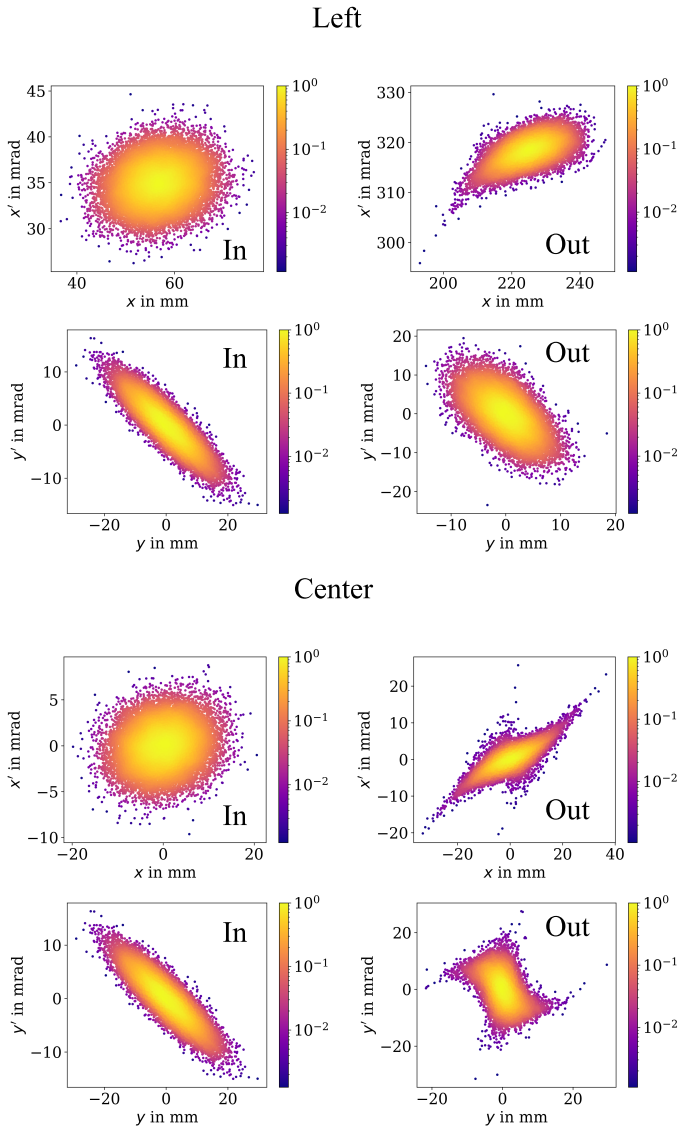

Figure 4.36.: Phase space distribution of the left beam ($x > 0$) and centered beam of figure 4.35a. The initial phase space distribution 150 mm in front of the septum magnet (In - parameters in table 4.11) and the phase space distribution 145 mm after the septum magnet (Out - parameters in table 4.12) are shown for both transversal subspaces ((x, x') and (y, y')). The plots show a normalized particle density distribution.

Table 4.12.: Summary of the results from the phase space distribution analysis 145 mm after the septum magnet. The corresponding beam trajectories are presented in figure 4.35 (left: $x > 0$, right: $x < 0$).

	Left	Centered	Right
$\bar{x'}$/mrad	318.3	0.0	-318.0
σ_x/mm	6.2	6.7	6.0
$\sigma_{x'}$/mrad	2.5	3.0	2.5
$\epsilon_{\mathrm{disp.},x}$/mm mrad	12.7	13.4	11.8
σ_y/mm	3.8	3.4	3.8
$\sigma_{y'}$/mrad	5.0	5.4	5.0
$\epsilon_{\mathrm{disp.},y}$/mm mrad	15.4	16.6	15.4

The spatial and angular rms envelopes in table 4.12 suggest that above 4 m drift without focusing through additional quadrupole magnets can be accepted behind the septum magnet. The defocusing of the beam throughout this drift length is such that the target with 150 mm edge length as employed in the JULIC neutron source test facility can be irradiated.

4.5. Three-Field Magnet (TFM)

As presented in section 4.1, the development and manufacture of the Three-Field Magnet (TFM) serves two purposes. One is to replace the kicker magnet in figure 4.2 in order to operate the outer target stations independently of the performance of the kicker magnet (as explained in figure 4.3). The other purpose is to prove the working principle of the Three-Field Septum Magnet (TFSM) and to show that the manufacture of such magnet is feasible. It is based on the concept shown in figure 4.23.

4.5.1. Layout

The design of the TFM is shown in figure 4.37. Conceptually it can be considered as one layer of the septum magnet in figure 4.27 but with different dimensions. The transverse dimensions are much larger than the front face of the septum magnet in figure 4.24, which is due to the fact that the beam spot separation is larger. As the magnet is not employed as septum with the beam spots being horizontally positioned as closely as possible but as horizontally movable magnet with three different field regions (as explained in figure 4.3), the design requirements are less stringent. To maintain three different field regions as in figure 4.23 without the necessity of additional small vertically magnetized permanent magnets in the central region as used in figure 4.24, the beam spot separation is chosen to be s = 230 mm. According to the beam transport simulation in figure 4.9, a beam size of 60 mm for 6 rms beam

widths is considered. Concerning the vertical dimensions of the magnet, a minimum gap height of $l_{\mathrm{gap}} = 112\,\mathrm{mm}$ is chosen in order to cover a beam tube with 104 mm outer diameter as employed as standard in the experimental area in figure 4.2.

With the transverse dimensions being fixed, the longitudinal extent of the TFM is adjusted in order to meet the geometric constraints in terms of beam deflection angle with the outer field regions. Figure 4.2 shows that the TFM is positioned 220 mm (from TFM yoke end to Kicker yoke front) in front of the kicker magnet. Similar to the kicker magnet in equation 4.17, the deflection angle which has to be provided by the TFM can be derived geometrically with the aim to encounter the outer field regions of the septum magnet, horizontally displaced by $\Delta x = 62\,\mathrm{mm}$ (figure 4.24), within a distance of $l = l_{\mathrm{kicker-septum}} + l_{\mathrm{kicker}} + l_{\mathrm{3-field-kicker}} = 1500\,\mathrm{mm} + 520\,\mathrm{mm} + 220\,\mathrm{mm} = 2240\,\mathrm{mm}$. Without knowledge of the effective length of the TFM, the first guess of the required beam deflection angle thus gives $62\,\mathrm{mm}/2240\,\mathrm{mm} \approx 28\,\mathrm{mrad}$. This results in a required integrated field of approximately $27.4\,\mathrm{mT\,m}$ with $(B\rho) = 0.98\,\mathrm{T\,m}$ from table 4.1 and equation 2.41. With the horizontal dimensions of the TFM given (figure 4.37a), the length can then be iterated such that the required integrated field is obtained. For the TFM, the length is chosen to be $l_{\mathrm{yoke}} = 140\,\mathrm{mm}$. As presented in figure 4.38b, this yields an integrated field $32.9\,\mathrm{mT\,m}$. The integrated magnetic field resulting from the simulation in figure 4.38b is approximately 20 % larger than the one, which is required geometrically. This is deliberately chosen to take into account uncertainties on the remanent flux density of the SmCo permanent magnets which are employed. The reduction of the magnetic field, as it is shown in figure 4.44a, is easier than the enhancement. Therefore, a larger integrated magnetic field is set due to unforeseeable effects from the manufacturing process.

As discussed in the previous paragraph, the beam deflection angle that is to be provided by the TFM is approximately $\approx 28\,\mathrm{mrad}$ in order to operate the outer field regions of the septum magnet at $\Delta x = 62\,\mathrm{mm}$ within a distance $l = 2240\,\mathrm{mm}$. With the knowledge about the effective length of the TFM, i.e. $l_{\mathrm{eff}} = 240\,\mathrm{mm}$, the required beam deflection angle can be reconsidered. The distance from the TFM to the TFSM reduces to $l' = l - (l_{\mathrm{eff}} - l_{\mathrm{yoke}})/2 = 2240\,\mathrm{mm} - (240\,\mathrm{mm} - 140\,\mathrm{mm})/2 = 2190\,\mathrm{mm}$ and following equation 4.17, one obtains a deflection angle

$$\Theta = \frac{\Delta x}{l' + l_{\mathrm{eff}}/2} = \frac{62\,\mathrm{mm}}{2190\,\mathrm{mm} + 240\,\mathrm{mm}/2} = 26.8\,\mathrm{mrad}, \tag{4.34}$$

with a corresponding integrated magnetic field of $26.3\,\mathrm{mT\,m}$. The necessary integrated field is supplied by shielding of the TFM with iron plates as discussed later in this section. However, during regular operation the proton beam can have an angular offset in the xz-plane (coordinate system from figure 4.37) when passing the TFM. This has to be compensated in order to reliably supply the outer field regions of the TFSM. For this, the TFM is positioned onto a support which is not only horizontally movable in order to switch between different target stations (figure 4.3) but also longitudinally, which allows to react to beam misalignments in the xz-plane at fixed

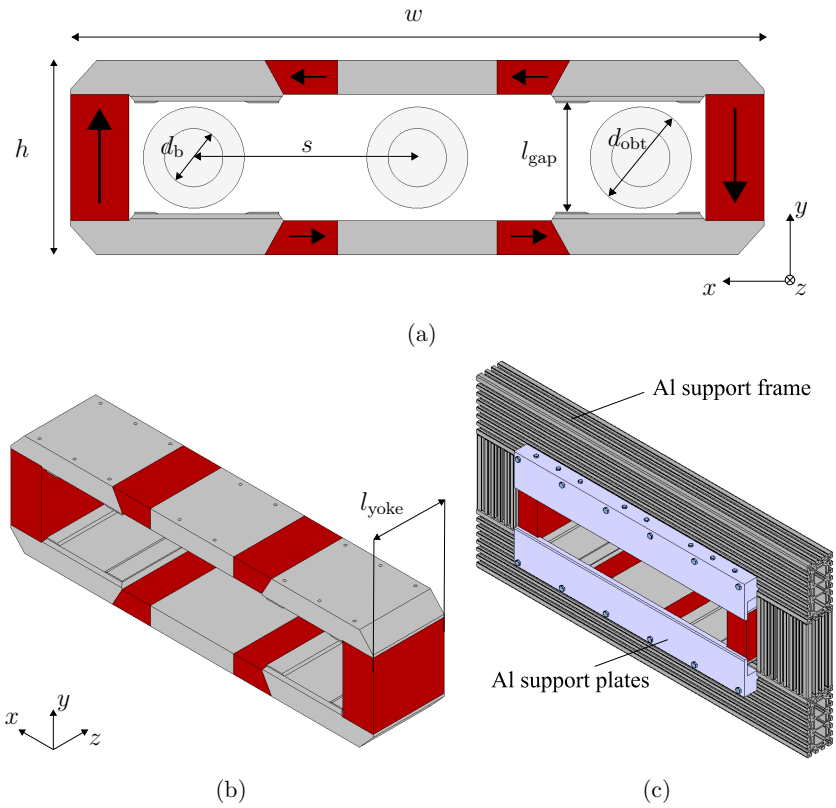

Figure 4.37.: (a): Technical layout of the TFM front face. The width of the front face is w = 714 mm and the height h amounts to 200 mm. The gap height l_{gap} = 112 mm allows to accommodate a beam tube with outer diameter d_{obt} = 104 mm. The expected beam diameter is d_b = 60 mm (6 rms beam widths according to figure 4.9). The separation of the beam spots is s = 230 mm. The red parts indicate SmCo magnets with B_r = 1.1 T, the gray parts show the magnet yoke. The magnetization directions of the permanent magnets are indicated with arrows. (b): Side view of the structure in (a) with a yoke length of l_{yoke} = 140 mm. (c): Full TFM setup with a customized Al support structure. Al support plates are mounted on the magnet yoke and connected to an Al support frame, which stabilizes the structure.

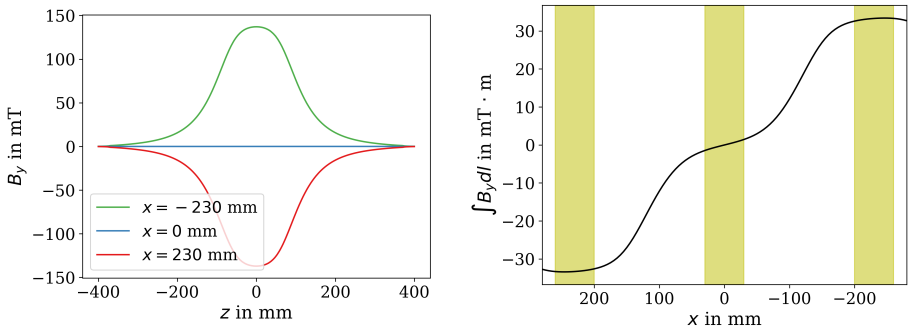

(a) (b)

Figure 4.38.: (a): Vertical magnetic flux density B_y versus z of the TFM design in figure 4.37 extended in z to 140 mm length at different horizontal coordinates x representing the beam centers as positioned in figure 4.37a. The origin of the coordinate system is the geometric center of the magnet. (b): Corresponding integrated vertical magnetic flux density $\int_{-400\,\mathrm{mm}}^{400\,\mathrm{mm}} B_y \mathrm{d}l$ versus horizontal coordinate x. The yellow shaded area marks the beam position (6 rms beam widths, i.e. ≈ 60 mm according to figure 4.9). The effective length can be derived to be $l_{\mathrm{eff}} = 240$ mm.

beam deflection angle of the TFM. The longitudinal displacement can be tuned by $\Delta z = \pm 100$ mm in 10 mm steps. This results in an angular acceptance of the beam in the TFM of ± 1.1 mrad which is shared between an angular offset of the beam itself as well as deviations of the integrated magnetic field of the TFM from the nominal value.

4.5.2. Magnetic field measurements

For characterization of the TFM, shown in figure 4.37, the magnetic flux density distribution is measured by a three-axis HALL probe as presented in figure 4.39. Here, the origin of the coordinate system is in the geometric center of the magnet. The HALL probe in figure 4.39 is moved within three different xz-planes at $y = 0$, i.e. referred to as main plane, and $y = \pm 20$ mm. Within each plane, the measurement covers the horizontal coordinates $x = \pm 280$ mm and the longitudinal coordinates $-280\,\mathrm{mm} \leq z \leq 200\,\mathrm{mm}$ both with 5 mm steps. The asymmetry in z results from the measurement setup in figure 4.39 which limits the measurement range in $z > 0$. At each position, the magnetic field components B_x, B_y and B_z are averaged over 200 ms while the positioning of the probe is changed every 3 s with 1 s idle time before the measurement for the stabilization of the probe.

A systematic effect which has to be taken into account when analyzing the magnetic

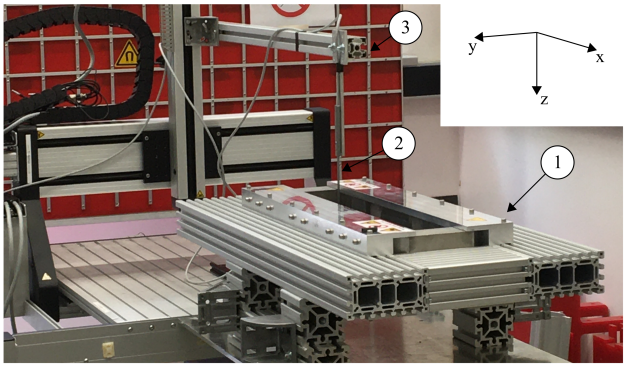

Figure 4.39.: Setup for 3-D magnetic flux distribution measurement. 1: TFM. 2: 3-axis HALL probe. 3: 3-dimensionally movable support of the HALL probe driven by a CNC machine. The origin of the coordinate system is located in the geometrical center of the magnet.

field measurements is the rotation of the HALL probe with respect to the magnet. For the compensation of this effect, a procedure introduced in [53] can be applied. Here, the imperfection angles pitch α, yaw β and roll γ of the probe as shown in figure 4.40 are introduced. When assuming the probe coordinate system in figure 4.40 to be aligned with the magnet coordinate system and positioned in a region with homogeneous dipole field, i.e. $B_y = B_0$ and $B_x = B_z = 0$, the introduction of a pitch angle $\alpha \neq 0$ results in a measured field component $B_{z,\mathrm{m}} \neq 0$ from the probe. The rotation of the probe by a roll angle $\gamma \neq 0$ additionally introduces a component $B_{x,\mathrm{m}} \neq 0$ from the probe. Thus, relating all magnetic field components $B_{x,\mathrm{m}}$, $B_{y,\mathrm{m}}$, $B_{z,\mathrm{m}}$ reported from the HALL probe in a homogeneous dipole field allows to derive

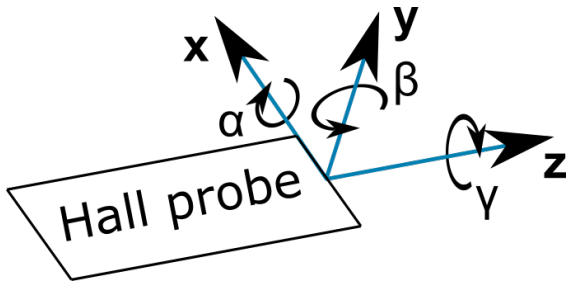

Figure 4.40.: Imperfection angles of the HALL probe. If the probe were perfectly aligned, its coordinate system would coincide with coordinate system of the magnet in figure 4.39. Taken and adapted from [53].

the pitch and roll angles according to

$$\alpha = \arctan\left(\frac{-B_{z,\mathrm{m}}}{B_{y,\mathrm{m}}}\right)$$
$$\gamma = \arctan\left(\frac{B_{x,\mathrm{m}} \cdot \cos\alpha}{B_{y,\mathrm{m}}}\right). \tag{4.35}$$

The yaw angle β has no influence in a homogeneous dipole field such that it can not be derived accordingly. However, it can be considered less critical as it mixes the field components $B_{x,\mathrm{m}}$ and $B_{z,\mathrm{m}}$ which are less important for dipole magnets. Having derived α and γ according to equation 4.35, the measured magnetic field can be corrected by rotation with

$$\begin{pmatrix} B_{x,\mathrm{m,rot.}} \\ B_{y,\mathrm{m,rot.}} \\ B_{z,\mathrm{m,rot.}} \end{pmatrix} = R_\gamma \cdot R_\alpha \cdot \begin{pmatrix} B_{x,\mathrm{m}} \\ B_{y,\mathrm{m}} \\ B_{z,\mathrm{m}} \end{pmatrix} \tag{4.36}$$

with R_γ and R_α being the corresponding rotation matrices.

In order to derive the imperfection angles α and γ, the dipole field region of the TFM at $x = -230\,\mathrm{mm}$ is considered at $z = 0$, i.e. longitudinally centered in the magnet. Within $\Delta x = \pm 20\,\mathrm{mm}$ the simulated average fractions of $< B_x > / < B_y >$ and $< B_z > / < B_y >$ are below 1×10^{-4} such that this region can be considered a homogeneous dipole field region, and any larger contributions of B_x and B_y are attributed to a tilt of the Hall probe or to manufacturing uncertainties. In order to exclude manufacturing uncertainties, averaging of the measured $B_{x,\mathrm{m}}$, $B_{y,\mathrm{m}}$ and $B_{z,\mathrm{m}}$ is performed over 27 individual positions equally distributed between three vertical positions $y = -20\,\mathrm{mm}, 0, 20\,\mathrm{mm}$ and nine horizontal positions within $x = [-250\,\mathrm{mm}, -210\,\mathrm{mm}]$. The resulting imperfection angles are

$$\alpha = -30(1)\,\mathrm{mrad}$$
$$\gamma = -33(2)\,\mathrm{mrad}. \tag{4.37}$$

The results are implemented into equation 4.36. With this, the vertical magnetic flux density $B_{y,\mathrm{m,rot.}}$ shown in figure 4.41 is obtained ($B_{x,\mathrm{m,rot.}}$ and $B_{z,\mathrm{m,rot.}}$ are presented in figure C.1). Here, the two outer dipole field regions with opposite polarity and a centered zero field region are clearly visible. The maximum vertical magnetic field in the dipole field regions amounts to 140 mT, which is about 1.5 % larger than the simulated maximum vertical magnetic field $B_{y,\mathrm{sim.}}$. The larger magnetic field can be attributed to inaccuracies in the specification of the remanent flux density of the permanent magnets used. The permanent magnets that are stronger than required lead to a global gain of the magnetic flux density in the air gap of the magnet. Thus, the measured and rotated magnetic field components $B_{i,\mathrm{m,rot.}}$ with $i = x, y, z$ can be scaled according to

$$B_{i,\mathrm{m,corr.}} = B_{i,\mathrm{m,rot.}} \cdot \frac{\max\left(B_{y,\mathrm{m,rot.}}\right)}{\max\left(B_{y,\mathrm{sim.}}\right)} \tag{4.38}$$

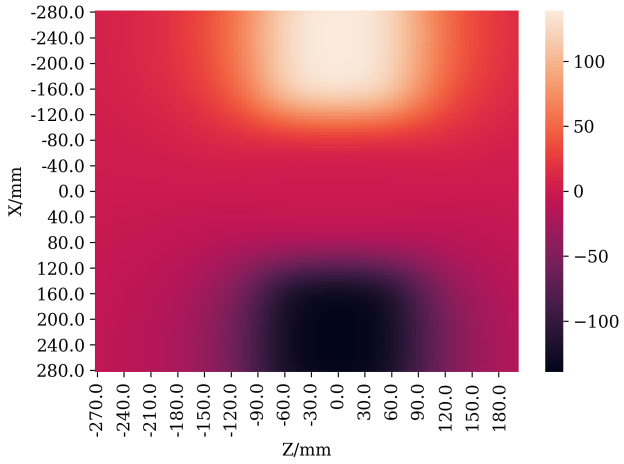

Figure 4.41.: Measured and rotated (according to equation 4.36) vertical magnetic flux density $B_{y,\mathrm{m,rot.}}$ in the central xz-plane, i.e. $y = 0$ in figure 4.39, in mT.

$$i = x, y, z$$

in order to correct for the magnetic field gain from the permanent magnets employed. With this, the characteristics of the measured magnetic flux density distribution can be compared in more detail to the simulated results. Figure 4.42 shows the difference between measurement and simulation of the magnetic flux density distribution considering the measured magnetic field components $B_{i,\mathrm{m}}$ as well as the corrected measurements according to equation 4.38 yielding $B_{i,\mathrm{m,corr.}}$. One observes a better agreement between measurement and simulation for $B_{i,\mathrm{m,corr.}}$. The difference between measurement and simulation is on average better than 8 ‰ for $|B_{i,\mathrm{m}} - B_{i,\mathrm{sim.}}|$ and better than 4 ‰ for $|B_{i,\mathrm{m,corr.}} - B_{i,\mathrm{sim.}}|$, each relative to the respective measured main maximum dipole field component $B_{y,\mathrm{m}} = 138.98\,\mathrm{mT}$ and $B_{y,\mathrm{m,corr.}} = 137.14\,\mathrm{mT}$, respectively. The same holds for two xz-sub-planes measured at $y = \pm 20\,\mathrm{mm}$ which are presented in figure C.2 and figure C.3 of the appendix, respectively. Concerning the installation of the TFM in the multiplexer setup in figure 4.2, the vertical and horizontal magnetic field components B_y and B_x, respectively, are the most critical ones as they induce a magnetic Lorentz force on the beam. Looking at figure 4.42, it can be seen that the largest difference between measurement and simulation occur in the areas where no beam is expected, e.g. in the region of vertical magnetic field gradient with $-80\,\mathrm{mm} > x > -120\,\mathrm{mm}$ and $120\,\mathrm{mm} > x > 80\,\mathrm{mm}$ for $|B_{x,\mathrm{m,corr.}} - B_{x,\mathrm{sim.}}|$ in figure 4.42d.

The magnetic measurements of the TFM prove the working concept of a permanent-

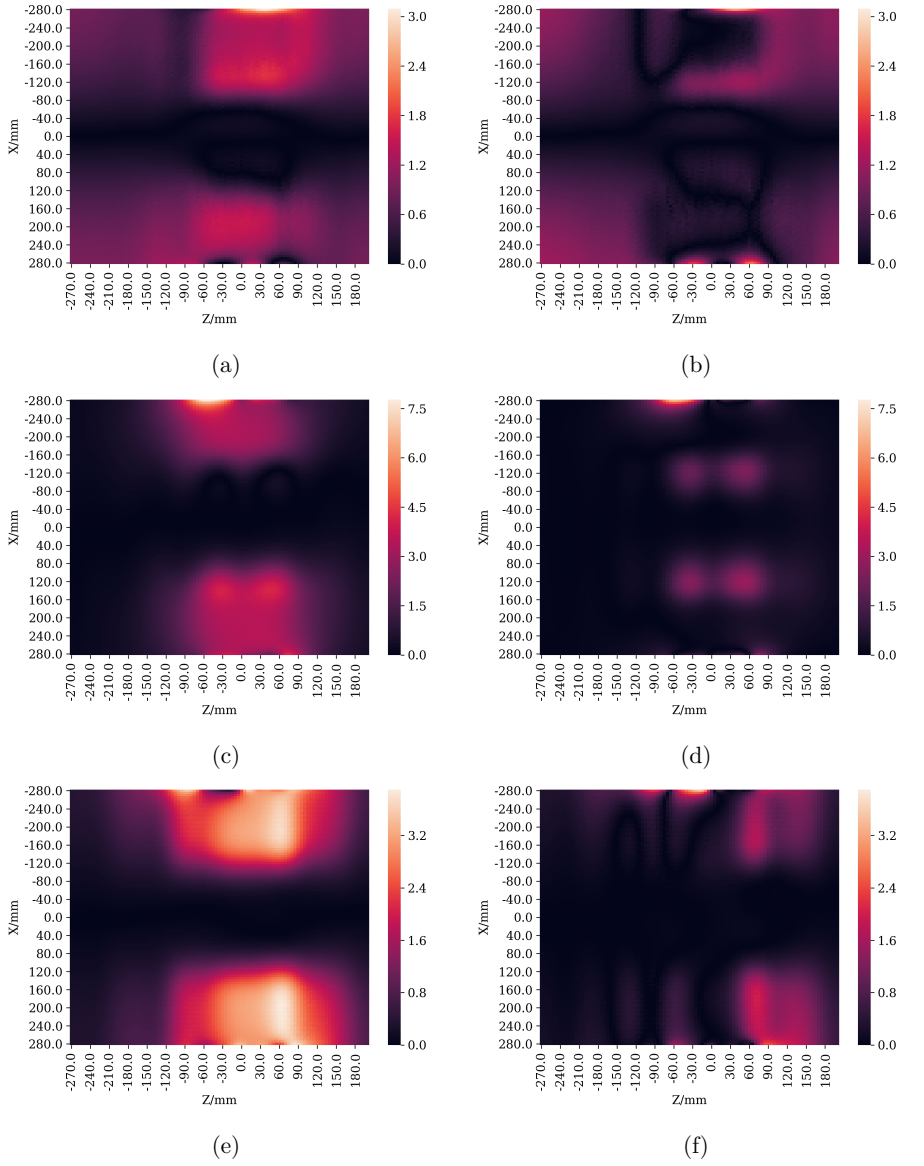

Figure 4.42.: Absolute difference between measurement and simulation of the magnetic flux density of the TFM for the center xz-plane in mT without (first column) and with correction (second column). (a) shows $|B_{y,\mathrm{m}} - B_{y,\mathrm{sim.}}|$, (b) shows $|B_{y,\mathrm{m,corr.}} - B_{y,\mathrm{sim.}}|$. (c) and (d) show the same for x and (e) and (f) for z, where both respective simulated components $B_{x,\mathrm{sim.}}$ and $B_{z,\mathrm{sim.}}$ are zero throughout the xz-plane at $y = 0$. The measured and corrected magnetic flux density $B_{i,\mathrm{m,corr.}}$ is calculated according to equation 4.38 for $i = x, y, z$.

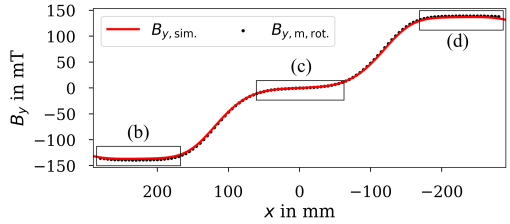

(a)

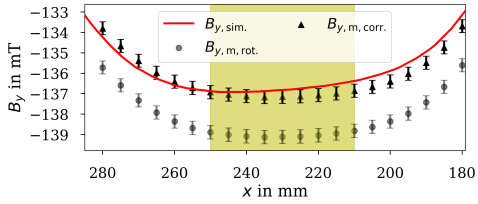

(b)

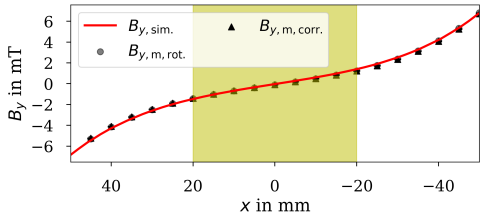

(c)

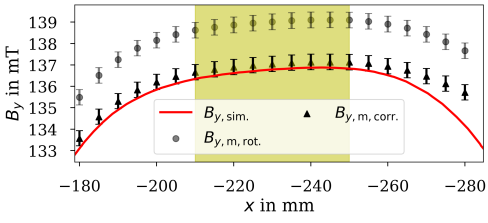

(d)

Figure 4.43.: Vertical magnetic flux density B_y versus horizontal position x at $z = 0$. (a) shows $B_{y,\mathrm{m,rot.}}$ and $B_{y,\mathrm{sim.}}$ for $-290\,\mathrm{mm} < x < 290\,\mathrm{mm}$ and the corresponding insets (b) - (d). The insets show $B_{y,\mathrm{m,rot.}}$, $B_{y,\mathrm{m,corr.}}$ and $B_{y,\mathrm{sim.}}$. The position and extension of the beam in the three field regions is indicated by the yellow shaded area. The beam size is considered as 6 rms beam widths from figure 4.9 at the position of the TFM.

magnet-based magnetic system featuring three different field regions as proposed in figure 4.23. The characteristic step-like horizontal evolution of the vertical magnetic flux density of such a magnet can be highlighted by analyzing B_y at $z = 0$ as shown in figure 4.43. The rotated and scaled vertical magnetic field component $B_{y,\mathrm{m,corr.}}$ agrees well with the simulated magnetic field in the areas with beam. Thus, the characteristics of the vertical magnetic flux density distribution are well reproduced by the manufactured magnet with respect to the simulations. However, the actual magnet maintains an up to 1.5 % stronger magnetic field in the dipole field regions, i.e. the scaling factor applied in equation 4.38 and shown as $B_{y,\mathrm{m,rot.}}$ in figure 4.43, which has to be considered. Furthermore, the magnet is initially designed to supply a larger integrated magnetic field than required from equation 4.34 in order to deal with manufacturing tolerances. Therefore, iron shields are added to the magnet in order to reduce the magnetic field as explained in the next paragraph.

Adjustment of the integrated field

The simulated envisaged integrated magnetic field amounts to 32.9 mT m with respect to 26.3 mT m which are geometrically required from equation 4.34. Including the 1.5 % gain of the manufactured magnet with respect to the simulations, a reduction by 7.1 mT m of the integrated magnetic field has to be carried out. This can be realized by shielding of the magnet with iron plates, which follow the contour of the magnet (as in figure 4.37) from both sides. The thickness of the iron plates influences the shielding effect. For the reduction of 7.1 mT m, two 8 mm iron plates are required which is deduced from an FEM simulation similar to figure 4.38. The plates are mounted on the magnet as shown in figure 4.44a. The resulting measured integrated magnetic field is shown in figure 4.44b. With $\mp 26.27(2)$ mT m at $x = \pm 230$ mm, the integrated magnetic field in the outer field regions is adjusted to fit the geometrically required 26.3 mT m. The measured field homogeneity of the integrated vertical magnetic field (similar to equation 4.27) in the outer field regions is 1.4 % throughout the horizontal extent of the beam. In the centered field region, the maximum deviation in integrated magnetic field from zero is 1.3 mT m.

4.6. Operational tests

In the scope of this thesis, a test operation of the kicker magnet as the dynamic part of the multiplexer in figure 4.2 was carried out. The main goal was establishing logics for synchronization of the kicker magnet and the pulsing of the proton beam from the JULIC accelerator. For this, the kicker magnet is installed at its designated position in the experimental area. At this stage, the kicker magnet did not include the insets presented in figure 4.16 nor feature the parallel wiring of two power supplies as presented in figure 4.11 and thus supplied a maximum dipole field of 35 mT as listed in table 4.6. The corresponding power supply can be operated bipolar, however the change of polarity is realized by contactors and thus not intended to be changed

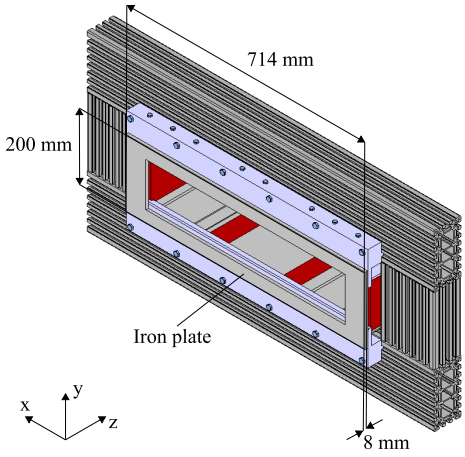

(a)

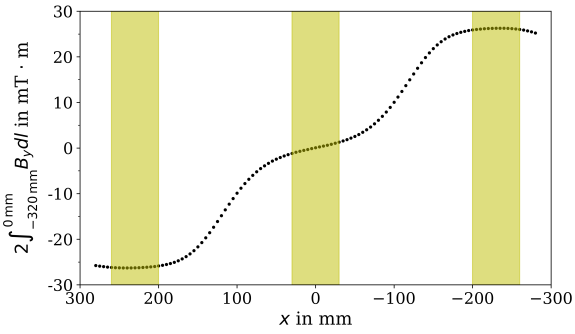

(b)

Figure 4.44.: (a): TFM (shown in figure 4.37) with iron shielding to reduce the integrated magnetic field. Two iron plates in total are mounted to the magnet with one plate per side. The iron plates are mounted such that they follow the contour of the magnetic structure shown in figure 4.37a. The origin of the coordinate system is in the center of the magnet. (b): Corresponding measurement of the integrated vertical magnetic field versus x of the TFM with iron shields. The measurement is carried out for $z = -320\,\mathrm{mm}$ to $z = 0\,\mathrm{mm}$ (at $y = 0\,\mathrm{mm}$) and then doubled making use of the symmetry of the magnetic flux density distribution as shown in figure 4.41. The integrated magnetic field in the outer field regions, i.e. at $x = \pm 230\,\mathrm{mm}$, amounts to $\mp 26.27(2)\,\mathrm{mT\,m}$. The yellow shaded areas mark the expected beam positions (6 rms beam widths as in figure 4.43).

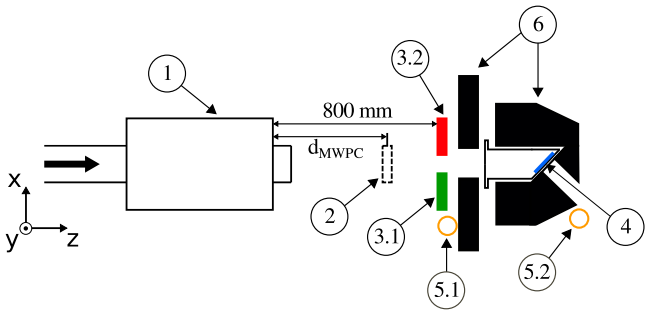

Figure 4.45.: Schematic drawing of the experimental setup for tests of the kicker magnet synchronized with the proton beam pulsing of the JULIC accelerator. The scheme shows the xz-plane, i.e. top view, from figure 4.2 with the proton beam passing from the left side as indicated by the black arrow. 1: Kicker magnet synchronized to JULIC 2: Movable multi-wire proportional chamber, 3.1: Electrically insulated right side of a collimator system (green), 3.2: Left side of the collimator system (red), 4: Tantalum target used as beam cup (blue), 5.1: ^{3}He detector at the collimator position (yellow), 5.2: ^{3}He detector at the extraction channel (yellow), 6: Polyethylene moderator.

periodically, e.g. between two subsequent proton pulses. Therefore, the testing of the kicker magnet synchronized with the pulsing of the cyclotron JULIC has been carried out with two different pulse components instead of three, as intended in figure 4.1, and the power supply being operated unipolar.

The experimental setup for the multiplexer tests with the kicker magnet at JULIC is schematically shown in figure 4.45. It can be considered as part of the multiplexer setup in figure 4.2 with the kicker magnet at the exact position but with the TFM and the TFSM excluded as these magnets were subject to ongoing developments during the tests. On a position 800 mm downstream the kicker magnet an aluminum collimator with two electrically insulated plates is installed and combined with a tantalum beam cup, which is positioned behind the collimator. The cup and the two collimator plates are wired individually to a multi-channel picoammeter such that a destructive current measurement of the proton beam can be carried out at three different horizontal positions. With this setup three potential target stations are mimicked without the necessity of a septum magnet for further spatial separation. The beam cup in figure 4.45 is completely housed in polyethylene acting as thermal moderator of the neutrons generated in the cup. Here, a neutron extraction channel is brought into the polyethylene being inclined by 45° to the proton beam axis. Additionally, two polyethylene plates are positioned on the right and on the left side behind the collimator such that neutrons emerging from the collimator plates are also partly

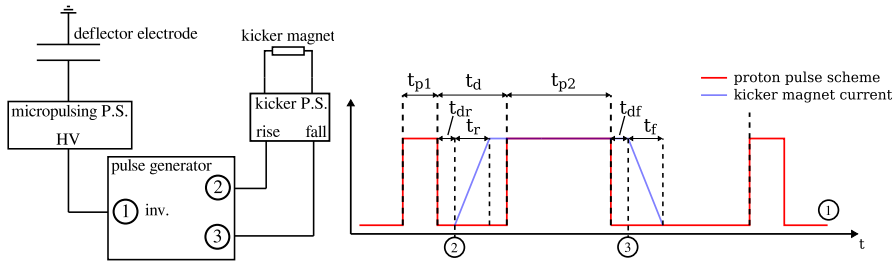

Figure 4.46.: (a): Logics for tests of the kicker magnet synchronized with the micropulsing (chopper) of the JULIC accelerator. A pulse generator controls the proton beam pulse structure by setting the HV applied from the micropulsing power supply to a deflector electrode, i.e. a chopper, in the source beamline of JULIC as in figure 3.7. The proton pulse structure is dictated by the pulse generator as inverted TTL sequence of the actual pulse structure (1). Simultaneously, the kicker magnets rise (2) and fall (3) sequences of the magnet current are controlled by the pulse generator. (b): Time diagram of the pulse generator with multiplexed pulse structure (1) and kicker magnet current rise (2) and fall (3) triggers as well as respective pulse lengths and delays. The temporal evolution of the proton pulse structure and the kicker magnet current is implied by red and blue lines, respectively.

moderated. The positioning of two ^{3}He-detectors indicated in figure 4.45 allows to measure the count rate of neutrons primarily generated by the beam cup and by the collimator separately. Between the collimator and the kicker magnet, a movable multi-wire proportional chamber (MWPC) is installed at variable distance d_{MWPC}, which allows to monitor the transversal beam position and beam size.

The kicker magnet is controlled by a pulse generator, which in parallel operates the pulsing of the proton beam. The corresponding logics are presented in figure 4.46. Here, a multiplexed proton pulsing scheme is generated through the micropulsing (chopper) of the JULIC accelerator containing short pulses with pulse length t_{p1} and period length T_{p1} as well as longer pulses with larger pulse length t_{p2} and larger period length T_{p2} which are delayed by t_{d} with respect to the short pulse. The proton pulse scheme is realized through a deflector electrode in the source beamline of JULIC as indicated in figure 3.7. For this reason, the pulse scheme which is intended for proton beam is inverted to trigger the high voltage (HV) being applied to the electrode as HV on at the electrode results in beam off. The rising of the kicker magnet current is triggered with a variable delay t_{dr} with respect to the short pulse. The rise time t_{r} is set to fit the gap between the two different pulses. The same applies for the falling of the kicker magnet current with t_{df} and t_{f} with respect to the long pulse component.

The delay of the kicker magnet current's rise and fall triggers t_{dr} and t_{df} is adjusted to take in to account the time-of-flight of protons from the pulse generation to the kicker magnet. The time-of-flight of protons t_{TOF} from the deflector electrode in the source beamline to the kicker magnet is dominated by the acceleration inside the cyclotron. The JULIC accelerator operates at a RF-frequency of $f_{\mathrm{RF}} = 29.646\,\mathrm{MHz}$ representing the third harmonic, i.e. $h = 3$, of the revolution frequency $f_{\mathrm{rev}} = 9.882\,\mathrm{MHz}$ for 45 MeV protons. The energy gain per turn in the cyclotron is 90 keV such that 500 turns inside JULIC are required to accelerate protons from 4.5 keV, i.e. the energy in the source beamline of figure 3.7, to 45 MeV. The acceleration time then totals $T_{\mathrm{acc}} = 500 \cdot 1/f_{\mathrm{rev}} \approx 50\,\mu\mathrm{s}$. Taking into account the time-of-flight in the source beamline at 4.5 keV of $\approx 10\,\mu\mathrm{s}$, the total time-of-flight can be approximated to be $\approx 60\,\mu\mathrm{s}$. Here, the time-of-flight at 45 MeV is neglected as this is below 1 µs. A conservative assumption of $t_{\mathrm{TOF}} < 100\,\mu\mathrm{s}$ is considered in the following and t_{dr}, t_{df} in figure 4.46b are adjusted accordingly.

To show the working kicker magnet synchronization, two different experiments are carried out. One experiment focuses on synchronous beam current measurements at the collimator plates and the beam cup in figure 4.45 representing a direct measurement of the spatial separation of the individual pulse components in the multiplexed proton beam. The other experiment operates the different ^{3}He neutron detectors at the collimator and beam cup position in time-of-flight mode to indirectly monitor the deflection of specific proton pulses.

For the beam current measurement, a multi-channel picoammeter providing 20 kHz sampling rate is used. The parameters for the multiplexed proton beam are chosen to be $t_{\mathrm{p1}} = 5\,\mathrm{ms}$, $T_{\mathrm{p1}} = 50\,\mathrm{ms}$ for the short pulse components and $t_{\mathrm{p2}} = 15\,\mathrm{ms}$, $T_{\mathrm{p2}} = 5\,\mathrm{s}$ for the long pulse components with a delay of $t_{\mathrm{d}} = 5\,\mathrm{ms}$ in figure 4.46b. The pulse and period lengths are chosen such that the timing provided by the kicker magnet power supply in table 4.7 is maxed out. For different applications, e.g. the experiment with the ^{3}He neutron detectors, the pulse lengths can be reduced. The kicker magnet rise and fall time are chosen to be $t_{\mathrm{r}} = 3\,\mathrm{ms}$ and $t_{\mathrm{f}} = 10\,\mathrm{ms}$, respectively. With these settings, the beam current measurements in figure 4.47 can be obtained. It can be seen from the beam current measurements at the collimator plates and the beam cup that the proton beam goes straight through the collimator for all pulse components when the kicker magnet is off as indicated by the left and right collimator signal being almost equal. When switching on the kicker magnet, which is synchronized to deflect the long pulse components, these pulse components exhibit a larger beam current signal on the right collimator plate and a smaller signal on the left collimator plate, thus indicating that the long proton pulses are deflected to the right while the short proton pulses pass the kicker magnet unperturbed. Note that, the proton pulses experience a linear increase of the beam current on a time scale of $\approx 10\,\mathrm{ms}$ which is attributed to a non-optimized injection process into the cyclotron. In addition to the beam current measurements in figure 4.47, an MWPC is used to determine the deflection angle of the long pulse components by measuring the proton beam position

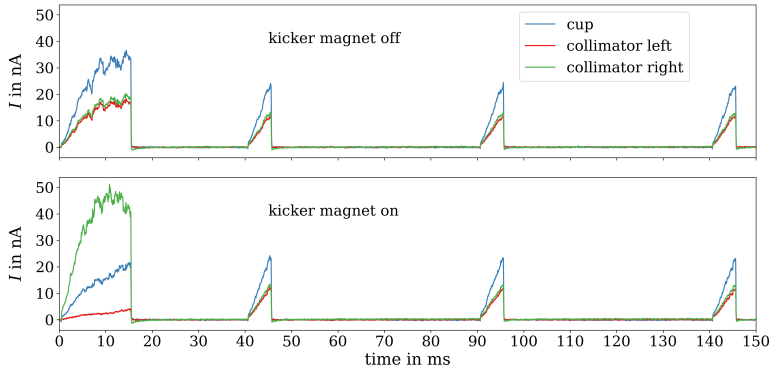

Figure 4.47.: Proton beam current measurement at the beam cup and collimator plates shown in figure 4.45 (same color scheme) for a multiplexed proton beam as presented in figure 4.46b with $t_{p1} = 5\,\text{ms}$, $T_{p1} = 50\,\text{ms}$, $t_{p2} = 15\,\text{ms}$, $T_{p2} = 5\,\text{s}$ and $t_d = 5\,\text{ms}$. The measurement is triggered by the long pulse components. With the kicker magnet being switched on, the long pulse components are deflected towards the right collimator plate while the short pulse components pass unperturbed. The measurements are averaged over ten times occurrence of the long 0.2 Hz pulse componets, i.e. 50 s.

at two different distances $d_{\text{MWPC}} = 445\,\text{mm}, 730\,\text{mm}$ in figure 4.45. The results are given in figure 4.48. From the fit results in figure 4.48, one obtains the average beam position for the different MWPC positions and kicker settings, which allows to derive the deflection angle from the kicker magnet to be

$$\Theta = -21.0(7)\,\text{mrad}. \tag{4.39}$$

According to table 4.6, the kicker magnet provides a maximum dipole field of 35 mT at 250 A. With an effective length of 610 mm, this yields 21.8 mrad deflection angle for 45 MeV protons, i.e. $B(\rho) = 0.98\,\text{T m}$, which is consistent with the result obtained in equation 4.39. In summary, the beam current measurement in figure 4.47 as well as the MWPC measurement in figure 4.48 show that the deflection of particular proton pulses in a multiplexed proton pulse scheme can be achieved with the synchronization of the kicker magnet to the chopper of JULIC.

For further investigations of the kicker magnet operation with multiplexed proton beam, the ^{3}He detectors in figure 4.45 are operated in time-of-flight (ToF) mode, which allows to record the time resolved neutron count rate at the position of the collimator and the beam cup separately. In figure 4.49, the TOF spectra for the ^{3}He detectors in figure 4.45 are shown. The TOF spectra are recorded for different states of the kicker magnet. To check the synchronization of the kicker magnet to the JULIC

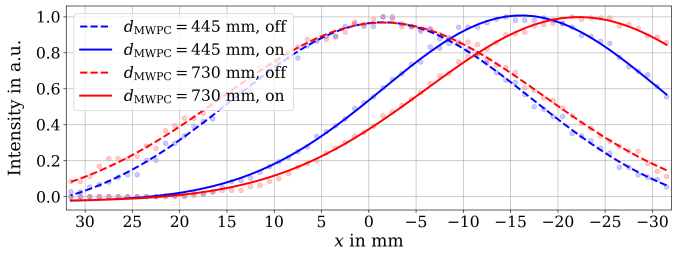

Figure 4.48.: MWPC measurement of the horizontal proton beam profile at $d_{\mathrm{MWPC}} = 445\,\mathrm{mm}, 730\,\mathrm{mm}$ in figure 4.45 triggered by the long pulse component in figure 4.47 with the kicker magnet being off and on, i.e. powered with 250 A. A gaussian fit is performed individually for all measurements with kicker magnet being off (dotted line) and on (solid line).

accelerator, a multiplexed proton pulse structure is used with identical pulse lengths, i.e. $t_{\mathrm{p1}} = t_{\mathrm{p2}} = 80\,\mu\mathrm{s}$, and different period lengths, i.e. $T_{\mathrm{p1}} = 80\,\mathrm{ms}$ and $T_{\mathrm{p2}} = 6\,\mathrm{s}$ (figure 4.46). The kicker magnet is synchronized to deflect the low frequency, i.e. $T_{\mathrm{p2}} = 6\,\mathrm{s}$, component. The pulse length of 80 µs is chosen such that dead time effects of the ^{3}He detectors are reduced. In figure 4.49, the two neutron pulses generated by the two 80 µs proton pulse components are well visible. The measurements are triggered on the high frequency component. In figure 4.49a, the TOF spectrum at the position of the extraction channel in the polyethylene moderator (detector 5.2 in figure 4.45) is shown, which primarily monitors neutrons emerging directly or indirectly through moderation in the polyethylene from the Ta target (beam cup). Therefore, the count rate at this detector position is dominated by the proton pulses impinging on the Ta target. Here, it can be seen that the count rate which is attributed to the high frequency proton pulse component, i.e. the first neutron pulse in the TOF spectrum, remains unchanged when switching on the kicker magnet. Whereas, the count rate which is attributed to the low frequency proton pulse component, i.e. the second neutron pulse in the TOF spectrum, reduces significantly by approximately 60 % when switching on the kicker magnet. The corresponding results in terms of the integrated count rate in the interval from 0 ms to 2 ms and 40 ms to 42 ms, which are attributed to the neutrons generated from the high frequency and low frequency proton pulse component, respectively, are presented in table 4.13. Here, it can be seen that the integrated count rate of the high frequency ($T = 80\,\mathrm{ms}$) neutron pulse does not change when the kicker magnet is switched on. The integrated count rate of the low frequency ($T = 6\,\mathrm{s}$) neutron pulse component is related by the ratio $80\,\mathrm{ms}/6\,\mathrm{s} = 1/75$ to the high frequency component. When the kicker magnet is switched on, the integrated count rate of the low frequency frequency reduces to a fraction of 0.35(2) of the corresponding value without kicker magnet operation. From the beam current measurement in figure 4.47, one observes that the intensity on the target (beam cup)

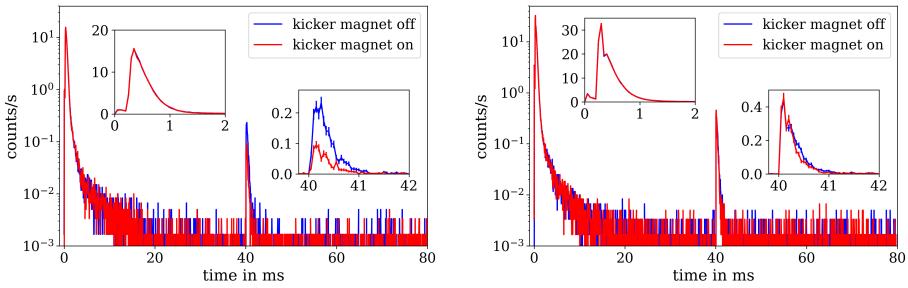

(a) (b)

Figure 4.49.: Neutron time-of-flight (ToF) spectra recorded with the ^{3}He detectors in figure 4.45 with and without the kicker magnet. For neutron generation, a multiplexed proton pulse structure is used with identical pulse lengths, i.e. $t_{p1} = t_{p2} = 80\,\mu s$, and different period lengths, i.e. $T_{p1} = 80\,ms$ and $T_{p2} = 6\,s$ (figure 4.46). The kicker magnet is synchronized to deflect the low frequency, i.e. $T_{p2} = 6\,s$, component. The TOF spectra are recorded within a 80 ms frame and triggered by the high frequency component ($T_{p1} = 80\,ms$). (a) TOF count rate from the ^{3}He detector at the extraction channel position (5.2 in figure 4.45). (b): TOF count rate from the ^{3}He detector at the collimator position (5.1 in figure 4.45). The insets show the spectrum at the time interval attributed to the high frequency (0 to 2 ms) and the low frequency proton pulse component (40 to 42 ms). The measurement time for all scenarios is 600 s. The beam intensity remains unchanged during the different measurements.

of the low frequency proton pulse component reduces to fraction of 0.57(6) when the kicker magnet is switched on. The reduction of the corresponding neutron count rate (by 0.35(2)) must therefore also be influenced by geometric effects which come from the inclination of the proton beam on the target when the kicker magnet is used. Nevertheless, the observations in figure 4.49a suggest that the low frequency proton pulse components are partly stopped before the target and thus selective deflection of the low frequency pulse components onto the collimator can be performed. This is also confirmed when looking at figure 4.49b showing the TOF spectrum at the position of the collimator (detector 5.1 in figure 4.45). The corresponding detector monitors neutrons primarily emerging from the collimator plates. In the corresponding TOF spectrum, the neutron pulse which is attributed to the low frequency proton pulse component gets shorter when the kicker magnet is switched on. This indicates that the neutron source is closer to the detector or that the thermal moderator is less extended in this scenario. Both indications suggest that the proton beam is deposited closer to the ^{3}He detector and thus deflected.

Table 4.13.: Integrated count rate of neutrons at the ^{3}He detector at the extraction channel of the polyethylene moderator (detector 5.2 in figure 4.45) from figure 4.49a. The integration intervals are 0 ms to 2 ms and 40 ms to 42 ms for the $T = 80$ ms and the $T = 6$ s component.

T/s	Counts/s kicker magnet off	Counts/s kicker magnet on
80×10^{-3}	133.1(5)	132.0(5)
6	2.02(6)	0.71(3)

In summary, the proton beam current measurement with the collimator and the Ta target beam cup, the proton beam profile measurement with the MWPC as well as the neutron TOF measurement with the ^{3}He detectors show that the generation of multiplexed proton beams and the selective deflection of specific proton pulses is feasible at JULIC. This can be realized by synchronizing the kicker magnet via a pulse generator to the chopper of JULIC. However, the measurement setup should be further optimized to study the performance limit of the multiplexer test setup systematically. For this, the injection process in the cyclotron should be optimized to obtain sharp proton pulses with beam intensity rise times which are well below 10 ms as it is observed in figure 4.47. Furthermore, the experiment should be repeated with the kicker magnet with insets. This increases the deflection angle and thus the whole beam can be deposited on the collimator plates. Finally, the setup should be operated with the performant power supply, which allows larger repetition rates. With this possible effects from the deflection of the low frequency proton pulse component onto the high frequency proton pulse component can be identified more easily.

5. Integration of the multiplexer system into the HBS framework

This chapter presents the layout of the multiplexer system at HBS based on the developments reported in the previous chapter for a multiplexer system at JULIC. The key component of the multiplexer system is the Three-Field Septum Magnet (TFSM). For application with 70 MeV protons at HBS, the magnet needs to be scaled to a larger magnetic rigidity which is $(B\rho)_{70\,\mathrm{MeV}} = 1.23\,\mathrm{T\,m}$ and thus 26 % larger than $(B\rho)_{45\,\mathrm{MeV}} = 0.98\,\mathrm{T\,m}$ for 45 MeV at JULIC. For this reason, the design of a HBS TFSM is presented in the following. The magnet design benefits from the scalability of the Three-Field Septum Magnet (TFSM) at JULIC. The other magnets employed in the multiplexer design are standard electromagnetic accelerator magnets and can be scaled easily. The HBS multiplexer system represents a central part of the HBS facility distributing the individual proton pulse components to the different target stations (figure 3.1). Thus, it needs to be integrated into the HBS High-Energy Beam Transport (HEBT) section which manages the proton transport from the accelerator to the target. Therefore, the top-level design of the HEBT, including the multiplexer section, is presented and corresponding beam dynamics calculations in terms of linear beam transport and particle tracking have been carried out. Finally, the radiation hardness of the multiplexer system is evaluated concentrating on the TFSM at HBS.

5.1. Layout

The layout of the HBS multiplexer system is based on the conceptual design presented in figure 4.1. The design parameters are given in table 4.1. In contrast to the multiplexer system which is employed at JULIC, the HBS multiplexer system will feature additional bending magnets in the outer beamlines as well as quadrupole magnets. This allows to increase the separation of the three different beamlines which emerge from the multiplexer system to 62° while maintaining achromatic beam optics in the arcs. This is important for the HBS facility as the larger angular separation of the beamlines provides more space for the individual target stations (figure 3.1).

Figure 5.1 presents the layout of the HBS multiplexer system. The system's kicker-septum magnet combination is arranged with 1150 mm distance (yoke-to-yoke) and provides 300 mrad deflection angle after the septum magnet which is divided between 48 mrad from the kicker and 252 mrad from the septum magnet. With this and equation 4.17, the beam spot separation at the front face of the septum magnet is

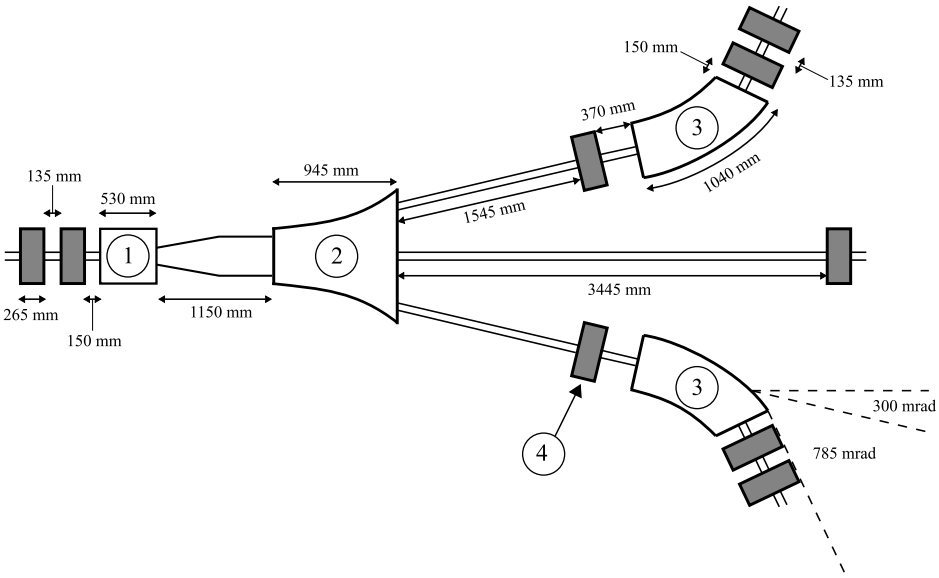

Figure 5.1.: Layout of the HBS multiplexer system. The layout is based on the concept presented in figure 4.1. 1: Kicker magnet, 2: HBS Three-Field Septum Magnet (TFSM), 3: 45° sector bending magnets, 4: Quadrupole magnets (all in gray). The total angular separation of the outer beamlines with respect to the centered beamline amounts for 1.085 rad, i.e. 62°.

68 mm taking into account an effective length of the kicker magnet of l_{eff} = 600 mm and a yoke length of 530 mm. The septum magnet is designed to have an effective length of l_{eff} = 1000 mm and a yoke length of 945 mm. The length increase of the HBS TFSM with respect to the one at JULIC allows a slightly weaker dipole field in the outer field regions such that the coexistence of the three different field regions relaxes. In the arcs of the multiplexer system, a quadrupole magnet between the septum and the 45° bending magnet is used in order to provide dispersion-free optics, i.e. $\sigma_{16} = \sigma_{26} = 0$ in equation 2.20 after the multiplexer system[1]. Two quadrupole magnets in front of the multiplexer system and at the end of the arcs, respectively, are used to control the beam size.

5.2. HBS Three-Field Septum Magnet (HBS TFSM)

The design procedure of the HBS Three-Field Septum Magnet (TFSM) follows closely the strategy for the JULIC septum which is presented in detail in section 4.4. Here, the knowledge gained throughout the design process of the JULIC septum magnet

[1]This holds only for $\sigma_{16} = \sigma_{26} = 0$ prior to the multiplexer system

can be used which eases the construction of the HBS septum significantly.

The design goals of the HBS TFSM can be derived primarily from the layout of the multiplexer system given in figure 5.1. The yoke length is chosen to be 945 mm with an envisaged effective length of 1000 mm. The deflection angle which has to be provided by the magnet amounts for 252 mrad while the beam spot separation at the front face of the magnet needs to be 68 mm. The planned beam size is 24 mm (4 rms beam widths). From the findings during the developments at JULIC in section 4.4, the HBS TFSM is constructed yielding the design which is shown in figure 5.2. The HBS septum magnet consists of 15 layers with 63 mm thickness each. The gap height of the magnet is 52 mm thus offering a safety margin for the 24 mm beam. This is important when considering the large beam power of 300 kW (section 3.1) at HBS. The actual beam is of elliptical shape with an extent of 24 mm in the vertical and 8 mm in the horizontal plane. Thus, the assumption of a circular beam with 24 mm diameter is conservative. From the construction of the prototype Three-Field Magnet (TFM) presented in section 4.5, it is known that the simulated magnetic field can be reproduced very accurately by the manufacturer (see figure 4.43). Thus, the HBS TFSM is constructed to fit an integrated field of 306.5 mT m precisely without the necessity to consider potential manufacturing uncertainties. Obtaining $\int B_y \mathrm{d}l = 306.5\,\mathrm{mT\,m}$ in the outer field regions as shown in figure 5.3 gives a deflection angle of $\alpha = \arcsin\left(\int B_y \mathrm{d}l/(B\rho)\right) = 252\,\mathrm{mrad}$. The field homogeneity in the outer field regions of the HBS TFSM according to equation 4.30 is 0.2 %. In the centered zero field region, a maximum deviation of the integrated magnetic field of 2 mT m from zero is observed. Both evaluations cover 8 mm beam size (4 rms beam widths) which is extracted from figure 5.7.

A particle tracking study similar to figure 4.35 is shown in figure 5.4 to prove the successful adaption of the aperture dimensions of the HBS septum magnet to the beam trajectories. In addition, the horizontal phase space distribution of the left beam in figure 4.35a at $\Delta z = -150\,\mathrm{mm}$ in front of the septum magnet and at $\Delta z = 150\,\mathrm{mm}$ after the septum magnet is shown in figure 5.4b and figure 5.4c, respectively. This demonstrates that the total deflection angle behind the septum magnet amounts for 300 mrad when setting the kicker magnet in figure 5.1 to 48 mrad such that the left outer dipole field region of the HBS septum magnet is operated.

Figure 5.5 shows the results of the harmonic content in the hard-edge approximation of the HBS TFSM similar to figure 4.33. The corresponding results are used for the particle tracking studies of the HBS HEBT which are presented in the following section. The field quality of the HBS septum magnet is slightly better than for the JULIC septum magnet which can be evaluated by considering the $2n$-pole magnetic field gradients (equation D.2), which take into account the different reference radii. A summary of the $2n$-pole magnetic field gradients is given in table D.1. The improved field quality of the HBS septum magnet with respect to the JULIC septum magnet can be attributed to the smaller dipole field strength in the outer field regions, the

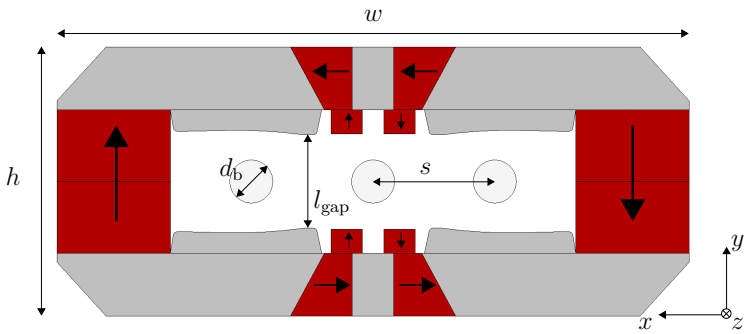

(a)

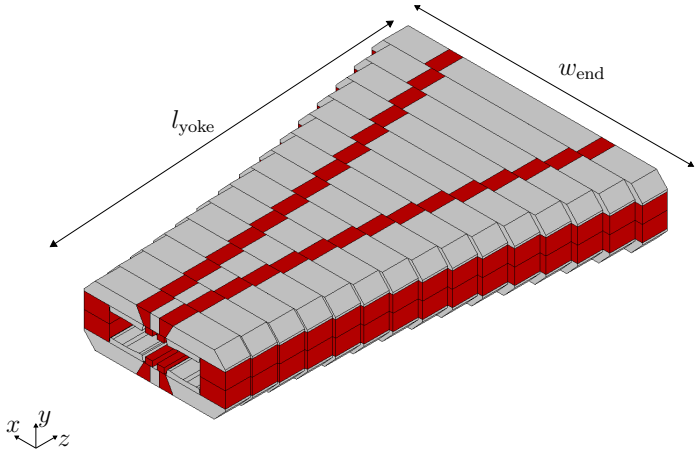

(b)

Figure 5.2.: (a): Technical layout of the HBS septum magnet front face based on the concept shown in figure 4.23. The width of the front face is w = 353 mm and the height h amounts for 150 mm. The gap height is l_{gap} = 52 mm. The planned beam diameter d_b is 24 mm with a beam spot separation of s = 68 mm. The red parts indicate SmCo magnets with B_r = 1.1 T, the gray parts show the magnet yoke. The magnetization of the permanent magnets is indicated with arrows. (b): 3D drawing of the HBS septum magnet with yoke length l_{yoke} = 945 mm and maximum width at the end of w_{end} = 676 mm. The HBS septum is segmented into 15 layers with a length of 63 mm each.

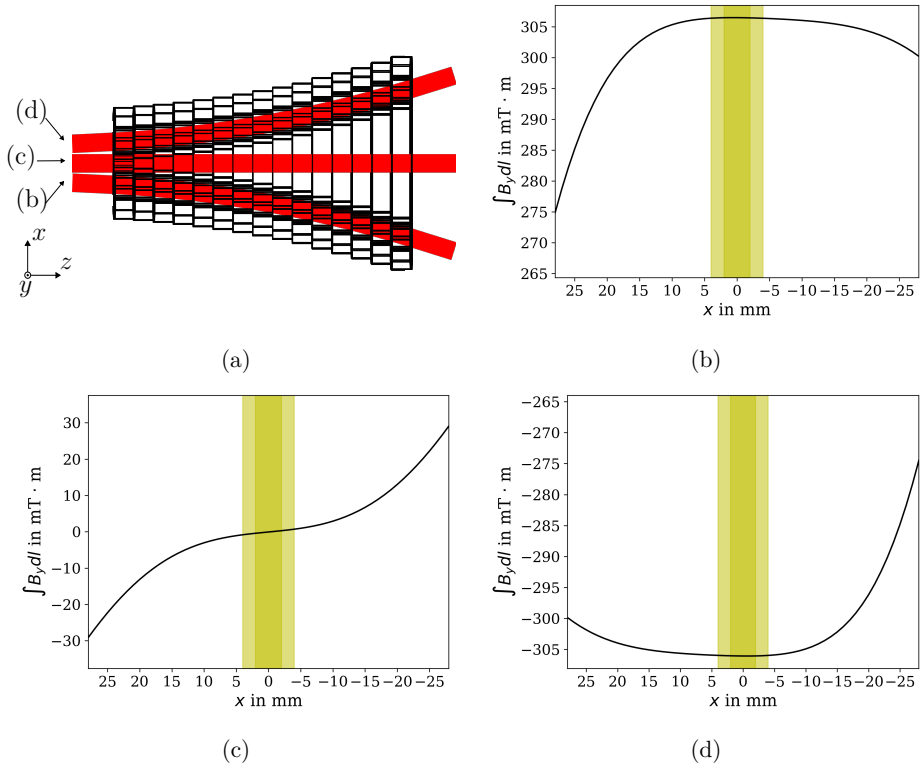

Figure 5.3.: (a): Integration planes for the calculation of the horizontal distribution of the integrated magnetic field of the HBS septum magnet shown in figure 5.2. The integration planes follow the expected beam trajectories. The integration limits are set from $z = -672\,\text{mm}$ to $z = 672\,\text{mm}$ ($z = 0$ in the center of the magnet). (b)-(d): Integrated vertical magnetic field $\int B_y \mathrm{d}l$ versus deviation along x from the center of the path following the different planes as indicated in (a). In each integration plane a horizontally centered co-moving cartesian coordinate system is used. The extent of the proton beam is indicated by the yellow shaded area (dark yellow: 2 rms beam widths, light yellow: 4 rms beam widths).

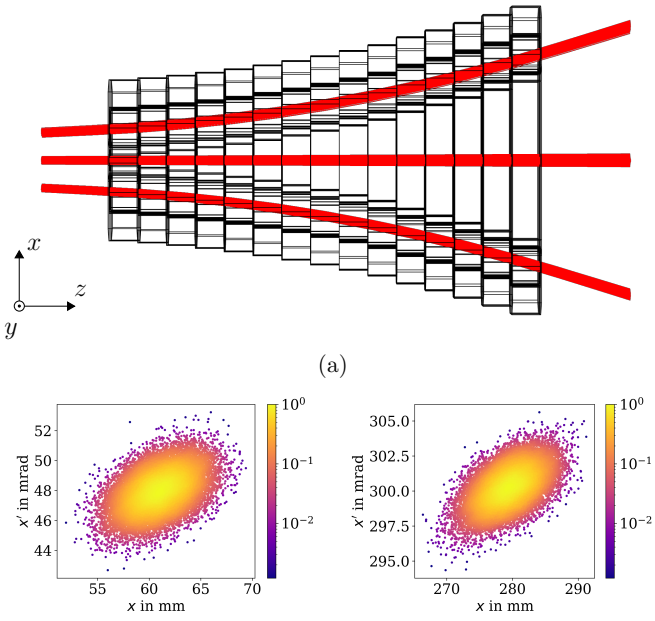

Figure 5.4.: (a): Particle tracking of 70 MeV protons through the HBS septum magnet for different settings of the corresponding kicker magnet with each setting serving a different field region of the septum magnet. The simulated transmission through all three field regions is 100 %. (b) and (c): Horizontal phase space distribution of the left ($x > 0$) beam in (a) at $\Delta z = -150$ mm in front of the septum magnet (b) and $\Delta z = 150$ mm after the septum magnet (c), respectively. The plots show a normalized particle density distribution.

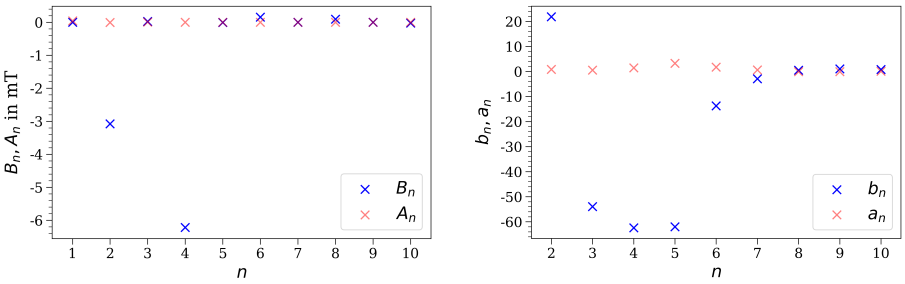

(a) (b)

Figure 5.5.: (a) Harmonic content of zero field region of HBS septum, i.e. at $x = 0$. (b) Harmonic content of the right dipole field region of the HBS septum magnet. Here, the multipole coefficients are normalized to the main dipole component B_1 and multiplied by 1×10^4 according to equation 4.33. Both (a) and (b) are evaluated on a reference radius $r_0 = 17\,\text{mm}$ in the hard-edge approximation.

larger horizontal separation of the different field regions at the front face of the septum magnet and a larger width of the pole pieces.

5.3. HBS High Energy Beam Transport (HBS HEBT)

5.3.1. Beam dynamics of HBS HEBT

The HBS High-Energy Beam Transport (HEBT) is a proton transport beamline connecting the linear accelerator and the individual target stations at HBS which is indicated in figure 3.1. It comprises the multiplexer system which is part of the design of the HEBT. The beam parameters which are considered for the HEBT, i.e. the parameters obtained at the end of the linac, are summarized in table 5.1.

The dimensions of the HEBT are fixed by the floor plan of HBS and the corresponding building geometry. With this, the top-level design of the HEBT results in the layout given in figure 5.6. Figure 5.6a shows the HEBT beamline of HBS which goes straight through the multiplexer system and supplies the 384 Hz target station in figure 3.1. The structure of the beamline can be segmented into different sections. The first section of the beamline is used as an achromatic elevator into the top floor where the multiplexer system is located. The elevator consists of two double bend achromats based on 45° sector bending magnets with five quadrupoles each. Each achromat performs a point-to-point imaging of the beam. In the top floor, the beam is then transferred to the second section of the straight HEBT beamline. Here, a quadrupole triplet with four quadrupoles is used to position the multiplexer in some

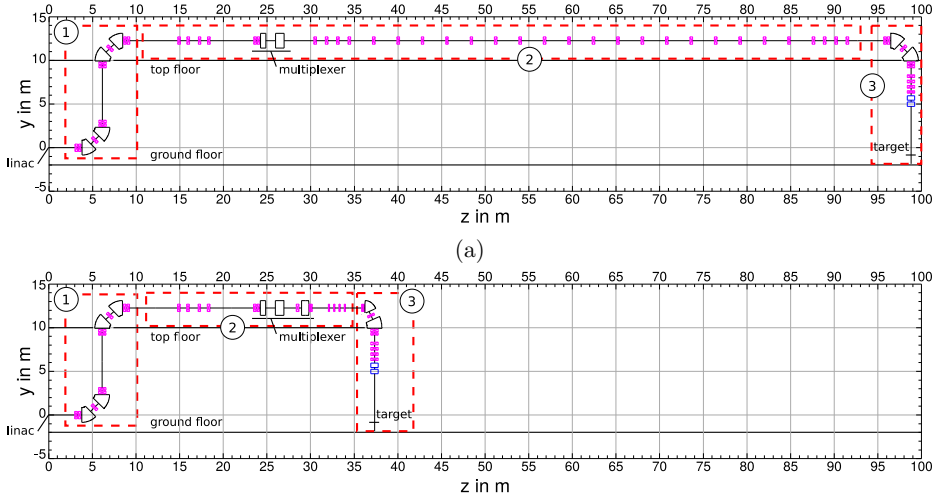

(a)

(b)

Figure 5.6.: Side view (yz-plane, x into the image plane) of the top-level design of the HBS High-Energy Beam Transport (HEBT) beamline. A list with all elements and positions is given in appendix E. (a): Straight HEBT beamline. The drawing shows the three different sections and the respective quadrupole (pink), dipole (black), kicker (black) and beam scanner (blue) magnet positions. The multiplexer is located in the second section as indicated. The target is positioned 1.35 m above the ground floor. (b): Left HEBT beamline projected on the yz-plane. The first section and the first six quadrupoles of the second section are shared with the straight HEBT beamline and the third section is identical. In the second section, the beam passes the left arc of the multiplexer system (shown in detail in figure 5.1).

Table 5.1.: Summary of the beam parameters at the end of the linac at HBS for the design of the HBS High-Energy Beam Transport (HEBT).

Name	Value
Beam kinetic energy T/MeV	70
Beam current I/mA	100
Particle	Proton
Magnetic rigidity $(B\rho)$/T m	1.23
Norm. rms emittance $\epsilon_{\mathrm{n,rms}}$/mm mrad	1
Rms emittance ϵ_{rms}/mm mrad	2.54
Twiss parameter $\beta_{0,x(y)}$/m	1.1
Twiss parameter $\alpha_{0,x(y)}$	0
Momentum uncertainty δ/%	0.5

distance to the elevator in combination with a point-to-point imaging. Then, the multiplexer section is foreseen with the geometry presented in figure 5.1. Here, the straight beamline sees only the first two quadrupoles of the multiplexer and the zero field region of the septum magnet. After the multiplexer, a matching section consisting of four quadrupoles is used in order to deal with parasitic defocusing from the HBS TFSM zero field region and in order to match the beam into a FODO (focusing-drift-defocusing-drift) structure for a long straight beam transport section. The cell length of the FODO structure is 5.6 m. Finally four quadrupoles are used to match the beam from the FODO structure into an achromat which bends the beam down to the target. The achromat is part of the third section of the HEBT and has the same geometry as the elevator achromats in the first section. Before the target, four quadrupoles are installed which allow corrections to the focusing of the beam if necessary. A vertical and a horizontal beam scanner magnet are used to distribute the beam over the target. The HEBT beamline which is going through the left arc of the multiplexer is shown in figure 5.6b (The right HEBT beamline follows the same concept). All three beamlines of the HEBT share the elevator in the first section, the quadrupole triplet of the second section and the first two quadrupoles of the multiplexer setup. Furthermore, the third section is identical. Thus, differences of the left (right) HEBT beamline with respect to the straight beamline manifest throughout the multiplexer and before the third section. This can be seen in figure 5.6b where the outer beamline of the multiplexer and a subsequent matching section are implemented. As the left (and right) HEBT beamline is shorter than the straight beamline, a FODO structure is not required.

The results of beam dynamics calculations corresponding to the beamline layouts presented in figure 5.6 are shown in figure 5.7. A linear beam transport calculation with the *Bmad* library [49] has been carried out yielding the horizontal[2] and

[2]Note that in the following the horizontal coordinate x and vertical coordinate y refer to the

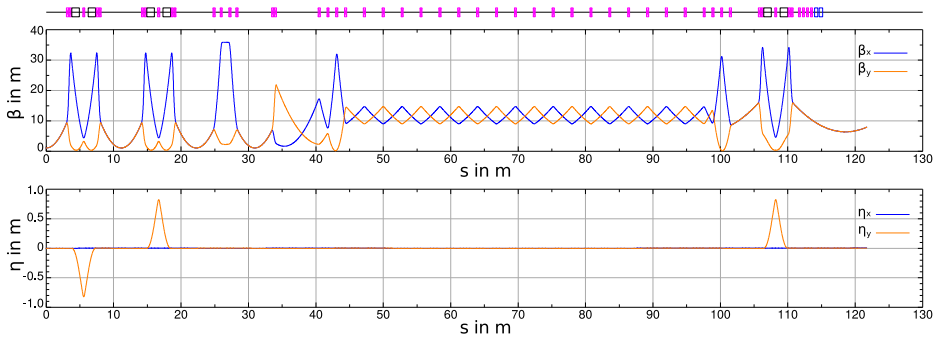

(a)

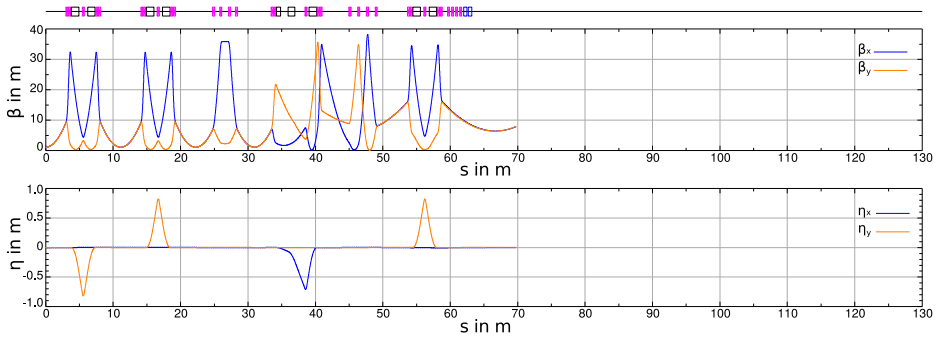

(b)

Figure 5.7.: Results from linear beam transport calculations with the *Bmad* library [49]. (a): Horizontal and vertical Beta function $\beta_{x(y)}(s)$ and dispersion function $\eta_{x(y)}(s)$ with respect to longitudinal position s along the straight HEBT beamline (presented in figure 5.6a). (b): Corresponding results for the left HEBT beamline (presented in figure 5.6b).

vertical betatron $\beta_{x(y)}$ (equation 2.15) and dispersion function $\eta_{x(y)}$ (equation 2.19). Note, the aperture of the HEBT beamline has been chosen to be 60 mm. Considering 6 rms beam widths as total beam size, one gets a maximum rms beam width of $\sigma_{x(y)} \leq 10\,\text{mm}$. The rms beam width relates to the betatron function and dispersion via equation 4.13. The geometry of the individual sections of the HEBT and the quadrupole strengths have been iterated to fit the beam size to the aperture ($\sigma_{x(y)} \leq 10\,\text{mm}$), i.e. $\beta_{x(y)} \leq 40\,\text{m}$ in the absence of dispersion ($\eta_{x(y)} = 0$) and $\beta_{x(y)} \leq 30\,\text{m}$ for the maximum dispersion of $\eta_{x(y),\text{max}} = 0.8\,\text{m}$ in the arcs. From the results in figure 5.7, one can deduce that the HEBT lattice enables achromatic beam transport, visible through the cancellation of the dispersion function after each bend-

co-moving coordinate system of the beam (figure 2.1).

ing section, with sufficiently small beam size. The beam diameter on the target is set to 30 mm. The beam is then distributed on the target with beam scanners as presented in figure 5.11.

In order to evaluate the performance of the HEBT beamline under more realistic conditions, a particle tracking study is performed using the *TraceWin* code [54]. Here, space-charge-induced defocusing can be considered. Furthermore, the harmonic content of all magnets employed in the HEBT beamline can be implemented representing a measure for the field quality of the magnets (see section 2.2.3). This is especially interesting for the results in figure 5.5 from the HBS TFSM as one can evaluate directly if the corresponding field quality is sufficient for the HBS facility. Note that in figure 5.5b the harmonic content of the right field region of the septum magnet is calculated. In order to implement the harmonic content of the HBS septum into the left HEBT beamline, the odd multipole components ($b_3, b_5, ...$) in figure 5.5b need to change sign. For all quadrupole magnets employed in the HEBT, the harmonic content is approximated by the measured harmonic content of the quadrupoles at COSY [55] since these possess comparable dimensions. For the dipole magnets, no comparable design is found. Therefore all harmonics allowed in the dipole magnet ($n = 3, 5, 7, 9, ...$) are approximated to be $b_n \approx 1 \times 10^{-4}$ (normalized to the dipole component). All others are set to $b_n \approx 1 \times 10^{-5}$. A corresponding reference radius of 35 mm representing half of the gap height of the dipole magnets is assumed. The results of the particle tracking studies for the straight and for the left HEBT beamline are summarized in figure 5.8 and figure 5.9, respectively.

Figure 5.8 shows the transversal phase-space distributions at the beginning and at the end of the straight HEBT beamline for different scenarios, i.e. no space charge, with space charge and with space charge and non-zero higher-order multipole components. The beam size at the target is consistent with what is observed from linear beam transport in figure 5.7a, i.e. 30 mm beam diameter (6 rms beam widths). The emittance growth is less than 8 %, whereas only 2 % of this can be attributed to the introduction of non-zero multipole components, which suggests that the field quality of the HBS septum magnet is sufficient for the implementation at the HBS facility. Furthermore, figure 5.8 shows the (x, δ) and (y, δ) subspaces, i.e. the horizontal and vertical position of the particles versus their respective momentum uncertainty, respectively. Here, an uncorrelated distribution is observed throughout all scenarios which shows that the achromatic feature of the straight HEBT beamline is preserved. Similar observations can be made for the left beamline, which are shown in figure 5.9, with a maximum emittance growth of 7 % (0.5 % from the non-zero multipole components only). For the left HEBT beamline, some correlation of the distribution in the $(x(y), \delta)$ subspaces can be observed, which are probably due to dispersion mixing between the horizontal and vertical plane as some finite but small dispersion is still present after the different achromats. For both the left and the straight HEBT beamline, the (y, y') phase space distributions at the target position show some non-linear signature when considering the multipole components of the magnets. Here, the shape

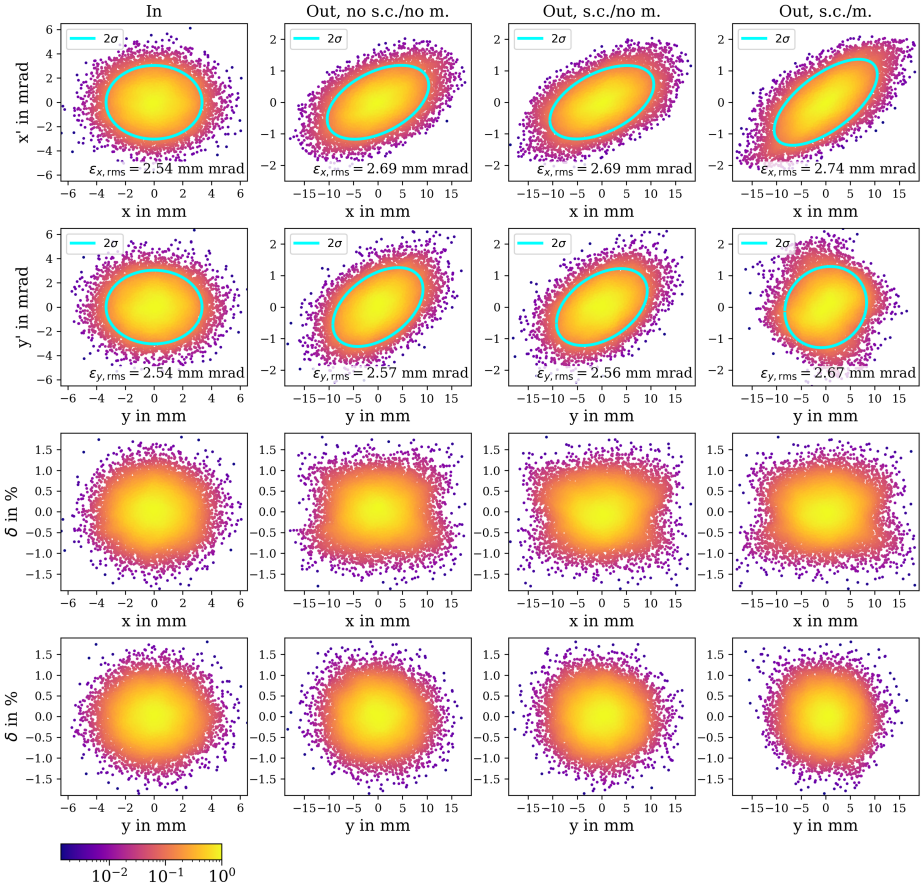

Figure 5.8.: Particle tracking results from *TraceWin* calculations [54] for the straight HEBT beamline. The corresponding lattice from linear beam transport in figure 5.7a is implemented and the phase space distribution at the target is investigated for different scenarios. The rows show the (x, x'), (y, y'), (x, δ) and (y, δ) phase spaces. For (x, x') and (y, y'), the 2σ phase ellipse (surrounding 86.5 % of the particles) and the rms emittance are shown. The columns show the corresponding phase spaces at the beginning (In), i.e. at the end of the linac at HBS, and at the target. The phase spaces at the target are calculated without space charge and multipole contributions (Out, no s.c./no m.), with space charge and without multipole contributions (Out, s.c./no m.) and with both effects (Out, s.c./m.), respectively. The plots show a normalized particle density distribution.

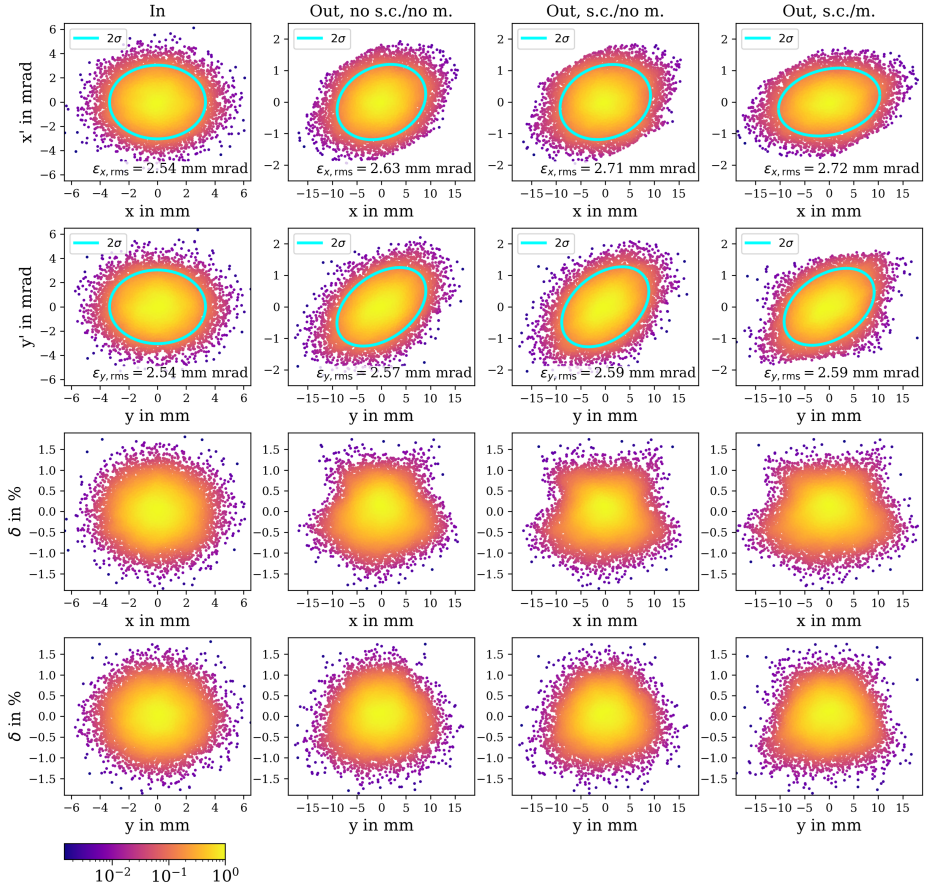

Figure 5.9.: Particle tracking results from *TraceWin* calculations [54] for the left HEBT beamline. The corresponding lattice from linear beam transport in figure 5.7b is implemented and the phase space distribution at the target is investigated for different scenarios. The rows show the (x, x'), (y, y'), (x, δ) and (y, δ) phase spaces. For (x, x') and (y, y'), the 2σ phase ellipse (surrounding 86.5 % of the particles) and the rms emittance are shown. The columns show the corresponding phase spaces at the beginning (In), i.e. at the end of the linac at HBS, and at the target. The phase spaces at the target are calculated without space charge and multipole contributions (Out, no s.c./no m.), with space charge and without multipole contributions (Out, s.c./no m.) and with both effects (Out, s.c./m.), respectively. The plots show a normalized particle density distribution.

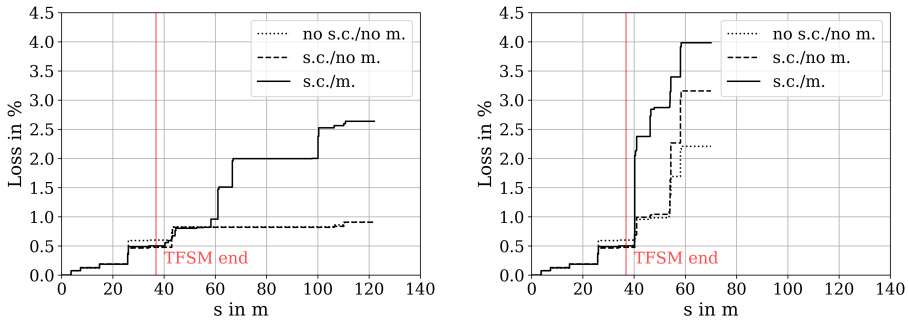

Figure 5.10.: Accumulated beam loss in the centered and left HEBT beamline corresponding to the particle tracking studies shown in figure 5.8 and figure 5.9, respectively. The beam loss is calculated without space charge and higher-order multipole components (no sc., no m.), with space charge only (sc., no m.) and with both effects (sc.,m.). The aperture throughout the HEBT beamline is 60 mm. The position of the end of the TFSM is indicated by a red line, i.e. 39.6 m. (a): Accumulated beam loss in the straight HEBT beamline. (b): Accumulated beam loss in the left HEBT beamline.

of the phase space distribution deviates slightly from an ellipse. This observation can be traced back to the higher-order multipole components in the HBS septum magnet. The effect is more dominant in the vertical phase space as the vertical beam size at the beginning of the septum magnet in figure 5.7a and figure 5.7b is larger than the horizontal beam size.

The accumulated beam loss from the linac to the target, which corresponds to the particle tracking studies for the straight HEBT beamline (figure 5.7a) and the left HEBT beamline (figure 5.7b), is shown in figure 5.10. Here, a maximum beam loss of 2.6 % and 4 % is observed for the straight and for the left HEBT beamline, respectively. Both beamlines show identical losses prior to the TFSM, where both beamlines share the same elements. Thereafter, the change of the beam loss differs, where for both beamlines the addition of non-zero multipole components in the septum magent seems to increase the beam loss. For the left beamline however, there is still some more general optimization required as the beam loss without space charge and without multipole components (no s.c./no m.) itself is already larger than the corresponding loss for the straight beamline. For optimization of the beamlines concentrating on the compensation of higher-order multipole components from the HBS septum magnet, non-linear magnets, e.g. sextupole and octupole magnets, and collimators can be used. Using these, the transmission should be improved within

future optimizations to obtain an average beam loss throughout the HEBT beamline which is less than $1\,\mathrm{W\,m^{-1}}$ [5]. So far, an average beam loss in terms of power of $38\,\mathrm{W\,m^{-1}}$ is obtained before the TFSM. For the straight beamline after the TFSM, one gets $22\,\mathrm{W\,m^{-1}}$, whereas the left and right beamline yield $115\,\mathrm{W\,m^{-1}}$ each. For the calculations an average beam power of 300 kW and 100 kW is considered before and after the TFSM, respectively. Note that a straightforward approach to reducing the average beam loss by the use of a 100 mm aperture diameter throughout the HEBT (instead of 60 mm) as well as a scraper in the beginning of the HEBT, which limits the beam size to 6 sigma, yields an average beam loss below $1\,\mathrm{W\,m^{-1}}$ in all beam lines.

At the end of the HBS HEBT beamline the beam is distributed in all three beamlines by a set of scanner magnets. The scanner magnets perform horizontal and vertical deflection of the beam separately. The horizontal scanner magnet is positioned 7.3 m in front of the target. The vertical scanner magnet is positioned 6.6 m in front of the target. Both magnets are planned to have a length of 0.5 m. The proton beam scanning technique is explained in the following.

5.3.2. Proton beam raster scanning

In order to achieve a homogeneous proton beam intensity distribution on the target, beam scanner magnets are employed at HBS. As presented in figure 5.6, a set of two beam scanner magnets is positioned in the end of the straight as well as the left and right HEBT beamline to perform horizontal and vertical deflection of the beam separately. The beam scanning strategy is similar to the one applied at ESS [56]. The goal is to distribute the beam power over a large fraction of the target area (12 cm × 12 cm according to figure 3.6) within the time interval of one proton pulse and to obtain a maximum average power density of $1\,\mathrm{kW\,cm^{-2}}$, which is design goal of the HBS target [5]. For this, the two scanner magnets are powered individually with a triangular current waveform generating a corresponding triangular beam deflection which results in a Lissajous-like beam raster pattern on the target. The triangle as waveform has the advantage that the scanning velocity is constant and thus no lingering at the edges of the target occurs. To ensure a closed beam raster pattern over the extent of the target within one proton pulse, the repetition rates of the triangular beam deflection in the horizontal (f_x) as well as the vertical (f_y) plane need to be integer multiples of the inverse proton pulse length t_p, i.e.

$$\begin{aligned} f_x &= n_x \cdot 1/t_p \\ f_y &= n_y \cdot 1/t_p \end{aligned} \tag{5.1}$$

with $n_x, n_y = \{2n+1, n \in \mathbb{N}\}$ being coprime integers such that a complex crosshatch pattern is generated. The larger (n_x, n_y), the finer the mesh. However, a large (n_x, n_y) requires a more demanding performance of the beam scanner magnets since the operation frequency increases. For the very short proton pulse lengths at HBS, i.e. 52 µs in figure 3.4 with a duty cycle of 2 % or even 37 µs if the duty cycle is reduced to 1.4 %

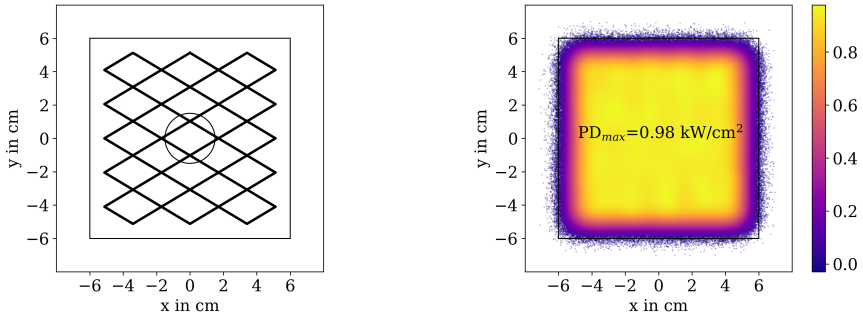

(a) (b)

Figure 5.11.: (a): Beam centroid position following a crosshatch pattern which is generated with a horizontal and a vertical beam scanner magnet driven by a triangle current waveform with the frequencies following equation 5.1 with $(n_x, n_y) = (5, 3)$ and a $\phi_y = -\pi/2$ phase shift. The beam size (30 mm) is indicated by a centered circle. (b): Average power density distribution on the target obtained from the beam raster scan pattern in (a) with the proton beam duty cycle being adapted such that 100 kW beam power is deposited on the target. The 12 cm × 12 cm target area is indicated by a rectangle. The maximum power density is 0.98 kW cm^{-2} with a fraction of 0.4 % of the beam power being outside the target area.

in order to operate at 70 MeV and 100 mA, (n_x, n_y) should be as small as possible and as large as necessary. As the beam raster pattern is convoluted with the proton beam size, a less dense mesh can be accepted when obtaining a larger beam size. However, distributing a larger beam spot over the target increases the fraction of particles impinging outside of the dedicated target area. Thus, one needs to iterate to a compromise between the smallest possible (n_x, n_y) and the beam size while envisaging a maximum average power density of 1 kW cm^{-2} on the target. At HBS, this results in a proton beam diameter of 30 mm (6 rms beam widths, as presented in figure 5.8 and figure 5.9) and $(n_x, n_y) = (5, 3)$. The corresponding crosshatch pattern is presented in figure 5.11a. Such a pattern can be generated for an arbitrary proton pulse length when obeying equation 5.1 with $(n_x, n_y) = (5, 3)$ and a $\phi_y = -\pi/2$ phase shift for the vertical triangular beam deflection. From figure 5.11, one can see that such a setting allows to operate the HBS target with a homogeneous beam power distribution and a maximum average power density which is below 1 kW cm^{-2}. The homogeneity of the beam power on the target can be represented by the average power density and the associated standard deviation. For the 12 cm × 12 cm target area in figure 5.11, the average power density amounts to 0.7(3) kW cm^{-2}. The homogeneity improves strongly when considering a slightly smaller fraction of the target, such that one obtains an average power density of 0.9(1) kW cm^{-2} for a central 10 cm x 10 cm area on the target.

The operation frequencies of the beam scanner magnets need to be adjusted to fulfill equation 5.1 with $(n_x, n_y) = (5, 3)$ such that one obtains a maximum operation frequency of the horizontal scanner magnet of up to 136 kHz when considering the shortest 37 µs proton pulses which corresponds to a proton pulse frequency of 384 Hz and a duty cycle of 1.4 %. The maximum operation frequency of the vertical beam scanner magnet is 81 kHz. The nominal deflection of the beam scanner magnets in figure 5.11b is chosen to be 51.25 mm which, together with the minimum distance from scanner magnet to target of 6.6 m (vertical scanner), results in a deflection angle of 8 mrad. Thus, an integrated magnetic field of 10 mT m needs to be provided by the magnets for 70 MeV protons. To ensure low Eddy current losses and a high frequency response, the beam scanner magnets should employ a NiZn ferrite yoke with high resistivity and narrow BH-loop such as CMD5005 from *Ceramic Magnetics* [57] which can be operated at up to 100 MHz. A similar magnet design can be found at ESS for the corresponding beam scanner magnets being operated with a triangular waveform with up to 40 kHz generating an integrated field of 5 mT m [56].

5.4. Evaluation of radiation hardness

The permanent magnet technology of the TFSM (figure 5.2) represents a possibly vulnerable part of the multiplexer system at HBS when considering radiation-induced damages. Radiation-induced demagnetization of permanent magnets is a phenomenon often observed in permanent magnet based accelerator magnets due to their exposure to a radiation environment containing e.g. protons, neutrons, gammas and electrons [58, 59]. The mechanism which drives the radiation-induced magnetic flux loss in permanent magnets is thought to be based on the generation of thermal spikes [60]. A thermal spike is generated by an incoming radiation particle which transfers a part of its energy to a primary knock-on atom after an collision. The thermal spike transfers the energy of the collision to the lattice structure of the magnet material. The area affected by the thermal spike may then undergo a domain reversal causing a loss of magnetization of the sample [61]. Neutrons and protons, interacting directly with the atoms of the permanent magnet material, represent the most critical type of radiation when considering the radiation hardness of permanent magnets.

The radiation hardness of permanent magnets not only depends on the radiation intensity but also on the material. In the work of T. Bizen et al. [62], the authors report that the radiation-induced demagnetization decreases with larger coercivity while in the work of R. D. Brown and J. R. Cost [63] it is reported that the geometry of the magnet significantly influences the demagnetization during irradiation with neutrons. In the latter, it is observed that a large length-to-diameter ratio L/D (with the magnetization along the symmetry axis of a cylinder) results in a larger radiation hardness. This can be explained by the geometry-dependent working point of permanent magnets. Increasing the length (along the magnetization axis) of a permanent

magnet at constant diameter or cross section, increases the permeance coefficient in equation 2.56. With this, the working point is shifted to a lower demagnetization field $-H$ and thus the loss of remanent magnetic flux density with temperature is smaller which is shown in figure 2.15. Concerning rare-earth permanent magnets as employed at the HBS septum, SmCo magnets exhibit a superior radiation resistance when compared to NdFeB permanent magnets [59]. The smaller radiation hardness of NdFeB magnets can properly be attributed to the boron which is used in these magnets as this has a large probability for thermal neutron capture and a low mass, which leads to a high energy primary knock-on atom. For the HBS (and JULIC) TFSM, the above findings are taken into account such that the permanent magnet material of choice is Sm_2Co_{17} with a coercivity of $H_c \geq 1990\,\mathrm{kA\,m^{-1}}$ and a remanent flux density of $B_r = 1.1\,\mathrm{T}$ (YXG-32H from *Bakker Magnetics* [64]) or $H_c \geq 1750\,\mathrm{kA\,m^{-1}}$, $B_r = 1.15\,\mathrm{T}$ (VACOMAX 262 HR from *Vacuumschmelze* [65]) depending on the manufacturer. The length-to-diameter ratio L/D of the left and right main magnets, which are most likely to be exposed to the proton beam, in figure 5.2 and figure 4.27 can be approximated to be 1.27 and 1.05 for HBS and JULIC, respectively.

In order to estimate the lifetime of the septum magnet at the HBS facility, experimental results from radiation-induced demagnetization measurements are scaled conservatively to the radiation environment expected during regular operation of HBS in the following. Here, the focus is on the radiation-induced damages from protons and neutrons as these are superior compared to electrons and photons [59]. During regular operation of the HBS facility, the beam loss is expected to be below $1\,\mathrm{W\,m^{-1}}$. This value is extracted from similar facilities [66] as corresponding simulations at HBS require a detailed material composition of each accelerator component which is not available from the conceptual design of HBS. In the work of E. Mauro et al. [66], it is shown that the $1\,\mathrm{W\,m^{-1}}$ beam loss can be represented by localized hot spots with 10 W beam loss every 10 m. As a conservative approach, such a hot spot is positioned in the centre of the septum magnet. Assuming that the protons emerging from that hot spot are completely deposited in the permanent magnet material with a total inner[3] cross section area of $2550\,\mathrm{cm^2}$, one gets a proton current density of approximately $5.6 \times 10^{-5}\,\mu\mathrm{A\,cm^{-2}}$ at the permanent magnets. In the work of E. W. Blackmore et al. [67], $1.6\,\mathrm{cm^2}$ Sm_2Co_{17} (2.5 cm thickness) magnet samples have been irradiated with 500 MeV protons at an integrated proton current of up to $12\,\mu\mathrm{A\,h}$. A linear radiation-induced demagnetization with respect to the integrated proton current is observed with a slope of $-0.02\,\%/(\mu\mathrm{A\,h})$, i.e. $-0.032\,\%/(\mu\mathrm{A\,h\,cm^{-2}})$. With an expected current density at the magnets of $5.6\times10^{-5}\,\mu\mathrm{A\,cm^{-2}}$ for the HBS septum, the demagnetization per year of HBS operation can be calculated being $-0.01\,\%$. Here, 5000 h operation of HBS per year are considered [5]. This lies within the uncertainties of the remanent flux given by the manufacturer particularly as the proton energy at HBS is much lower. Considering neutron induced demagnetization of Sm_2Co_{17},

[3] The area of the permanent magnets in the septum magnet which points into the direction of the proton beam, i.e. to the air gap of the magnet.

C. H. Chen et al. [60] showed that no magnetic flux loss of the magnets occurred when irradiated with neutrons at fluences up to $2.1 \times 10^{13}\,\mathrm{cm}^{-2}$. The magnet samples employed have a similar length-to-diameter ratio, i.e. $L/D = 1.25$, as for the HBS septum. Furthermore, R. Hardekopf [68] observed no flux loss of Sm_2Co_{17} up to neutron fluences of $\approx 1 \times 10^{20}\,\mathrm{cm}^{-2}$. In order to approximate the neutron fluence emerging from beam loss during regular operation at HBS, radiation protection studies at comparable facilities such as LINAC4 at CERN, i.e. 160 MeV protons at 40 mA, are considered [69]. The total neutron fluence per primary proton can be extracted by integrating the neutron fluence spectrum in [69] calculated for the highest proton energy of 160 MeV and generated from the accelerating structures. This yields a neutron fluence of $\approx 9 \times 10^{-3}\,\mathrm{cm}^{-2}$ per proton. Assuming that the 10 W beam loss, i.e. $9 \times 10^{11}\,\mathrm{s}^{-1}$ protons at HBS, inside the septum magnet contribute completely to the generation of neutrons, one gets a neutron flux of $8.1 \times 10^{9}\,\mathrm{cm}^{-2}\,\mathrm{s}^{-1}$. This gives a neutron fluence of $1.5 \times 10^{17}\,\mathrm{cm}^{-2}$ per year and thus there would be no observable magnetic flux loss in the permanent magnets of the HBS septum magnet after several hundred years of operation according the findings of R. Hardekopf [68].

Considerations of proton and neutron induced radiation damages based on beam loss studies at comparable facilities and measurements of the radiation-induced magnetic flux loss in Sm_2Co_{17} magnets show that the HBS TFSM can be employed at the HBS facility without considerable demagnetization of the permanent magnets. Even though a conservative analysis of the radiation hardness of the HBS septum magnet has been performed, more detailed studies of the beam loss and associated neutron fluence spectra should be performed based on the exact environment of the HBS facility in terms of FLUKA simulations [70]. Furthermore, it should be noted that the radiation hardness of the HBS septum magnet is evaluated for regular HBS operation. In the case of failures, where the proton beam accidentally hits parts of the beamline directly, a beam mitigation device has to be used which triggers a fast shut down of the proton beam. For this, beam loss monitors should be installed directly in front and behind the septum magnet. A spare septum magnet should be available anytime in the rare case of unforeseeable scenarios leading to unexpected magnetic flux loss.

6. Neutron yield measurement

In this chapter[1], the experimental determination of the total neutron yield, i.e. taking into account all the reaction channels that generate neutrons, for 22, 27, 33, 42 MeV protons on beryllium (Be), vanadium (V) and tantalum (Ta) targets is presented. For this purpose, a novel method for the experimental determination of the neutron yield via measurement of the 2.2 MeV prompt gamma-ray of hydrogen induced by thermal neutron capture in a polyethylene moderator is introduced. Furthermore, simulations of the experiment with MNCP [11] and the ENDF/B-VII.1 database [33] are performed in order to apply corrections to the measurements and to access the proton-induced neutron yield, i.e. considering only neutrons generated through the (p,n) reaction channel. The experimental results are compared with the results obtained from the corresponding numerical simulations as well as from analytical calculations [8] allowing to benchmark the simulations. This supports target material selection and estimation of the efficiency at future low-energy accelerator-driven neutron sources.

6.1. Experimental setup

The experimental setup for the determination of the neutron yield has been installed at the NESP experimental area of the JULIC accelerator (figure 3.7). For the experiment, H^- ions with 45 MeV are extracted from JULIC and subsequently decelerated and stripped to 22, 27, 33 and 42 MeV protons with a moveable graphite degrader which is positioned just behind the cyclotron as shown in figure 3.7.

[1] This chapter comprises parts of an associated publication [12]. Many authors contributed to the publication and the individual contributions are specified in the following (according to `https://www.elsevier.com/authors/policies-and-guidelines/credit-author-statement`): **Marius Rimmler:** Writing - original draft, Formal analysis, Data curation, Visualization, Investigation. **Johannes Baggemann:** Investigation. **Sarah Böhm:** Formal analysis. **Paul-Emmanuel Doege:** Investigation. **Olaf Felden:** Resources, Supervision. **Nils-Oliver Fröhlich:** Resources. **Ralf Gebel:** Resources, Funding acquisition. **Jiatong Li:** Formal analysis. **Jingjing Li:** Writing - review & editing, Investigation. **Eric Mauerhofer:** Writing - review & editing, Conceptualization, Investigation, Supervision. **Ulrich Rücker:** Methodology, Supervision. **Mathias Strothmann:** Investigation. **Yury Valdau:** Resources. **Paul Zakalek:** Writing - review & editing, Data curation, Methodology, Investigation. **Thomas Gutberlet:** Writing - review & editing, Supervision. **Thomas Brückel:** Project administration, Funding acquisition.

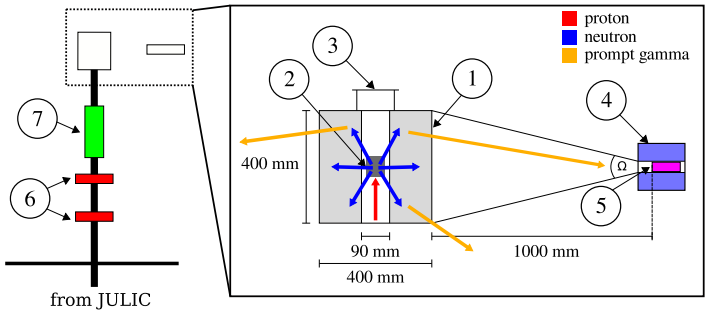

Figure 6.1.: Sketch of the experiment for the determination of the neutron yield via prompt gamma spectroscopy being positioned in the NESP experimental area of JULIC shown in figure 3.7. The zoom shows the experimental setup with 1: Polyethylene moderator cylinder with 400 mm length, 400 mm outer diameter and 90 mm inner diameter, 2: Target holder with targets as listed in table 6.5 with electronic connection to a picoammeter, 3: Kapton vacuum window , 4: Lead collimator cylinder with copper inner layer, 5: HPGe-detector. The HPGe-detector and the lead collimator are positioned such that a solid angle Ω includes the whole polyethylene moderator cylinder, 6: Quadrupole doublet, 7: Set of non-destructive beam diagnostics. Taken and adapted from [12].

Layout

The experiment is installed downstream of a quadrupole doublet and a set of non-destructive beam diagnostics, including a beam position monitor (BPM) and a fast current transformer (FCT) [71] as shown in figure 6.1. Here, the proton beamline is connected to the experimental setup for neutron yield determination consisting of a hollow polyethylene moderator cylinder, which surrounds the exchangeable targets. The setup includes a FARRADAY cup type current measurement connected to the targets and a gamma spectroscopy system. In figure 6.1, exchangeable Be, V or Ta targets are irradiated with protons. The Be target is a cylinder with a radius of 35 mm and a thickness of 100 mm. Here, the thickness exceeds the stopping range of the protons by several tens of mm. The V and Ta targets are disks with a radius of 40 mm. The corresponding thicknesses range between 2.56 mm to 4.54 mm for V and between 1.6 mm to 3 mm for Ta in order to account for the increasing stopping range of protons with an energy of 22 MeV to 42 MeV, respectively. The target thicknesses are chosen such that the proton beam is just stopped completely inside the target. The targets are placed in the center of a 400 mm long hollow polyethylene cylinder with a wall thickness of 155 mm acting as neutron moderator and as neutron monitor. The proton beam current on the target is measured by maintaining an electrical connection from the target to a calibrated current amplifier (Keithley 18000-20, calibration in appendix F). Upstream of the target, the proton beam passes a set

of non-destructive diagnostics, which allows to perform beam current measurements without a target and thus without the connected FARADAY cup type current measurement. This is used to extrapolate the target proton beam current during background measurements when no target is installed. A thin Kapton foil exit window behind the polyethylene moderator is installed to bring the setup under vacuum. The exit window allows to perform background measurements with minimal influence from the passing proton beam.

To determine the total neutron yield in equation 6.2, a gamma-ray spectrometer is employed to measure count rate of the 2.2 MeV prompt gamma line of hydrogen induced by thermal neutron capture in the polyethylene moderator. The gamma-ray spectrometer consists of a high-purity germanium (HPGe) coaxial detector (Canberra GR1020 with relative efficiency of 10 %, energy resolution of 2.2 keV at 1.32 MeV for 6 µs shaping time), which is shielded by a cylindrical lead collimator with an opening diameter of 125 mm and a wall thickness of 80 mm. The gamma-ray spectrometer is aligned orthogonal to the flight direction of the protons pointing onto the target position. The distance between the collimated HPGe-detector and the outer surface of the polyethylene moderator is 1 m such that the whole volume of the moderator is seen by the detector.

Proton beam profile

The background in the gamma-ray spectrum containing gammas generated through other structures than the target, which are unintentionally irradiated by the proton beam, should be reduced as much as possible. For this, the quadrupole doublet in figure 6.1 is used to focus the proton beam onto the targets inside the polyethylene moderator. This is especially important for measurements at low proton energies where the neutron yield is expected to be small. The quadrupole magnet settings are iterated by monitoring the proton beam profile at the exact position of the targets prior to the measurements of the neutron yield at each proton energy. For the measurement of the beam profile an in-house developed multi wire proportional chamber (MWPC) is used. The MWPC measures the beam intensity by 64 wires along the horizontal axis and 64 wires along the vertical axis. The wires are separated by 1 mm. The beam profile measurements are shown in figure 6.2. It can be seen that the beam is focused such that most of its intensity is deposited on the targets with radius $r = 35$ mm for Be and $r = 40$ mm for V and Ta. Note that for 42 MeV, the beam has a small horizontal offset. However, due to the small beam size at this energy, one irradiates almost exclusively the targets. The beam size in full width at half maximum (FWHM) corresponding to the measurements in figure 6.2 is summarized in table 6.1. With this, the background of the prompt gamma line of hydrogen, which is measured in the absence of a target in the polyethylene moderator in figure 6.1, is reduced to less than 1 % with respect to the recorded intensity during measurements with target (see table 6.5).

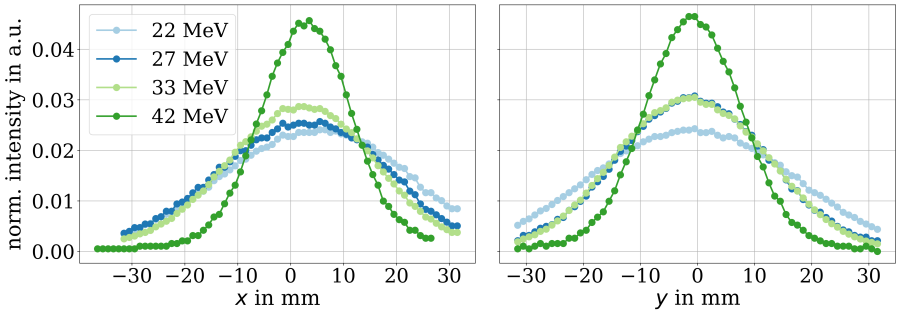

Figure 6.2.: Horizontally (left) and vertically (right) projected beam profile measured with a MWPC at the exact position of the targets prior to the neutron yield measurement for the different energies. Taken and adapted from supplementary material of [12].

Table 6.1.: Summary of the beam size in FWHM corresponding to the measurement with MWPC in figure 6.2. The minimum target diameter is 70 mm. Taken from supplementary material of [12].

Energy (MeV)	x_{FWHM} (mm)	y_{FWHM} (mm)
22	43	42
27	39	31
33	34	31
40	21	20

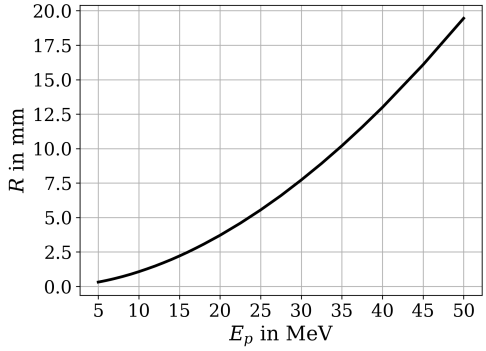

Figure 6.3.: Stopping range R versus proton energy E_p in PMMA. Simulated with the SRIM toolkit [39]. Taken and adapted from supplementary material of [12].

Table 6.2.: Measured stopping range in PMMA cube R and associated proton energies E_p according to figure 6.3. Taken from supplementary material of [12].

R (mm)	E_p (MeV)
4.3(2)	22(1)
6.2(2)	27(1)
9.4(2)	33(1)
13.9(2)	42(1)

Proton energy determination

As shown in figure 2.19, the neutron yield obtained from a specific target material strongly depends on the energy of the primary proton. It is therefore important to have good knowledge of the proton energy employed for the neutron yield measurement to properly benchmark the corresponding simulations. For this reason, the proton energy is characterized experimentally with two independent methods.

First, the energy of the proton beam is determined for the different settings of the graphite degrader at JULIC by measuring the stopping range of the beam in a PMMA cube via a GAFchromic film as described in [72]. The relation of the stopping range in PMMA to the energy of the proton beam is calculated with the SRIM toolkit [39] and displayed in figure 6.3. With figure 6.3 the measured stopping range can be associated with a proton energy as shown in table 6.2. The uncertainty of the determined energy value comes from the alignment of the GAFchromic film with the

Table 6.3.: $(B\rho)$-values and associated proton energies (equation 2.40) calculated according to equation 6.1 with $N = 264$, $l_{\mathrm{eff}} = 965.4\,\mathrm{mm}$, $l_{\mathrm{gap}} = 60.35\,\mathrm{mm}$ and $\alpha = 38.25°$ of the first dipole in the beamline from JULIC to NESP (figure 3.7).

I (A)	$(B\rho)$ (Tm)	E_{p} (MeV)
86.25	0.69	22.3
93.96	0.75	26.4
103.95	0.83	32.2
115.77	0.92	39.8

PMMA cube, which is estimated to be not better than 0.2 mm.

Another method for determination of the proton energy uses the energy-dependent strength of the first dipole in the beamline from JULIC to NESP (figure 3.7). This allows to crosscheck the energies derived in table 6.2. With equation 2.41 and the deflection angle $\alpha = 38.25°$ of the first dipole magnet being fixed by the geometry of the beamline, the required maximum field in the dipole magnet B_{max} scales with the magnetic rigidity $(B\rho)$ of the protons. Thus, according to equation 2.48, the dipole current I, which is required to obtain the appropriate deflection angle, scales linearly with $(B\rho)$. Therefore $(B\rho)$, and thus also the proton energy, can be deduced from the dipole current I with

$$(B\rho) = \frac{\mu_0 N l_{\mathrm{eff}}}{l_{\mathrm{gap}}\alpha} I \tag{6.1}$$

with N being the Ampere turns, l_{eff} the effective length and l_{gap} the gap height of the magnet. The corresponding results including the proton energy (from equation 2.40) are summarized in The results obtained from the evaluation of the dipole settings in table 6.3 and the results obtained from the measurement of the stopping range in a PMMA cube in table 6.2 agree within the uncertainties. Since the measurement with the PMMA cube represents a direct approach to extract the proton energy and the evaluation of the dipole settings works only with certain approximations, e.g. neglection of hysteresis in the iron of the dipole magnet, the results in table 6.2 are considered for the determination of the neutron yield.

6.2. Method

The target total neutron yield Y ($\mathrm{s^{-1}\ mA^{-1}}$) is determined from the measured count rate of the 2.2 MeV prompt gamma line of hydrogen induced by thermal neutron capture in the polyethylene moderator and using an AmBe source of well-known

neutron emission for calibration as follows:

$$Y = \left[\frac{Z_{\text{target}}}{I_{\text{target}}} - \frac{Z_{\text{no target}}}{I_{\text{no target}}} \right] \cdot \frac{N_{\text{AmBe}}}{Z_{\text{AmBe}}} \cdot \frac{f_{\text{AmBe}}}{f_{\text{target}}} \cdot \frac{g_{\text{AmBe}}}{g_{\text{target}}}, \tag{6.2}$$

with Z (s^{-1}) being the count rate of the 2.2 MeV gamma line, I (mA) the average proton beam current measured on the target or extrapolated from the non-destructive current measurement in the case of the measurements without target and $N_{\text{AmBe}} = 2.59 \times 10^4\,s^{-1}$ being the neutron emission of the AmBe source (Amersham Buchler, $N_{\text{AmBe}} = 2.8 \times 10^4\,s^{-1}$ at 10 mCi in 1970, $T_{1/2} = 433\,y$). f is a correction factor for neutrons leaving the system and not contributing to the production of 2.2 MeV photons which is given by

$$f = 1 - n_{\text{escape}}, \tag{6.3}$$

where n_{escape} is the fraction of neutrons escaping the polyethylene moderator. In equation 6.2, g is a correction factor related to the geometrical efficiency for the detection of 2.2 MeV photons which is expressed by

$$g = \frac{p}{f}, \tag{6.4}$$

where p is the total number of 2.2 MeV photons emitted from the polyethylene moderator towards the HPGe-detector normalized to the fraction of absorbed neutrons with the target or AmBe source f. Therefore, $p_{\text{AmBe}}/p_{\text{target}}$ represents the overall correction of the experiment in terms of efficiency when comparing the measurements with target and with AmBe calibration source in equation 6.2. Note that the correction is applied as ratio of correction factors for the target and for the AmBe measurements, such that it does not need to be considered that not all neutrons absorbed in the polyethylene moderator contribute to the production of 2.2 MeV photons.

The measured values of the count rate Z and of the current I, are given in table 6.5 and discussed in the following. The values of n_{escape} and p are estimated numerically and summarized in table 6.4.

Gamma spectra analysis

Each gamma-ray spectrum is recorded for 1 to 2 hours (real time) and analysed with Gamma-W software [73]. To obtain a live time of the detector of around 75 % of the real time or larger, the proton beam intensity is adjusted accordingly. As an example the prompt gamma-ray spectra recorded during irradiation with 42 MeV protons with and without Be target are shown in figure 6.4. The identified isotopes are given on the spectra. The spectrum recorded with the Be target is dominated by the prompt gamma line of hydrogen (H-1) in figure 6.4c. The prompt gamma lines of carbon (C-12) induced by thermal neutron capture and by inelastic scattering of fast neutrons in the polyethylene moderator are also observed (figure 6.4d). The remaining gamma

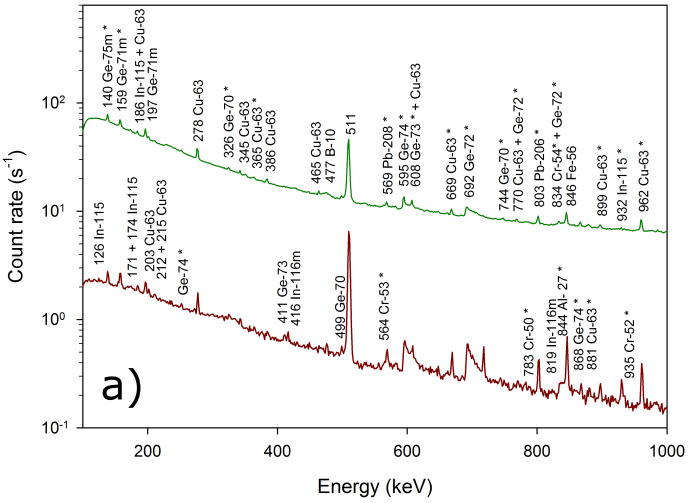
Count rate (s^{-1})
Energy (keV)
a)
140 Ge-75m *
159 Ge-71m *
186 In-115 + Cu-63
197 Ge-71m
278 Cu-63
326 Ge-70 *
345 Cu-63 *
365 Cu-63 *
386 Cu-63
465 Cu-63
477 B-10
511
569 Pb-208 *
595 Ge-74 *
608 Ge-73 * + Cu-63
669 Cu-63 *
692 Ge-72 *
744 Ge-70 *
770 Cu-63 + Ge-72 *
803 Pb-206 *
834 Cr-54* + Ge-72 *
846 Fe-56
899 Cu-63 *
932 In-115 *
962 Cu-63 *
126 In-115
171 + 174 In-115
203 Cu-63
212 + 215 Cu-63
Ge-74 *
411 Ge-73
416 In-116m
499 Ge-70
564 Cr-53 *
783 Cr-50 *
819 In-116m
844 Al- 27 *
868 Ge-74 *
881 Cu-63 *
935 Cr-52 *

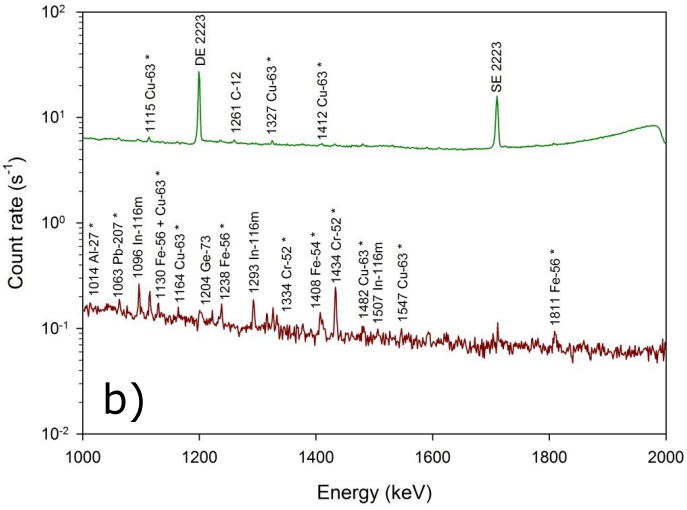
Count rate (s^{-1})
Energy (keV)
b)
1115 Cu-63 *
DE 2223
1261 C-12
1327 Cu-63 *
1412 Cu-63 *
SE 2223
1014 Al-27 *
1063 Pb-207 *
1096 In-116m
1130 Fe-56 + Cu-63 *
1164 Cu-63 *
1204 Ge-73
1238 Fe-56 *
1293 In-116m
1334 Cr-52 *
1408 Fe-54 *
1434 Cr-52 *
1482 Cu-63 *
1507 In-116m
1547 Cu-63 *
1811 Fe-56 *

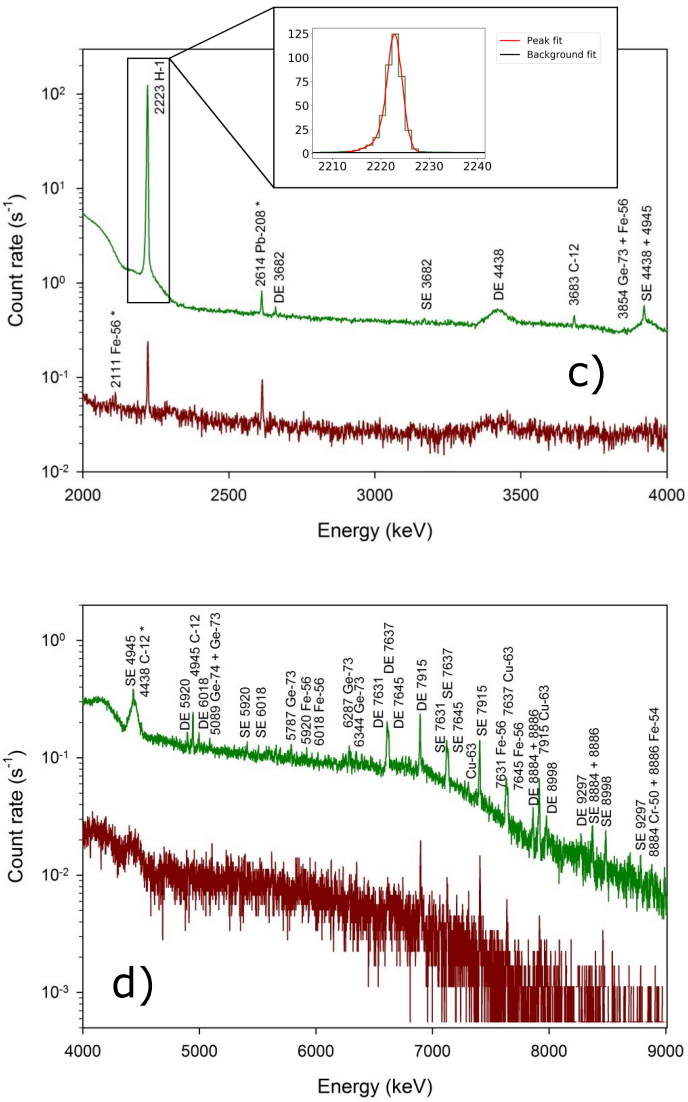

Figure 6.4.: Prompt gamma-ray spectra in the energy range a) 100 – 1.000 keV, b) 1.000 - 2.000 keV, c) 2.000 - 4.000 keV and d) 4.000 - 9.000 keV recorded with (green) and without Be target (red) for an irradiation with 42 MeV protons. The gamma lines labeled with an asterisk are induced by inelastic scattering of fast neutrons, the other being issued from neutron capture. The prompt gamma line of hydrogen (H-1) at 2.2 MeV is highlighted by the inset showing the fitted data. The live time of the measurement is 2834 s (3600 s real time) and 1780 s (1800 s real time) with and without Be target, respectively. Taken and adapted from [12].

lines are induced by interaction of slow and fast neutrons escaping the moderator with the HPGe-detector (Ge, In), the collimator shielding (Pb, Cu) and surrounding structural materials (Al, Fe, Cr). The same gamma lines with lower count rates are also observed in the spectrum recorded without the Be target, i.e. the corresponding background measurement yielding $Z_{\text{no target}}$ in equation 6.2. The spectra recorded for all targets at various proton energies show the same gamma-ray signature with the exception of some target-specific characteristics such as gamma lines for inelastic neutron scattering of fast neutrons from V in the case of the V target which do not influence the determination of the neutron yield.

Target current analysis

The average proton beam current on the target directly influences the measured neutron yield in equation 6.2 and it therefore needs to be analysed precisely. The target beam current is measured with a current amplifier and ranges on average between 0.1 nA and 2 nA as presented in table 6.5. It is adjusted such that the live time of the HPGe-detector is not below 75 %. The current amplifier is calibrated with an external picoampere source and the offset during the experiment is measured in between the measurements with different targets as explained in the appendix (appendix F). In order to extrapolate the beam current on the target for the background measurements where no target is installed in the polyethylene moderator, i.e. $I_{\text{no target}}$ in equation 6.2, the BPM (beam position monitor) signal recorded upstream of the experimental setup shown in figure 6.1 is used. The sum of the voltage signal induced at the four capacitive pick-up plates of the BPM $U_{\text{BPM}} = U_{\text{left}} + U_{\text{right}} + U_{\text{top}} + U_{\text{bottom}}$ scales with the proton beam current [74]. It is used to evaluate the ratio $\bar{I}_{\text{target}}/\bar{U}_{\text{BPM,target}}$ separately for all different proton beam energies. Here, $\bar{I}_{\text{target}}$ is the target proton beam current and $\bar{U}_{\text{BPM,target}}$ the BPM signal averaged at fixed proton energy for all target materials. With this $I_{\text{no target}}$ is extrapolated for each proton beam energy following

$$I_{\text{no target}} = U_{\text{BPM,no target}} \cdot \frac{\bar{I}_{\text{target}}}{\bar{U}_{\text{BPM,target}}}. \tag{6.5}$$

Since the recording of the gamma-ray spectra and the proton beam current measurement are not synchronized, the measured average proton beam current additionally has to be scaled in order to consider the dead time of the HPGe-detector. This is done with

$$I = I_{\text{raw}} \cdot \frac{t_{\text{LT}}}{t_{\text{RT}}} \tag{6.6}$$

with t_{LT} being the live time and t_{RT} the real time of the HPGe-detector. I_{raw} is the average proton beam current directly extracted from the current amplifier.

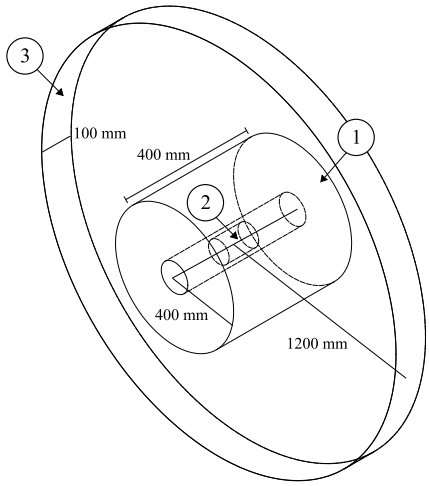

Figure 6.5.: Layout of the simulation geometry. 1: Polyethylene moderator cylinder, 2: Target, 3: Gamma detector band with 1200 mm radius from the target center and 100 mm width. Taken from [12].

6.3. Simulation of experiment

6.3.1. Simulation setup

The simulation of the experiment is carried out with the Monte-Carlo N-Particle Transport Code (MCNP) [11]. The corresponding cross section data is based on the Evaluated Nuclear Data File database (ENDF/B-VII.1) [33]. The geometry of the simulation environment is identical to the experimental setup as shown in figure 6.1 except that the HPGe-detector is replaced by a spherical detector band with the radius being the distance from the target center to the HPGe-detector, i.e. 1200 mm, and with a width being similar to the HPGe-detector entrance width, i.e. 100 mm. This allows one to speed up the computation time by taking advantage of the cylindrical symmetry of the setup. Figure 6.5 shows the geometry of the simulation. All simulations with targets are carried out with a primary proton beam with 1×10^7 protons (except for 42 MeV protons on Be, where the number of protons is limited by MCNP to 1.7×10^5 resulting into a larger statistical error) while simulations with the AmBe calibration source are performed with a virtual neutron source and 1×10^7 neutrons distributed through a neutron spectrum deduced from the specifications of the AmBe source [75]. The target thickness and diameter in the simulation geometry is adapted according to the experiment and identical to the ones in table 6.5.

The relevant simulation output for the different target and energy combinations is summarized in table 6.4. Here, the total neutron yield Y, the neutron yield from the (p,n)-reactions $Y_{(p,n)}$, the neutron yield from (n,2n)-reactions $Y_{(n,2n)}$ and the average neutron energy $\bar{E}_n$ are extracted from a sphere surrounding only the target without

Table 6.4.: Summary of MCNP simulation results with Y being the total neutron yield and $Y_{(p,n)}$ being the proton-induced neutron yield. $Y_{(n,2n)}$ amounts for the neutron yield of (n,2n) reactions. $\bar{E}_n$ is the average neutron energy. n_{escape} represents the fraction of neutrons escaping the polyethylene moderator, p gives the total number of 2.2 MeV photons detected on the cylindrical detector band normalized to the generated neutrons and g gives a correction factor related to the detection efficiency of 2.2 MeV photons. Taken from [12].

Target	Y (s^{-1} mA^{-1})	$Y_{(p,n)}$ (s^{-1} mA^{-1})	$Y_{(n,2n)}$ (s^{-1} mA^{-1})	$\bar{E}_n$ (MeV)	n_{escape}	p	g
22 MeV							
Be	1.251(3)E+14	1.107(3)E+14	1.44(1)E+13	4.00(6)	0.304(1)	1.38(3)E-02	1.99(4)E-02
V	0.599(2)E+14	0.599(2)E+14	7(2)E+10	1.73(4)	0.245(2)	1.50(4)E-02	1.99(5)E-02
Ta	0.494(2)E+14	0.493(2)E+14	1.8(3)E+10	1.26(3)	0.213(2)	1.49(4)E-02	1.89(6)E-02
27 MeV							
Be	1.771(3)E+14	1.555(3)E+14	2.16(1)E+13	4.86(9)	0.326(1)	1.32(2)E-02	1.96(3)E-02
V	0.914(2)E+14	0.914(2)E+14	2.5(4)E+10	2.08(6)	0.262(2)	1.45(3)E-02	1.96(4)E-02
Ta	0.931(2)E+14	0.931(2)E+14	6.4(6)E+10	1.46(5)	0.223(1)	1.50(3)E-02	1.93(4)E-02
33 MeV							
Be	2.490(4)E+14	2.184(4)E+14	3.06(1)E+13	6.1(1)	0.354(1)	1.24(2)E-02	1.91(3)E-02
V	1.400(3)E+14	1.399(3)E+14	9.4(8)E+10	2.5(1)	0.281(1)	1.44(3)E-02	2.01(4)E-02
Ta	1.669(3)E+14	1.668(3)E+14	1.7(1)E+11	1.67(9)	0.233(1)	1.44(2)E-02	1.88(3)E-02
42 MeV							
Be	3.74(4)E+14	3.27(4)E+14	4.7(1)E+13	7.8(2)	0.402(7)	1.2(2)E-02	2.0(3)E-02
V	2.328(4)E+14	2.325(4)E+14	2.7(1)E+11	3.1(2)	0.305(1)	1.36(2)E-02	1.96(3)E-02
Ta	3.143(4)E+14	3.137(4)E+14	6.5(2)E+11	2.0(1)	0.245(1)	1.44(2)E-02	1.91(2)E-02
AmBe	-	-		5(3)	0.3702(2)	1.280(4)E-02	2.030(6)E-02

polyethylene moderator in figure 6.5. n_{escape} is defined as the number of neutrons escaping from the complete system, i.e. neutrons passing through a sphere surrounding target and moderator, normalized to the total number of neutrons generated from the target. The gamma correction factor g (equation 6.4) is derived from the photons at 2.2 MeV energy detected on the spherical detector band in figure 6.5 normalized to the fraction of neutrons f (equation 6.3), which are absorbed by the polyethylene.

It should be mentioned that Y represents the total neutron yield, i.e. taking into account all reaction channels that generate neutrons in the experimental setup. Y depends strongly on the geometry of the setup including the target as well as the moderator. In order to be more independent from the experimental setup, it is useful to consider additionally the proton-induced neutron yield, i.e. taking into account neutrons only generated from the (p,n) reaction channel. To access the proton-induced neutron yield, one has to subtract the contribution of all other reaction channels to the neutron production from the neutron yield Y. Consulting the ENDF/B-VII.1 [33] database, it turns out that the (n,2n) reaction channel is the most dominant of these

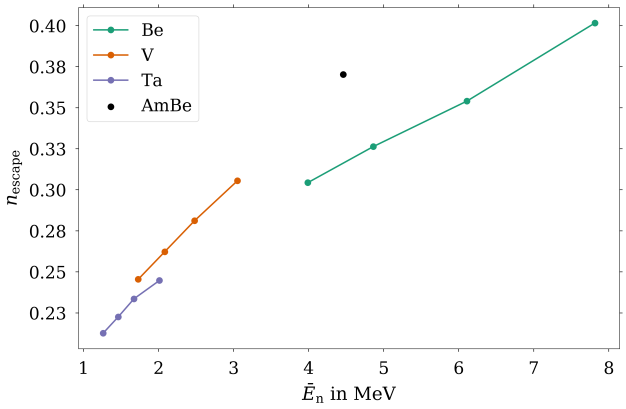

Figure 6.6.: Simulated neutron escape ratio n_{escape} versus simulated average neutron energy $\bar{E}_{\mathrm{n}}$ of neutrons emerging from the targets and the AmBe calibration source. A line is drawn to guide the eye for each target material. All data taken from table 6.4. Taken and adapted from [12].

reaction channels whereas other reaction channels are negligible. Therefore

$$\mathrm{Y}_{(\mathrm{p,n})} = \mathrm{Y} - \mathrm{Y}_{(\mathrm{n,2n})} \tag{6.7}$$

approximates the proton-induced neutron yield with $\mathrm{Y}_{(\mathrm{n,2n})}$ being the neutron yield of (n,2n) reactions.

6.3.2. Simulation results

Concerning the results from the MCNP simulation, one starts with focusing on the correction factors, which are applied to determine the total neutron yield by means of equation 6.2. The correction factor f in equation 6.3 which takes into account the neutron escape ratio n_{escape} appears to have the greatest influence as n_{escape} differs strongly for the different target and energy compositions with respect to the simulation with AmBe (see table 6.4). The neutron escape ratio can be associated with the neutron energy, assuming that neutrons emitted from the target with higher energy have a lower probability to be absorbed in the polyethylene moderator, thus escaping from the moderator without generating 2.2 MeV photons. However, for all targets and for the AmBe calibration source, n_{escape} cannot solely be related to the neutron energy. The proton-energy-dependent angular distribution of the neutron emission additionally influences n_{escape} due to the geometric anisotropy of the cylindrical moderator. From figure 6.6 showing n_{escape} versus $\bar{E}_{\mathrm{n}}$, one can conclude that the neutron escape ratio nonetheless scales approximately linearly with the average energy of the neutrons produced by the target. The average neutron energy itself scales with the

proton energy (see table 6.4) and depends on the atomic number of the target. Here, the average neutron energy is determined from the neutron spectrum of a bare target.

In summary, all simulated n_{escape} in table 6.4, except for Be at 42 MeV proton energy, are smaller than n_{escape} for the AmBe calibration source and therefore the correction $f_{\mathrm{AmBe}}/f_{\mathrm{target}}$ primarily lowers the measured yield. Applying n_{escape} via equation 6.3 as a correction factor to the calculated total neutron yield introduces a systematic uncertainty based on the database (ENDF/B-VII.1) [33] employed in the simulations. The plausibility of the simulated n_{escape} for all targets is given by the linear behavior between the measured photon yield of the gammas induced by interaction of slow and fast neutrons escaping the moderator with the HPGe-detector collimator $\mathrm{PY}_{\mathrm{collimator}}$ with respect to the simulated yield of escaping neutrons. $\mathrm{PY}_{\mathrm{collimator}}$ is determined by the gamma count rate of the 278 keV, 962 keV and 2614 keV gamma lines in figure 6.4a and figure 6.4c which are induced by the interaction of slow and fast neutrons with Cu and fast neutrons with Pb, respectively. All materials are employed in the collimator of the HPGe-detector. $\mathrm{PY}_{\mathrm{collimator}}$ is defined as

$$\mathrm{PY}_{\mathrm{collimator}} = \frac{Z_{278\,\mathrm{keV}} + Z_{962\,\mathrm{keV}} + Z_{2614\,\mathrm{keV}}}{I} \tag{6.8}$$

with Z being the gamma count rate of the respective gamma lines and I being the average proton beam current. Note that for the background measurements, i.e. without target, the gamma count rates are negligibly small. With equation 6.8, $\mathrm{PY}_{\mathrm{collimator}}$ monitors neutrons escaping the polyethylene moderator. Hence, it is expected that $\mathrm{PY}_{\mathrm{collimator}}$ scales linearly with the neutron yield of neutrons escaping the polyethylene moderator

$$\mathrm{Y}_{\mathrm{escape}} = \mathrm{Y} \cdot n_{\mathrm{escape}} \tag{6.9}$$

with Y being the simulated total neutron yield and n_{escape} being the neutron escape ratio taken from table 6.4. Since the angular distribution of the neutron emission from the target can be material-specific, it is expected that $\mathrm{PY}_{\mathrm{collimator}}$ scales linearly with $\mathrm{Y}_{\mathrm{escape}}$ individually for all targets. Such behavior is shown in figure 6.7 presenting a linear fit through the data points for each target material separately. Note that for V the corresponding gamma lines are only poorly or, as in the case of 22 MeV protons, not identifiable leading to large error on the count rate and thus overfitting. For Be and Ta however, the linear behavior is confirmed. Thus the simulated n_{escape} is validated by experimental observations and can therefore be well applied as a correction factor to the calculation of the measured total neutron yield. Note that the photon yield of all individual gamma count rates in equation 6.8 shows this linear trend individually such that, for the sake of compactness, the accumulated photon yield $\mathrm{PY}_{\mathrm{collimator}}$ can be introduced.

Concerning the gamma detection efficiency factor g (see table 6.4) for the different energy and material combinations as well as for AmBe, one observes identical values. This suggests that the gamma-detector sees a similar gamma source and that changes

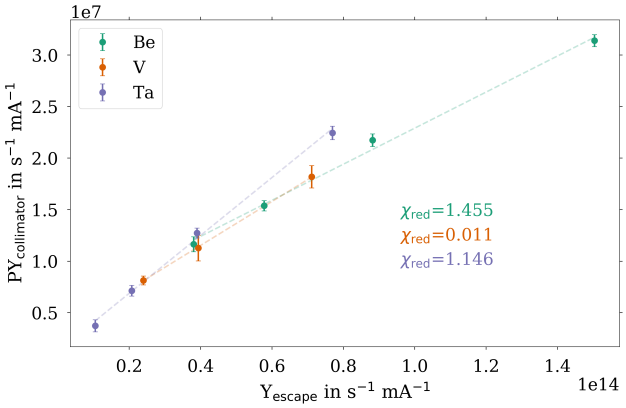

Figure 6.7.: Measured photon yield $PY_{collimator}$ (equation 6.8) of prompt gammas induced by slow and fast neutrons at the collimator of the HPGe-detector shown in figure 6.1 versus simulated neutron yield of neutrons escaping the polyethylene moderator cylinder Y_{escape} for all target materials. A linear fit is shown for each target material separately to crosscheck the proportionality between $PY_{collimator}$ and Y_{escape}. Taken and adapted from [12].

of the thermal neutron cloud in the polyethylene moderator have a negligibly small effect on the gamma emission for all experiments.

As stated in the previous section (see equation 6.7), the total and proton-induced neutron yield primarily differ by the contribution of the (n,2n) reaction. Looking at table 6.4, it can be seen that the (n,2n) reaction yield of Be is typically between two or three orders of magnitude larger than for V and Ta. This is partly because of the large volume of the Be target with respect to the V and Ta targets, but not entirely as it can be seen when looking at the neutron yield of the (n,2n) reaction channel $Y_{(n,2n)}$ normalized to the target volume as shown in figure 6.8. Thus Be has the largest neutron yield of (n,2n) reactions for the geometry of the setup used in this work. The neutron yield of (n,2n) reactions for Be is up to 12 % of the total neutron yield, whereas it is below 0.1 % of the total neutron yield for V and Ta.

6.4. Results

The proton-energy dependence of the experimental and simulated total and proton-induced neutron yield for the different targets is shown in figure 6.9a and figure 6.9b, respectively. In both cases, the simulated data agree well with the experimental ones

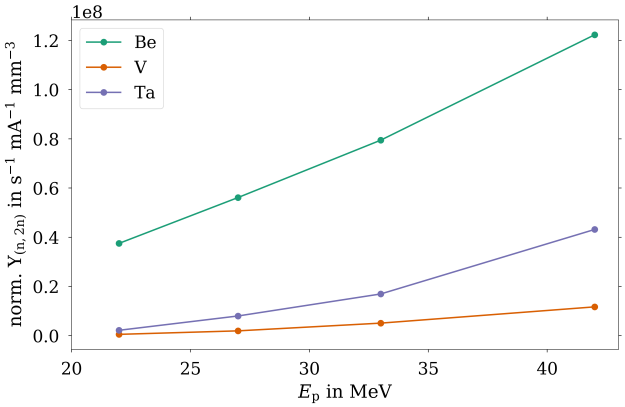

Figure 6.8.: Simulated neutron yield of (n,2n) reaction channel $Y_{(n,2n)}$ normalized to the target volume versus proton energy. All data taken from table 6.4. Taken and adapted from [12].

for all targets and proton energies taking into account the uncertainties. The relative uncertainties on the measured values Y and $Y_{(p,n)}$ are of statistical nature and vary between 6 and 18 %. The results are summarized in table 6.5.

The total neutron yield of Be is about a factor 2 higher than that of V over the entire range of proton energy. When compared to Ta, the gain in the total neutron emission of Be decreases with increasing proton energy from 2.6 at 22 MeV to 1.2 at 42 MeV. In the energy range 22-27 MeV, V and Ta perform similar whilst Ta exhibits a stronger increase in the total neutron yield above 30 MeV.

The proton-induced neutron yield shows a similar tendency compared to the total neutron yield. The proton-induced neutron yield of Be is higher than that of V by a factor of about 1.9 in the energy range 22-33 MeV and by a factor 1.6 at 42 MeV. When compared to Ta, the gain in the proton-induced neutron emission of Be decreases with increasing proton energy from 2.2 at 22 MeV to 1.0 at 42 MeV. Thus it can be expected that Ta will outperform Be at proton energies above 50 MeV. This can be further investigated when extrapolating the results of $Y_{(p,n)}$ in figure 6.9b to larger proton energies, which is shown in figure 6.10. Here, Be and Ta are compared in the proton energy range of 22 MeV to 70 MeV by fitting a growing function of $Y_{(p,n)} = A \cdot (E_p[\mathrm{MeV}])^2$ and $Y_{(p,n)} = A \cdot (E_p[\mathrm{MeV}])^3$ to the experimental results obtained from Be and Ta, respectively. The models are chosen such that a reduced chi-squared $\chi_{red} \approx 1$ is obtained. For Be, one gets $A = 2.12(7) \times 10^{11}\,\mathrm{s^{-1}\,mA^{-1}\,MeV^{-2}}$, whereas for Ta $A = 4.7(1) \times 10^{9}\,\mathrm{s^{-1}\,mA^{-1}\,MeV^{-3}}$. At 70 MeV, i.e. the nominal proton energy of HBS, the proton induced neutron yield can be extrapolated to be

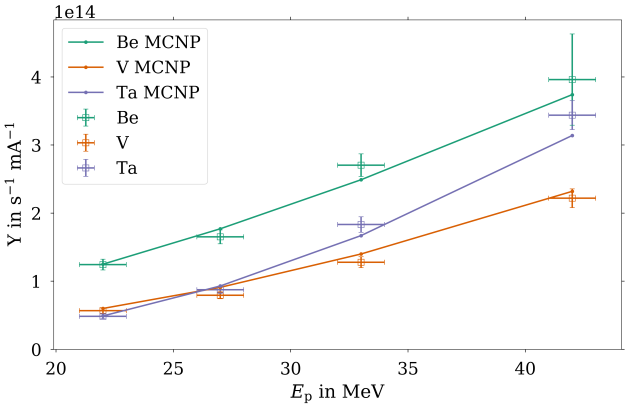

(a)

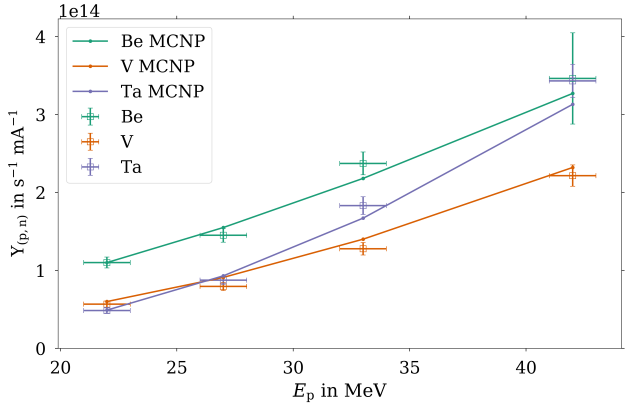

(b)

Figure 6.9.: (a): Experimental total neutron yield Y (open rectangle) and simulated total neutron yield (circle). (b): Experimental proton-induced neutron yield $Y_{(p,n)}$ (open rectangle) and simulated proton-induced neutron yield (circle). A line for the simulation results is drawn to guide the eye. The experimental data is taken from table 6.5 and the simulated data is taken from table 6.4. Taken and adapted from [12].

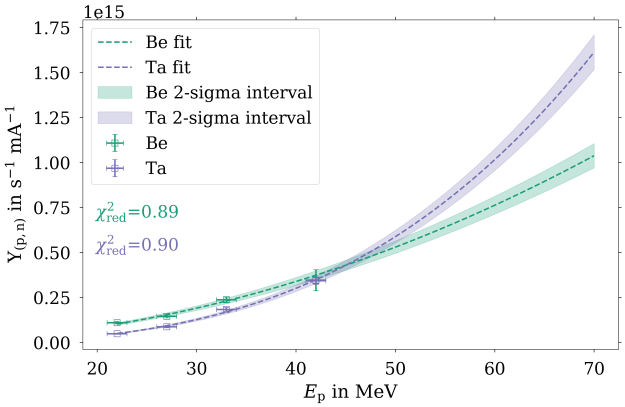

Figure 6.10.: Extrapolation of the proton induced neutron yield for Be and Ta targets to proton energies of up to 70 MeV based on the results obtained from figure 6.9b.

$1.04(3) \times 10^{15}\,s^{-1}\,mA^{-1}$ for Be and $1.61(5) \times 10^{15}\,s^{-1}\,mA^{-1}$ for Ta. Thus, the usage of Ta for HBS is preferred in terms of the proton induced neutron yield as suggested already by the analytical calculations in figure 2.19. Moreover, the extrapolated proton induced neutron yield from Ta in figure 6.10 of $1.61(5) \times 10^{15}\,s^{-1}\,mA^{-1}$ is larger than the corresponding result from analytical calculations yielding $9 \times 10^{14}\,s^{-1}\,mA^{-1}$.

Table 6.6 shows a summary of measurements and calculations of the total neutron yield Y and the proton induced neutron yield $Y_{(p,n)}$ from various publications. When comparing the results for the determination of the neutron yield from a Be target irradiated with 22 MeV protons in table 6.5 with measurements from [76] using TOF techniques ($Y = 1.50(6) \times 10^{14}\,s^{-1}\,mA^{-1}$), one observes that the result in table 6.5 is a factor of 0.83(6) smaller. In [77], experiments using the "manganese bath" technique with Be and 23, 35 and 45 MeV protons result in measured total neutron yields of 1.2(1), 2.3(2) and $3.2(3) \times 10^{14}\,s^{-1}\,mA^{-1}$, respectively. The results in table 6.5 are slightly larger but in reasonable agreement deviating by a factor of 1.0(1), 1.2(1) and 1.3(2) at the most similar measured energies of 22, 33 and 42 MeV, respectively. In the work of [10], which also uses the "manganese bath" technique, a total neutron yield of 1.77(8), 9.2(4) and $1.26(6) \times 10^{14}\,s^{-1}\,mA^{-1}$ for Be, V and Ta, respectively, at 32 MeV proton energy was measured. Here, at 33 MeV for the same targets, the results for Y in table 6.5 are typically larger by a factor of 1.5(1), 1.4(1) and 1.4(1) for Be, V and Ta, respectively. A comparison of the total neutron yield for targets with a large (n,2n) contribution is generally rather difficult as it depends strongly on the experiment condition, i.e. the moderator and target geometry. The differences in the measured neutron yield, especially for Be, can most likely be attributed to this. In

order to have a more consistent comparison of the values from different experiments, the proton induced neutron yield $Y_{(p,n)}$ should be considered which can unfortunately not be extracted from the literature data.

Comparing the experimental results of the proton-induced neutron yield $Y_{(p,n)}$ in table 6.5 to the analytical calculations based on the TALYS nuclear code in [8] (shown in figure 2.19 and summarized in table 6.6), one sees that the dominance of high-Z materials as Ta over low-Z materials as Be seems to be shifted from 20 MeV to higher energies (> 42 MeV). This can be attributed to the much larger $Y_{(p,n)}$ of Be in table 6.5, i.e. up to three times as large as in [8] (table 6.6), while the measured $Y_{(p,n)}$ for V and Ta are in agreement with the analytical calculations, deviating by maximum 16 and 17 %, respectively. As stated already in [8], the large deviation in $Y_{(p,n)}$ of Be can most likely be traced back to the underlying TALYS nuclear code producing inaccurate cross-sections for light elements.

In summary, the good agreement between the neutron yield measurements, the numerical simulations and the analytical calculations shows that the performance in terms of the neutron yield of low-energy accelerator-driven neutron sources such as HBS can be well investigated using MCNP based on ENDF/B-VII.1 or approximated with calculations following equation 2.83 with the cross sections from the TALYS nuclear code [38].

Table 6.5.: Summary of experimental data, i.e. average proton beam current I and count rate for the 2.2 MeV gamma line Z, according to proton energy and target, target radius r and target length l. The neutron yield Y is calculated according to equation 6.2 and the proton-induced neutron yield $Y_{(p,n)}$ according to equation 6.7. Taken from [12].

Target	r, l (mm,mm)	I (mA)	Z (s^{-1})	Y (s^{-1} mA^{-1})	$Y_{(p,n)}$ (s^{-1} mA^{-1})
22(1) MeV					
Be	35, 100	1.474(1)E-07	22.8(3)	1.24(8)E+14	1.10(7)E+14
V	40, 2.56	1.373(1)E-07	10.6(3)	0.57(4)E+14	0.57(4)E+14
Ta	40, 1.6	1.426(1)E-07	9.4(2)	0.49(3)E+14	0.49(3)E+14
no target	-	1.4168(8)E-07	0.10(1)	-	-
27(1) MeV					
Be	35, 100	2.610(4)E-07	51.2(3)	1.7(1)E+14	1.45(9)E+14
V	40, 2.56	2.623(5)E-07	27.2(4)	0.79(5)E+14	0.79(5)E+14
Ta	40, 1.6	2.535(5)E-07	30.0(3)	0.87(6)E+14	0.87(6)E+14
no target	-	3.064(3)E-07	0.13(1)	-	-
33(1) MeV					
Be	35, 100	6.025(4)E-07	181(1)	2.7(2)E+14	2.4(1)E+14
V	40, 3.69	6.352(4)E-07	105(1)	1.28(8)E+14	1.28(8)E+14
Ta	40, 2.0	6.459(3)E-07	153(1)	1.8(1)E+14	1.8(1)E+14
no target	-	6.171(2)E-07	0.42(3)	-	-
42(1) MeV					
Be	35, 100	8.670(1)E-07	379(3)	4.0(7)E+14	3.5(6)E+14
V	40, 4.54	7.997(1)E-07	217(2)	2.2(1)E+14	2.2(1)E+14
Ta	40, 3.0	7.859(1)E-07	349(4)	3.4(2)E+14	3.4(2)E+14
no target	-	17.137(1)E-07	0.57(4)	-	-
AmBe	-	-	0.0297(18)	-	-

Table 6.6.: Summary of the total neutron yield Y and the the proton induced neutron yield $Y_{(p,n)}$ with respect to target material and proton energy taken from literature. Taken from supplementary material of [12].

	Target	Energy (MeV)	Y (s^{-1} mA^{-1})	$Y_{(p,n)}$ (s^{-1} mA^{-1})	Technique
[76]	Be	22	1.50(6)E+14		TOF
[78]	Be	23	3.32E+14		TOF
[77]	Be	23	1.2(1)E+14		Manganese bath
	Be	35	2.3(2)E+14		
	Be	45	3.2(3)E+14		
[10]	Be	32	1.77(8)E+14		Manganese bath
	V	32	9.2(4)E+13		
	Ta	32	1.26(6)E+14		
[8]	Be	22		0.34E+14	TALYS-based
	Be	27		0.46E+14	analytical calculations
	Be	33		0.7E+14	
	Be	42		1.2E+14	
	V	22		0.6E+14	
	V	27		0.95E+14	
	V	33		1.44E+14	
	V	42		2.3E+14	
	Ta	22		0.42E+14	
	Ta	27		0.84E+14	
	Ta	33		1.56E+14	
	Ta	42		3.1E+14	

7. Conclusion and Outlook

The High-Brilliance neutron Source project (HBS) aims at developing a low-energy accelerator-driven neutron source with maximum beam brilliance to source strength ratio. A high beam brilliance will be ensured by an optimal balance between relative wavelength uncertainty and bandwidth for all instruments operating at different neutron wavelengths. Depending on the neutron wavelength range, different requirements for the proton pulsing scheme lead to the operation of three different target stations with three different proton pulsing schemes. Such operation schemes can be realized by generating an interlaced proton pulse structure in the linear accelerator using a chopper and by then unraveling the proton pulse structure with a multiplexer system, which is integrated in the proton beam transport section connecting the accelerator and the target stations.

The multiplexer system is synchronized to the chopper and distributes the different proton pulse components to the associated target stations. The development of the concept of a multiplexer system for HBS is described in this thesis. A test setup has been realized at the JULIC accelerator facility at Forschungszentrum Jülich GmbH for this purpose. The multiplexer system is based on a bipolar kicker magnet and a newly developed septum magnet, which features two magnetic dipole field regions of opposite polarity and a central zero field region. To estimate the dimensions of the associated magnets in terms of gap height, emittance measurements at the JULIC accelerator and subsequent proton beam transport calculations have been carried out yielding the expected beam size at the position of the multiplexer test setup. The kicker magnet of the multiplexer test setup is based on a reused magnet of the COSY facility that has been modified to provide larger field strengths while preserving low rise and fall times of the magnetic field. First tests of the kicker magnet being synchronized to the chopper of the JULIC accelerator have been performed with an interlaced proton pulse sequence. For the challenging proton pulse sequences which are foreseen for HBS, a new kicker magnet power supply needs to be developed, which remains a challenge in electrical engineering.

The septum magnet represents the key technology of the multiplexer system. The design is based on permanent magnets due to the fixed beam parameters in terms of energy and particle type at HBS. A detailed report on the construction of the magnet and an analysis of the performance in terms of calculations of the harmonic content as well as particle tracking through the magnet are given. The design proves to be feasible for the operation at JULIC. To show the working concept of the septum magnet with its three different field regions, a prototype magnet has been manufactured

and tested successfully. In order to operate the complete setup of the multiplexer at JULIC, the septum magnet should be obtained from the same manufacturer requiring the design of a support structure similar to the one employed at the prototype magnet. For the application of the multiplexer system at HBS, the setup at JULIC has been scaled to be able to operate at higher beam energies and to maintain low emittances. For this purpose, a HBS septum magnet is developed based on the design of the corresponding magnet at JULIC. The harmonic content of the HBS septum magnet has been calculated and considered in the design of the High-Energy Beam Transport (HEBT) section at HBS. The transmission through the HEBT beamlines in consideration of the field quality of the HBS septum magnet has been shown to be above 96 %. Further optimizations of the beamline in terms of the addition of nonlinear magnetic elements such as sextupole and octupole magnets should be performed to increase the transmission obtaining a maximum beam loss of 1 W/m (now being 115 W/m). The radiation hardness of the permanent-magnet-based septum magnet has been evaluated based on the radiation environment at comparable facilities showing that the septum magnet can be employed at HBS. However, detailed simulations of the radioactivity at HBS should be used to make more accurate estimations of the lifetime of the septum magnet. Furthermore, a safety concept for accidental beam loss that might damage the magnet needs to be developed.

Another contribution towards the maximization of the neutron beam brilliance at HBS has been done in terms of neutron yield measurements of different potential target materials for low-energy accelerator-driven neutron sources, i.e. beryllium, vanadium and tantalum [12]. This helps to benchmark calculations and simulations which are used for the decision on the target material which provides the highest neutron yield and thus neutron beam brilliance. The neutron yield is determined by the measurement of the 2.2 MeV prompt gamma line induced by thermal neutron capture of hydrogen in a polyethylene moderator cylinder surrounding the target with a Ge-detector. The neutron to gamma conversion factor of the experiment is determined using an AmBe calibration neutron source. The measurement of the neutron yield has been carried out at JULIC for different proton energies, i.e. at 22, 27, 33, 42 MeV. To correct the experimental results for the ratio of neutrons escaping from the polyethylene moderator without generating 2.2 MeV gammas and to deduce the proton induced neutron yield from the measured total neutron yield, numerical simulations of the experimental setup are performed using MCNP [11]. The final results of the total and proton induced neutron yield agree well with the corresponding neutron yield obtained from the simulations. Considering proton energies below 42 MeV, the results indicate that the proton induced neutron yield obtained from beryllium is highest when compared to vanadium and tantalum. At 42 MeV and above, tantalum seems to outperform beryllium. The measured proton induced neutron yield can be extrapolated to a proton energy of 70 MeV as obtained at HBS. The corresponding results indicate that tantalum provides the largest neutron yield for HBS, i.e. $1.61(5) \times 10^{15}\,\mathrm{s^{-1}mA^{-1}}$, in comparison to beryllium and vanadium. As the experimental determination of the neutron yield includes corrections obtained from numerical

simulations of the experiment, an unknown systematic error is introduced to the results. The plausibility of the correction factor for neutrons escaping the polyethylene moderator is checked by monitoring the photon yield of gammas induced by thermal and fast neutrons captured by the Ge-detector and its surrounding shielding material. However, a dedicated measurement should be performed for the experimental determination of the neutrons escaping the moderator in order to be independent of the numerical simulations of the setup. This could be done by calibrating the gammas generated from the Ge-detector with the bare AmBe neutron source, i.e. without the surrounding polyethylene moderator. This then allows to determine the fraction of neutrons escaping the polyethylene moderator directly during the subsequent experiment. However, if this technique is used, the measurement time must be extended as the gamma count rate emerging from the Ge-detector material is much smaller than the corresponding signal from thermal neutron capture of hydrogen in the moderator. In addition, it would be interesting to perform the experiment together with a second Ge-detector, which is positioned behind the moderator following the direction of the proton beam, allowing to investigate a potential angular dependence of the experiment.

In summary, two individual steps towards the optimization of the neutron beam brilliance at HBS have been done in terms of the development of a multiplexer system and the measurement of the neutron yield for different target materials. In parallel, further contributions concentrating on the increase of the brilliance at HBS are being investigated in our workgroup. Among these are the optimization of the target-moderator-reflector unit with respect to the moderator and reflector material as well as their associated geometry, the design of one dimensional cold finger moderators being inserted into the thermal moderator and the development of neutron guide systems, which preserve the source brilliance. Coalescing all these contributions within the HBS facility helps to provide a future low-energy accelerator-driven neutron source, which successfully replaces the fading out research reactor neutron sources allowing an adequate provision of neutrons to the scientific community.

A. Relativistic kinematics

The momentum p and kinetic T of relativistic particles with mass m are related with $p = \sqrt{T^2 + 2Tm}$, if $c = 1$ and all units in eV are set, and thus

$$\frac{\mathrm{d}p}{\mathrm{d}T} = \frac{T+m}{p}. \tag{A.1}$$

With this and the LORENTZ factor $\gamma = (T+m)/m$, the momentum and the kinetic energy uncertainty can be related as follows

$$\begin{aligned}\frac{\mathrm{d}p}{p} &= \frac{\mathrm{d}T}{p^2}(T+m) \\ &= \frac{\mathrm{d}T}{T}\frac{T+m}{T+2m} \\ &= \frac{\mathrm{d}T}{T}\frac{\gamma}{\gamma+1}.\end{aligned} \tag{A.2}$$

A summary of important kinematic factors used throughout this thesis is given in table A.1.

Table A.1.: Summary of the kinematic factors for the test facility at JULIC and the HBS facility with the kinetic energy T, the momentum p, the LORENTZ factor $\gamma = (T+m)/m$ and $\beta = (1 - 1/\gamma^2)^{1/2} = v/c$. Here, v is the velocity of the particles and c is the speed of light. For protons, $m \approx 938\,\mathrm{MeV/c^2}$.

	JULIC	HBS
T/MeV	45	70
p/(MeV/c)	294	369
γ	1.05	1.08
β	0.30	0.37
$\beta\gamma$	0.32	0.4

B. List of elements in the NESP beamline

A list of important elements used in the NESP beamline (presented in figure 4.4) is given. The element name and type, path length of the reference particle s at the end of the respective element (co-moving coordinate system in figure 2.1) and element length l (effective length) are given. Additional remarks containing bend angles Θ of dipole magnets and further information are presented. Note that for the *Bmad* library [49], positive bend angles in the horizontal plane bend towards negative x values.

Table B.1.: List of elements in the NESP beamline. For bending magnets (SBend), H denotes horizontal deflection of the beam (Θ: bend angle of dipole magnets, $\beta_{1(2)}$: edge angles according to figure 2.8).

Index	Name	Type	s/m	l/m	Remark
0	BEGINNING	Beginning	0.000	—	
1	D1	Drift	0.860	0.860	
2	QI11	Quadrupole	1.160	0.300	
3	D2	Drift	1.460	0.300	
4	QI12	Quadrupole	1.760	0.300	
5	D3	Drift	2.060	0.300	
6	DI11	Sbend	3.025	0.965	H, $\Theta = 38.25°$, $\beta_1 = \beta_2 = 10.3°$
7	D4	Drift	3.325	0.300	
8	QI13	Quadrupole	3.625	0.300	
9	D5	Drift	4.125	0.500	
10	QI14	Quadrupole	4.425	0.300	
11	D6	Drift	4.925	0.500	
12	QI15	Quadrupole	5.225	0.300	
13	D7	Drift	5.525	0.300	
14	DI12	SBend	6.491	0.965	off
15	D8	Drift	11.291	4.800	
16	QN1	Quadrupole	11.630	0.339	
17	D9	Drift	12.530	0.900	
18	QN2	Quadrupole	12.869	0.339	
19	D10	Drift	16.443	3.575	
20	SEPT	SBend	17.113	0.670	TFSM, off
21	D12	Drift	20.913	3.800	

22	END	Marker	20.913	0.000

C. Magnetic field measurements of the Three-Field Magnet (TFM)

This chapter comprises additional material from the magnetic field measurements of the Three-Field Magnet (TFM) presented in section 4.5.2.

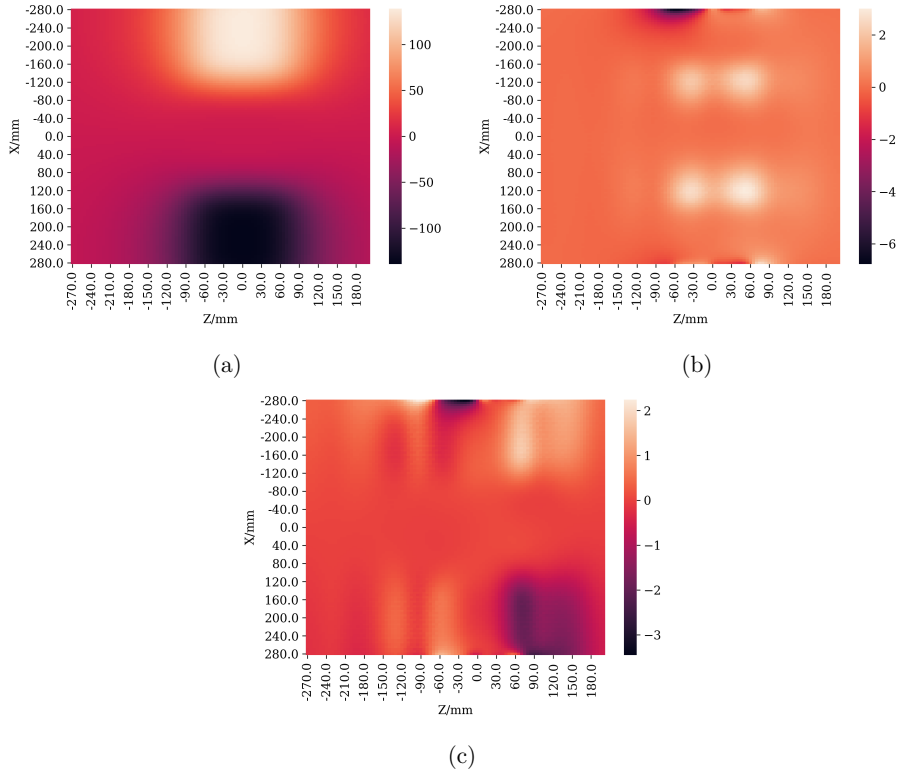

Figure C.1.: Measured and rotated magnetic flux density (according to equation 4.36) in the central xz-plane ($y = 0$). (a) shows the vertical magnetic flux density $B_{y,\mathrm{m,rot.}}$ in mT. (b) and (c) show $B_{x,\mathrm{m,rot.}}$ and $B_{z,\mathrm{m,rot.}}$, respectively.

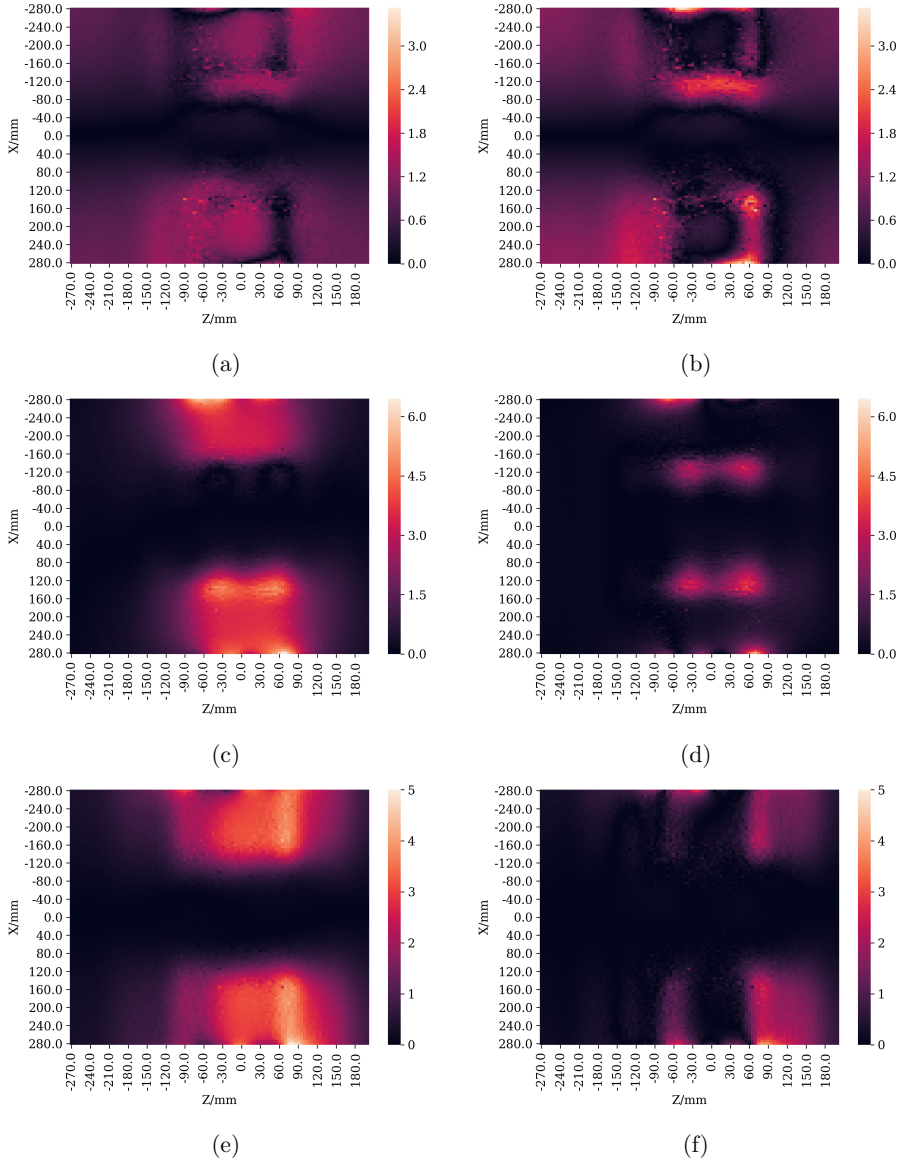

Figure C.2.: Absolute difference between measurement and simulation of the magnetic flux density ΔB of the TFM for the xz-plane at $y = 20\,\mathrm{mm}$ in mT without (first column) and with correction (second column). The measured and corrected magnetic flux density $B_{i,\mathrm{m,corr.}}$ is calculated according to equation 4.38 for $i = x, y, z$. (a),(b): ΔB_y. (c),(d): ΔB_x, (e),(f): ΔB_z.

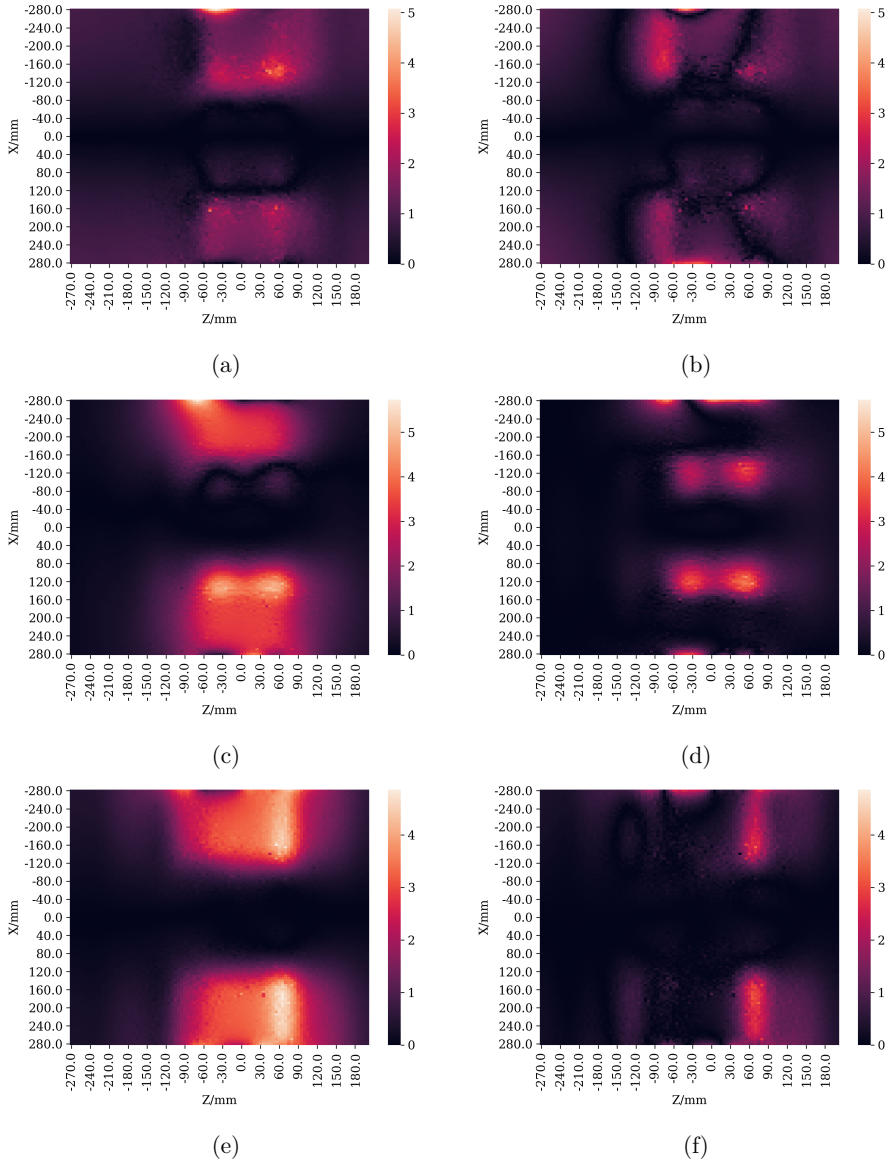

Figure C.3.: Absolute difference between measurement and simulation of the magnetic flux density ΔB of the TFM for the xz-plane at $y = -20\,\mathrm{mm}$ in mT without (first column) and with correction (second column). The measured and corrected magnetic flux density $B_{i,\mathrm{m,corr.}}$ is calculated according to equation 4.38 for $i = x, y, z$. (a),(b): ΔB_y. (c),(d): ΔB_x, (e),(f): ΔB_z.

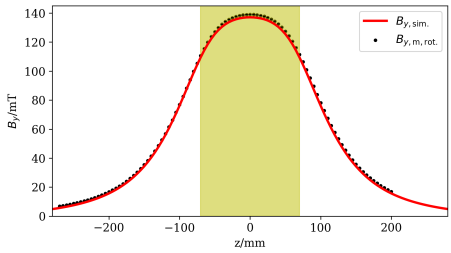

(a)

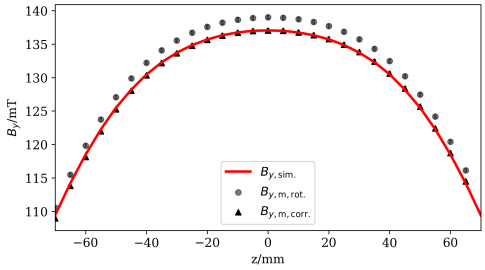

(b)

Figure C.4.: Vertical magnetic flux density B_y versus longitudinal position z at $x = -230\,\mathrm{mm}$. (a) shows $B_{y,\mathrm{m,rot.}}$ and $B_{y,\mathrm{sim.}}$ for $-280\,\mathrm{mm} < z < 280\,\mathrm{mm}$. The yellow shaded area marks the extent of the magnet. (b) shows $B_{y,\mathrm{m,rot.}}$, $B_{y,\mathrm{m,corr.}}$ and $B_{y,\mathrm{sim.}}$ inside the magnet.

D. $2n$-pole magnetic field gradients

For the implementation of the harmonic content of the HBS Three-Field Septum Magnet (TFSM) into *TraceWin*, one needs to calculate the $2n$-pole magnetic field gradients corresponding to the multipole components n in figure 5.5. Considering the real part of the complex magnetic flux density in equation 2.78 at $y = 0$, one gets the vertical magnetic flux density

$$B_y(x) = \sum_{n=1}^{\infty} B_{y,n}(x) = \sum_{n=1}^{\infty} B_n \left(\frac{x}{r_0}\right)^{n-1}. \tag{D.1}$$

The skew components A_n are negligible for the magnets treated in this thesis. With equation D.1,

$$G_n = \frac{\partial^{n-1} B_{y,n}(x)}{\partial x^{n-1}} = (n-1)! \frac{B_n}{r_0^{n-1}} \tag{D.2}$$

is typically defined as the $2n$-pole gradient. A summary of the $2n$-pole gradients for the JULIC and for the HBS septum magnet is given in table D.1.

In *TraceWin* [54], a slightly different definition of the $2n$-pole gradient is used which has to be considered, i.e.

$$G_{n,\mathrm{TraceWin}} = \frac{1}{(n-1)!} \frac{\partial^{n-1} B_{y,n}(x)}{\partial x^{n-1}} = \frac{B_n}{r_0^{n-1}}. \tag{D.3}$$

The results from figure 5.5 can be cross checked for plausibility when inserting the obtained normal components B_n into equation D.1 with the corresponding reference

Table D.1.: Summary of $2n$-pole gradients calculated according to equation D.2 with the harmonic content taken from figure 4.33 (JULIC) and figure 5.5 (HBS).

G_n	JULIC center	JULIC right	HBS center	HBS right
$G_2/(\mathrm{Tm}^{-1})$	-3.23×10^{-1}	-2.14×10^{-1}	-1.82×10^{-1}	0.40×10^{-1}
$G_3/(\mathrm{Tm}^{-2})$	-	-2.65×10^{1}	-	-1.14×10^{1}
$G_4/(\mathrm{Tm}^{-3})$	-1.26×10^{4}	-0.23×10^{4}	-0.76×10^{4}	-0.23×10^{4}
$G_5/(\mathrm{Tm}^{-4})$	-	-1.04×10^{6}	-	-0.55×10^{6}
$G_6/(\mathrm{Tm}^{-5})$	-	-1.15×10^{8}	-	-0.36×10^{8}

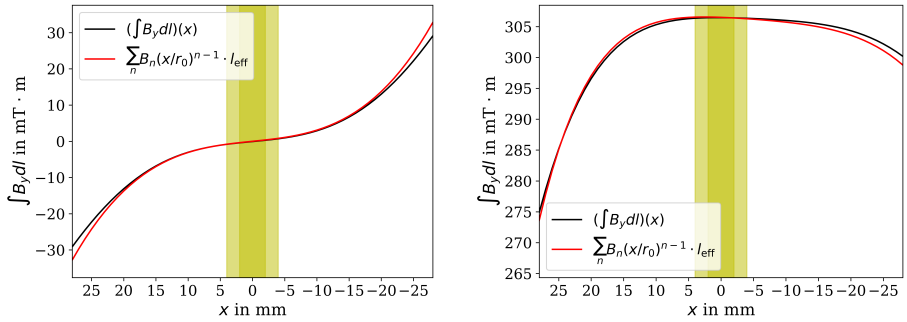

Figure D.1.: Horizontal distribution of the integrated vertical magnetic flux density of the HBS septum magnet (figure 5.3) compared to the vertical magnetic flux density calculated using equation D.1 with the harmonic content from figure 5.5. The results from equation D.1 are multiplied with the effective length $l_{\text{eff}} = 1000\,\text{mm}$ of the HBS septum magnet. The extent of the proton beam is indicated by the yellow shaded area (dark yellow: 2 rms beam widths, light yellow: 4 rms beam widths). (a): Central zero field region of the septum magnet. (b): Right dipole field region of the septum magnet.

radius of $r_0 = 17\,\text{mm}$. The resulting vertical magnetic flux density can be compared with the horizontal evolution of the integrated vertical magnetic flux density in figure 5.3 which shows good agreement as presented in figure D.1. For the right field region (figure D.1b), the vertical magnetic flux density which is reconstructed from the harmonic content calculations seems to yield a larger quadrupole component in the vicinity of the beam when compared to the integrated vertical magnetic flux density. This is probably due to reference radius ($r_0 = 17\,\text{mm}$) exceeding the beam size such that the harmonic content represents a worse magnetic field quality than actually present within the beam spot. This is nevertheless a conservative representation of field quality and thus appropriate for the particle tracking studies in figure 5.8 and figure 5.9.

E. List of elements in the HBS HEBT beamlines

This appendix gives a comprehensive list of all elements employed in the HBS HEBT beamlines, which are described in detail in section 5.3. The lists are divided into a list comprising all elements shared between all three, i.e. straight, left and right, HEBT beamlines (table E.1) and two lists for the elements exclusively used in the straight HEBT beamline (table E.2) and in the left HEBT beamline (table E.3), respectively. The lists are separated at the position of the kicker magnet of the multiplexer. The element name and type, path length of the reference particle s at the end of the respective element (co-moving coordinate system in figure 2.1, used in figure 5.7) and element length l (effective length) are given. Additional remarks containing quadrupole strenghts k, bend angles Θ of dipole magnets and further information are presented. Note that for the *Bmad* library [49], positive bend angles in the horizontal plane bend towards negative x values (right in figure 5.6), whereas positive bend angles in the vertical plane bend towards positive y values (up in figure 5.6).

Table E.1.: List of elements in the first section and in parts of the second section of the HBS HEBT beamline (Layout shown in Figure 5.6). The list comprises all elements which are shared among the three HEBT beamlines (straight, left, right) before the kicker magnet of the multiplexer. For bending magnets (SBend), H and V denote horizontal and vertical deflection of the beam, respectively (Θ: bend angle of dipole magnets, k: quadrupole strength).

Index	Name	Type	s/m	l/m	Remark
0	BEGINNING	Beginning	0.000	—	
1	D11	Drift	3.000	3.000	
2	Q11	Quadrupole	3.300	0.300	$k = -5.796\,000\,58\,\mathrm{m}^{-2}$
3	D12	Drift	3.400	0.100	
4	Q12	Quadrupole	3.700	0.300	$k = 5.489\,401\,37\,\mathrm{m}^{-2}$
5	D13	Drift	3.800	0.100	
6	DI11	Sbend	4.910	1.110	V, $\Theta = 45°$
7	D14	Drift	5.410	0.500	
8	Q13	Quadrupole	5.710	0.300	$k = 5.869\,371\,81\,\mathrm{m}^{-2}$
9	D15	Drift	6.210	0.500	
10	DI12	Sbend	7.320	1.110	V, $\Theta = 45°$

11	D16	Drift	7.420	0.100	
12	Q14	Quadrupole	7.720	0.300	$k = 5.489\,401\,37\,\mathrm{m}^{-2}$
13	D17	Drift	7.820	0.100	
14	Q15	Quadrupole	8.120	0.300	$k = -5.796\,000\,58\,\mathrm{m}^{-2}$
15	D18	Drift	11.120	3.000	
16	D19	Drift	14.120	3.000	
17	Q16	Quadrupole	14.420	0.300	$k = -5.796\,000\,58\,\mathrm{m}^{-2}$
18	D110	Drift	14.520	0.100	
19	Q17	Quadrupole	14.820	0.300	$k = 5.489\,401\,37\,\mathrm{m}^{-2}$
20	D111	Drift	14.920	0.100	
21	DI13	Sbend	16.030	1.110	V, $\Theta = -45°$
22	D112	Drift	16.530	0.500	
23	Q18	Quadrupole	16.830	0.300	$k = -5.869\,371\,81\,\mathrm{m}^{-2}$
24	D113	Drift	17.330	0.500	
25	DI14	Sbend	18.440	1.110	V, $\Theta = -45°$
26	D114	Drift	18.540	0.100	
27	Q19	Quadrupole	18.840	0.300	$k = 5.489\,401\,37\,\mathrm{m}^{-2}$
28	D115	Drift	18.940	0.100	
29	Q110	Quadrupole	19.240	0.300	$k = -5.796\,000\,58\,\mathrm{m}^{-2}$
30	D116	Drift	22.240	3.000	
31	D20	Drift	24.740	2.500	Second section
32	Q21	Quadrupole	25.040	0.300	$k = -2.589\,750\,63\,\mathrm{m}^{-2}$
33	D21	Drift	25.790	0.750	
34	Q22	Quadrupole	26.090	0.300	$k = 1.777\,847\,09\,\mathrm{m}^{-2}$
35	D22	Drift	27.090	1.000	
36	Q23	Quadrupole	27.390	0.300	$k = 1.777\,847\,09\,\mathrm{m}^{-2}$
37	D23	Drift	28.140	0.750	
38	Q24	Quadrupole	28.440	0.300	$k = -2.589\,750\,63\,\mathrm{m}^{-2}$
39	D24	Drift	30.940	2.500	
40	D25	Drift	33.440	2.500	
41	Q25	Quadrupole	33.740	0.300	$k = 4.760\,088\,59\,\mathrm{m}^{-2}$
42	D26	Drift	33.840	0.100	
43	Q26	Quadrupole	34.140	0.300	$k = -4.266\,241\,34\,\mathrm{m}^{-2}$
44	D27	Drift	34.240	0.100	

Table E.2.: List of elements in parts of the second and in the third section of the straight HBS HEBT beamline (Layout shown in Figure 5.6a). The list comprises all elements of the straight HEBT beamline starting with the kicker magnet of the multiplexer. For bending magnets (SBend), H and V denote horizontal and vertical deflection of the beam, respectively (Θ: bend angle of dipole magnets, k: quadrupole strength).

Index	Name	Type	s/m	l/m	Remark
45	K21	Sbend	34.840	0.600	Kicker, off
46	D28	Drift	35.940	1.100	
47	DI21	Sbend	36.940	1.000	TFSM, off
48	D29	Drift	40.340	3.400	
49	Q27	Quadrupole	40.640	0.300	$k = 1.586\,243\,63\,\mathrm{m}^{-2}$
50	D210	Drift	41.640	1.000	
51	Q28	Quadrupole	41.940	0.300	$k = -4.272\,677\,32\,\mathrm{m}^{-2}$
52	D211	Drift	42.940	1.000	
53	Q29	Quadrupole	43.240	0.300	$k = 2.772\,567\,02\,\mathrm{m}^{-2}$
54	D212	Drift	44.240	1.000	
55	Q210	Quadrupole	44.540	0.300	$k = -2.628\,246\,09\,\mathrm{m}^{-2}$
56	D213	Drift	47.040	2.500	
57	Q211	Quadrupole	47.340	0.300	$k = 0.600\,000\,00\,\mathrm{m}^{-2}$
58	D214	Drift	49.840	2.500	
59	Q212	Quadrupole	50.140	0.300	$k = -0.600\,000\,00\,\mathrm{m}^{-2}$
60	D215	Drift	52.640	2.500	
61	Q213	Quadrupole	52.940	0.300	$k = 0.600\,000\,00\,\mathrm{m}^{-2}$
62	D216	Drift	55.440	2.500	
63	Q214	Quadrupole	55.740	0.300	$k = -0.600\,000\,00\,\mathrm{m}^{-2}$
64	D217	Drift	58.240	2.500	
65	Q215	Quadrupole	58.540	0.300	$k = 0.600\,000\,00\,\mathrm{m}^{-2}$
66	D218	Drift	61.040	2.500	
67	Q216	Quadrupole	61.340	0.300	$k = -0.600\,000\,00\,\mathrm{m}^{-2}$
68	D219	Drift	63.840	2.500	
69	Q217	Quadrupole	64.140	0.300	$k = 0.600\,000\,00\,\mathrm{m}^{-2}$
70	D220	Drift	66.640	2.500	
71	Q218	Quadrupole	66.940	0.300	$k = -0.600\,000\,00\,\mathrm{m}^{-2}$
72	D221	Drift	69.440	2.500	
73	Q219	Quadrupole	69.740	0.300	$k = 0.600\,000\,00\,\mathrm{m}^{-2}$
74	D222	Drift	72.240	2.500	
75	Q220	Quadrupole	72.540	0.300	$k = -0.600\,000\,00\,\mathrm{m}^{-2}$
76	D223	Drift	75.040	2.500	
77	Q221	Quadrupole	75.340	0.300	$k = 0.600\,000\,00\,\mathrm{m}^{-2}$
78	D224	Drift	77.840	2.500	
79	Q222	Quadrupole	78.140	0.300	$k = -0.600\,000\,00\,\mathrm{m}^{-2}$

80	D225	Drift	80.640	2.500	
81	Q223	Quadrupole	80.940	0.300	$k = 0.600\,000\,00\,\mathrm{m}^{-2}$
82	D226	Drift	83.440	2.500	
83	Q224	Quadrupole	83.740	0.300	$k = -0.600\,000\,00\,\mathrm{m}^{-2}$
84	D227	Drift	86.240	2.500	
85	Q225	Quadrupole	86.540	0.300	$k = 0.600\,000\,00\,\mathrm{m}^{-2}$
86	D228	Drift	89.040	2.500	
87	Q226	Quadrupole	89.340	0.300	$k = -0.600\,000\,00\,\mathrm{m}^{-2}$
88	D229	Drift	91.840	2.500	
89	Q227	Quadrupole	92.140	0.300	$k = 0.600\,000\,00\,\mathrm{m}^{-2}$
90	D230	Drift	94.640	2.500	
91	Q228	Quadrupole	94.940	0.300	$k = -0.600\,000\,00\,\mathrm{m}^{-2}$
92	D231	Drift	97.440	2.500	
93	Q229	Quadrupole	97.740	0.300	$k = 0.914\,198\,86\,\mathrm{m}^{-2}$
94	D232	Drift	98.740	1.000	
95	Q230	Quadrupole	99.040	0.300	$k = -2.995\,064\,78\,\mathrm{m}^{-2}$
96	D233	Drift	100.040	1.000	
97	Q231	Quadrupole	100.340	0.300	$k = 2.613\,597\,26\,\mathrm{m}^{-2}$
98	D234	Drift	101.340	1.000	
99	Q232	Quadrupole	101.640	0.300	$k = -2.603\,963\,58\,\mathrm{m}^{-2}$
100	D235	Drift	102.640	1.000	
101	D31	Drift	105.640	3.000	Third section
102	Q31	Quadrupole	105.940	0.300	$k = -3.755\,320\,89\,\mathrm{m}^{-2}$
103	D32	Drift	106.040	0.100	
104	Q32	Quadrupole	106.340	0.300	$k = 4.234\,481\,63\,\mathrm{m}^{-2}$
105	D33	Drift	106.440	0.100	
106	DI31	Sbend	107.550	1.110	V, $\Theta = -45°$
107	D34	Drift	108.050	0.500	
108	Q33	Quadrupole	108.350	0.300	$k = -5.869\,371\,81\,\mathrm{m}^{-2}$
109	D35	Drift	108.850	0.500	
110	DI32	Sbend	109.960	1.110	V, $\Theta = -45°$
111	D36	Drift	110.060	0.100	
112	Q34	Quadrupole	110.360	0.300	$k = 4.234\,481\,63\,\mathrm{m}^{-2}$
113	D37	Drift	110.460	0.100	
114	Q35	Quadrupole	110.760	0.300	$k = -3.755\,320\,89\,\mathrm{m}^{-2}$
115	D38	Drift	111.560	0.800	
116	Q36	Quadrupole	111.860	0.300	optional, not used
117	D39	Drift	112.160	0.300	
118	Q37	Quadrupole	112.460	0.300	optional, not used
119	D310	Drift	112.760	0.300	
120	Q38	Quadrupole	113.060	0.300	optional, not used
121	D311	Drift	113.360	0.300	
122	Q39	Quadrupole	113.660	0.300	optional, not used
123	D312	Drift	113.960	0.300	

124	KH31	Kicker	114.460	0.500	Beam scanner (H)
125	D313	Drift	114.660	0.200	
126	KV31	Kicker	115.160	0.500	Beam scanner (V)
127	D314	Drift	121.760	6.600	
128	END	End	121.760	0.000	

Table E.3.: List of elements in parts of the second and in the third section of the left HBS HEBT beamline (Layout shown in Figure 5.6b). The list comprises all elements of the left HEBT beamline starting with the kicker magnet of the multiplexer. For bending magnets (SBend), H and V denote horizontal and vertical deflection of the beam, respectively (Θ: bend angle of dipole magnets, k: quadrupole strength).

Index	Name	Type	s/m	l/m	Remark
45	K21L	Sbend	34.840	0.600	Kicker - H, $\Theta = -2.75°$
46	D23L	Drift	35.940	1.100	
47	DI21L	Sbend	36.940	1.000	TFSM - H, $\Theta = -14.44°$
48	D24L	Drift	38.440	1.500	
49	Q27L	Quadrupole	38.740	0.300	$k = 4.891\,222\,11\,\mathrm{m}^{-2}$
50	D25L	Drift	39.050	0.310	
51	DI22L	Sbend	40.160	1.110	H, $\Theta = -45°$
52	D26L	Drift	40.260	0.100	
53	Q28L	Quadrupole	40.560	0.300	$k = -5.216\,794\,12\,\mathrm{m}^{-2}$
54	D27L	Drift	40.660	0.100	
55	Q29L	Quadrupole	40.960	0.300	$k = 5.330\,999\,58\,\mathrm{m}^{-2}$
56	D28L	Drift	44.960	4.000	
57	Q210L	Quadrupole	45.260	0.300	$k = 2.715\,799\,11\,\mathrm{m}^{-2}$
58	D29L	Drift	46.260	1.000	
59	Q211L	Quadrupole	46.560	0.300	$k = -3.681\,817\,56\,\mathrm{m}^{-2}$
60	D210L	Drift	47.560	1.000	
61	Q212L	Quadrupole	47.860	0.300	$k = 3.622\,253\,79\,\mathrm{m}^{-2}$
62	D211L	Drift	48.860	1.000	
63	Q213L	Quadrupole	49.160	0.300	$k = -3.331\,384\,57\,\mathrm{m}^{-2}$
64	D212L	Drift	50.660	1.500	
65	D31L	Drift	53.660	3.000	Third section
66	Q31L	Quadrupole	53.960	0.300	$k = -3.755\,320\,89\,\mathrm{m}^{-2}$
67	D32L	Drift	54.060	0.100	
68	Q32L	Quadrupole	54.360	0.300	$k = 4.234\,481\,63\,\mathrm{m}^{-2}$
69	D33L	Drift	54.460	0.100	
70	DI31L	Sbend	55.570	1.110	V, $\Theta = -45°$
71	D34L	Drift	56.070	0.500	
72	Q33L	Quadrupole	56.370	0.300	$k = -5.869\,371\,81\,\mathrm{m}^{-2}$
73	D35L	Drift	56.870	0.500	
74	DI32L	Sbend	57.980	1.110	V, $\Theta = -45°$
75	D36L	Drift	58.080	0.100	
76	Q34L	Quadrupole	58.380	0.300	$k = 4.234\,481\,63\,\mathrm{m}^{-2}$
77	D37L	Drift	58.480	0.100	
78	Q35L	Quadrupole	58.780	0.300	$k = -3.755\,320\,89\,\mathrm{m}^{-2}$
79	D38L	Drift	59.580	0.800	

80	Q36L	Quadrupole	59.880	0.300	optional, not used
81	D39L	Drift	60.180	0.300	
82	Q37L	Quadrupole	60.480	0.300	optional, not used
83	D310L	Drift	60.780	0.300	
84	Q38L	Quadrupole	61.080	0.300	optional, not used
85	D311L	Drift	61.380	0.300	
86	Q39L	Quadrupole	61.680	0.300	optional, not used
87	D312L	Drift	61.980	0.300	
88	KH31L	Kicker	62.480	0.500	Beam scanner (H)
89	D313L	Drift	62.680	0.200	
90	KV31L	Kicker	63.180	0.500	Beam scanner (V)
91	D314L	Drift	69.780	6.600	
92	END	End	69.780	0.000	

F. Calibration of target current measurements

The experimental determination of the neutron yield, which is described in detail in chapter 6, requires to measure the proton beam current on the target with high accuracy. For the target beam current measurement, a current amplifier (Keithley 18000-20) is electrically connected to the isolated target. The current amplifier converts the small current signal (< 2 nA) to a voltage signal which is then processed by subsequent ADC electronics. The conversion factor from current to voltage depends on the range which is selected at the current amplifier. For our measurements, two different ranges are used depending on the target beam current. Either a 10 nA range, i.e. 10 nA corresponding to 10 V voltage signal, or a 100 nA range, i.e. 100 nA corresponding to 10 V voltage signal, are used such that the input signal at the ADC does not exceed 1 V. This limitation comes from the specifications of the ADC (Red Pitaya, model V1.1). In order to determine the proton beam current accurately, both range settings of the current amplifier are calibrated using a picoampere source (Keithley 261). The picoampere source is connected to the current amplifier and the corresponding voltage signal is recorded. In addition, the picoampere source current signal is recorded with a calibrated amperemeter (Keithley 2400). figure F.1 shows the voltage signal recorded through the current amplifier versus the current signal measured with the calibrated amperemeter for different settings of the picoampere source for the 10 nA and 100 nA range of the current amplifier. A linear fit yields the calibration data.

During the neutron yield measurement, the current amplifier is wired differently than during calibration with the targets being connected directly to the current amplifier. This might influence the voltage offset. Therefore, the voltage offset of the current amplifier is measured prior to each run for ≈5 minutes in between the neutron yield measurement and in the absence of the proton beam. The corresponding results for the different range settings of the current amplifier are presented in figure F.2. The offset measured during calibration is shown for comparison.

The offset during calibration and during the measurement generally agrees within the uncertainties. The offset during the measurements seems to be stable.

With the calibration data from figure F.1 and the voltage offset during the neutron yield measurement in figure F.2, the corrected average proton beam current I is

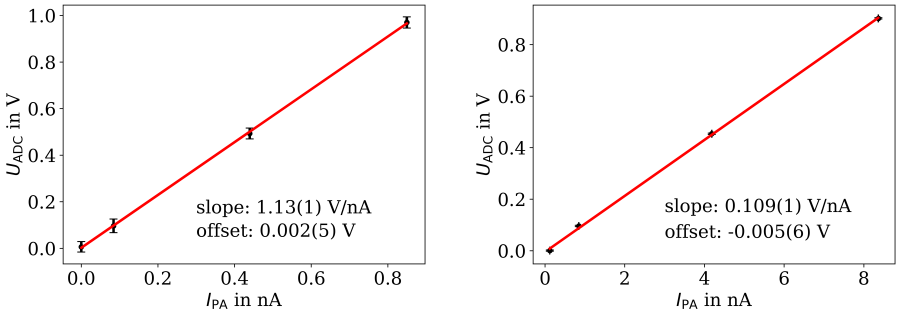

(a) (b)

Figure F.1.: Calibration of the current amplifier used for the measurement of the proton beam current on the target in chapter 6. I_{PA} is the current applied with a picoampere source to the current amplifier as measured with a calibrated amperemeter. U_{ADC} is the voltage signal recorded at the current amplifier. (a): 10 nA range setting at the current amplifier. (b): 100 nA range setting at the current amplifier.

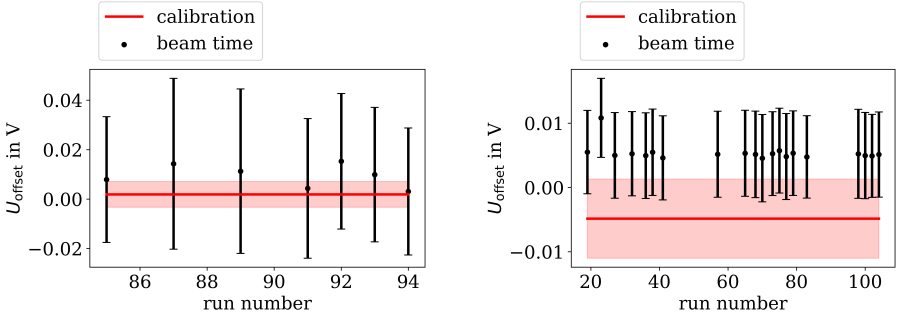

(a) (b)

Figure F.2.: Measurement of the voltage offset recorded at the current amplifier for the different runs during the neutron yield measurement with the proton beam being shut off. For comparison the voltage offset from the calibration in figure F.1 is shown. (a): runs with 10 nA range setting at the current amplifier. (b): runs with 100 nA range setting at the current amplifier.

extracted from the voltage signal via

$$I = (U_{\text{target}} - U_{\text{offset,b.t.}}) \cdot \frac{1}{\text{slope}} \tag{F.1}$$

with U_{target} being the voltage signal recorded during the neutron yield measurements with beam and $U_{\text{offset,b.t.}}$ being the offset signal recorded in between the neutron yield measurements without beam (from figure F.2). The conversion factor from voltage to current 1/slope is taken from the results in figure F.1.

Bibliography

[1] European Neutron Scattering Association. *Neutrons for Science and Technology, 2. Ed.* 2017. URL: https://europeanspallationsource.se/sites/default/files/files/document/2017-09/20170207_2ndensa-brochure_web.pdf.

[2] R. Garoby et al. "The European Spallation Source Design". In: *Physica Scripta* 93.1 (2017), p. 014001. DOI: 10.1088/1402-4896/aa9bff.

[3] Neutron Landscape Group. "ESFRI Physical Sciences and Engineering Strategy Working Group". In: *ESFRI Scripta* I (2016).

[4] P. Zakalek et al. "High-Brilliance Neutron Source Project". In: *Journal of Physics: Conference Series* 1401 (2020), p. 012010. DOI: 10.1088/1742-6596/1401/1/012010.

[5] T. Brückel et al. *Conceptual Design Report Jülich High Brilliance Neutron Source (HBS)*. Tech. rep. Forschungszentrum Jülich GmbH, 2020.

[6] U. Rücker et al. "The Jülich high-brilliance neutron source project". In: *Eur. Phys. J. Plus* 131.19 (2016). DOI: 10.1140/epjp/i2016-16019-5.

[7] J. M. Carpenter and C.-K. Loong. *Elements of Slow-Neutron Scattering: Basics, Techniques, and Applications*. Cambridge University Press, 2015. DOI: 10.1017/CBO9781139029315.

[8] P. Zakalek et al. "Energy and target material dependence of the neutron yield induced by proton and deuteron bombardment". In: *EPJ Web Conf.* 231 (2020), p. 03006. DOI: 10.1051/epjconf/202023103006.

[9] I. Tilquin et al. "Experimental measurements of neutron fluxes produced by proton beams (23–80MeV) on Be and Pb targets". In: *Nuclear Instruments and Methods in Physics Research Section A* 545.1 (2005), pp. 339–343. DOI: 10.1016/j.nima.2005.01.325.

[10] Y.-K. Tai et al. "Neutron Yields from Thick Targets Bombarded by 18- and 32-Mev Protons". In: *Phys. Rev.* 109 (6 1958), pp. 2086–2091. DOI: 10.1103/PhysRev.109.2086.

[11] T. Goorley et al. "Initial MCNP6 Release Overview". In: *Nuclear Technology* 180.3 (2012), pp. 298–315. DOI: 10.13182/NT11-135.

[12] M. Rimmler et al. "Determination of the neutron yield of Be, V and Ta targets irradiated with protons (22-42MeV) by means of prompt gamma neutron activation analysis". In: *Nuclear Instruments and Methods in Physics Research Section A* 990 (2021), p. 164989. DOI: 10.1016/j.nima.2020.164989.

[13] Wolfgang Nolting. *Grundkurs Theoretische Physik 2: Analytische Mechanik, 8. Aufl.* Springer-Verlag Berlin Heidelberg, 2011. DOI: 10.1007/978-3-642-12950-6.

[14] Jürgen Struckmeier. *Liouville's theorem: Basics, Applications and Limitations.* Vortrag. 2006. URL: https://web-docs.gsi.de/~struck/hp/wsem/lvtheo.pdf.

[15] Helmut Wiedemann. *Particle Accelerator Physics, 4. Ed.* Springer International Publishing, 2015. DOI: 10.1007/978-3-319-18317-6.

[16] Frank Hinterberger. *Physik der Teilchenbeschleuniger und Ionenoptik, 2. Aufl.* Springer-Verlag Berlin Heidelberg, 2008. DOI: 10.1007/978-3-540-75282-0.

[17] E.D. Courant and H.S. Snyder. "Theory of the Alternating-Gradient Synchrotron". In: *Annals of Physics* 281.1 (2000), pp. 360–408. DOI: 10.1006/aphy.2000.6012.

[18] Andrzej Wolski. *Beam Dynamics In High Energy Particle Accelerators.* Imperial College Press, 2014. DOI: 10.1142/p899.

[19] David Sagan. *Bmad Manual.* 21, 2021. URL: https://www.classe.cornell.edu/bmad/manual.html.

[20] Stephan Russenschuck. *Field Computation for Accelerator Magnets: Analytical and Numerical Methods for Electromagnetic Design and Optimization.* Wiley-VCH, 2011. DOI: 10.1002/9783527635467.

[21] Jian-Hong Yi. "Development of samarium–cobalt rare earth permanent magnetic materials". In: *Rare Metals* 33.6 (2014), pp. 633–640. DOI: 10.1007/s12598-014-0405-1.

[22] Esma Mobs. *The CERN accelerator complex - 2019. Complexe des accélérateurs du CERN - 2019.* General Photo. 2019. URL: https://cds.cern.ch/record/2684277.

[23] M. J. Barnes et al. *Injection and extraction magnets: kicker magnets.* 2011. arXiv: 1103.1583 [physics.acc-ph].

[24] D. C. Fiander, P. Pearce, and K. D. Metzmacher. *Kickers and Septa at the PS Complex, CERN.* Tech. rep. CM-P00059157, 1988.

[25] C. R. Ader et al. "Recent experience in the fabrication and brazing of ceramic beam tubes for kicker magnets at FNAL". In: *Conf. Proc. C0806233: wepc139, 2008.* FERMILAB-CONF-08-188-AD. Fermi National Accelerator Lab.(FNAL), Batavia, IL (United States). 2008.

[26] Th. Zickler. *Basic design and engineering of normal-conducting, iron-dominated electromagnets.* 2011. arXiv: 1103.1119 [physics.acc-ph].

[27] Frank Tecker. *Injection and extraction.* Vortrag. 2019. URL: https://cas.web.cern.ch/sites/cas.web.cern.ch/files/2019-Injection-Extraction.pdf.

[28] M. J. Barnes et al. *Injection and extraction magnets: septa*. 2011. arXiv: 1103.1062 [physics.acc-ph].

[29] M. Paraliev. "Septa". In: *CERN Yellow Reports: School Proceedings* 5 (2018), pp. 363–363. DOI: 10.23730/CYRSP-2018-005.363.

[30] Y. Iwashita and A. Noda. "Massless septum with hybrid magnet". In: *Proc. 6th European Particle Accelerator Conference (EPAC'98), Stockholm, Sweden*. 1998, pp. 2109–2110.

[31] C. A. Bertulani. *Nuclear Reactions*. 2010. arXiv: 0908.3275 [nucl-th].

[32] N. Soppera, M. Bossant, and E. Dupont. "JANIS 4: An Improved Version of the NEA Java-based Nuclear Data Information System". In: *Nuclear Data Sheets* 120 (2014), pp. 294–296. DOI: 10.1016/j.nds.2014.07.071.

[33] M.B. Chadwick et al. "ENDF/B-VII.1 Nuclear Data for Science and Technology: Cross Sections, Covariances, Fission Product Yields and Decay Data". In: *Nuclear Data Sheets* 112.12 (2011), pp. 2887–2996. DOI: 10.1016/j.nds.2011.11.002.

[34] A. Allisy et al. "Fundamental Quantities and Units for Ionizing Radiation". In: *Journal of the International Commission on Radiation Units and Measurements* os31.1 (2016), p. 1. DOI: 10.1093/jicru/os31.1.1.

[35] B. A. Weaver and A. J. Westphal. "Energy loss of relativistic heavy ions in matter". In: *Nuclear Instruments and Methods in Physics Research Section B* 187.3 (2002), pp. 285–301. DOI: 10.1016/S0168-583X(01)01143-0.

[36] Claude Leroy and Pier-Giorgio Rancoita. *Principles of Radiation Interaction in Matter and Detection, 2. Ed.* World Scientific Publishing, 2009. DOI: 10.1142/6872.

[37] Eric Sheldon and Pierre Marmier. *Physics of Nuclei and Particles, 2. Ed.* Academic Press, 1970. DOI: 10.1016/C2013-0-11142-7.

[38] A. J. Koning, S. Hilaire, and M. C. Duijvestijn. "TALYS: Comprehensive Nuclear Reaction Modeling". In: *AIP Conference Proceedings* 769.1 (2005), pp. 1154–1159. DOI: 10.1063/1.1945212.

[39] James F. Ziegler, M.D. Ziegler, and J.P. Biersack. "SRIM – The stopping and range of ions in matter (2010)". In: *Nuclear Instruments and Methods in Physics Research Section B* 268.11 (2010), pp. 1818–1823. DOI: 10.1016/j.nimb.2010.02.091.

[40] C. Wiesner. "Chopping and transport of high-intensity ion beams". Dissertation. Frankfurt University, 2014.

[41] A. Schempp. "Radiofrequency quadrupoles (RFQ)". In: *CERN - Rutherford Accelerator School: RF Engineering for Particle Accelerators*. 1991, pp. 522–537.

[42] H. Podlech et al. “Conceptual Design of the Proton LINAC for the High Brilliance Neutron Source HBS”. In: *Proc. 10th International Particle Accelerator Conference (IPAC'19), Melbourne, Australia, 19-24 May 2019*. 2019, pp. 910–913. DOI: 10.18429/JACoW-IPAC2019-MOPTS027.

[43] Mathias Strothmann. “Efficiency of a mesitylene based cold moderator system for a compact accelerator driven neutron source”. MA thesis. RWTH Aachen University, 2020.

[44] P. D. Eversheim et al. In: *Annual Report IKP* Jül-3365 (1996), p. 251.

[45] Y. Otake. “Compact neutron systems expand in applications. RIKEN RANS”. In: *Kasokuki* 13.4 (2017), pp. 229–233.

[46] M. Rimmler et al. “Septa”. In: *Journal of Neutron Research* 23 (2021), pp. 143–156. DOI: 10.3233/JNR-210009.

[47] Sung Oh Cho et al. “Time-resolved measurement of electron beam emittance and energy spread with optical transition radiation”. In: *Nuclear Instruments and Methods in Physics Research Section A* 407.1 (1998), pp. 359–363. DOI: 10.1016/S0168-9002(98)00050-3.

[48] William H. Press et al. *Numerical Recipes Handbook, 3. Ed.* Cambridge University Press, 1992.

[49] David Sagan. *Bmad*. 18, 2018. URL: https://www.classe.cornell.edu/bmad/.

[50] U. Bechstedt et al. “Injection and extraction magnets of COSY-Jülich”. In: *Proceedings, 2nd European Particle Accelerator Conference (EPAC 90)*. Nice, France: Conf.Proc.C 900612, 1990, pp. 1257–1259.

[51] COMSOL Inc. *COMSOL software version 5.6*. 22, 2021. URL: https://www.comsol.de/release/5.6.

[52] Wilfried Weißgerber. *Elektrotechnik für Ingenieure 2, 9. Aufl.* Springer Vieweg, 2015. DOI: 10.1007/978-3-658-09100-2.

[53] Jan Henry Hetzel. “Beam-dynamics calculations including magnetic field measurements for the high-energy storage ring (HESR) at FAIR”. Dissertation. Aachen: RWTH Aachen University, 2018. URL: https://publications.rwth-aachen.de/record/723015.

[54] N. Pichoff D. Uriot. *TraceWin*. 12, 2021. URL: http://irfu.cea.fr/dacm/logiciels/.

[55] Dominic Markus Welsch. “Investigation and Optimization of TransverseNon-Linear Beam Dynamics in the High-Energy Storage Ring HESR”. Dissertation. Bonn: Mathematisch-Naturwissenschaftliche Fakultät der Rheinischen Friedrich-Wilhelms-Universität Bonn, 2010.

[56] H. Thomsen and S. Møller. “The Design of the Fast Raster System for the European Spallation Source”. In: *5th International Particle Accelerator Conference*. 2014. DOI: 10.18429/JACoW-IPAC2014-WEPRO072.

[57] Ceramic Magnetics Inc. *CMD5005*. 5, 2021. URL: https://www.magneticsgroup.com/wp-content/uploads/2019/09/CMD5005-ISO-WEB-DATA.pdf.

[58] J. Alderman et al. "Measurement of radiation-induced demagnetization of Nd–Fe–B permanent magnets". In: *Nuclear Instruments and Methods in Physics Research Section A* 481.1 (2002), pp. 9–28. DOI: 10.1016/S0168-9002(01)01329-8.

[59] A. J. Samin. "A review of radiation-induced demagnetization of permanent magnets". In: *Journal of Nuclear Materials* 503 (2018), pp. 42–55. DOI: 10.1016/j.jnucmat.2018.02.029.

[60] C. H. Chen et al. "The effect of neutron irradiation on NdFeB and Sm2Co17-based high-temperature magnets". In: *IEEE Transactions on Magnetics* 41.10 (2005), pp. 3832–3834. DOI: 10.1109/TMAG.2005.854985.

[61] J. R. Cost et al. "Effects of neutron irradiation on Nd-Fe-B magnetic properties". In: *IEEE Transactions on Magnetics* 24.3 (1988), pp. 2016–2019. DOI: 10.1109/20.3393.

[62] T. Bizen et al. "Idea of Mechanism and Protection of Radiation Damage on Undulator Permanent Magnet". In: *AIP Conference Proceedings* 879.1 (2007), pp. 420–423. DOI: 10.1063/1.2436089.

[63] R. D. Brown and J. R. Cost. "Radiation-induced changes in magnetic properties of Nd-Fe-B permanent magnets". In: *IEEE Transactions on Magnetics* 25.4 (1989), pp. 3117–3120. DOI: 10.1109/20.34383.

[64] Bakker Magnetics BV. *Samarium Cobalt - Sintered*. 24, 2021. URL: https://bakkermagnetics.com/wp-content/uploads/2019/01/samarium_cobalt_-_sintered_0.pdf.

[65] VACUUMSCHMELZE GmbH Co. KG. *SmCo Magnete aus VACOMAX*. 24, 2021. URL: https://vacuumschmelze.de/Produkte/Dauermagnete/SmCo-Magnete---VACOMAX.

[66] E. Mauro and M. Silari. "Radiation protection studies for a high-power 160MeV proton linac". In: *Nuclear Instruments and Methods in Physics Research Section A* 605.3 (2009), pp. 249–265. DOI: 10.1016/j.nima.2009.03.250.

[67] E. W. Blackmore. "Radiation Effects of Protons on Samarium-Cobalt Permanent Magnets". In: *IEEE Transactions on Nuclear Science* 32.5 (1985), pp. 3669–3671. DOI: 10.1109/TNS.1985.4334463.

[68] R. Hardekopf. *Permanent magnet radiation resistance in the SNS linac*. Tech. rep. SNS technical note, 2001.

[69] J. Blaha et al. "Long-term residual radioactivity in an intermediate-energy proton linac". In: *Nuclear Instruments and Methods in Physics Research Section A* 753 (2014), pp. 61–71. DOI: 10.1016/j.nima.2014.03.058.

[70] T. T. Böhlen et al. "The FLUKA code: developments and challenges for high energy and medical applications". In: *Nuclear data sheets* 120 (2014), pp. 211–214. DOI: 10.1016/j.nds.2014.07.049.

[71] Yu. Valdau et al. In: *IBIC2016 Conference proceedings*. Barcelona, Spain, 2017, pp. 434–437.

[72] O. Felden et al. "Recent Extensions of JULIC for HBS Investigations". In: 22nd Int. Conf. on Cyclotrons and their Applications. 22, 2019. DOI: 10.18429/JACoW-Cyclotrons2019-TUP019.

[73] Dr. Westmeier GmbH. *HPGe Software*. 11, 2020. URL: http://www.westmeier.com/hpge-spektrometrie/hpge-software/.

[74] P. Forck. *Beam Instrumentation and Diagnostics*. 2020. arXiv: 2009.10411 [physics.acc-ph].

[75] A. Boston. *Introduction to MCNP - the monte carlo transport code*. University of Liverpool, 2014.

[76] H.J. Brede et al. "Neutron yields from thick Be targets bombarded with deuterons or protons". In: *Nuclear Instruments and Methods in Physics Research Section A* 274.1 (1989), pp. 332–344. DOI: 10.1016/0168-9002(89)90399-9.

[77] I. Tilquin et al. "Experimental measurements of neutron fluxes produced by proton beams (23–80MeV) on Be and Pb targets". In: *Nuclear Instruments and Methods in Physics Research Section A* 545.1 (2005), pp. 339–343. DOI: 10.1016/j.nima.2005.01.325.

[78] M.A. Lone et al. "Thick target neutron yields and spectral distributions from the 7Li(pd, n) and 9Be(pd, n) reactions". In: *Nuclear Instruments and Methods* 143.2 (1977), pp. 331–344. DOI: 10.1016/0029-554X(77)90616-4.

[79] P. Zakalek et al. "Efficiency of a cold moderator system based on a liquid ortho-para hydrogen mixing cryostat". to be published. 2021.

[80] A. J. Koning et al. "TENDL: Complete Nuclear Data Library for Innovative Nuclear Science and Technology". In: *Nuclear Data Sheets* 155 (2019). Special Issue on Nuclear Reaction Data, pp. 1–55. DOI: 10.1016/j.nds.2019.01.002.

List of Figures

List of Tables

Abbreviations

ADC Analog Digital Converter

AVF Azimuthally Varying Field

BPM Beam Position Monitor

CBS Colliding Beam Source

CERN Conseil Européen pour la Recherche Nucléaire

CH Crossbar H-mode

CNC Computerized Numerical Control

COSY COoler SYnchrotron

CPU Central Processing Unit

CW Continuous Wave

DAC Digital Analog Converter

DC Direct Voltage

DCCT DC Current Transformer

DTL Drift Tube Linac

ECR Electron Cyclotron Resonance

ENDF Evaluated Nuclear Data File

ESS European Spallation Source

FCT Fast Current Transformer

FEM Finite Element Method

FLUKA FLUktuierende KAskade

FODO Focusing-drift-defocusing-drift

FWHM Full Width at Half Maximum

HBS High Brilliance neutron Source

HEBT High Energy Beam Transport

HPGe High-Purity Germanium

HPM Horizontally magnetized Permanent Magnet

HV High Voltage

IBP IndustrieBestrahlungsPlatz (industry irradiation site)

IGBT Insulating-Gate Bipolar Transistor

IKP Institut für Kernphysik (nuclear physics institute)

JULIC JUelich Light Ion Cyclotron

LEBT Low Energy Beam Transport

LHC Large Hadron Collider

LV Low Voltage

MCNP Monte-Carlo N-Particle Transport

MEBT Medium Energy Beam Transport

MWPC Multi-Wire Proportional Chamber

NESP NiederEnergiebeStrahlungsPlatz (low energy irradiation site)

PE Polyethylene

PGNAA Prompt Gamma Neutron Activation Analysis

PMMA Poly methyl methacrylate

RANS RIKEN Accelerator-driven compact Neutron Source

RF Radio Frequency

RFQ Radio Frequency Quadrupole

SRIM Stopping and Range of Ions in Matter

TFM Three-Field Magnet

TFSM Three-Field Septum Magnet

TMR Target-Moderator-Reflector

ToF Time-of-Flight

TTL Transistor–Transistor Logic

Danksagung

Die Vollendung dieser Dissertation ist für mich ein wichtiger und lange ersehnter Meilenstein, welchen ich ohne die tatkräftige und motivierende Unterstützung vieler Menschen nicht erreicht hätte. Daher möchte ich allen danken, die mir auf verschiedenste Weise geholfen haben.

- Ich möchte Prof. Dr. Thomas Brückel dafür danken, dass er es mir als Doktorvater ermöglicht hat an diesem interdisziplinären und somit sehr abwechslungsreichen Thema zu arbeiten, welches Aspekte der Beschleuniger- und Kernphysik sowie der Neutronenstreuung vereint.

- Ich danke Prof. Dr. Jörg Pretz für die Übernahme des zweiten Berichters.

- Ein großer Dank gebührt Dr. Ralf Gebel, der mir die Möglichkeit geboten hat am Institut für Kernphysik zu arbeiten und mich bei meiner Arbeit mit Fachwissen, Strategie und materieller Unterstützung bekräftigt hat. Außerdem möchte ich mich dafür bedanken, dass ich in der Zeit meiner Promotion mehrere Fortbildungen und Workshops besuchen konnte.

- Darüberhinaus danke ich Dr. Thomas Gutberlet für die Aufnahme in die HBS Arbeitsgruppe und für die Unterstützung bei Publikationen.

- Ich danke meinen Betreuern Dr. Olaf Felden und Dr. Ulrich Rücker für die intensive und hilfreiche Betreuung während meiner Doktorarbeit. Insbesondere für die Ünterstützung bei der Durchführung von Experimenten, für regelmäßgie gemeinsame Beratungen über den weiteren Verlauf der Doktorarbeit und für das intensive und konstruktive Korrekturlesen der Arbeit möchte ich mich bedanken.

- Dr. Helmut Soltner möchte ich für die Hilfe bei der Auslegung permanentmagnetischer Systeme und generelle Beratungen bezüglich des Designs von magnetischen Systemen sowie deren Herstellung danken. Die Entwicklung und die Konstruktion des "Three-Field Septum Magnet" wäre ohne diese Unterstützung nicht so erfolgreich gewesen.

- Ein großer Dank gebührt auch Dr. Paul Zakalek für die Hilfe und Beratung bei der Neutron Yield Messung und der daraus resultierenden Publikation. Seine positive Einstellung hat selbst in problematischen Situation für eine gute Motivation gesorgt.

- In diesem Zusammenhang danke ich weiteren Kollegen, welche an der Neutron Yield Publikation mitgewirkt haben: Dr. Jingjing Li, Dr. Eric Mauerhofer.
- Ich möchte mich besonders bei Nils-Oliver Fröhlich und Dr. Yury Valdau bedanken. Danke für die tolle gemeinsame Zeit am IKP, die große Hilfe (und Unterhaltung) bei Strahlzeiten (auch am Wochenende oder am späten Abend!) und die Möglichkeit selbst am Zyklotron zu arbeiten.
- Danke an Nils Demary für seine tolle Unterstützung in Form von Konstruktionszeichnungen und ingenieurstechnischer Beratung.
- Danke an Markus Retzlaff für die Hilfe bei elektrotechnischen Problemen, Plänen und Anliegen.
- Prof. Dr. Andreas Lehrach danke ich für seine Hilfe bei beschleunigerphysikalischen Fragestellungen.
- Dr. Sig Martin† gebührt ein besonderer Dank dafür, dass er mich am Anfang meiner Promotion mit seinem sehr umfassenden Wissen und seiner langjährigen Erfahrung unterstützt hat.
- Ich danke dem ganzen restlichen HBS Team, Dr. Johannes Baggemann, Qi Ding, Paul-Emmanuel Doege, Dr. Klaus Lieutenant, Dr. Zhanwen Ma, Alexander Schwab, Robin Similon, Mathias Strothmann und Dr. Jörg Voigt für die gemeinsamen Diskussionen, Kaffeegespräche und insbesondere tolle Gesellschaft bei Konferenzen und Workshops. Besonders der HBS Unkel Workshop war immer ein Vergnügen.
- Danke an Phuong Ho und Sebastian Kock für die tolle Zeit in der Mitfahrgelegenheit.
- Danke an alle Kollegen und Freunde, welche die Arbeit Korrektur gelesen haben: Dr. Helmut Soltner, Dr. Paul Zakalek, Patrick Krömer.
- Danke an die Kollegen des IAP in Frankfurt: Prof. Dr. Holger Podlech und Dr. Oliver Meusel (auch für die Einladung zum Ski-Workshop). Insbesondere möchte ich Malte Schwarz für die tatkräftige Unterstützung bei der Verwendung der *TraceWin* Software danken. Ich weiß diese Hilfe sehr zu schätzen!

Ich möchte ganz besonders meinen Freunden und meiner Familie danken. Danke an meine Eltern, die mich immer unterstützt und in meinen Entscheidungen bekräftigt haben.

Schließlich geht ein sehr großer Dank an meine Freundin Christin für ihre Geduld und ihre Unterstützung in der ganzen Zeit und insbesondere an den langen Schreibtagen in den letzten Monaten. Danke, dass du trotz Lockdown und langen Arbeitstagen so positiv geblieben bist und danke, dass es dich gibt!

Band / Volume 236
Nanoparticle assemblies: Order by self-organization and collective magnetism
A. Qdemat (2021), xix, 282 pp
ISBN: 978-3-95806-542-0

Band / Volume 237
γ-Aminobutyrate as carbon and nitrogen source for *Corynebacterium glutamicum* and regulation of the catabolic genes by GabR
L. Zhu (2021), 111 pp
ISBN: 978-3-95806-543-7

Band / Volume 238
Single-Trap Phenomena in Nanowire Biosensors
Y. Kutovyi (2021), 171 pp
ISBN: 978-3-95806-544-4

Band / Volume 239
Single crystal growth and neutron scattering studies of novel quantum materials
X. Wang (2021), VI, 145 pp
ISBN: 978-3-95806-546-8

Band / Volume 240
Structure and Dynamics of Magnetocaloric Materials
N. A. Maraytta (2021), vii, 146 pp
ISBN: 978-3-95806-557-4

Band / Volume 241
Novel insights into the transcriptional regulation of cell division in *Corynebacterium glutamicum*
K. J. Kraxner (2021), V, 83 pp
ISBN: 978-3-95806-560-4

Band / Volume 242
Interplay of proximity effects in superconductor/ferromagnet heterostructures
A. Stellhorn (2021), ix, 219 pp
ISBN: 978-3-95806-562-8

Band / Volume 243
Silencing and counter-silencing of the Lsr2-like protein CgpS in *Corynebacterium glutamicum*
J. Wiechert (2021), IV, 265 pp
ISBN: 978-3-95806-569-7

Band / Volume 244
Molecular Layer Functionalized Neuroelectronic Interfaces:
From Sub-Nanometer Molecular Surface Functionalization to
Improved Mechanical and Electronic Cell-Chip Coupling
N. R. Wolf (2021), IV, 101, xx pp
ISBN: 978-3-95806-570-3

Band / Volume 245
Surface Acoustic Waves in Strain-Engineered Thin (K,Na)NbO_3 Films:
From Basic Research to Application in Molecular Sensing
S. Liang (2021), VI, 125 pp
ISBN: 978-3-95806-571-0

Band / Volume 246
Tailoring neuroelectronic interfaces via combinations of oxides and molecular layers
X. Yuan (2021), 113 pp
ISBN: 978-3-95806-572-7

Band / Volume 247
Stoichiometric control and magnetoelectric coupling in artificial multiferroic heterostructures
P. Schöffmann (2021), vii, 176 pp
ISBN: 978-3-95806-575-8

Band / Volume 248
A Unified Framework for Functional Renormalisation Group Calculations and its Application to Three Dimensional Hubbard Models
J. Ehrlich (2021), xvi, 213 pp
ISBN: 978-3-95806-582-6

Band / Volume 249
Photoemission electron microscopy of magneto-ionic effects in $La_{0.7}Sr_{0.3}MnO_3$
M. Wilhelm (2021), 134 pp
ISBN: 978-3-95806-592-5

Band / Volume 250
Development of a Multiplexer System and Measurement of the Neutron Yield for a Low-Energy Accelerator-Driven Neutron Source
M. Rimmler (2021), v, 200 pp
ISBN: 978-3-95806-600-7

Weitere ***Schriften des Verlags im Forschungszentrum Jülich*** unter
http://wwwzb1.fz-juelich.de/verlagextern1/index.asp

Schlüsseltechnologien / Key Technologies
Band / Volume 250
ISBN 978-3-95806-600-7

Mitglied der Helmholtz-Gemeinschaft

JÜLICH
Forschungszentrum